

Electronic Thesis and Dissertation Repository

2-22-2011 12:00 AM

Hemodynamics in the Stenosed Carotid Bifurcation with Plaque Ulceration

Emily Y. Wong
The University of Western Ontario

Supervisor
Dr. David Holdsworth
The University of Western Ontario

Graduate Program in Medical Biophysics
A thesis submitted in partial fulfillment of the requirements for the degree in Doctor of
Philosophy
© Emily Y. Wong 2011

Follow this and additional works at: <https://ir.lib.uwo.ca/etd>



Part of the [Diagnosis Commons](#), [Fluid Dynamics Commons](#), and the [Medical Biophysics Commons](#)

Recommended Citation

Wong, Emily Y., "Hemodynamics in the Stenosed Carotid Bifurcation with Plaque Ulceration" (2011).
Electronic Thesis and Dissertation Repository. 94.
<https://ir.lib.uwo.ca/etd/94>

This Dissertation/Thesis is brought to you for free and open access by Scholarship@Western. It has been accepted for inclusion in Electronic Thesis and Dissertation Repository by an authorized administrator of Scholarship@Western. For more information, please contact wlsadmin@uwo.ca.

HEMODYNAMICS IN THE STENOSED CAROTID BIFURCATION WITH
PLAQUE ULCERATION

(Spine title: Hemodynamics in the Ulcerated Carotid Stenosis)

(Thesis format: Integrated-Article)

by

Emily Yee-Wah Wong

Graduate Program in Medical Biophysics

A thesis submitted in partial fulfillment
of the requirements for the degree of
Doctor of Philosophy

The School of Graduate and Postdoctoral Studies
The University of Western Ontario
London, Ontario, Canada

© Emily Y. Wong 2011

THE UNIVERSITY OF WESTERN ONTARIO
School of Graduate and Postdoctoral Studies

Certificate of Examination

Supervisor

Dr. David Holdsworth

Co-Supervisor

Dr. Tamie Poepping

Supervisory Committee

Dr. Richard Rankin

Dr. James Lacefield

Examiners

Dr. Brian Fowlkes

Dr. Kamran Siddiqui

Dr. Daniel Goldman

Dr. Grace Parraga

The thesis by

Emily Yee-Wah Wong

entitled:

**Hemodynamics in the Stenosed Carotid Bifurcation with Plaque
Ulceration**

is accepted in partial fulfillment of the
requirements for the degree of
Doctor of Philosophy

Date

Chair of Examining Board

Abstract

The presence of irregular plaque surface morphology or ulceration of the atherosclerotic lesion has been identified as an independent risk factor for ischemic stroke. Doppler ultrasound (DUS) is the most commonly performed non-invasive technique used to assess patients suspected of having carotid artery disease, but currently does not incorporate the diagnosis of plaque ulceration. Advanced Doppler analyses incorporating quantitative estimates of flow disturbances may result in diagnostic indices that identify plaque ulcerative conditions.

A technique for the fabrication of DUS-compatible flow phantoms was developed, using a direct-machining method that is amenable to comprehensive DUS investigations. *In vitro* flow studies in an ensemble of matched-model vessel geometries determined that ulceration as small as 2 mm can generate significant disturbances in the downstream flow field in a moderately stenosed carotid artery, which are detectable using the DUS velocity-derived parameter turbulence intensity (TI) measured with a clinical system. Further experimental results showed that distal TI was significantly elevated ($P < 0.001$) due to proximal plaque ulceration in the mild and moderately stenosed carotid bifurcation (30%, 50%, 60% diameter reduction), and also increased with stenosis severity. Pulsatile computational fluid dynamics (CFD) models, with simulated particle tracking, demonstrated enhanced flow disruption of the stenotic jet and slight elevations in path-dependent shear exposure parameters in a stenosed carotid bifurcation model with ulceration. In addition, CFD models were used to evaluate the DUS index TI using finite volume sampling.

Keywords: atherosclerosis, carotid artery, plaque ulceration, flow disturbances, Doppler ultrasound, computational fluid dynamics, flow models

Co-Authorship Statement

This thesis contains material presented in manuscripts that have been published in peer-reviewed journals. Permissions to reproduce these manuscripts appear in Appendix A.

Chapter 2 presents material from an article entitled “Doppler ultrasound compatible plastic material for use in rigid flow models,” which has been published in *Ultrasound in Medicine and Biology*. The article is co-authored by E. Y. Wong, M. L. Thorne, H. N. Nikolov, T. L. Poepping, and D. W. Holdsworth. I performed the experiments, analyzed the results and wrote the manuscript. H. N. Nikolov performed the fabrication of the phantom and reviewed the manuscript prior to submission. M. L. Thorne, T. L. Poepping, and D. W. Holdsworth reviewed the results and manuscript prior to submission.

Chapter 3 presents material from an article entitled “Clinical Doppler ultrasound for the assessment of plaque ulceration in the stenosed carotid bifurcation by detection of distal turbulence intensity: a matched model study,” which has been published in *European Radiology*. The article is co-authored by E. Y. Wong, H. N. Nikolov, M. L. Thorne, T. L. Poepping, R. N. Rankin, and D. W. Holdsworth. I designed the phantom geometries, performed the experiments, analyzed the results and wrote the manuscript. H. N. Nikolov performed the fabrication of the phantoms and reviewed the manuscript prior to submission. M. L. Thorne, R. N. Rankin, T. L. Poepping, and D. W. Holdsworth reviewed the results and manuscript prior to submission.

Dedication

For my grandmother Wai Fong Chang

Acknowledgments

I would like to express my deep thankfulness and gratitude to many people who have been kindly generous with their help and support throughout the forming of this thesis (which I have sometimes light-heartedly likened to a particular submarinal epic).

Thank you, especially, to my supervisors Dr. David Holdsworth and Dr. Tamie Poepping, who have helped me to navigate the new landscapes and from whom I have learned much. David, thank you for your guidance and timely insights (and valuable insights on insights) with respect to research and on transforming the knowledge which lies in the tacit dimensions. Tamie, thank you for your endless patience and encouragement. Our conversations were always inspirational and creative roots to future developments.

A great measure of thanks to Hristo Nikolov for his tireless consideration and prudent advice, and exceptional standards, in spite of the work that I would spring upon him. Thanks to Jaques Milner for his work on the numerical models, and for taking the time to teach me the essentials of a complex field. To Dr. Dick Rankin and Dr. Jim Lacefield for their helpful observations and for sharing their expertise on research matters.

Much love and thanks to my family, especially to my parents, Christine and David. Appreciation and love to my brother, Nathaniel, who is boundlessly inspiring. Thank you to Andrew for helping me to seal many leaky phantoms, which seemed to disclose their contents quite irrationally in time and space. Finally, thank you to the many people whom I have had the honour of meeting and have inscribed their indelible mark on my experience.

Repetition is a form of change

~ Brian Eno

Table of Contents

Certificate of Examination	ii
Abstract.....	iii
Co-Authorship Statement	iv
Dedication	v
Acknowledgments	vi
Table of Contents	viii
List of Tables.....	xiii
List of Figures	xiv
List of Abbreviations and Symbols.....	xix
1 Introduction	1
1.1 Thromboembolic Stroke.....	1
1.1.1 Growing burden of stroke	2
1.2 Carotid Atherosclerosis.....	3
1.3 Management of Carotid Plaque.....	6
1.3.1 Selection for therapy	7
1.3.1.1 <i>Symptomatic patients</i>	7
1.3.1.2 <i>Asymptomatic patients</i>	8
1.3.2 Selection of therapy: carotid endarterectomy and stenting	8
1.3.3 Current diagnosis.....	9
1.3.4 Limitations of current diagnosis.....	10
1.3.5 Considerations for carotid plaque ulcerations in diagnosis	11
1.4 Carotid Plaque Pathology.....	12
1.4.1 Morphology and risk	12
1.4.1.1 <i>Internal plaque morphology</i>	12
1.4.1.2 <i>Plaque surface ulcerations</i>	13
1.5 Diagnostic Imaging of Carotid Plaque Surface Morphology	16
1.5.1 Angiography	16
1.5.1.1 <i>X-ray digital subtraction angiography (DSA)</i>	16
1.5.1.2 <i>Computed tomography angiography (CTA)</i>	17

1.5.1.3	<i>Magnetic resonance angiography (MRA)</i>	17
1.5.2	Ultrasound.....	18
1.6	Carotid Artery Hemodynamics.....	19
1.7	Abnormal Hemodynamics and Thrombogenesis	20
1.7.1	Blood and thrombosis.....	21
1.7.1.1	<i>Role of platelets</i>	22
1.8	Hemodynamic Factors in Thrombogenesis	23
1.8.1	Turbulence and disturbed flow	23
1.8.2	Fluid shear stress and wall shear stress.....	24
1.8.3	Recirculation zones and residence time	25
1.8.4	Platelet activation models.....	26
1.8.5	Effect of carotid plaque symmetry.....	28
1.8.6	Effect of carotid plaque ulceration.....	29
1.9	Blood Flow Characterization	30
1.9.1	Doppler ultrasound (DUS).....	30
1.9.1.1	<i>Ultrasound principles</i>	30
1.9.1.2	<i>Doppler ultrasound principles</i>	32
1.9.1.3	<i>The Doppler ultrasound spectrum</i>	32
1.9.1.4	<i>Characterization of flow disturbances</i>	34
1.9.1.5	<i>Doppler spectral indices</i>	35
1.9.2	Computational fluid dynamics (CFD)	37
1.10	Research Objectives and Thesis Outline.....	38
1.11	References	40
2	Doppler Ultrasound Compatible Plastic Material for Use in Rigid Flow Models	70
2.1	Introduction.....	70
2.2	Materials and Methods	72
2.2.1	Candidate materials.....	72
2.2.2	Characterization of acoustic properties.....	73
2.2.3	Phantom fabrication.....	74
2.2.4	Non-destructive evaluation.....	77
2.2.5	Phantom measurements	77
2.2.5.1	<i>Comparison of velocity profiles</i>	77
2.2.5.2	<i>Mean velocity mapping under pulsatile flow conditions</i>	80
2.3	Results	81
2.3.1	Speed of sound and attenuation characterization	81
2.3.2	Fidelity of fabrication technique.....	83

2.3.3	Comparison of velocity profiles.....	84
2.3.4	Mean velocity mapping under pulsatile flow conditions	87
2.4	Discussion.....	89
2.5	Conclusion	93
2.6	References	93
3	Clinical Doppler Ultrasound for the Assessment of Plaque Ulceration in the Stenosed Carotid Bifurcation By Detection of Distal Turbulence Intensity: A Matched Model Study.....	103
3.1	Introduction.....	103
3.2	Materials and Methods	106
3.2.1	Phantom design.....	106
3.2.1.1	<i>Vessel and ulcer geometry.....</i>	<i>106</i>
3.2.1.2	<i>Fabrication technique.....</i>	<i>108</i>
3.2.1.3	<i>Evaluation of vessel geometry.....</i>	<i>109</i>
3.2.2	Doppler data acquisition.....	109
3.2.3	Data analysis.....	111
3.2.4	Statistical analysis	112
3.3	Results	113
3.3.1	Verification of phantom geometry	113
3.3.2	Turbulence intensity (TI).....	113
3.3.2.1	<i>Ulcer size and shape.....</i>	<i>118</i>
3.3.3	Other velocity parameters	119
3.4	Discussion.....	123
3.5	Conclusion	128
3.6	References	128
4	The Effect of Both Plaque Ulceration and Stenosis Grade on Distal Turbulence Intensity in the Carotid Bifurcation Using Clinical Doppler Ultrasound	144
4.1	Introduction.....	144
4.2	Methods	146
4.2.1	Carotid bifurcation flow phantoms.....	146
4.2.2	Doppler data acquisition.....	148
4.2.3	Data analysis.....	149
4.2.4	Statistical analysis	150
4.3	Results	152
4.4	Discussion.....	160
4.5	Conclusion	169

4.6	References	169
5	Numerical Evaluation of Ulceration on Simulated Blood-Particle Shear Exposure and Turbulence Intensity Index in the Stenosed Bifurcation ..	180
5.1	Introduction.....	180
5.2	Methods	183
5.2.1	Model geometries	183
5.2.2	Doppler ultrasound <i>in vitro</i> flow measurements	187
5.2.3	CFD simulations	187
5.2.4	CFD simulated turbulence intensity (TI).....	188
5.2.5	Virtual particle tracking	189
5.2.6	Assessment of particle shear stress history	190
5.3	Results	192
5.3.1	Flow features	192
5.3.2	CFD simulated turbulence intensity (TI).....	194
5.3.3	Virtual particle tracking	197
	<i>5.3.3.1 Particle pathlines</i>	197
	<i>5.3.3.2 Particle shear stress histories</i>	197
5.4	Discussion.....	204
5.4.1	Simulated turbulence intensity (TI).....	205
5.4.2	Virtual particle tracking	206
5.5	Conclusion	208
5.6	References	209
6	Summary and Future Work	216
6.1	Summary	216
6.1.1	Summary of Chapter 2.....	216
6.1.2	Summary of Chapter 3.....	216
6.1.3	Summary of Chapter 4.....	217
6.1.4	Summary of Chapter 5.....	218
6.2	Future Directions.....	219
6.2.1	Directly machined Doppler ultrasound compatible phantoms....	219
6.2.2	Doppler ultrasound turbulence intensity (TI).....	220
6.2.3	Numerical analysis of Doppler ultrasound TI	222
6.3	References	223
	Appendix A.....	226
	Appendix B.....	229

Appendix C.....	231
Appendix D.....	234
Curriculum Vitae	235

List of Tables

Table 2.1: Speed of sound and acoustic attenuation values measured for the five candidate materials. The percent difference in SoS is calculated with respect to the SoS value of 1540 m s^{-1} for the soft tissue average.....	81
Table 3.1: Maximum TI in the ROI located within the distal ICA.	119
Table 4.1: TI values from the ROI located within the distal ICA. Maximum TI in the cardiac cycle, TI averaged over a 24-ms window (3 time points) centred on the time of maximum TI, and highest TI value from a single site in the ROI are reported. Values are mean TI \pm SD based on ^a 10 $\overline{\text{TI}}_{24}$, ^b 30 $\overline{\text{TI}}_{24}$ ($3 \times 10 \overline{\text{TI}}_{24}$), and ^c 10 repeated measurements of TI at a single location in the ROI.	154
Table 4.2: Differences in post-peak systolic TI and p -values from two-way ANOVA post-hoc analysis. TI values are averaged from three consecutive time points for a 24-ms window following peak systole centred on the time of maximum TI. ns = not statistically significant ($P > 0.05$). Δ TI is calculated as the TI value in the row-indicated model subtracted from the TI value in the column-indicated model.....	155
Table 4.3: Variability statistics in TI measured in the distal ROI at the time of maximum TI in the cardiac cycle in each model. Reported SD are in cm s^{-1}	159
Table C.1: Mean differences and p -values from repeated measures one-way ANOVA post-hoc analysis for the parameters spectral width (SW), spectral broadening index (SBI), standard deviation in peak velocity (SDPV) and turbulence intensity (TI), corresponding to data in Chapter 3. Mean differences (mean Δ) are calculated as the difference in the value of the parameter ($N = 240$) within the distal ROI in Model B subtracted from the value of the parameter in Model A, averaged for 79 time points ($N = 79$). ns = not statistically significant ($P > 0.05$).....	233

List of Figures

Figure 1.1: The carotid artery bifurcation in the neck, where the internal and the external carotid arteries branch from the common carotid artery at the apex of the bifurcation.....	5
Figure 1.2: Examples of four types of angiographic carotid plaque surface ulceration.....	15
Figure 1.3: Duplex ultrasound display from a carotid Doppler examination. http://www.nvcardiology.com/vascular_testing.htm	33
Figure 2.1: Carotid bifurcation flow phantom showing (a) 3-D CAD design of the two-part phantom, (b) photograph of the machined halves, and (c) fully assembled phantom. The <i>concave arrows</i> indicate the locations of the centering pins.....	76
Figure 2.2: Carotid bifurcation phantom mounted in a water bath with the ultrasound probe attached to the translational stage and mechanically tilted at a 10° angle from the vessel axis.	79
Figure 2.3: Attenuation coefficient as a function of frequency for Teflon®. Each error bar is determined from the linear regression for the corresponding attenuation coefficient. The R-squared value of the regression is 0.999.....	82
Figure 2.4: Micro-computed tomography surface mesh of the lumen geometry in the Teflon® carotid bifurcation phantom.	83
Figure 2.5: Relative (a) vertical and (b) horizontal v_{mean} profiles and relative (c) vertical and (d) horizontal standard deviations of v_{mean} profiles from the Teflon® phantom and the silicone-walled phantom. The expected parabolic velocity profile for mean velocity is shown for comparison (<i>solid line</i>).	85
Figure 2.6: Point-by-point differences in mean velocity between the measured v_{mean} profiles and the expected parabolic profile through the centerline of the Teflon® phantom and the silicone-walled phantom. The vertical profile is shown in (a) and the horizontal profile is shown in (b).	86
Figure 2.7: Colour-encoded maps for a transverse slice of the 8-mm CCA for the Teflon® phantom (<i>left panels</i>) and the silicone-walled phantom (<i>right panels</i>) representing (a, b) mean velocity, (c, d) standard deviation in mean velocity, (e, f) peak velocity and (g, h) integrated power.....	88
Figure 2.8: Colour-encoded flow map of ensemble-averaged mean velocity, \bar{v}_{mean} , in the longitudinal central plane of the Teflon® bifurcation phantom, measured in a 12-ms acquisition window near peak systole.....	89

Figure 3.1: The carotid bifurcation lumen geometries used in our study. The CAD models are of an idealized 50% eccentric carotid bifurcation with (a) a smooth non-ulcerated wall; a hemispherical ulcer of (b) 2-mm, (c) 3-mm and (d) 4-mm diameter; (e) a mushroom-shaped ulcer; an ellipsoidal ulcer pointing (f) distally and (g) proximally. The boundary defined by the normal carotid bifurcation geometry is shown in *light grey* to illustrate the location of plaque deposition. 108

Figure 3.2: Colour-encoded maps of turbulence intensity in the central plane of the (a) non-ulcerated phantom and the (b, c) 2-mm, (d, e) 3-mm, and (f, g) 4-mm hemispherical ulcer phantoms, at 48 ms post-peak systole, where (c, e, g) are subtraction maps of turbulence intensity in the ICA of the ulcer phantom relative to the non-ulcerated phantom. 115

Figure 3.3: Turbulence intensity versus cardiac cycle time in the ROI for the non-ulcerated phantom, and the 2-mm, 3-mm and 4-mm hemispherical ulcer phantoms. The value of turbulence intensity at each time point is an average of ten repetitions (each of ten cardiac cycles) at each of the 24 acquisition sites in the ROI ($N = 240$). Standard errors are shown for two time points: in end diastole (seen at a time of 60 ms) and at 48 ms post-peak systole (seen at a time of 264 ms). A schematic of the carotid flow-rate waveform is overlaid (*solid grey line*) to indicate the relative positions of systole and diastole. Peak systole occurs at approximately 210 ms, as indicated by the *vertical dashed line*. 116

Figure 3.4: Turbulence intensity versus cardiac cycle time in the ROI for ulcer phantoms of various shapes (mushroom, ellipsoidal pointing distally and ellipsoidal pointing proximally) and for the non-ulcerated phantom. Standard errors are shown in end diastole (seen at a time of 60 ms). A schematic of the carotid flow-rate waveform is overlaid (*solid grey line*) to indicate the relative positions of systole and diastole. Peak systole occurs at approximately 210 ms. 117

Figure 3.5: Colour-encoded maps of ensemble-averaged (a, b) mean velocity and (c, d) peak velocity in the central plane of the non-ulcerated phantom (*left column*) and the 4-mm hemispherical ulcer phantom (*right column*) at peak systole. 121

Figure 3.6: Colour-encoded maps of ensemble-averaged (a, b) spectral width, (c, d) spectral broadening index, and (e, f) standard deviation in peak velocity in the central plane of the non-ulcerated phantom (*left column*) and the 4-mm hemispherical ulcer phantom (*right column*) at 48 ms post-peak systole. 121

Figure 3.7: The Doppler ultrasound parameters (a, b) spectral width, (c, d) spectral broadening index, and (e, f) standard deviation in peak velocity versus cardiac cycle time in the ROI, where a comparison with ulcer size is shown in the *left column* (2-mm, 3-mm and 4-mm hemispherical ulcers)

and a comparison with ulcer shape is shown in the *right column* (mushroom, ellipsoidal pointing distally and ellipsoidal pointing proximally). Schematics of the carotid flow-rate waveform are overlaid on each graph (*solid grey line*) to indicate the relative positions of systole and diastole. Peak systole occurs at approximately 210 ms. Standard errors are shown for a representative time point of 60 ms. 122

Figure 4.1: Carotid bifurcation geometries used in this study. The *top row* (a–d) consists of the non-ulcerated geometries corresponding to 30%, 50%, 60% and 70% stenosis, by NASCET criteria (left to right). The *bottom row* (e–h) consists of the respective ulcerated geometries. Phantoms extended from over 100 mm proximal to 50 mm distal to the apex of the bifurcation. The normal carotid bifurcation geometry is shown in *light grey* to illustrate the location of plaque deposition. 147

Figure 4.2: Distal TI from ten $\overline{\text{TI}}_{24}$ versus cardiac cycle time for the non-ulcerated (*solid-line*) and ulcerated (*dashed-line*) phantoms. The value of TI at each time point is an average of ten repetitions of $\overline{\text{TI}}_{24}$ from the distal ICA. Standard deviations of ten $\overline{\text{TI}}_{24}$ are shown at three representative time points: 156 ms prior to peak systole, and 36 ms and 636 ms following peak systole. A schematic of the carotid flow-rate waveform is overlaid (*solid grey line*) to indicate the relative positions of systole and diastole. Peak systole occurs at approximately 210 ms, as indicated by the *vertical dashed line*. 151

Figure 4.3: Distal TI according to stenosis severity and plaque morphology. The value of TI is the average of 30 $\overline{\text{TI}}_{24}$ from three consecutive time points for a 24-ms window centered on the time of maximum TI. Error bars depict standard deviation in 30 $\overline{\text{TI}}_{24}$ 153

Figure 4.4: Colour-encoded maps of TI in the central plane of the non-ulcerated (*left*) and ulcerated (*right*) (a, b) 30%, (c, d) 50%, (e, f) 60%, and (g, h) 70% phantoms at 24 ms following peak systole. 156

Figure 4.5: Colour-encoded maps of ensemble-averaged mean velocity, \bar{v}_{mean} , in the central plane of the non-ulcerated (*left*) and ulcerated (*right*) (a, b) 30%, (c, d) 50%, (e, f) 60%, and (g, h) 70% phantoms at 24 ms following peak systole. 157

Figure 5.1: 3-D geometry of the 50% eccentrically stenosed carotid bifurcation with ellipsoidal ulcer used in this study, showing (a) the 3-D micro-CT image volume of the original DUS phantom, and the corresponding (b) extracted geometric surface model and (c) surface mesh. The *two right panels* show the finite element mesh of (d) the ulcerated and (e) the non-ulcerated models (overlaid on the image data of the ulcerated model for comparison) used in this study, with mid-side nodes tessellated in order to illustrate the nodal distribution. 186

- Figure 5.2: Colour-encoded maps of the CFD-computed flow field in (a, c) the non-ulcerated model and (b, d) the ulcerated model at 35 ms following peak systole for cycle 5 (*first row*) and cycle 7 (*second row*); and of (e, f) spectral mean velocities from experimental DUS measurements. The axial component of velocities in the central plane of the models is shown in the CFD velocity fields..... 193
- Figure 5.3: Colour-encoded TI maps in the central plane of the non-ulcerated geometry (*left column*) and ulcerated geometry (*right column*) in the CFD models using (a, b) RMS deviations in instantaneous nodal velocities and (c, d) finite volume sampling, shown at approximately 35 ms following peak systole; and from (e, f) experimental DUS measurements. 195
- Figure 5.4: Shear stress-encoded particle tracks for 10×10 uniform seeding in the non-ulcerated (*top row*) and ulcerated (*bottom row*) CFD models for two representative seeding time points during diastole. Colour-encoding indicates the shear stress, $\bar{\tau}_{max}$, experienced at each point along the particle track. 198
- Figure 5.5: Shear stress-encoded particle tracks for near-wall seeding in the non-ulcerated (*top row*) and ulcerated (*bottom row*) CFD models for a representative seeding time point during late diastole. Colour-encoding indicates (a, c) the shear stress, $\bar{\tau}_{max}$, experienced at each point along the track and (b, d) the maximum $\bar{\tau}_{max}$ experienced up to the indicated point in the particle track..... 199
- Figure 5.6: (a, f) Transit time; (b, g) maximum shear stress up to the point in the track; and cumulative shear exposure parameters: (c, h) CSE , (d, i) CSE_{step} and (e, j) CSE_{post} along particle tracks for 10×10 uniform seeding in the non-ulcerated model (*top row*) and ulcerated model (*bottom row*), corresponding to a seeding time point in early diastole. 200
- Figure 5.7: Frequency distributions of (a) maximum shear stress (maximum $\bar{\tau}_{max}$), (b) total transit time, and (c) transit time post-threshold for over 250,000 seeded particles. *Grey bars* represent particle frequency distributions for the non-ulcerated model and *white bars* for the ulcerated model. Less than 1% of the seeded particles are excluded from the histograms by the upper cutoff..... 202
- Figure 5.8: Frequency distributions of cumulative shear stress particle track parameters for over 250,000 seeded particles. *Grey bars* represent particle frequency distributions for the non-ulcerated model and *white bars* for the ulcerated model. Less than 1% of the seeded particles are excluded from the histograms by the upper cutoff. 203
- Figure B.1: Schematic of the *in vitro* Doppler ultrasound acquisition system..... 229

Figure C.1: (a) Cardiac-gated spectral mean velocity (v_{mean}) over ten successive cardiac cycles allowing for the determination of v_{mean} at the same time point in each cardiac cycle (*black lines and arrows*). (b) The v_{mean} from ten successive cardiac cycles (C_1, C_2, \dots, C_{10}) displayed in terms of cardiac cycle time for the generation of (c) an ensemble of ten cardiac cycles of data. Turbulence intensity (TI) is calculated as the root-mean-square (RMS) fluctuation in v_{mean} about the ensemble-averaged v_{mean} at a given time point in the cardiac cycle, and is indicated in (c) as σ_{RMS} 231

Figure C.2: Schematic indicating the location of the 24 measurement sites in the distal region of interest used for the calculation of \overline{TI}_{24} in Chapter 3 (*pink dots*). The 24 measurement sites used for the calculation of \overline{TI}_{24} in Chapter 4 are located 1 mm more distal to the apex of the bifurcation. 232

Figure D.1: The difference in three-component computed L_2 for each mesh (171k, 281k and 370k elements) at mean Re (*blue squares*), twice mean Re (*red diamonds*) and peak Re (*yellow triangles*) steady flow versus the highest resolution (538k elements) mesh velocity field..... 234

List of Abbreviations and Symbols

Alphanumeric

a, b	fitting parameters for power-law
c	speed of sound in tissue
D	vessel diameter
$D_{ICA,distal}$	distal luminal diameter in the internal carotid artery
$D_{ICA,min}$	minimum luminal diameter in the internal carotid artery
f	frequency
f_D	Doppler frequency shift
f_o	transmit frequency
L	inlet length
N	sample size
P	p -value
Re	Reynolds number
Δt	time interval of a particle track step
t	time in simulated particle track
T	time when particle exits distal boundary for tracking
t^*	time when particle first exceeds shear stress threshold
u	mean fluid velocity
v	velocity of scatterer
v_{mean}	mean velocity
v_{peak}	peak velocity
\bar{v}_{mean}	ensemble-averaged mean velocity
\bar{v}_{peak}	ensemble-averaged peak velocity

Greek

α	acoustic attenuation coefficient
θ_D	Doppler beam-to-flow angle
μ	dynamic viscosity
ν	kinematic viscosity
$\bar{\tau}_{max}$	maximum shear stress
$\bar{\tau}_{max}^*$	maximum shear stress that exceeds shear stress threshold

Abbreviations

2-D	two-dimensional
3-D	three-dimensional
ANOVA	analysis of variance
ACAS	Asymptomatic Carotid Atherosclerosis Study
ACST	Asymptomatic Carotid Surgery Trial
BMF	blood-mimicking fluid
B-mode	brightness-mode
CAD	computer-aided design

CAS	carotid artery stenting
CCA	common carotid artery
CEA	carotid endarterectomy
CFD	computational fluid dynamics
CREST	Carotid Revascularization Endarterectomy vs. Stenting Trial
<i>CSE</i>	cumulative shear exposure
<i>CSE_{step}</i>	step-thresholded cumulative shear exposure
<i>CSE_{post}</i>	cumulative shear exposure post-threshold
CT	computed tomography
CTA	computed tomography angiography
DSA	digital subtraction angiography
DUS	Doppler ultrasound
ECA	external carotid artery
ECST	European Carotid Surgery Trial
FFT	fast Fourier transform
Gd-MRA	gadolinium-enhanced magnetic resonance angiography
HDPE	high-density polyethylene
HU	Hounsfield units
ICA	internal carotid artery
micro-CT	micro-computed tomography
MRA	magnetic resonance angiography
MRI	magnetic resonance imaging
NASCET	North American Symptomatic Carotid Endarterectomy Trial
NC	numerically controlled
PIV	particle imaging velocimetry
RMS	root-mean-square
ROI	region of interest
SBI	ensemble-averaged spectral broadening index
SDPV	standard deviation in v_{peak}
SoS	speed of sound
SPACE	Stent-Protected Angioplasty versus Carotid Endarterectomy trial
SW	ensemble-averaged spectral width
Teflon®	polytetrafluoroethylene
TI	turbulence intensity
\overline{TI}_{24}	averaged turbulence intensity from 24 sites in region of interest
TPX	polymethylpentene
UHMW	ultra-high molecular weight polyethylene

Chapter 1

Introduction

1.1 Thromboembolic Stroke

Stroke is a prevalent and severe medical condition that imposes an immense loss of health and heavy economic burden worldwide. Globally, stroke is the second leading cause of death and the leading cause of long-term disability [1, 2]. A 2010 report from the American Heart Association estimates that there are 2,400 new strokes per one million people each year [2]. The adverse effects are both extensive and long-lasting, as one third of new strokes result in death and most stroke survivors are afflicted by a neurological disability that requires rehabilitation or long-term care [3]. Moreover, once a stroke has occurred, the risk of stroke recurrence increases substantially [4, 5].

In Canada, more than 14,000 people die from stroke each year, and the cost to the Canadian economy is estimated at \$2.7 billion per year. Cardiovascular diseases remain the leading cause of hospitalization and over one percent of the adult population live with the effects of stroke [6, 7].

Strokes comprise a group of conditions that compromise cerebral blood flow causing persisting brain injury or neurologic deficit. In the 1970s, the first computed tomography scans enabled the differentiation of the two main sub-categories of stroke – ischemic and hemorrhagic.

By far, the most common form of stroke is due to ischemia – a restriction or shortage in cerebral blood supply – which accounts for 78% of strokes [8]. Ischemia is most often caused by a thrombus or clot that has embolized and travelled to the brain causing arterial occlusion of a narrow cerebral vessel [9, 10]. The thrombus typically originates from a proximal location in the body, such as the heart (cardiogenic embolism) or from

atherosclerotic plaque in a large proximal artery (artery-to-artery embolism), commonly the aorta or internal carotid artery (ICA). Although a less frequent cause, occlusion can instead result from a local thrombus that forms within the cerebral arteries themselves [10].

In contrast to ischemic injury, hemorrhagic strokes – resulting from excessive cerebral bleeding due to rupture of the cerebral blood vessels – account for approximately 20% of all strokes [8]. Although both are acute events requiring rapid, time-dependent care, they are now known to have very different etiologies and have consequently led to very different schemes of diagnosis and treatment.

1.1.1 Growing burden of stroke

Based on comprehensive World Health Organization data, which contains information on the vast majority (72%) of the world's population, the number of stroke deaths is expected to increase from 5.7 million in 2005 to 7.8 million in 2030, with mortality rates increasing from 89 to 98 per 100,000 over the same period (e.g. due to the aging population, poor diet, physical inactivity, and rising tobacco use). The demand for rehabilitation and long-term care are also projected to rise substantially (by 24%) over the next twenty years [11].

Contrary to common conception, stroke is not a problem exclusive to developed, high-income countries; primary and secondary prevention and therapy have effectively mitigated the rates of stroke mortality in high-income countries over the last ten years, reducing the stroke death rates by 33% in the United States from 1996 to 2006 [2]. Despite this, the global burden of stroke is a growing issue due to the faster increase in stroke mortality in low- and middle-income countries, which already accounted for more than three quarters of stroke mortality in 2005 [11].

It is evident that the prevention and effective treatment of stroke patients is critical to address the burden imposed by stroke. In particular, it is important to identify modifiable stroke risk factors and potential therapies, and to determine optimal strategies for patient case management. Additionally, low-cost and widely distributed diagnostic and treatment tools are necessary to combat the global burden of disease incurred by stroke, especially given the rising burden of stroke in low- and middle-income countries.

1.2 Carotid Atherosclerosis

Atherosclerosis – a degenerative, progressive disease characterized by the formation of atheroma or plaques composed of lipid accumulation, inflammatory cells and fibrous elements in the large arteries – is considered the “single most important contributor to [the] growing burden of cardiovascular disease” [12]. Although it is clear that the pathogenesis of atherosclerosis closely underlies ischemic stroke and myocardial infarction (ischemic symptoms), this relationship is complex, multifactorial, and still not completely understood.

In the development of atherosclerosis, plasma cholesterol, particularly low-density lipoprotein, is thought to drive the development of disease, although serum-cholesterol levels alone are not predictive of clinically significant disease. The atherogenic process is enhanced by other risk factors, including: hypertension, smoking, diabetes, male gender, and potentially, inflammatory biomarkers [13]. The clear overlap in risk factors of atherogenesis and ischemic stroke indicates a link between the disease and the disorder.

The presence of atherosclerotic lesions itself is widespread and frequently benign [14-16]. It is only when a lesion is complicated with thrombosis that it becomes hazardous and clinically significant – an event

that is frequently caused by plaque rupture or erosion. Effective management of stroke patients therefore hinges on the specificity of diagnostic techniques to predict which atherosclerotic plaques are prone to thrombosis [17].

Researchers have long noted with curiosity that although vascular risk factors, such as serum cholesterol and blood pressure, affect the body uniformly, the formation of atherosclerosis in the body is highly focal and non-uniform. Glagov *et al.* [18] attributed this selective localization to geometrically susceptible blood vessels, noting that “the propensity for plaque formation at bifurcations, branchings, and curvatures has led to conjectures that local mechanical factors such as wall shear stress and mural tensile stress potentiate atherogenesis.” Studies have since shown that vessel morphology and accompanying mechanical hemodynamic factors, such as shear stress patterns, play a key role in the site selectivity of atherosclerotic plaque development and, importantly, in subsequent plaque vulnerability.

A major site that is prone to atherosclerotic plaque formation is the carotid artery, a major artery leading to the brain that bifurcates from a common proximal vessel (common carotid artery (CCA)) into two distal branches (internal carotid artery (ICA) and external carotid artery (ECA)) (Fig. 1.1) [19]. Atherosclerotic lesions tend to form at the bifurcation, particularly at the origin of the internal carotid artery, which has a unique bulb or vessel expansion, called the carotid sinus [20]. This vessel divergence in the carotid sinus causes flow deceleration. The resultant increase in the pressure gradient along the direction of flow can create flow separation along the wall of the internal carotid artery sinus, producing zones of recirculating flow and possible flow disturbances. This generates low, oscillating wall shear stresses under pulsatile flow, which are conditions where atherosclerotic plaque tends to localize [20].

Atherosclerosis localized in the carotid arteries is not only prevalent, but also represents a significant risk for clinical cerebrovascular events. The carotid artery is the most frequently involved site in large artery atherothrombotic stroke. Carotid artery atherothrombosis is estimated to be responsible for 10 – 30% of all strokes [9, 21-23].

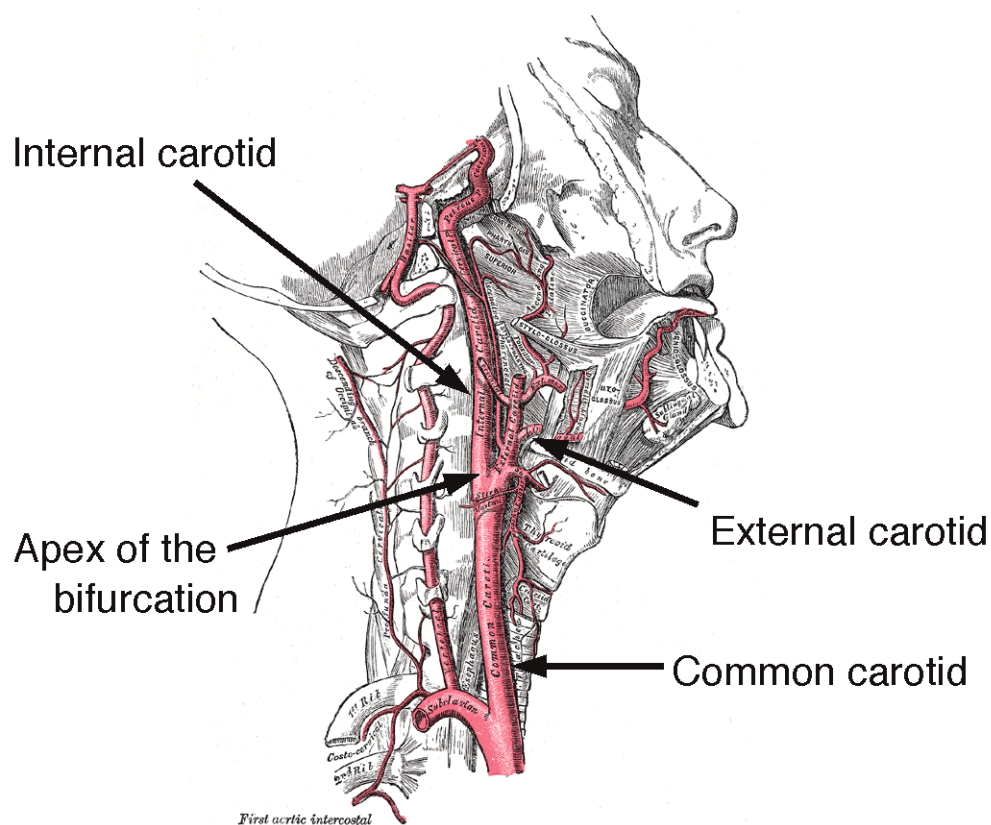


Figure 1.1: The carotid artery bifurcation in the neck, where the internal and the external carotid arteries branch from the common carotid artery at the apex of the bifurcation.[†]

[†] From Henry Gray's *Anatomy of the Human Body* [24].

Large multicentre randomized clinical trials, such as the North American Symptomatic Carotid Endarterectomy Trial (NASCET) and the European Carotid Surgery Trial (ECST), provided strong evidence for a causal relationship between carotid plaque and the risk of stroke on the same (ipsilateral) side. Surgical removal of the carotid plaque by carotid endarterectomy (CEA), particularly in symptomatic patients, significantly reduced the risk of ipsilateral carotid territory symptoms. These trials demonstrated that angiographic definition of the severity of vessel luminal narrowing, or stenosis, is correlated to stroke rate. Specifically, severe carotid artery disease presents a 7–20% annual risk of stroke in symptomatic patients with recent ischemic events [25] and a lower 0.34–8% annual risk of stroke in asymptomatic patients [26-28].

1.3 Management of Carotid Plaque

The prevention of acute stroke associated with carotid artery atherosclerosis focuses on the reduction of cardiovascular risk factors with medical management and selection for surgical intervention in specific patient subgroups. However, due to intrinsic surgical risks, it is vital to determine which stroke patients would benefit from surgical therapy, versus medical treatment alone.

CEA involves the surgical removal of the carotid atherosclerotic plaque to reduce the associated risk of artery-to-artery thrombosis. Largely due to NASCET and ECST results, CEA is the primary interventional treatment and gold standard of therapy for carotid artery stenosis. The use of CEA is well-established, and is typically the preferred strategy for most patient groups in most centres [29]. More recently, carotid artery stenting (CAS) – an endovascular rather than traditional surgical approach – has emerged as an alternative procedure for treating carotid artery stenosis. In CAS, a stent, or expandable metal-mesh device, is deployed at the site of carotid plaque to

revascularize the arterial stenosis, commonly in conjunction with a distal emboli-catching neuroprotection device. The postoperative stroke rates are estimated to be 1.1% with CEA and 1.8% with CAS, although the rates are higher in some centres [29, 30].

Medical treatment is used to decrease modifiable vascular risk factors, particularly hypertension and lipid disorders, such as hypercholesterolemia. Drug therapy commonly involves the prescription of aspirin as anti-platelet therapy, statins to lower lipid levels, and blood pressure reduction [31].

1.3.1 Selection for therapy

Several features of carotid plaque have emerged as important stroke risk factors: stenosis severity, plaque composition or internal morphology, irregular surface morphology or ulceration, and, more recently, molecular inflammatory components [25, 32-34]. Management of risk factors in individual patients is complex. Stroke risk prediction models, such as the Framingham Stroke Risk Profile [35], or simpler tables (e.g. www.stroke.ox.ac.uk) are tools utilized in clinical practice to estimate an individual patient's risk of stroke based on multiple clinical prognostic variables [31]. These prediction tools are based on a number of multicentre randomized clinical trials.

1.3.1.1 Symptomatic patients

The NASCET study was a large, multicentre, prospective controlled trial in which over 2000 patients with carotid artery stenosis and previous ischemic symptoms, were randomized to CEA or best medical treatment. This trial found a significant risk reduction in symptomatic patients with severe stenosis (> 70%) and moderate stenosis (50 – 69%) who were treated with CEA. The two-year risk of ipsilateral stroke was reduced from 26% in patients treated medically to 9% in patients treated with CEA [36]. Patients with symptomatic moderate (50 – 69%) and mild (30 – 49%) stenosis also

showed benefit from CEA, but less than in the patient group with severe (70 – 99%) symptomatic stenosis. A similar trial conducted in Europe (ECST), had almost identical findings once corrections were made for differences in measurement criteria [37].

Analysis of pooled data from NASCET and ECST, emphasized that CEA was beneficial for patients with symptomatic stenosis above 50%, although the benefit was higher in patients with 70 – 99% stenosis [38].

1.3.1.2 Asymptomatic patients

In contrast, a higher degree of arterial stenosis, while important for symptomatic carotid plaques, does not correlate strongly with surgical benefit for patients with asymptomatic plaques. The Asymptomatic Carotid Atherosclerosis Study (ACAS) and Asymptomatic Carotid Surgery Trial (ACST) both determined that stenosis severity was not an adequate indication for CEA in asymptomatic patients [39, 40]. Factors associated with higher risk asymptomatic plaques are varied, but include heterogeneous plaque and angiographic plaque ulceration [41].

1.3.2 Selection of therapy: carotid endarterectomy and stenting

Thus far, randomized controlled clinical trials comparing outcomes after carotid artery stenting versus carotid endarterectomy have produced contradictory evidence. The safety and utility of carotid stenting versus CEA is an ongoing debate. The Stent-Protected Angioplasty versus Endarterectomy (SPACE) trial was not able to show that stenting was inferior to CEA [42-44], while other trials demonstrated a significantly lower rate of stroke or death in patients undergoing CEA versus carotid stenting [45-47]. Limitations of these previous trials have been noted [44]. Primary results of the most recent randomized controlled trial comparing CEA versus carotid artery stenting, the Carotid Revascularization Endarterectomy vs.

Stenting Trial (CREST), showed no significant difference in overall outcomes between the two procedures [48, 49].

Current recommendations are that CEA should remain the treatment of choice for patients who are suitable candidates for surgery. However, select patient subgroups may benefit from carotid artery stenting, although the procedure should be performed under certain standards (e.g. with acceptable procedural risk and rapid intervention) [50].

1.3.3 Current diagnosis

At present, interventional strategy is primarily selected by categorizing the severity of carotid artery disease, based on the conventional measure of atherosclerotic burden: the degree of vessel stenosis.

The degree of stenosis is defined as the percentage of luminal diameter reduction relative to a reference measure of luminal diameter. The standard, widely adopted definition of degree of stenosis is the one used in the NASCET study:

$$\text{Degree of stenosis} = 100 \times (1 - D_{ICA,min} / D_{ICA,distal}) \quad (1.1)$$

where $D_{ICA,min}$ is the minimum luminal diameter in the internal carotid artery, and $D_{ICA,distal}$ is the luminal diameter in the internal carotid artery distal to the carotid bulb, where the walls are parallel and disease-free [51].

Lumen dimensions in NASCET were determined by X-ray digital subtraction angiography (DSA). DSA remains the gold standard for defining carotid stenosis severity. However, DSA is a costly invasive procedure that is associated with a significant rate of neurological complication (0.52 – 8.5%) [39, 52], negative contrast reactions and renal dysfunction due to the use of an iodinated contrast medium.

Due to these drawbacks, non-invasive imaging techniques have largely supplanted DSA for evaluating the degree of carotid artery stenosis and the associated risk of carotid ipsilateral ischemic stroke [53]. Currently, duplex ultrasound is the primary, most frequently used method for the diagnosis of carotid artery disease to assess stroke patients [53]. Computed tomography angiography (CTA) or magnetic resonance angiography (MRA) is sometimes used to confirm the diagnosis prior to surgery or if DUS is inconclusive [54, 55].

In a Duplex ultrasound examination, Doppler ultrasound is used to measure increased velocities in the stenotic jet, using blood-flow velocity criteria, to estimate stenosis severity [56]. The peak systolic velocity in the ICA is used as the primary criteria for grading stenosis, where values of greater than 230 cm s^{-1} , $125 - 230 \text{ cm s}^{-1}$, and less than 125 cm s^{-1} , indicate severe ($\geq 70\%$), moderate ($50 - 69\%$) and mild ($< 50\%$) degrees of stenosis. Secondary parameters used in the assessment include the ICA/CCA systolic velocity ratio and ICA end-diastolic velocity [53, 56].

1.3.4 Limitations of current diagnosis

Current carotid examinations have limited accuracy for predicting the risk of ischemic stroke in patients with carotid bifurcation stenosis. In its current implementation, DUS provides only moderate sensitivity (89%) and specificity (84%) for the detection of stenoses appropriate for surgery [57]. Firstly, Doppler ultrasound – utilizing peak systole velocity ratios as a surrogate measure of vessel narrowing – has suboptimal accuracy for estimating the degree of carotid stenosis. It has been estimated that DUS may lead to misclassification in up to 28% of patients compared to the degree of stenosis on angiograms [58].

Secondly, studies have recognized the limitation of degree of stenosis as a predictor of true plaque burden and stroke risk [59-61]. A risk

stratification model based on stenosis severity alone may fundamentally lead to significant numbers of unprevented strokes. Furthermore, these studies indicate the importance of accounting for additional features of carotid atherosclerosis that contribute to higher risks of stroke. In particular, plaque ulceration and plaque vulnerability have been identified as critical risk factors to select sub-populations at significant risk, who would benefit from surgical therapy [25].

Although DUS measurements provide spectra of velocity data over the cardiac cycle, reflecting the range of blood-flow velocities captured in the sampling volume, current methods only extract a single spectral parameter, the maximum (peak) spectral velocity, at a limited number (one or two) of cardiac time points. Therefore, current techniques may be underutilizing the information available in the measured Doppler ultrasound velocity spectrum. Advanced Doppler analyses – incorporating more sophisticated quantitative characterization of flow conditions – may improve the prediction of stroke risk.

1.3.5 Considerations for carotid plaque ulcerations in diagnosis

Both NASCET and ECST provide compelling evidence that the presence of plaque irregularity or ulceration on carotid angiography is a strong risk factor for ischemic stroke, independent of stenosis severity [62, 63]. Ulcerations of carotid plaque are correlated with adherent surface thrombus, plaque hemorrhage, distal cerebral emboli, and general plaque instability [41, 60, 64-66]. The identification of moderate plaque with ulceration is of particular importance, as these plaques may represent higher risk [34]. There is a current need for a non-invasive, translatable diagnostic technique for the detection of carotid plaque ulcers, and improved understanding of the role of ulcerative plaques in the carotid artery.

1.4 Carotid Plaque Pathology

The progression of atherosclerotic plaques is a slow process that involves intima-media alterations [12]. Initial stages involve the accumulation of neutrophils and smooth muscle cells in the intima layer, subsequent development of lipid-filled foam cells and appearance of fatty streaks in the intima, followed by the gradual formation of a thick, fibrous plaque. Some plaques advance to become complicated plaques that are prone to rupture [60, 61].

To explain how a chronic disease characterized by stable, asymptomatic plaques transitions to one with unstable plaques that trigger, often suddenly, the onset of acute cerebro-ischemic events, the idea of the “vulnerable plaque” was proposed [67-71]. Vulnerable plaques are lesions that are more susceptible to rupture. These unstable plaques tend to be complicated and have certain morphological characteristics.

1.4.1 Morphology and risk

Plaque rupture can occur even in lesions that do not produce significant luminal narrowing or hemodynamic stenosis [72, 73]. Research currently focuses on: plaque composition (i.e. internal plaque morphology); surface irregularity of the carotid artery wall or ulcerations (i.e. plaque surface morphology); and direct plaque burden measurements (e.g. plaque area and volume, vessel wall volume, intima-media thickness).

1.4.1.1 Internal plaque morphology

In terms of internal plaque morphology, several internal plaque characteristics have been linked to the vulnerable plaque hypothesis. Lesions that are more likely to trigger ischemic events have a large lipid-rich necrotic core, thin overlying fibrous cap, and the presence of intraplaque hemorrhage (due to rupture of intraplaque vasa vasorum) and elevated

inflammatory activity [61, 74, 75]. Recently, advances have been made in plaque imaging techniques, such as in magnetic resonance imaging (using soft tissue contrast) [76, 77] and ultrasound (based on heterogeneity in plaque echolucency) [53, 78, 79], to determine plaque composition and identify complicated plaques. Future diagnostic tests may be able to ascertain the chemical makeup and inflammatory status of plaques, such as by magnetic resonance spectroscopy or biomarkers [80, 81]. These techniques are still in development and have not yet been incorporated into routine clinical practice.

1.4.1.2 Plaque surface ulcerations

Plaque ulceration is a defect in the artery wall at the site of an atherosclerotic lesion, with loss of the endothelial cell layer and excavation into the plaque. On diagnostic images, ulceration is defined as a protrusion into the arterial wall on angiograms, or into the plaque on sonograms. Typically, ulceration is defined as a surface recess with depth and length of at least 2 mm [62, 82, 83].

Ulcerations tend to occur on the proximal shoulder of plaque, where there are higher shear stresses on the plaque surface [84-86]. In the carotid artery, ulceration is more likely to occur proximal to the site of maximal stenosis (69 – 72% proximal location) [87, 88].

Ulcerations develop following plaque degeneration by rupture or erosion, typically at a site of high fluid mechanical shear stresses on an unstable lesion [89, 90]. Therefore, the presence of an ulcer cavity is thought to indicate that the atherosclerotic plaque has advanced to a complex, vulnerable lesion, which is prone to further fragmentation and disruption exposing thrombotic plaque contents.

Lovett *et al.* [91] categorized ulcer shape in clinically observed carotid artery plaques as four types: a Type 1 ulcer with walls that are parallel or come to a point; a Type 2 mushroom-shaped ulcer; a Type 3 ulcer with a proximal neck and the ulcer cavity pointing distally; and a Type 4 ulcer with a neck that is distal and the cavity of the ulcer pointing proximally (Fig. 1.2). In this study, Type 1 and Type 3 ulcerations were observed more frequently (38% and 28% of detected ulcerations, respectively) than Type 2 and Type 4 ulcerations (21% and 13%, respectively). A subsequent study confirmed that Type 1 and Type 3 ulcers occur more frequently (48% and 27%, respectively) than Type 2 and Type 4 ulcerations (13% and 12%, respectively) [88], although the clinical significance of different ulcer types has yet to be established.

Carotid plaque surface ulcerations and irregularity are highly predictive of ischemic stroke [63, 92-94]. The NASCET study found that the presence of ulceration on carotid angiography signified a greater than two-fold increase in the risk of ischemic stroke [93]. Another large, prospective study (the Northern Manhattan Study) demonstrated a three-fold increase in stroke risk with plaque irregularity on B-mode ultrasonography. This elevation in risk held even for moderate grade (< 60%) stenoses [92]. Several other prospective studies reaffirmed that carotid plaque ulcerations are a stroke risk factor [41, 94, 95]. Moreover, the association with increased risk vanished with CEA, indicating a causal relationship between ulceration and ischemic stroke. Irregular plaque surface morphology is associated with increased stroke risk, independent of stenosis severity [63]. Analysis of ECST data showed that while stenosis severity is only an independent predictor of stroke within the first two years, plaque irregularity remains an independent predictor for longer [63]. Furthermore, there is substantive evidence that ulcerations in carotid plaques indicate plaque instability [41, 60, 64-66], and are a significant source of thromboembolic events [96, 97].

In addition, as carotid stenosis can be determined more accurately than carotid plaque surface morphology, the true risk associated with plaque ulcerations is likely to be even higher than indicated [63, 98].

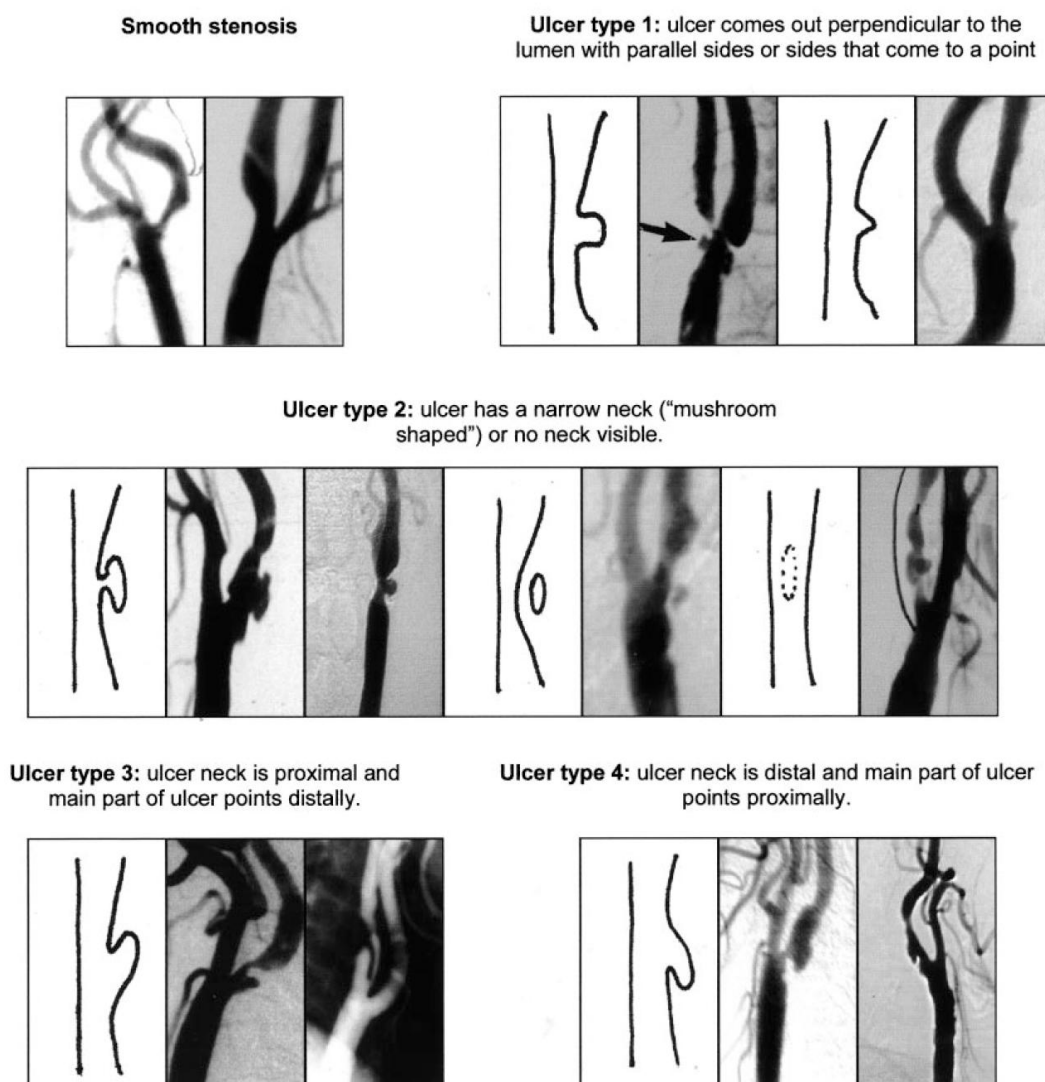


Figure 1.2: Examples of four types of angiographic carotid plaque surface ulceration.[†]

[†] From Lovett *et al.* (2004) *Circulation* 110:2190-2197 [91].

1.5 Diagnostic Imaging of Carotid Plaque Surface Morphology

Following NASCET and the recognition of stenosis severity as a significant diagnostic factor, much work has been done to develop imaging techniques to characterize the linear reduction in carotid artery lumen diameter, as an estimate of plaque burden. Many of these techniques can be classified as “lumenographic” imaging techniques, in which lumen-vessel contrast is used to determine the anatomical geometry of the arterial lumen. Lumenographic techniques currently implemented for carotid examinations include: X-ray digital subtraction angiography, computed tomography angiography, magnetic resonance angiography, and B-mode ultrasound.

Several of these techniques have also been evaluated for their ability to identify and characterize carotid plaque surface ulcerations, in addition to stenosis severity. Current techniques have had less success in delineating plaque morphology than vessel stenosis, achieving only suboptimal preoperative diagnosis of ulcerative plaques.

1.5.1 Angiography

1.5.1.1 X-ray digital subtraction angiography (DSA)

Intra-arterial digital subtraction angiography is the standard of reference for evaluating stenosis severity in the carotid artery. However, DSA assessment of carotid ulcerations has been less successful [98]. The sensitivity and specificity in NASCET for the detection of ulcerative plaques was only 46% and 74%, respectively, when compared to surgical specimens [62]. Additionally, accuracy varied with stenosis severity: sensitivity was 77% for stenotic degrees less than or equal to 50%, but was only 48% for stenosis grades greater than 50% [99]. Poor diagnostic sensitivity of DSA to ulcerated plaques is due to its limited views of the vessel lumen [62]. Conventional angiography is also associated with a high complication rate,

owing to its invasiveness and use of iodinated contrast, and is both time and cost intensive [100].

1.5.1.2 Computed tomography angiography (CTA)

Computed tomography angiography can provide precise high-resolution delineation of the carotid artery lumen anatomy, and is minimally invasive compared to DSA. However, the accuracy of CTA for assessing carotid plaque ulceration has mixed results. Although CTA correlates well with DSA for carotid artery stenosis, it has been shown to correlate only moderately for the detection of plaque ulcerations [82]. Single-slice spiral CT has had limited success defining ulcerative plaques, achieving a sensitivity of only 60%, specificity of 74%, and a moderate predictive value [82]. However, multi-detector CTA may provide some improvement over single-slice CT, which is limited by the thickness of the imaging slice (greater than 1 mm). Multi-detector CTA has been shown to have high sensitivity and specificity (94% and 98.6%, respectively), when compared to surgical specimens [101]. As well, CTA provides good interobserver variability, and anatomical information that is largely independent of hemodynamic conditions [102]. However, CTA involves the use of iodinated contrast material and ionizing radiation, and is less reliable with calcified plaques [103].

1.5.1.3 Magnetic resonance angiography (MRA)

Alternatively, non-invasive magnetic resonance angiography does not involve ionizing radiation, and yet still offers relatively high spatial resolution and suppression of venous signal intensity [104]. Although earlier MRA techniques have suffered from restrictive limitations in evaluating stenosis severity and the detection of plaque irregularities, the use of black-blood techniques have provided a sensitivity and specificity of greater than 80% for larger ulcers, but a sensitivity of only 52% for small ulcers [105].

In addition, three-dimensional (3-D) gadolinium-enhanced magnetic resonance angiography may provide comparable accuracy to DSA [106].

The main limitations of MRA are: high cost and low availability; the lack of standardization between systems (e.g. scanner platform and coil design) and imaging sequence protocols; and contraindications in patients with pacemakers and other ferromagnetic devices.

1.5.2 Ultrasound

Ultrasound imaging is non-invasive, widely available, and relatively low cost. Conventional two-dimensional (2-D) ultrasound has been shown to have a high specificity (85 – 93%), but low sensitivity (17 – 38%) for detecting ulcerations in the carotid plaque [101, 107]. The diagnostic accuracy is dependent on stenosis severity, with a sensitivity of 77% for mild and moderate stenosis grades ($\leq 50\%$), while only 41% for greater than 50% stenosis [99]. Accurate assessment is particularly difficult in the presence of calcifications due to acoustic shadowing artifacts. Other shortcomings of current ultrasound methods are relatively large inter- and intra-observer discrepancies, and accordingly reduced reliability and reproducibility.

Contrast-enhanced ultrasound may improve definition of the vessel wall-lumen and plaque morphology [108]. Ultrasound echomorphology may provide added information in relation to internal plaque morphology [109]. In addition, advances in 3-D ultrasound have the potential to improve plaque ulcer detection. A recent study using 3-D ultrasound was able to detect carotid plaque ulceration more frequently than conventional 2-D ultrasound [110]. As well, automated and objective plaque morphological characterization approaches using 3-D ultrasound may facilitate the quantification of carotid lesion surface ulcerations in cross-sectional or longitudinal patient studies [111, 112].

The utility of Doppler ultrasound for the detection of carotid plaque ulceration has not yet been evaluated. We propose that Doppler ultrasound

may provide a non-invasive assessment of carotid plaque ulcerations based on hemodynamic information. Such a diagnostic test would be particularly advantageous given that Doppler ultrasound is already routinely used for assessing carotid artery stenosis.

1.6 Carotid Artery Hemodynamics

In fluid-dynamic systems, the geometry of the flow vessel is a key determinant of its flow characteristics. It has been well established that stenoses, bifurcations, and surface roughness are associated with flow disturbances and complex flow [113-115].

The influence of vessel geometry on flow is exemplified in the arterial vasculature. Even in the normal, healthy vasculature, vessel bends and bifurcations, as well as the pulsatile flow of the cardiac cycle, introduce secondary flows and oscillating shear stresses. Atherosclerosis admits yet more complications, particularly where arterial disease is severe enough to cause a vessel stenosis [116]. Whereas flow in normal arteries is complex but typically laminar, stenoses are associated with shear layers, eddy formation, distal flow disturbances [117], and velocity fluctuations [118]. Tortuous, irregular vessel surfaces are likely to further contribute to flow disturbances [113, 114].

By a confluence of geometric features, the stenosed carotid bifurcation is uniquely susceptible to complex and aberrant flow behaviour, particularly under physiological pulsatile flow conditions; these flow characteristics have been studied quite extensively [18, 19, 119-123]. At the stenosed carotid artery, flow first encounters an asymmetric bifurcating junction, then immediately goes through a stenotic flow constriction, followed downstream by a sudden expansion into the carotid bulb. The bifurcation imposes a flow division that affects the boundary layers along both the inside and outside bends, which is dependent on the exact branch geometry. Maintenance of

volumetric blood flow and conversion of energy in the vessel narrowing generates a high-velocity, low-pressure fluid jet in the throat of the stenosis. The post-stenotic divergence of the vessel wall in the carotid sinus is associated with a velocity drop and pressure rise, producing flow detachment in the expansion region downstream of the stenosis, and creating zones of recirculating or stagnant flow, with eddy formation. Spatial and temporal flow deceleration can generate distal turbulence and flow disturbances. As well, the shear layer between the high-velocity stenotic jet and the recirculation zone can produce vortices, or turbulent or transitional flow downstream. These are conditions that favour thrombus formation [124].

Vessel and plaque geometry – which determine the space through which blood flows – have a strong influence on the distal flow field. Stenosis grade and vessel tortuosity play a major role [125, 126]. However, independent of the degree of stenosis, factors such as plaque geometry (eccentricity) and surface irregularity or ulceration may have a significant effect on the local flow field [127-129]. In particular, vessel and plaque surface contour are likely to determine whether post-stenotic turbulence or disturbed flow occur. The hemodynamic effects of an ulcerated carotid artery lumen have been studied much less extensively.

1.7 Abnormal Hemodynamics and Thrombogenesis

Local blood characteristics are important in the induction of artery-to-artery embolic stroke. There is strong evidence to suggest that a combination of biochemical factors (such as systemic factors and exposed substrate-related effects at the site of arterial wall injury) and mechanical factors (arising from the local fluid-dynamics) can lead to thrombogenesis at ruptured atherosclerotic plaques, by triggering platelet activation and the coagulation cascade [125, 130].

Hemodynamics act to influence the thrombogenic potential of the vessel wall and of the blood. Normal structure and function of vascular endothelial cells lining the vessel wall are thought to be maintained by laminar flow conditions. Abnormal flow conditions can have diverse pathological effects: change endothelial cell morphology and cause endothelial dysfunction [20, 131]; alter the thrombogenic potential of blood; and modify the stability and composition of thrombi [132, 133]. Flow patterns influence biochemical interactions by affecting molecular and cellular transport. Blood shear can also injure and erode plaque or cause fibrous cap rupture, which can expose prothrombogenic material to the blood, and precipitate thrombotic events leading to ischemic stroke. Finally, fluid mechanical stresses can also cause the embolization of a thrombus, dislodging fragments and thereby leading to downstream occlusion of smaller vessels [125].

In addition to blood-wall interactions, abnormal blood flow can more directly contribute to thrombus formation. Vortices [125, 130], disturbed flow [134], high or oscillating shear stress [135, 136], and turbulence [137-140], have been implicated in platelet activation [135, 141]. Stagnation zones and regions of recirculation proximal and distal to stenotic lesions – where flow encounters the wall perpendicularly – are thought to promote the deposition or aggregation of thrombogenic particles [142, 143].

1.7.1 Blood and thrombosis

Blood is a complex and highly dynamic fluid composed of cells and plasma proteins. The dynamic state of these blood constituents, the vessel walls, and their biochemical expression reflect the balance of multiple entangled positive and negative feedback loops involved in the function of blood in healing wounds and infection. Numerous molecular and cellular events in these inflammatory and coagulation processes play an integral role in the development, progression and rupture of atherosclerotic plaque [12, 61].

The interaction of blood particles, in particular activated platelets and leukocytes, with vascular endothelial cells lining the vessel walls has a critical and intrinsically linked role in vascular inflammation, thrombosis and throughout atherosclerosis [144, 145]. These interactions in both hemostatic and pathological processes are modulated by the hemodynamic environment, such as by patterns of mechanical shear stresses. Patterns of mechanical shear stresses are known to influence platelet function, and to be a crucial mechanism for thrombogenesis.

1.7.1.1 Role of platelets

Platelets are blood cells that have an essential role in regulating protective hemostasis, leading to the formation of blood clots to control excessive bleeding at sites of vascular injury. In the event of vascular intimal injury, the exposure of thrombogenic substrates below the endothelium can trigger events that lead to thrombus formation and stabilization that occur through activated platelets and plasma proteins [146].

However, by the same mechanisms, platelets also mediate pathologic response to injury that can lead to thrombosis and consequently to ischemic stroke. Thrombogenic events are also triggered by abnormal forms of intimal injury, such as the rupture or erosion of atherosclerotic plaque. It is thought that thrombosis due to excessive platelet aggregation at the site of plaque rupture is a key event in stroke [16].

Platelet activation is central to thrombosis. Unactivated platelets circulating in the vascular system do not adhere to the vessel wall. However, in response to fluid mechanical and chemical agonists (both proinflammatory or prothrombotic), platelets can become activated, causing conformational transformations of the platelet and platelet receptors, which are pivotal to upregulating the formation of a thrombotic platelet plug [147, 148].

1.8 Hemodynamic Factors in Thrombogenesis

Abnormal blood flow in the human vasculature, particularly in the carotid artery bifurcation, has a considerable deleterious effect [19]. Within an atherosclerotic artery, blood flow dynamics influence pathophysiological mechanisms of atherothrombosis by causing injury at the site of the lesion leading to plaque erosion and fragmentation, and by promoting surface thrombus formation. As Mustard *et al.* observed early on in thrombosis research, several hemodynamic factors influence thrombus formation in blood, including vortices, turbulence, and flow stagnation [140].

1.8.1 Turbulence and disturbed flow

There are decades of evidence that turbulent and disturbed flow – irregular fluid motion with random variations in time and space [149] – contribute to thrombus formation. As such, artery stenoses have long been examined by listening to the turbulent blood noise, or bruit, in regions of disturbed blood flow distal to a stenosis with the use of a stethoscope. Studies by Smith *et al.* [139], Stein and Sabbah [138], and Mustard *et al.* [140] demonstrated thrombus formation in a turbulent system *in vivo* (in animal models). Stein and Sabbah [138] observed a linear relationship between thrombus size and intensity of turbulence (defined as the root-mean-square of fluctuating components of velocity) under pulsatile flow. Disturbed flow and high shear stresses have also been shown to enhance damage [150] and permeability [151] of the endothelial wall. Combined with increased molecular transport by perpendicular fluid motion, these factors could heighten flux of atherothrombotic molecules.

Turbulent and disturbed flows are characterized by velocity fluctuations and associated pressure fluctuations, which are thought to affect thrombosis by several means. One effect of the velocity fluctuations is to enhance the level of shear stresses, as well as collision rates among blood

particles, which may assist in platelet aggregation [139]. Due to molecular transport between fluid layers and convection by turbulent eddies, the motion of flow perpendicular to the wall and duration of contact is increased.

1.8.2 Fluid shear stress and wall shear stress

As noted by Huang and Hellums, fluid mechanical shear stress is a parallel frictional drag force that can have profound effects on human blood cells [152]. By mechanisms that are not yet fully understood, shear stress forces are mechanotransduced into biophysiological signals that modulate vascular [85] and platelet [153] behavior (both structure and function). Exposure of blood to abnormally high shear stress, such as in the stenosed carotid artery, is widely accepted as a cause of increased risk of thrombosis, mainly due to its effects on platelet activation and aggregation.

The effect of shear stresses and shear rates on platelets may be to promote activation or aggregation processes [154, 155]. With respect to platelet aggregation, work is still being done to characterize the effect of shear. However, several recent studies indicate that platelet aggregation is induced by high shear stress and further enhanced by rapid changes from high to low shear [153, 156]. Shear rate has also been shown to determine the platelet receptor binding mechanism of platelet aggregation, and conceivably the reversibility of agglomeration [155, 157-160]. The mechanisms of shear-modulated aggregation are complex and current understanding is incomplete [161]. Platelet activation is also likely influenced by both shear stress level and temporal patterns of shear stress exposure; although a multitude of chemical agonists, such as von Willebrand factor, act synergistically with mechanical shear stress. Research has shown that the type, level, extent and pattern of shear stress influence the extent of platelet activation.

In addition, it has recently been shown that platelet adhesion and aggregation leading to stable thrombus formation can occur independent of platelet activation in conditions of high shear rates [162] and high (temporal) shear gradients [153]. Shear-sensitive mechanisms in restructuring platelet membrane tethers are indicated in activation-independent platelet thrombus formation, although further studies are needed to understand these additional shear-regulated mechanisms of platelet aggregation.

Either by platelet-activation dependent or independent mechanisms, fluid shear stress has an unequivocal role in thrombosis. Insight into the relative role of shear- and chemical agonist-regulated platelet activation and aggregation, and the conditions under which these occur, may be useful in directing future therapies.

Alterations in wall shear stress – or shear stresses tangential to the vessel wall – can also have adverse effects. Turbulent or sudden decreases in shear stress have been shown to induce endothelial cell apoptosis [163], while high shear stress can induce apoptosis in platelets [164]. Additionally, wall shear stress is increased at a stenosis, specifically on the upstream shoulder of the plaque that intrudes into the lumen [86]. This exposure to increased wall shear stress at the proximal plaque shoulder, combined with fracture stress across the plaque due to the pressure drop across the stenotic plaque, is thought to promote destabilization of the plaque and precipitate rupture [85, 86, 165].

1.8.3 Recirculation zones and residence time

It has been recognized that adhering platelets and thrombi localize at the site of stagnation point flow, where platelets and other blood particles are potentially propelled towards an injured vessel wall [166]. The incidence and duration of blood particle contact with the wall seem to be dual components promoting thrombosis in these regions.

Particle deposition in stagnation zones has been demonstrated in both experimental [142, 167] and computational [168, 169] studies. Surface thrombi can form in separated flow regions, even under high flow rates [142, 170]. In arterial flow, zones of recirculating flow distal to a stenotic lesion, with flow reattachment points where flow is perpendicular and towards the wall, may be prone to monocyte and platelet deposition [125, 143].

Regions of flow stagnation, stationary vortices and slow flow, have been shown to prolong particle contact with the wall and therefore particle adhesion and aggregation [171]. In particular, the residence time – or the amount of time that flow (or a fluid particle) spends within a system, or within a region of a system – is an important parameter determining thrombus formation [172]. Reininger *et al.* [142] showed that residence time influences thrombus growth in arterial branching flow *in vitro*, as fibrin-containing clots formed in stagnation zones with convergent flow and high particle residence times. In contrast, another study by this group looking at platelet instead of fibrin clots, showed evidence that shear rate may be more indicative of platelet deposition in stagnation point flow [173].

1.8.4 Platelet activation models

In the atherosclerotic carotid artery, platelet activation may depend on both shear stress exposure and residence times. However, the magnitude of shear stress required for activation has varied between studies, due to variations in the technique used, particularly in experimental parameters such as the constitution of blood used (e.g. variations in agonists content and platelet count), shear stress exposure time and pattern applied, and sensitivity of the technique used to detect activated platelets [174].

Platelet activation has been observed to occur even under very brief (1 ms) exposure [175] and under relatively low shear stress levels (50 dynes cm⁻²) [152]. The precise model describing critical shear stress

conditions for shear-induced activation, particularly *in vivo*, is still under debate. However, it has been noted that chemical agonists may reduce the required shear stress *in vivo* by an order of magnitude [152].

Hellums [176] hypothesized that once a platelet is subjected to a critical level of shear stress, the platelet is more susceptible to subsequent exposures to shear stress. Based on a compilation of numerous studies measuring the time required to reach activation under known, controlled shear conditions, Hellums developed a shear-exposure time plane to predict the platelet activation threshold. In this model, a critical, threshold level of shear stress, as well as the shear-exposure time following critical levels, is important [176].

In contrast, work by Bluestein and colleagues proposed that there is not an absolute value of shear stress that is crucial to determining platelet activation. Their studies support the notion that platelet activation is reversible; therefore a cumulative product of shear stress level and the duration of shear stress exposure determine the level of platelet activation, irrespective of early exposure to high shear stress [177-179]. Other models indicate flow-induced platelet stimulation to have a non-linear dependence on shear stress and duration of exposure [180, 181].

Zhang *et al.* [182] observed that the duration of shear stress is critical to aggregate stability and reversibility. They reported that shorter exposure can yield reversible platelet aggregation with little platelet activation, while longer exposures induce platelet activation and irreversible aggregation. The type of applied shear stress also affects the activation of platelets. Purvis and Giorgio found that elongational shear stresses, which occur in secondary flows, activate at lower shear levels, as well as tend to form larger aggregates [183].

Dynamic or changing shear stress patterns have also been indicated to induce platelet activation. Sudden decreases from transiently high shear stresses may be important in geometries such as those incurred by an arterial stenosis or developing thrombus, where exposure of blood to high shear stresses would only be imposed for a brief length of time [135]. Accumulation of platelet activation occurs even when low shear “relaxation” periods are applied between high shear pulses [184]. Pulsed exposure has also been found to result in greater platelet aggregation than continuous exposure [185].

1.8.5 Effect of carotid plaque symmetry

Atherosclerotic lesions that effect the same severity of luminal narrowing, can have very distinct geometric characteristics. Therefore, lesions that have the same degree of stenosis can produce very different local hemodynamics, and possibly present distinct pathogenic mechanisms or risks of stroke. Plaque irregularity and symmetry are characteristics that have considerable impact on blood flow patterns [128].

Plaque in the internal carotid artery tends to form in one of two manners: (1) with equal deposition on the inner flow divider wall and the outer non-flow divider wall (concentric plaque), or (2) preferential plaque deposition on the outer non-flow divider wall (eccentric plaque). Eccentric plaque formation is not only more common [127], but more frequently associated with adverse symptoms than concentric plaques in the carotid [186] and coronary arteries [187-189].

Carotid plaque symmetry has been investigated in several hemodynamic studies, using both experimental and numerical techniques. Eccentric geometries have been shown to produce greater flow disturbances downstream than concentric plaque geometries [190, 191]. Specifically, plaques with eccentric geometries produce a greater pressure drop than their

concentric counterparts, which generates greater disturbances, under either pulsatile [190] or steady [191] flow conditions. In an *in vitro* flow study, the paths of the high-velocity stenotic jets suggested higher wall shear stresses along the wall through the stenosis in an eccentric model of the stenosed carotid bifurcation, as compared to a concentric model of the same stenosis grade [192]. The stagnant region in the major recirculation zone in the eccentric model had greater extent and was more stationary than in the concentric geometry [192]. Tang *et al.* [193] found that an eccentric geometry produced greater shear stress and separation zones. A study by Tambasco and Steinman [143], using computational fluid dynamics (CFD) models, demonstrated higher platelet activation and particle deposition in an eccentric 30% carotid geometry. In contrast, numerical and experimental evidence reported by Raz *et al.* in a coronary stenosis, indicated higher platelet activation levels and particle deposition in a symmetric geometry compared to an eccentric model [194].

The clinical significance of these findings is not yet clear; many geometric parameters are still being investigated in both normal and diseased arteries. Other features of plaque geometry, such as surface irregularity, may also be influential.

1.8.6 Effect of carotid plaque ulceration

Since hemodynamic factors are determined by vessel geometry, it is likely that plaque irregularities could alter local flow dynamics in the vessel region. Indeed, several studies have shown that plaque surface morphology can further contribute to the abnormality of local hemodynamics in the carotid artery, particularly under complex physiological pulsatile flow conditions.

In vitro investigations performed by Lesniak and colleagues demonstrated that protruding surface irregularities were a source of flow disturbances in a stenotic carotid bifurcation geometry [195, 196], which

affected the associated DUS spectra measured in the abnormal flow regions [197, 198]. More specific to ulcerations, Birchall *et al.* [199] reported that a numerical model of a stenosed carotid bifurcation with a deep ellipsoidal (Type 3) ulcer exhibited low-velocity turbulent flow within the ulcer cavity and swirling jets downstream. An *in vitro* flow dynamics study by Imbesi and Kerber [200] found that flow slipstreams assumed a disturbed, helical flow pattern downstream from ulcers located in a stenotic carotid bulb.

The evidence connecting, firstly, disturbed flow and thrombus formation and, secondly, plaque ulceration and disturbed flow, suggests that there may be hemodynamic mechanisms tying surface ulcers to enhanced thrombogenicity and risk of stroke.

1.9 Blood Flow Characterization

The work in this thesis employs two principle techniques to characterize blood velocities and flow patterns in the carotid artery bifurcation. Experimental investigations were performed using clinical Doppler ultrasound, while numerical studies were executed using computational fluid dynamics.

1.9.1 Doppler ultrasound (DUS)

1.9.1.1 *Ultrasound principles*

Medical ultrasound is a versatile modality that can provide anatomical images of stationary and moving tissues in two- and three-dimensions, as well as blood velocity estimation using Doppler ultrasound techniques. Due to the low cost and portability of ultrasound scanners relative to most alternative imaging systems – such as those used in magnetic resonance imaging and computed tomography – medical ultrasound has maintained a broad scope of applications in diagnostic radiology.

Ultrasonography uses frequencies of sound well above the upper audible limit of human hearing, which is approximately 20 kHz. Typically, diagnostic ultrasound employs frequencies between 2 to 10 MHz, a range that provides favourable tradeoffs between imaging parameters of consideration, such as depth of penetration, resolution, and potential bioeffects [201].

Ultrasound imaging is a pulse-echo technique that utilizes short pulses of high frequency sound waves and the detection of the returning echoes produced from the interaction of the acoustic pulse with tissue. Transmission and reception is typically done using an acoustic transducer, or probe. Echoes, or reflections of the transmitted sound pulse, arise due to differences in the acoustic properties within the tissue structure, specifically, due to acoustic impedance mismatch at tissue interfaces. An acoustically reflective, or echogenic, structure is localized in the direction of the beam path by determining the time between the ultrasound pulse transmission and the received echo. Depth assignment of echoes along the linear beam path is possible with the pulse-echo time and knowledge that the average speed of sound in soft tissue is 1540 m s^{-1} .

The anatomical information along each beam line can be displayed (e.g. as a function of depth and traced as a function of time) by brightness encoding the received signal amplitude (B-mode). Real-time 2-D images can thus be generated by acquiring and encoding multiple scan lines over an imaging plane, which are obtained by sweeping the beam across a scanning plane. More recently, techniques have been developed to construct 3-D B-mode ultrasound images, such as by stacking 2-D images from a volume of interest [202]. Two- and three- dimensional B-mode images, or maps, of acoustic reflector positions provide useful diagnostic information of the insonated anatomy based on the different acoustic properties of the tissues.

1.9.1.2 Doppler ultrasound principles

In addition to structural images, ultrasound systems also provide blood flow estimation by virtue of the Doppler effect. When the ultrasound beam interacts with a moving reflector, such as a red blood cell, the frequency of the echo received from the moving object will be shifted relative to the original transmitted frequency. The shift in frequency depends directly on the velocity and on the direction of the moving scatterer, according to the Doppler principle:

$$f_D = 2 (v \cos \theta_D) f_o / c \quad (1.2)$$

where f_D is the Doppler frequency shift, f_o is the transmit frequency, c is the speed of sound in tissue, v is the velocity of the scatterer, and θ_D is the angle between the ultrasound beam and the direction of flow. Note that since $v \cos \theta_D$ is the magnitude of the component of the velocity in the direction of the ultrasound beam, the angle, θ_D , must be known accurately in order for accurate velocity estimation [203].

1.9.1.3 The Doppler ultrasound spectrum

Real DUS measurements will produce a range of blood-flow velocities, rather than a single velocity as in the case of a single scatterer. Since the ultrasound beam has finite dimensions (typically 1 mm axial), Doppler shift measurements are taken from within a finite volume of interrogation (sample volume), which will encompass blood cells moving in a range of velocities and directions. This results in a frequency power spectrum, and correspondingly a spectrum of calculated velocities, or a histogram where spectral amplitude represents the number of red blood cells traveling at a particular velocity within the sample volume.

However, several factors complicate this proportional relationship, including sources of spectral broadening and the complex scattering

characteristics of blood. The mechanism of interrogating flow using a focused ultrasound beam with finite dimensions fundamentally gives rise to a spread of the frequency content in the measured spectrum. Intrinsic spectral broadening has been attributed to two unique effects: the finite transit time that a scatterer spends under a beam with limited beamwidth (transit-time broadening) and the presence of a range of insonation angles (geometric broadening) [204-206]. In addition, further spectral broadening may arise from velocity gradients within the sample volume or temporally varying velocities (signal non-stationarity broadening) [207-209].

A comprehensive discussion of the physical principles of DUS and Doppler processing are described in several texts [210, 211].

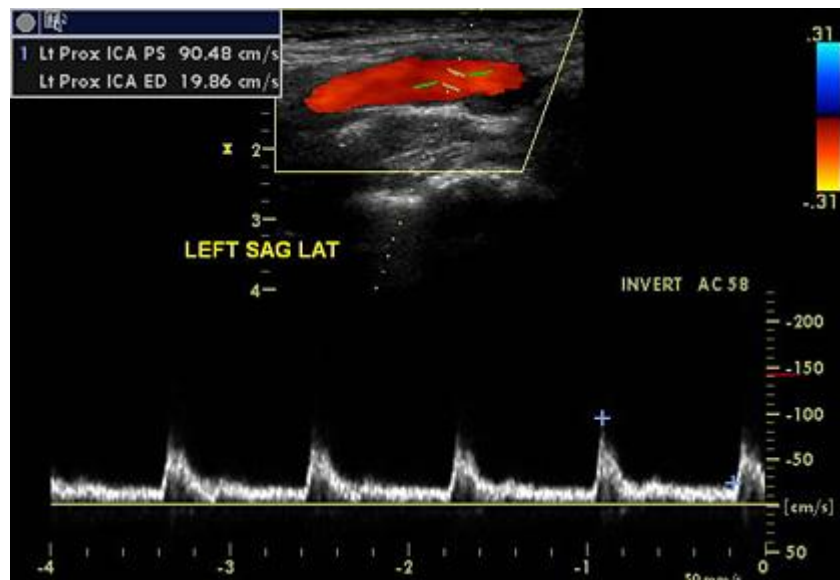


Figure 1.3: Duplex ultrasound display from a carotid Doppler examination.
http://www.nvcardiology.com/vascular_testing.htm

To view variations in blood-flow velocity over time on a clinical ultrasound scanner, the spectral information is displayed as a moving trace of spectral amplitude that is continually updated in real-time. In this spectral-time display, the Doppler motion spectrum is exhibited as the

Doppler frequency or velocity on the vertical axis – where the amplitude of the Doppler shift frequency or corresponding velocity is grey-scale encoded – versus time on the horizontal axis. An example of a Doppler spectral display for a carotid artery examination is shown in Fig. 1.3.

In clinical diagnosis, a single spectral parameter – the peak velocity, or maximum detected spectral velocity – is identified manually from the spectral display or automatically using peak velocity estimators on the scanner. For this reason, conventional DUS systems are equipped with a maximum frequency envelope detector, which produces a peak velocity trace overlaid on the spectral display.

In addition to spectral peak velocity, other derived velocity-based DUS spectral parameters not currently implemented on a clinical scanner may provide supplementary information on the nature of the flow field and therefore possibly on the diagnosis of vascular disease and stroke risk.

1.9.1.4 Characterization of flow disturbances

Research has explored various methods of quantifying the character of the measured Doppler signal to provide information on the blood flow field being interrogated, particularly, by extracting attributes of the spectral shape or power characteristics. Various approaches and spectral parameters have been investigated for distinguishing laminar flow from turbulent flow [210], and several relevant to the work in this thesis are described below.

Disturbed flow and turbulence produce velocity and pressure fluctuations superimposed on the bulk forward flow [149]. Studies have previously characterized fluctuations in velocity and pressure as a direct measure of flow disturbances [212-214]. Spectral width is also affected by turbulence, vortices and recirculation, which tend to broaden the velocity spectrum. Sigel *et al.* [215] found that it is possible to identify disturbed flow

conditions using the width of the Doppler spectrum, which has greater high frequency content under turbulent flow than laminar conditions. Several studies have since observed that spectral width is altered by the post-stenotic velocity field [120, 216-220]. The greater spectral broadening distal to diseased arteries is thought to be due to disturbed, out-of-plane flow. Hutchison [221] observed that the shape of the Doppler spectrum is different in the distal region of jet breakup and at the interface between the jet and the recirculation zone. Broadened, single-peaked Gaussian-shaped spectra are found in the distal flow breakup region, which have been proposed to arise from random particle motion in flow turbulence. In contrast, spectra from the region between the jet and the recirculation zone can have dual peaks, which likely arise from the interrogation of both the forward jet and the reverse, non-axial flow in the recirculation zone.

Studies have found that returned, or backscattered, Doppler power is also enhanced in regions of turbulence and disturbed flow. Research groups, such as Shung and Cloutier, have made advances in characterizing the complex relationship between Doppler power and turbulence [222-226]. Spectral power has also been used to characterize the presence of vortices by observing the power ratio between the forward and reverse flow velocity spectral components [227, 228]. Returned power is also sensitive to scatterer characteristics, with complex relationships to factors such as hematocrit, red blood cell aggregation [229], and to the nature of the flow insonated [223].

1.9.1.5 Doppler spectral indices

Several Doppler ultrasound spectral parameters are indicative of disturbances in blood-flow, including indices based on the increased width of the Doppler spectrum (e.g. spectral width and spectral broadening index) [120, 215, 220, 221], enhanced Doppler backscatter [117, 223, 226, 230] and

velocity fluctuations (e.g. absolute turbulence intensity (TI) and relative turbulence intensity) [212-214, 231, 232].

Absolute spectral broadening is defined as the difference between the maximum and minimum spectral frequencies (or equivalent velocities). Relative spectral broadening indices can also be calculated as the absolute spectral broadening divided by another spectral parameter, such as the mean or median spectral frequency [233, 234]. Brown *et al.* [235] defined a spectral broadening index as the ratio of absolute spectral broadening to peak frequency. A multitude of indices describing relative spectral width have been defined, and are summarized in Evans and McDicken (Table 9.2) [210]. In practice, the extraction of maximum and minimum velocities can be sensitive to the method of implementation, as well as to noise and sample volume characteristics [210]. The Doppler velocity power spectrum can be characterized by the integrated power between defined minimum and maximum frequency limits. Power ratios can also be calculated, based on integrated power from different bandwidths of the spectrum (e.g. from reverse and forward flow) [117, 223, 226-228, 230].

Absolute turbulence intensity (TI) can be defined as the root-mean-square of the velocity fluctuations [149]. A relative turbulence intensity parameter can also be defined as the ratio of the root-mean-square of the velocity fluctuations to the mean velocity. Turbulence intensity parameters are indicators of disturbed or turbulent flow. It has also been found that relative spectral broadening, velocity fluctuation, and power indices are better for assessing turbulent flow in the carotid bifurcation, as the interfacial regions between the jet and recirculation produce inconsistent absolute spectral broadening readings [224, 236].

1.9.2 Computational fluid dynamics (CFD)

Computational fluid dynamics (CFD) uses numerical methods to predict the flow of fluids. More specifically, CFD uses numerical discretization techniques (typically finite element or finite volume methods) to obtain numerical solutions to the complex, coupled partial differential equations governing the dynamical motion of fluids.

Although finite element methods have traditionally been used to study structural mechanics applications, such as to predict stresses and strains within a solid structure, they have recently been developed for use in the study of flow mechanics. In the finite element method – such as is used in the CFD work in this thesis – the fluid domain is divided (or discretized) into sub-domains, known as elements. The grid defined by these subdivisions within the domain is known as the finite element mesh. In models of complex geometries, such as realistic vascular vessels, the 3-D shape of these elements is commonly chosen to be tetrahedral, in order to accurately conform to the curved boundaries within the domain using fewer required elements. Reference points on the elements, typically at the vertices and sometimes at mid-side locations, are called nodes. The solution to the flow field generated by the CFD solver will be defined at these nodes, with functional variation describing the field over the remainder of the element. In this way, CFD provides a piecewise solution of the flow variables (e.g. velocity or pressure) as they vary over the entire domain. More details can be found in texts such as that by Zienkiewicz [237].

CFD has recently been applied to vascular flows, such as in the study of the pulsatile flow dynamics in the stenosed carotid bifurcation [126, 127, 199, 238, 239] and cerebral aneurysms [240-242]. In addition, CFD with numerical simulations of DUS has been developed as a potential interactive training environment for sonographers [243], as well as to evaluate novel

ultrasound techniques [244]. Numerical simulations using CFD are able to predict detailed time-resolved 3-D velocity vector information from pulsatile flow dynamics within a 3-D vessel volume.

1.10 Research Objectives and Thesis Outline

Ulcerations of the carotid atherosclerotic plaque have been identified as an independent risk factor for stroke, although they remain difficult to diagnose using lumenographic imaging techniques. Doppler ultrasound is the most widely performed non-invasive test used in the assessment of stroke patients suspected of having carotid arterial disease. However, current DUS examinations are used solely to identify patients with high-velocity jets within the internal carotid artery indicative of vessel luminal narrowing, and do not include a diagnosis of plaque surface ulcerations. Advanced Doppler analyses incorporating quantitative estimates of flow disturbances may result in diagnostic indices that identify pathological plaque conditions and predict the risk of thromboembolic stroke associated with the carotid artery, in particular, due to thromboemboli formed in the disturbed flow regions. As noted in Section 1.9.6 detailing the potential effect of plaque surface irregularity on blood flow, ulceration of carotid atherosclerotic plaque is a pathology for which diagnosis may benefit from a hemodynamic approach.

The overall objectives of the work in the thesis are to investigate quantitative Doppler velocity-based diagnostic parameters for the detection of ulceration and to perform basic investigations of local flow alterations due to ulceration in the carotid bifurcation, using a combination of controlled *in vitro* experimentation and CFD models. The in-house *in vitro* facility in our laboratory includes a multi-component ultrasound-compatible flow system, which allows for comprehensive DUS analyses under physiologically realistic flow conditions. We utilize this experimental setup to test our hypothesis that DUS velocity-derived parameters related to disturbed

blood-flow can provide a diagnostic index for the detection of plaque ulcerations within the stenosed carotid artery. In addition, we study, in more detail, the flow effects due to the inclusion of ulceration at the site of carotid atherosclerosis using CFD pulsatile flow simulations.

The goals of this thesis are to:

- (1) Develop a Doppler ultrasound compatible flow model to facilitate the study of blood flow parameters in an ensemble of anthropomorphic phantoms with variations in vascular geometry;
- (2) Determine a Doppler ultrasound velocity-based spectral parameter for the detection of plaque ulceration in the moderately stenosed carotid bifurcation in an *in vitro* matched-model flow study;
- (3) Evaluate the effect of shape (Type 1 – 4) and size of ulceration on the selected Doppler ultrasound diagnostic parameter;
- (4) Investigate the effect of both ulceration and stenosis severity in the carotid artery on the selected Doppler ultrasound spectral parameter using matched-models *in vitro*;
- (5) Determine the effect of ulcerations on simulated particle platelet activation parameters and numerical simulations of the selected DUS index using computational fluid dynamics models.

These goals were accomplished in the four studies detailed in this thesis. Chapter 2 will address the first goal, by developing a technique for fabricating phantoms from DUS-compatible material using a numerically controlled direct-machining technique. Chapters 3 and 4 will describe how we employed an *in vitro* flow facility and the phantoms developed in Chapter 2 to achieve the second, third, and fourth goals. Towards our fifth goal, Chapter 5 will detail our numerical CFD analysis of 3-D flow and shear

stress patterns, to assess the potential for enhanced hemodynamically induced platelet activation due to the presence of ulceration in the stenosed carotid bifurcation. This chapter will also describe the study of CFD as a tool for numerically evaluating the selected DUS index from Chapter 3, using finite sampling simulations. To close, Chapter 6 will provide summaries of the work described in the previous chapters, and will discuss future directions.

1.11 References

1. Lopez AD, Mathers CD, Ezzati M, Jamison DT and Murray CJ (2006) Global and regional burden of disease and risk factors, 2001: systematic analysis of population health data. *Lancet* 367:1747-1757.
2. Lloyd-Jones D, Adams RJ, Brown TM, Carnethon M, Dai S, *et al.* (2010) Heart disease and stroke statistics--2010 update: a report from the American Heart Association. *Circulation* 121:e46-e215.
3. Hankey GJ, Jamrozik K, Broadhurst RJ, Forbes S and Anderson CS (2002) Long-term disability after first-ever stroke and related prognostic factors in the Perth Community Stroke Study, 1989-1990. *Stroke* 33:1034-1040.
4. Mohan KM, Crichton SL, Grieve AP, Rudd AG, Wolfe CD, *et al.* (2009) Frequency and predictors for the risk of stroke recurrence up to 10 years after stroke: the South London Stroke Register. *J Neurol Neurosurg Psychiatry* 80:1012-1018.
5. Putaala J, Haapaniemi E, Metso AJ, Metso TM, Artto V, *et al.* (2010) Recurrent ischemic events in young adults after first-ever ischemic stroke. *Ann Neurol* 68:661-671.

6. Heart and Stroke Foundation of Canada (2006) *Tipping the scales of progress: heart disease and stroke in Canada 2006*. [Online] Available at: http://www.heartandstroke.com/atf/cf/%7B99452D8B-E7F1-4BD6-A57D-B136CE6C95BF%7D/Tipping_the_Scales_new.pdf
7. Public Health Agency of Canada (2009) *Tracking disease and stroke in Canada*. [Online] Available at: <http://www.phac-aspc.gc.ca/publicat/2009/cvd-avc/pdf/cvd-avs-2009-eng.pdf>
8. O'Donnell MJ, Xavier D, Liu L, Zhang H, Chin SL, *et al.* (2010) Risk factors for ischaemic and intracerebral haemorrhagic stroke in 22 countries (the INTERSTROKE study): a case-control study. *Lancet* 376:112-123.
9. Foulkes MA, Wolf PA, Price TR, Mohr JP and Hier DB (1988) The Stroke Data Bank: design, methods, and baseline characteristics. *Stroke* 19:547-554.
10. Bamford J, Sandercock P, Dennis M, Burn J and Warlow C (1991) Classification and natural history of clinically identifiable subtypes of cerebral infarction. *Lancet* 337:1521-1526.
11. Strong K, Mathers C and Bonita R (2007) Preventing stroke: saving lives around the world. *Lancet Neurol* 6:182-187.
12. Libby P (2002) Inflammation in atherosclerosis. *Nature* 420:868-874.
13. Sacco RL (2001) Newer risk factors for stroke. *Neurology* 57:S31-34.
14. Naghavi M, Libby P, Falk E, Casscells SW, Litovsky S, *et al.* (2003) From vulnerable plaque to vulnerable patient: a call for new definitions and risk assessment strategies: Part I. *Circulation* 108:1664-1672.

15. Naghavi M, Libby P, Falk E, Casscells SW, Litovsky S, *et al.* (2003) From vulnerable plaque to vulnerable patient: a call for new definitions and risk assessment strategies: Part II. *Circulation* 108:1772-1778.
16. Spagnoli LG, Mauriello A, Sangiorgi G, Fratoni S, Bonanno E, *et al.* (2004) Extracranial thrombotically active carotid plaque as a risk factor for ischemic stroke. *Jama* 292:1845-1852.
17. Casscells W, Naghavi M and Willerson JT (2003) Vulnerable atherosclerotic plaque: a multifocal disease. *Circulation* 107:2072-2075.
18. Glagov S, Zarins C, Giddens DP and Ku DN (1988) Hemodynamics and atherosclerosis. Insights and perspectives gained from studies of human arteries. *Arch Pathol Lab Med* 112:1018-1031.
19. Motomiya M and Karino T (1984) Flow patterns in the human carotid artery bifurcation. *Stroke* 15:50-56.
20. Malek AM, Alper SL and Izumo S (1999) Hemodynamic shear stress and its role in atherosclerosis. *Jama* 282:2035-2042.
21. Warlow C, Sudlow C, Dennis M, Wardlaw J and Sandercock P (2003) Stroke. *Lancet* 362:1211-1224.
22. Fairhead JF and Rothwell PM (2005) The need for urgency in identification and treatment of symptomatic carotid stenosis is already established. *Cerebrovasc Dis* 19:355-358.
23. Faries PL, Chaer RA, Patel S, Lin SC, DeRubertis B, *et al.* (2006) Current management of extracranial carotid artery disease. *Vasc Endovascular Surg* 40:165-175.
24. Gray H (1918), *Anatomy of the Human Body*. Lea & Febiger. [Online] Available at: <http://www.bartleby.com/107/>

25. Rundek T (2007) Beyond percent stenosis: carotid plaque surface irregularity and risk of stroke. *Int J Stroke* 2:169-171.
26. Norris JW, Zhu CZ, Bornstein NM and Chambers BR (1991) Vascular risks of asymptomatic carotid stenosis. *Stroke* 22:1485-1490.
27. Bock RW, Gray-Weale AC, Mock PA, App Stats M, Robinson DA, *et al.* (1993) The natural history of asymptomatic carotid artery disease. *J Vasc Surg* 17:160-169; discussion 170-161.
28. Marquardt L, Geraghty OC, Mehta Z and Rothwell PM (2010) Low risk of ipsilateral stroke in patients with asymptomatic carotid stenosis on best medical treatment: a prospective, population-based study. *Stroke* 41:e11-17.
29. McPhee JT, Schanzer A, Messina LM and Eslami MH (2008) Carotid artery stenting has increased rates of postprocedure stroke, death, and resource utilization than does carotid endarterectomy in the United States, 2005. *J Vasc Surg* 48:1442-1450, 1450.e1441.
30. McPhee JT, Hill JS, Ciocca RG, Messina LM and Eslami MH (2007) Carotid endarterectomy was performed with lower stroke and death rates than carotid artery stenting in the United States in 2003 and 2004. *J Vasc Surg* 46:1112-1118.
31. Paciaroni M and Bogousslavsky J (2010) Primary and secondary prevention of ischemic stroke. *Eur Neurol* 63:267-278.
32. Nighoghossian N, Derex L and Douek P (2005) The vulnerable carotid artery plaque: current imaging methods and new perspectives. *Stroke* 36:2764-2772.

33. Golledge J and Siew DA (2008) Identifying the carotid 'high risk' plaque: is it still a riddle wrapped up in an enigma? *Eur J Vasc Endovasc Surg* 35:2-8.
34. Chalela JA (2009) Evaluating the carotid plaque: going beyond stenosis. *Cerebrovasc Dis* 27 Suppl 1:19-24.
35. Wolf PA, D'Agostino RB, Belanger AJ and Kannel WB (1991) Probability of stroke: a risk profile from the Framingham Study. *Stroke* 22:312-318.
36. Barnett HJ, Taylor DW, Eliasziw M, Fox AJ, Ferguson GG, *et al.* (1998) Benefit of carotid endarterectomy in patients with symptomatic moderate or severe stenosis. North American Symptomatic Carotid Endarterectomy Trial Collaborators. *N Engl J Med* 339:1415-1425.
37. Rothwell PM, Gutnikov SA and Warlow CP (2003) Reanalysis of the final results of the European Carotid Surgery Trial. *Stroke* 34:514-523.
38. Rothwell PM, Eliasziw M, Gutnikov SA, Fox AJ, Taylor DW, *et al.* (2003) Analysis of pooled data from the randomised controlled trials of endarterectomy for symptomatic carotid stenosis. *Lancet* 361:107-116.
39. Rothwell PM and Goldstein LB (2004) Carotid endarterectomy for asymptomatic carotid stenosis: asymptomatic carotid surgery trial. *Stroke* 35:2425-2427.
40. Sleight SP, Poloniecki J and Halliday AW (2002) Asymptomatic carotid stenosis in patients on medical treatment alone. *Eur J Vasc Endovasc Surg* 23:519-523.

41. Fisher M, Paganini-Hill A, Martin A, Cosgrove M, Toole JF, *et al.* (2005) Carotid plaque pathology: thrombosis, ulceration, and stroke pathogenesis. *Stroke* 36:253-257.
42. Eckstein HH, Ringleb P, Allenberg JR, Berger J, Fraedrich G, *et al.* (2008) Results of the Stent-Protected Angioplasty versus Carotid Endarterectomy (SPACE) study to treat symptomatic stenoses at 2 years: a multinational, prospective, randomised trial. *Lancet Neurol* 7:893-902.
43. Ringleb PA, Allenberg J, Bruckmann H, Eckstein HH, Fraedrich G, *et al.* (2006) 30 day results from the SPACE trial of stent-protected angioplasty versus carotid endarterectomy in symptomatic patients: a randomised non-inferiority trial. *Lancet* 368:1239-1247.
44. Fiehler J, Bakke SJ, Clifton A, Houdart E, Jansen O, *et al.* (2010) Plea of the defence-critical comments on the interpretation of EVA3S, SPACE and ICSS. *Neuroradiology* 52:601-610.
45. Mas JL, Trinquart L, Leys D, Albucher JF, Rousseau H, *et al.* (2008) Endarterectomy Versus Angioplasty in Patients with Symptomatic Severe Carotid Stenosis (EVA-3S) trial: results up to 4 years from a randomised, multicentre trial. *Lancet Neurol* 7:885-892.
46. Mas JL, Chatellier G, Beyssen B, Branchereau A, Moulin T, *et al.* (2006) Endarterectomy versus stenting in patients with symptomatic severe carotid stenosis. *N Engl J Med* 355:1660-1671.
47. Ederle J, Dobson J, Featherstone RL, Bonati LH, van der Worp HB, *et al.* (2010) Carotid artery stenting compared with endarterectomy in patients with symptomatic carotid stenosis (International Carotid Stenting Study): an interim analysis of a randomised controlled trial. *Lancet* 375:985-997.

48. Brott TG, Hobson RW, 2nd, Howard G, Roubin GS, Clark WM, *et al.* (2010) Stenting versus endarterectomy for treatment of carotid-artery stenosis. *N Engl J Med* 363:11-23.
49. Forbes TL (2010) Preliminary results of carotid revascularization endarterectomy vs stenting trial (CREST). *J Vasc Surg* 51:1300-1301.
50. Naylor AR (2009) ICSS and EXACT/CAPTURE: More questions than answers. *Eur J Vasc Endovasc Surg* 38:397-401.
51. Fox AJ (1993) How to measure carotid stenosis. *Radiology* 186:316-318.
52. Fayed AM, White CJ, Ramee SR, Jenkins JS and Collins TJ (2002) Carotid and cerebral angiography performed by cardiologists: cerebrovascular complications. *Catheter Cardiovasc Interv* 55:277-280.
53. Tahmasebpour HR, Buckley AR, Cooperberg PL and Fix CH (2005) Sonographic examination of the carotid arteries. *Radiographics* 25:1561-1575.
54. Dawson DL, Roseberry CA and Fujitani RM (1997) Preoperative testing before carotid endarterectomy: a survey of vascular surgeons' attitudes. *Ann Vasc Surg* 11:264-272.
55. Back MR, Wilson JS, Rushing G, Stordahl N, Linden C, *et al.* (2000) Magnetic resonance angiography is an accurate imaging adjunct to duplex ultrasound scan in patient selection for carotid endarterectomy. *J Vasc Surg* 32:429-438; discussion 439-440.
56. Grant EG, Benson CB, Moneta GL, Alexandrov AV, Baker JD, *et al.* (2003) Carotid artery stenosis: grayscale and Doppler ultrasound diagnosis--Society of Radiologists in Ultrasound consensus conference. *Ultrasound Q* 19:190-198.

57. Wardlaw JM, Chappell FM, Best JJ, Wartolowska K and Berry E (2006) Non-invasive imaging compared with intra-arterial angiography in the diagnosis of symptomatic carotid stenosis: a meta-analysis. *Lancet* 367:1503-1512.
58. Johnston DC and Goldstein LB (2001) Clinical carotid endarterectomy decision making: noninvasive vascular imaging versus angiography. *Neurology* 56:1009-1015.
59. Hankey GJ (1999) Stroke prediction and prevention by carotid endarterectomy: keep an eye on the doughnut and not just the hole. *Cerebrovasc Dis* 9:345-350.
60. Hennerici MG (2004) The unstable plaque. *Cerebrovasc Dis* 17 Suppl 3:17-22.
61. Falk E (2006) Pathogenesis of atherosclerosis. *J Am Coll Cardiol* 47:C7-12.
62. Streifler JY, Eliasziw M, Fox AJ, Benavente OR, Hachinski VC, *et al.* (1994) Angiographic detection of carotid plaque ulceration. Comparison with surgical observations in a multicenter study. North American Symptomatic Carotid Endarterectomy Trial. *Stroke* 25:1130-1132.
63. Rothwell PM, Gibson R and Warlow CP (2000) Interrelation between plaque surface morphology and degree of stenosis on carotid angiograms and the risk of ischemic stroke in patients with symptomatic carotid stenosis. On behalf of the European Carotid Surgery Trialists' Collaborative Group. *Stroke* 31:615-621.
64. Imparato AM, Riles TS, Mintzer R and Baumann FG (1983) The importance of hemorrhage in the relationship between gross morphologic

characteristics and cerebral symptoms in 376 carotid artery plaques. *Ann Surg* 197:195-203.

65. Arapoglou B, Kondi-Pafiti A, Katsenis K and Dimakakos P (1994) The clinical significance of carotid plaque haemorrhage. *Int Angiol* 13:323-326.

66. AbuRahma AF, Kyer PD, 3rd, Robinson PA and Hannay RS (1998) The correlation of ultrasonic carotid plaque morphology and carotid plaque hemorrhage: clinical implications. *Surgery* 124:721-726; discussion 726-728.

67. Richardson PD, Davies MJ and Born GV (1989) Influence of plaque configuration and stress distribution on fissuring of coronary atherosclerotic plaques. *Lancet* 2:941-944.

68. Muller JE, Tofler GH and Stone PH (1989) Circadian variation and triggers of onset of acute cardiovascular disease. *Circulation* 79:733-743.

69. Richardson PD (2002) Biomechanics of plaque rupture: progress, problems, and new frontiers. *Ann Biomed Eng* 30:524-536.

70. Fuster V, Badimon J, Chesebro JH and Fallon JT (1996) Plaque rupture, thrombosis, and therapeutic implications. *Haemostasis* 26 Suppl 4:269-284.

71. Maseri A and Fuster V (2003) Is there a vulnerable plaque? *Circulation* 107:2068-2071.

72. Wasserman BA, Wityk RJ, Trout HH, 3rd and Virmani R (2005) Low-grade carotid stenosis: looking beyond the lumen with MRI. *Stroke* 36:2504-2513.

73. Ahmed RM, Harris JP, Anderson CS, Makeham V and Halmagyi GM (2010) Carotid endarterectomy for symptomatic, but "haemodynamically insignificant" carotid stenosis. *Eur J Vasc Endovasc Surg* 40:475-482.

74. Li ZY, Howarth SP, Tang T and Gillard JH (2006) How critical is fibrous cap thickness to carotid plaque stability? A flow-plaque interaction model. *Stroke* 37:1195-1199.
75. Saam T, Cai J, Ma L, Cai YQ, Ferguson MS, *et al.* (2006) Comparison of symptomatic and asymptomatic atherosclerotic carotid plaque features with in vivo MR imaging. *Radiology* 240:464-472.
76. Wasserman BA (2010) Advanced contrast-enhanced MRI for looking beyond the lumen to predict stroke: building a risk profile for carotid plaque. *Stroke* 41:S12-16.
77. Watanabe Y and Nagayama M (2010) MR plaque imaging of the carotid artery. *Neuroradiology* 52:253-274.
78. AbuRahma AF, Wulu JT, Jr. and Crotty B (2002) Carotid plaque ultrasonic heterogeneity and severity of stenosis. *Stroke* 33:1772-1775.
79. Ainsworth CD, Blake CC, Tamayo A, Beletsky V, Fenster A, *et al.* (2005) 3D ultrasound measurement of change in carotid plaque volume: a tool for rapid evaluation of new therapies. *Stroke* 36:1904-1909.
80. Cipollone F, Fazia M, Mincione G, Iezzi A, Pini B, *et al.* (2004) Increased expression of transforming growth factor-beta1 as a stabilizing factor in human atherosclerotic plaques. *Stroke* 35:2253-2257.
81. Libby P, DiCarli M and Weissleder R (2010) The vascular biology of atherosclerosis and imaging targets. *J Nucl Med* 51 Suppl 1:33S-37S.
82. Walker LJ, Ismail A, McMeekin W, Lambert D, Mendelow AD, *et al.* (2002) Computed tomography angiography for the evaluation of carotid atherosclerotic plaque: correlation with histopathology of endarterectomy specimens. *Stroke* 33:977-981.

83. Wintermark M, Jawadi SS, Rapp JH, Tihan T, Tong E, *et al.* (2008) High-resolution CT imaging of carotid artery atherosclerotic plaques. *AJNR Am J Neuroradiol* 29:875-882.
84. Fujii K, Kobayashi Y, Mintz GS, Takebayashi H, Dangas G, *et al.* (2003) Intravascular ultrasound assessment of ulcerated ruptured plaques: a comparison of culprit and nonculprit lesions of patients with acute coronary syndromes and lesions in patients without acute coronary syndromes. *Circulation* 108:2473-2478.
85. Slager CJ, Wentzel JJ, Gijzen FJ, Thury A, van der Wal AC, *et al.* (2005) The role of shear stress in the destabilization of vulnerable plaques and related therapeutic implications. *Nat Clin Pract Cardiovasc Med* 2:456-464.
86. Groen HC, Gijzen FJ, van der Lugt A, Ferguson MS, Hatsukami TS, *et al.* (2007) Plaque rupture in the carotid artery is localized at the high shear stress region: a case report. *Stroke* 38:2379-2381.
87. Lovett JK and Rothwell PM (2003) Site of carotid plaque ulceration in relation to direction of blood flow: an angiographic and pathological study. *Cerebrovasc Dis* 16:369-375.
88. de Weert TT, Cretier S, Groen HC, Homburg P, Cakir H, *et al.* (2009) Atherosclerotic plaque surface morphology in the carotid bifurcation assessed with multidetector computed tomography angiography. *Stroke* 40:1334-1340.
89. Tang D, Teng Z, Canton G, Yang C, Ferguson M, *et al.* (2009) Sites of rupture in human atherosclerotic carotid plaques are associated with high structural stresses: an in vivo MRI-based 3D fluid-structure interaction study. *Stroke* 40:3258-3263.

90. Groen HC, Gijzen FJ, van der Lugt A, Ferguson MS, Hatsukami TS, *et al.* (2008) High shear stress influences plaque vulnerability Part of the data presented in this paper were published in *Stroke* 2007;38:2379-81. *Neth Heart J* 16:280-283.
91. Lovett JK, Gallagher PJ, Hands LJ, Walton J and Rothwell PM (2004) Histological correlates of carotid plaque surface morphology on lumen contrast imaging. *Circulation* 110:2190-2197.
92. Prabhakaran S, Rundek T, Ramas R, Elkind MS, Paik MC, *et al.* (2006) Carotid plaque surface irregularity predicts ischemic stroke: the northern Manhattan study. *Stroke* 37:2696-2701.
93. Eliasziw M, Streifler JY, Spence JD, Fox AJ, Hachinski VC, *et al.* (1995) Prognosis for patients following a transient ischemic attack with and without a cerebral infarction on brain CT. North American Symptomatic Carotid Endarterectomy Trial (NASCET) Group. *Neurology* 45:428-431.
94. Handa N, Matsumoto M, Maeda H, Hougaku H and Kamada T (1995) Ischemic stroke events and carotid atherosclerosis. Results of the Osaka Follow-up Study for Ultrasonographic Assessment of Carotid Atherosclerosis (the OSACA Study). *Stroke* 26:1781-1786.
95. Kitamura A, Iso H, Imano H, Ohira T, Okada T, *et al.* (2004) Carotid intima-media thickness and plaque characteristics as a risk factor for stroke in Japanese elderly men. *Stroke* 35:2788-2794.
96. Sitzer M, Muller W, Siebler M, Hort W, Kniemeyer HW, *et al.* (1995) Plaque ulceration and lumen thrombus are the main sources of cerebral microemboli in high-grade internal carotid artery stenosis. *Stroke* 26:1231-1233.

97. Orlandi G, Parenti G, Landucci Pellegrini L, Sartucci F, Paoli C, *et al.* (1999) Plaque surface and microembolic signals in moderate carotid stenosis. *Ital J Neurol Sci* 20:179-182.
98. Eikelboom BC, Riles TR, Mintzer R, Baumann FG, DeFillip G, *et al.* (1983) Inaccuracy of angiography in the diagnosis of carotid ulceration. *Stroke* 14:882-885.
99. Comerota AJ, Katz ML, White JV and Grosh JD (1990) The preoperative diagnosis of the ulcerated carotid atheroma. *J Vasc Surg* 11:505-510.
100. Randoux B, Marro B, Koskas F, Duyme M, Sahel M, *et al.* (2001) Carotid artery stenosis: prospective comparison of CT, three-dimensional gadolinium-enhanced MR, and conventional angiography. *Radiology* 220:179-185.
101. Saba L, Caddeo G, Sanfilippo R, Montisci R and Mallarini G (2007) CT and ultrasound in the study of ulcerated carotid plaque compared with surgical results: potentialities and advantages of multidetector row CT angiography. *AJNR Am J Neuroradiol* 28:1061-1066.
102. Schuknecht B (2007) High-concentration contrast media (HCCM) in CT angiography of the carotid system: impact on therapeutic decision making. *Neuroradiology* 49 Suppl 1:S15-26.
103. Cinat ME, Casalme C, Wilson SE, Pham H and Anderson P (2003) Computed tomography angiography validates duplex sonographic evaluation of carotid artery stenosis. *Am Surg* 69:842-847.
104. Huston J, 3rd, Fain SB, Wald JT, Luetmer PH, Rydberg CH, *et al.* (2001) Carotid artery: elliptic centric contrast-enhanced MR angiography compared with conventional angiography. *Radiology* 218:138-143.

105. Yu W, Underhill HR, Ferguson MS, Hippe DS, Hatsukami TS, *et al.* (2009) The added value of longitudinal black-blood cardiovascular magnetic resonance angiography in the cross sectional identification of carotid atherosclerotic ulceration. *J Cardiovasc Magn Reson* 11:31.
106. Remonda L, Senn P, Barth A, Arnold M, Lovblad KO, *et al.* (2002) Contrast-enhanced 3D MR angiography of the carotid artery: comparison with conventional digital subtraction angiography. *AJNR Am J Neuroradiol* 23:213-219.
107. Barry R, Pienaar C and Nel CJ (1990) Accuracy of B-mode ultrasonography in detecting carotid plaque hemorrhage and ulceration. *Ann Vasc Surg* 4:466-470.
108. Magnoni M, Coli S and Cianflone D (2009) A surprise behind the dark. *Eur J Echocardiogr* 10:887-888.
109. Tegos TJ, Kalodiki E, Daskalopoulou SS and Nicolaides AN (2000) Stroke: epidemiology, clinical picture, and risk factors--Part I of III. *Angiology* 51:793-808.
110. Heliopoulos J, Vadikolias K, Piperidou C and Mitsias P (2009) Detection of carotid artery plaque ulceration using 3-dimensional ultrasound. *J Neuroimaging*. DOI: 10.1111/j.1552-6569.2009.00450.
111. Chiu B, Beletsky V, Spence JD, Parraga G and Fenster A (2009) Analysis of carotid lumen surface morphology using three-dimensional ultrasound imaging. *Phys Med Biol* 54:1149-1167.
112. Fenster A, Blake C, Gyacskov I, Landry A and Spence JD (2006) 3D ultrasound analysis of carotid plaque volume and surface morphology. *Ultrasonics* 44 Suppl 1:e153-157.

113. Granger RA (1995) *Fluid Mechanics*. Dover, New York.
114. Bakker PG (1991) *Bifurcations in Flow Patterns: Some Applications of the Qualitative Theory of Differential Equations in Fluid Dynamics*. Springer, New York.
115. Fung YC (1997) *Biomechanics: circulation*. Springer, New York.
116. Berger SA and Jou LD (2000) Flows in stenotic vessels. *Annual Review of Fluid Mechanics* 32:347-382.
117. Bascom PA, Cobbold RS, Routh HF and Johnston KW (1993) On the Doppler signal from a steady flow asymmetrical stenosis model: effects of turbulence. *Ultrasound Med Biol* 19:197-210.
118. Dunmire B, Pagel G, Beach KW and Labs KH (2001) Post stenotic flow disturbances in a steady flow model. In: Proceedings of the SPIE, San Diego, pp 502-513.
119. Ku DN, Giddens DP, Zarins CK and Glagov S (1985) Pulsatile flow and atherosclerosis in the human carotid bifurcation. Positive correlation between plaque location and low oscillating shear stress. *Arteriosclerosis* 5:293-302.
120. Hutchison KJ and Karpinski E (1985) In vivo demonstration of flow recirculation and turbulence downstream of graded stenoses in canine arteries. *J Biomech* 18:285-296.
121. Ku DN, Giddens DP, Phillips DJ and Strandness DE, Jr. (1985) Hemodynamics of the normal human carotid bifurcation: in vitro and in vivo studies. *Ultrasound Med Biol* 11:13-26.
122. Fei DY, Billian C and Rittgers SE (1988) Flow dynamics in a stenosed carotid bifurcation model--Part I: Basic velocity measurements. *Ultrasound Med Biol* 14:21-31.

123. Giddens DP, Tang TD and Loth F (1995) Fluid mechanics of arterial bifurcations. In: Jaffrin MY and Caro CG (ed) *Biological Flows*, 1st edn. Plenum, New York, pp 51-68.
124. Ku DN (1997) Blood flow in arteries. *Annu Rev Fluid Mech* 29:399-434.
125. Sakariassen KS and Barstad RM (1993) Mechanisms of thromboembolism at arterial plaques. *Blood Coagul Fibrinolysis* 4:615-625.
126. Lee SW, Antiga L, Spence JD and Steinman DA (2008) Geometry of the carotid bifurcation predicts its exposure to disturbed flow. *Stroke* 39:2341-2347.
127. Steinman DA, Poepping TL, Tambasco M, Rankin RN and Holdsworth DW (2000) Flow patterns at the stenosed carotid bifurcation: effect of concentric versus eccentric stenosis. *Ann Biomed Eng* 28:415-423.
128. Stroud JS, Berger SA and Saloner D (2000) Influence of stenosis morphology on flow through severely stenotic vessels: implications for plaque rupture. *Journal of Biomechanics* 33:443-455.
129. Hjortdal JO, Pedersen EM, Hjortdal VE, Hasenkam JM, Nygaard H, *et al.* (1991) Velocity field studies at surgically imposed arterial stenoses on the abdominal aorta in pigs. *J Biomech* 24:1081-1093.
130. Badimon L, Chesebro JH and Badimon JJ (1992) Thrombus formation on ruptured atherosclerotic plaques and rethrombosis on evolving thrombi. *Circulation* 86:III74-85.
131. Dewey CF, Jr., Bussolari SR, Gimbrone MA, Jr. and Davies PF (1981) The dynamic response of vascular endothelial cells to fluid shear stress. *J Biomech Eng* 103:177-185.

132. Strony J, Beaudoin A, Brands D and Adelman B (1993) Analysis of shear stress and hemodynamic factors in a model of coronary artery stenosis and thrombosis. *Am J Physiol* 265:H1787-1796.
133. Cadroy Y, Horbett TA and Hanson SR (1989) Discrimination between platelet-mediated and coagulation-mediated mechanisms in a model of complex thrombus formation in vivo. *J Lab Clin Med* 113:436-448.
134. Mustard JF and Packham MA (1970) Thromboembolism: manifestation of the response of blood to injury. *Circulation* 42:1-21.
135. Holme PA, Orvim U, Hamers MJ, Solum NO, Brosstad FR, *et al.* (1997) Shear-induced platelet activation and platelet microparticle formation at blood flow conditions as in arteries with a severe stenosis. *Arterioscler Thromb Vasc Biol* 17:646-653.
136. Sakariassen KS, Holme PA, Orvim U, Barstad RM, Solum NO, *et al.* (1998) Shear-induced platelet activation and platelet microparticle formation in native human blood. *Thromb Res* 92:S33-41.
137. Constantinides P (1989) The role of arterial wall injury in atherogenesis and arterial thrombogenesis. *Zentralbl Allg Pathol* 135:517-530.
138. Stein PD and Sabbah HN (1974) Measured turbulence and its effect on thrombus formation. *Circ Res* 35:608-614.
139. Smith RL, Blick FB, Coalson J and Stein PD (1972) Thrombus production by turbulence. *J Applied Physiology* 32:261-264.
140. Mustard JF, Murphy EA, Rowsell HC and Downie HG (1962) Factors influencing thrombus formation in vivo. *Am J Med* 33:621-647.

141. Merten M, Chow T, Hellums JD and Thiagarajan P (2000) A new role for P-selectin in shear-induced platelet aggregation. *Circulation* 102:2045-2050.
142. Reininger AJ, Reininger CB, Heinzmann U and Wurzinger LJ (1995) Residence time in niches of stagnant flow determines fibrin clot formation in an arterial branching model--detailed flow analysis and experimental results. *Thromb Haemost* 74:916-922.
143. Tambasco M and Steinman DA (2003) Path-dependent hemodynamics of the stenosed carotid bifurcation. *Ann Biomed Eng* 31:1054-1065.
144. Langer HF and Gawaz M (2008) Platelet-vessel wall interactions in atherosclerotic disease. *Thromb Haemost* 99:480-486.
145. Jennings LK (2009) Mechanisms of platelet activation: need for new strategies to protect against platelet-mediated atherothrombosis. *Thromb Haemost* 102:248-257.
146. Wootton DM and Ku DN (1999) Fluid mechanics of vascular systems, diseases, and thrombosis. *Annu Rev Biomed Eng* 1:299-329.
147. Hagberg IA, Roald HE and Lyberg T (1997) Platelet activation in flowing blood passing growing arterial thrombi. *Arterioscler Thromb Vasc Biol* 17:1331-1336.
148. Davi G and Patrono C (2007) Platelet activation and atherothrombosis. *N Engl J Med* 357:2482-2494.
149. Hinze JO (1959) *Turbulence. An Introduction to its Mechanism and Theory*. McGraw-Hill, New York.
150. Davies PF, Dewey CF, Jr., Bussolari SR, Gordon EJ and Gimbrone MA, Jr. (1984) Influence of hemodynamic forces on vascular endothelial

function. In vitro studies of shear stress and pinocytosis in bovine aortic cells. *J Clin Invest* 73:1121-1129.

151. Zand T, Nunnari JJ, Hoffman AH, Savelonis BJ, MacWilliams B, *et al.* (1988) Endothelial adaptations in aortic stenosis. Correlation with flow parameters. *Am J Pathol* 133:407-418.

152. Huang PY and Hellums JD (1993) Aggregation and disaggregation kinetics of human blood platelets: Part II. Shear-induced platelet aggregation. *Biophys J* 65:344-353.

153. Nesbitt WS, Westein E, Tovar-Lopez FJ, Tolouei E, Mitchell A, *et al.* (2009) A shear gradient-dependent platelet aggregation mechanism drives thrombus formation. *Nat Med* 15:665-673.

154. Kroll MH, Hellums JD, McIntire LV, Schafer AI and Moake JL (1996) Platelets and shear stress. *Blood* 88:1525-1541.

155. Maxwell MJ, Westein E, Nesbitt WS, Giuliano S, Dopheide SM, *et al.* (2007) Identification of a 2-stage platelet aggregation process mediating shear-dependent thrombus formation. *Blood* 109:566-576.

156. Zhang JN, Bergeron AL, Yu Q, Sun C, McIntire LV, *et al.* (2002) Platelet aggregation and activation under complex patterns of shear stress. *Thromb Haemost* 88:817-821.

157. Ruggeri ZM (1993) Mechanisms of shear-induced platelet adhesion and aggregation. *Thromb Haemost* 70:119-123.

158. Savage B, Sixma JJ and Ruggeri ZM (2002) Functional self-association of von Willebrand factor during platelet adhesion under flow. *Proc Natl Acad Sci U S A* 99:425-430.

159. Savage B, Almus-Jacobs F and Ruggeri ZM (1998) Specific synergy of multiple substrate-receptor interactions in platelet thrombus formation under flow. *Cell* 94:657-666.
160. Li F, Li CQ, Moake JL, Lopez JA and McIntire LV (2004) Shear stress-induced binding of large and unusually large von Willebrand factor to human platelet glycoprotein I α . *Ann Biomed Eng* 32:961-969.
161. Jackson SP, Nesbitt WS and Westein E (2009) Dynamics of platelet thrombus formation. *J Thromb Haemost* 7 Suppl 1:17-20.
162. Ruggeri ZM, Orje JN, Habermann R, Federici AB and Reininger AJ (2006) Activation-independent platelet adhesion and aggregation under elevated shear stress. *Blood* 108:1903-1910.
163. Tabas I (2010) The role of endoplasmic reticulum stress in the progression of atherosclerosis. *Circ Res* 107:839-850.
164. Leytin V, Allen DJ, Mykhaylov S, Mis L, Lyubimov EV, *et al.* (2004) Pathologic high shear stress induces apoptosis events in human platelets. *Biochem Biophys Res Commun* 320:303-310.
165. Gijzen FJ, Wentzel JJ, Thury A, Mastik F, Schaar JA, *et al.* (2008) Strain distribution over plaques in human coronary arteries relates to shear stress. *Am J Physiol Heart Circ Physiol* 295:H1608-1614.
166. Goldsmith HL (1970) Motion of particles in a flowing stream. *Thromb Diath Haemorrhag Suppl* 40:91-110.
167. Muller-Mohnssen H (1976) Experimental results to the deposition hypothesis of atherosclerosis. *Thromb Res* 8:553-566.

168. Affeld K, Goubergrits L, Kertzsch U, Gadischke J and Reininger A (2004) Mathematical model of platelet deposition under flow conditions. *Int J Artif Organs* 27:699-708.
169. Reininger CB, Lasser R, Rumitz M, Boger C and Schweiberer L (1999) Computational analysis of platelet adhesion and aggregation under stagnation point flow conditions. *Comput Biol Med* 29:1-18.
170. Morton WA, Parmentier EM and Petschek HE (1975) Study of aggregate formation in region of separated blood flow. *Thromb Diath Haemorrh* 34:840-854.
171. Schoephoerster RT, Oynes F, Nunez G, Kapadvanjwala M and Dewanjee MK (1993) Effects of local geometry and fluid dynamics on regional platelet deposition on artificial surfaces. *Arterioscler Thromb* 13:1806-1813.
172. Turitto VT and Hall CL (1998) Mechanical factors affecting hemostasis and thrombosis. *Thromb Res* 92:S25-31.
173. Affeld K, Reininger AJ, Gadischke J, Grunert K, Schmidt S, *et al.* (1995) Fluid mechanics of the stagnation point flow chamber and its platelet deposition. *Artif Organs* 19:597-602.
174. Hellums JD (1994) 1993 Whitaker Lecture: biorheology in thrombosis research. *Ann Biomed Eng* 22:445-455.
175. Wurzinger LJ, Opitz R, Blasberg P and Schmid-Schonbein H (1985) Platelet and coagulation parameters following millisecond exposure to laminar shear stress. *Thromb Haemost* 54:381-386.
176. Hellums JD, Peterson DM, Stathopoulos NA, Moake JL and Giorgio TD (1987) *Studies on the Mechanisms of Shear-Induced Platelet Activation*. Springer-Verlag, New York.

177. Bluestein D, Niu L, Schoepfoerster RT and Dewanjee MK (1997) Fluid mechanics of arterial stenosis: relationship to the development of mural thrombus. *Ann Biomed Eng* 25:344-356.
178. Rubenstein DA and Yin W (2010) Quantifying the effects of shear stress and shear exposure duration regulation on flow induced platelet activation and aggregation. *J Thromb Thrombolysis* 30:36-45.
179. Jesty J, Yin W, Perrotta P and Bluestein D (2003) Platelet activation in a circulating flow loop: combined effects of shear stress and exposure time. *Platelets* 14:143-149.
180. Ramstack JM, Zuckerman L and Mockros LF (1979) Shear-induced activation of platelets. *J Biomech* 12:113-125.
181. Boreda R, Fatemi RS and Rittgers SE (1995) Potential for platelet stimulation in critically stenosed carotid and coronary arteries. *J Vasc Invest* 1:26-37.
182. Zhang JN, Bergeron AL, Yu Q, Sun C, McBride L, *et al.* (2003) Duration of exposure to high fluid shear stress is critical in shear-induced platelet activation-aggregation. *Thromb Haemost* 90:672-678.
183. Purvis NB, Jr. and Giorgio TD (1991) The effects of elongational stress exposure on the activation and aggregation of blood platelets. *Biorheology* 28:355-367.
184. Nobili M, Sheriff J, Morbiducci U, Redaelli A and Bluestein D (2008) Platelet activation due to hemodynamic shear stresses: damage accumulation model and comparison to in vitro measurements. *Asaio J* 54:64-72.

185. Suter SP, Nowak MD, Joist JH, Zeffren DJ and Bauman JE (1988) A programmable, computer-controlled cone-plate viscometer for the application of pulsatile shear stress to platelet suspensions. *Biorheology* 25:449-459.
186. Ohara T, Toyoda K, Otsubo R, Nagatsuka K, Kubota Y, *et al.* (2008) Eccentric stenosis of the carotid artery associated with ipsilateral cerebrovascular events. *AJNR Am J Neuroradiol* 29:1200-1203.
187. Ellis S, Alderman EL, Cain K, Wright A, Bourassa M, *et al.* (1989) Morphology of left anterior descending coronary territory lesions as a predictor of anterior myocardial infarction: a CASS Registry Study. *J Am Coll Cardiol* 13:1481-1491.
188. Ellis S, Alderman E, Cain K, Fisher L, Sanders W, *et al.* (1988) Prediction of risk of anterior myocardial infarction by lesion severity and measurement method of stenoses in the left anterior descending coronary distribution: a CASS Registry Study. *J Am Coll Cardiol* 11:908-916.
189. Tousoulis D, Davies G, Crake T, Lefroy DC, Rosen S, *et al.* (1998) Angiographic characteristics of infarct-related and non-infarct-related stenoses in patients in whom stable angina progressed to acute myocardial infarction. *Am Heart J* 136:382-388.
190. Loree HM, Kamm RD, Atkinson CM and Lee RT (1991) Turbulent pressure fluctuations on surface of model vascular stenoses. *Am J Physiol* 261:H644-H650.
191. Young DF and Tsai FY (1973) Flow characteristics in models of arterial stenoses: I. Steady flow. *J Biomech* 6:395-410.
192. Poepping TL, Rankin RN and Holdsworth DW (2010) Flow patterns in carotid bifurcation models using pulsed Doppler ultrasound: effect of

concentric vs. eccentric stenosis on turbulence and recirculation. *Ultrasound Med Biol* 36:1125-1134.

193. Tang D, Yang C, Kobayashi S, Zheng J and Vito RP (2003) Effect of stenosis asymmetry on blood flow and artery compression: a three-dimensional fluid-structure interaction model. *Ann Biomed Eng* 31:1182-1193.

194. Raz S, Einav S, Alemu Y and Bluestein D (2007) DPIV prediction of flow induced platelet activation-comparison to numerical predictions. *Ann Biomed Eng* 35:493-504.

195. Kaluzynski K, Lesniak B, Mikolajczyk K and Liepsch D (1997) Analysis of ultrasonic Doppler velocity data obtained in models of stenosed carotid bifurcations with irregular lesion surface. *Technol Health Care* 5:199-206.

196. Kaluzynski K and Liepsch D (1995) The effect of wall roughness on velocity distribution in a model of the carotid sinus bifurcation--analysis of laser and ultrasound Doppler velocity data. *Technol Health Care* 3:153-159.

197. Lesniak B, Kaluzynski K, Liepsch D and Palko T (2002) The discrimination of stenosed carotid bifurcation models with smooth and irregular plaque surface. Part I. Laser and ultrasonic Doppler flow studies. *Med Eng Phys* 24:309-318.

198. Lesniak B, Kaluzynski K, Liepsch D and Palko T (2002) The discrimination of stenosed carotid bifurcation models with smooth and irregular plaque surface. Part II. The multivariate statistical analysis of ultrasonic Doppler velocity data. *Med Eng Phys* 24:319-323.

199. Birchall D, Zaman A, Hacker J, Davies G and Mendelow D (2006) Analysis of haemodynamic disturbance in the atherosclerotic carotid artery using computational fluid dynamics. *Eur Radiol* 16:1074-1083.
200. Imbesi SG and Kerber CW (1998) Why do ulcerated atherosclerotic carotid artery plaques embolize? A flow dynamics study. *AJNR Am J Neuroradiol* 19:761-766.
201. Szabo TL (2004) *Diagnostic ultrasound imaging*. Elsevier Academic Press, Burlington.
202. Fenster A and Downey DB (1996) 3-D ultrasound imaging: a review. *IEEE Engineering in Medicine and Biology Magazine* 15:41-51.
203. Hoskins PR (1999) A review of the measurement of blood velocity and related quantities using Doppler ultrasound. *Proc Inst Mech Eng [H], J Eng Med* 213:391-400.
204. Newhouse VL, Bendick PJ and Varner LW (1976) Analysis of transit time effects on Doppler flow measurement. *IEEE Trans Biomed Eng* 23:381-386.
205. Newhouse VL, Varner LW and Bendick PJ (1977) Geometrical spectrum broadening in ultrasonic Doppler systems. *IEEE Trans Biomed Eng* 24:478-480.
206. Guidi G, Licciardello C and Falteri S (2000) Intrinsic spectral broadening (ISB) in ultrasound Doppler as a combination of transit time and local geometrical broadening. *Ultrasound Med Biol* 26:853-862.
207. Fish PJ (1991) Nonstationarity broadening in pulsed Doppler spectrum measurements. *Ultrasound Med Biol* 17:147-155.

208. Cardoso JC, Ruano MG and Fish PJ (1996) Nonstationarity broadening reduction in pulsed Doppler spectrum measurements using time-frequency estimators. *IEEE Trans Biomed Eng* 43:1176-1186.
209. Bastos CC, Fish PJ and Vaz F (1999) Spectrum of Doppler ultrasound signals from nonstationary blood flow. *IEEE Trans Ultrason Ferroelectr Freq Control* 46:1201-1217.
210. Evans DH and McDicken WN (2000) *Doppler Ultrasound: Physics, Instrumentation and Signal Processing*. Wiley, Chichester.
211. Jensen JA (1996) *Estimation of Blood Velocities Using Ultrasound: A Signal Processing Approach*. Cambridge University Press, Cambridge.
212. Walburn FJ, Sabbah HN and Stein PD (1983) An experimental evaluation of the use of an ensemble average for the calculation of turbulence in pulsatile flow. *Ann Biomed Eng* 11:385-399.
213. Garbini JL, Forster FK and Jorgensen JE (1982) Measurement of fluid turbulence based on pulsed ultrasound techniques - 2. Experimental investigation. *J Fluid Mech* 118:471-505.
214. Forster FK, Garbini JL and Jorgensen JE (1976) Hemodynamics turbulence measurements using ultrasonic techniques. In: Proc 4th Ann New England Bioeng Conf, New Haven, pp 1223-1226.
215. Sigel B, Gibson RJ, Amatneek KV, Felix WR, Jr., Edelstein AL, *et al.* (1970) A doppler ultrasound method for distinguishing laminar from turbulent flow. A preliminary report. *J Surg Res* 10:221-224.
216. Barnes RW, Bone GE, Reinertson J, Slaymaker EE, Hokanson DE, *et al.* (1976) Noninvasive ultrasonic carotid angiography: prospective validation by contrast arteriography. *Surgery* 80:328-335.

217. Blackshear WM, Jr., Phillips DJ, Thiele BL, Hirsch JH, Chikos PM, *et al.* (1979) Detection of carotid occlusive disease by ultrasonic imaging and pulsed Doppler spectrum analysis. *Surgery* 86:698-706.
218. Reneman RS and Spencer MP (1979) Local Doppler audio spectra in normal and stenosed carotid arteries in man. *Ultrasound Med Biol* 5:1-11.
219. Campbell JD, Hutchison KJ and Karpinski E (1989) Variation of Doppler ultrasound spectral width in the post-stenotic velocity field. *Ultrasound Med Biol* 15:611-619.
220. Morin JF, Johnston KW and Law YF (1987) In vitro study of continuous wave Doppler spectral changes resulting from stenoses and bulbs. *Ultrasound Med Biol* 13:5-13.
221. Hutchison KJ (1993) Doppler ultrasound spectral shape in the poststenotic velocity field. *Ultrasound Med Biol* 19:649-659.
222. Shung KK, Yuan YW, Fei DY and Tarbell JM (1984) Effect of flow disturbance on ultrasonic backscatter from blood. *J Acoust Soc Am* 75:1265-1272.
223. Shung KK, Cloutier G and Lim CC (1992) The effects of hematocrit, shear rate, and turbulence on ultrasonic Doppler spectrum from blood. *IEEE Trans Biomed Eng* 39:462-469.
224. Cloutier G, Allard L and Durand LG (1996) Characterization of blood flow turbulence with pulsed-wave and power Doppler ultrasound imaging. *J Biomech Eng* 118:318-325.
225. Cloutier G and Shung KK (1993) Cyclic variation of the power of ultrasonic Doppler signals backscattered by polystyrene microspheres and porcine erythrocyte suspensions. *IEEE Trans Biomed Eng* 40:953-962.

226. Wu SJ, Shung KK and Brasseur JG (1998) In situ measurements of Doppler power vs. flow turbulence intensity in red cell suspensions. *Ultrasound Med Biol* 24:1009-1021.
227. Tamura T and Fronek A (1990) Detection of moving flow separation in pulsatile flow and the degree of stenosis by power of Doppler shift signals. *Circ Res* 67:166-174.
228. Tamura T and Fronek A (1990) Determination of volume of vortices in poststenotic pulsatile flow by ultrasonic Doppler power ratio and spectrum analysis. *J Biomech* 23:195-200.
229. Cloutier G and Qin Z (2000) Shear rate dependence of ultrasound backscattering from blood samples characterized by different levels of erythrocyte aggregation. *Ann Biomed Eng* 28:399-407.
230. Bascom PA, Johnston KW, Cobbold RS and Ojha M (1997) Relation of the flow field distal to a moderate stenosis to the Doppler power. *Ultrasound Med Biol* 23:25-39.
231. Garbini JL, Forster FK and Jorgensen JE (1982) Measurement of fluid turbulence based on pulsed ultrasound techniques - 1. Analysis. *J Fluid Mech* 118:445-470.
232. Hanai S, Yamaguchi T and Kikkawa S (1991) Turbulence in the canine ascending aorta and the blood pressure. *Biorheology* 28:107-116.
233. Woodcock JP, Shedden J, Skidmore R, Machleder H, Evans J, *et al.* (1982) Doppler spectral broadening and anomalous vessel wall movement in the study of atherosclerosis of the carotid arteries. *Ultrasound Med Biol* 8:211.

234. Woodcock JP, Shedden J, Aldoori M, Skidmore R, Burns P, *et al.* (1983) Doppler spectral broadening and anomalous vessel wall movement in the study of atherosclerosis of the carotid arteries. *Ultrasound Med Biol Suppl* 2:235-237.
235. Brown PM, Johnston KW, Kassam M and Cobbold RS (1982) A critical study of ultrasound Doppler spectral analysis for detecting carotid disease. *Ultrasound Med Biol* 8:515-523.
236. Kalman PG, Johnston KW, Zuech P, Kassam M and Poots K (1985) In vitro comparison of alternative methods for quantifying the severity of Doppler spectral broadening for the diagnosis of carotid arterial occlusive disease. *Ultrasound Med Biol* 11:435-440.
237. Zienkiewicz OC, Taylor RL and Nithiarasu P (2005) *The Finite Element Method for Fluid Dynamics*. Butterworth-Heinemann, Oxford.
238. Bressloff NW (2006) Parametric geometry exploration of the human carotid artery bifurcation. *J Biomech* 40:2483-2491.
239. Maurits NM, Loots GE and Veldman AE (2007) The influence of vessel wall elasticity and peripheral resistance on the carotid artery flow wave form: a CFD model compared to in vivo ultrasound measurements. *J Biomech* 40:427-436.
240. Ford MD, Nikolov HN, Milner JS, Lownie SP, Demont EM, *et al.* (2008) PIV-measured versus CFD-predicted flow dynamics in anatomically realistic cerebral aneurysm models. *J Biomech Eng* 130:021015.
241. Dempere-Marco L, Oubel E, Castro M, Putman C, Frangi A, *et al.* (2006) CFD analysis incorporating the influence of wall motion: application to intracranial aneurysms. *Med Image Comput Comput Assist Interv Int Conf Med Image Comput Comput Assist Interv* 9:438-445.

242. Stuhne GR and Steinman DA (2004) Finite-element modeling of the hemodynamics of stented aneurysms. *J Biomech Eng* 126:382-387.
243. Khoshniat M, Thorne ML, Poepping TL, Hirji S, Holdsworth DW, *et al.* (2005) Real-time numerical simulation of Doppler ultrasound in the presence of nonaxial flow. *Ultrasound Med Biol* 31:519-528.
244. Swillens A, Segers P, Torp H and Lovstakken L (2010) Two-dimensional blood velocity estimation with ultrasound: speckle tracking versus crossed-beam vector Doppler based on flow simulations in a carotid bifurcation model. *IEEE Trans Ultrason Ferroelectr Freq Control* 57:327-339.

Chapter 2

Doppler Ultrasound Compatible Plastic Material for Use in Rigid Flow Models[†]

2.1 Introduction

The risk of ischemic stroke is known to vary with the extent of atherosclerotic plaque in the carotid artery bifurcation. Methods based on peak-systolic velocity measurements from Doppler ultrasound (DUS) have supplanted conventional angiography as the technique most widely used to quantify stenosis grade in the internal carotid artery (ICA) and select for subsequent diagnostic tests, or surgical or medical therapy [1, 2]. However, current DUS techniques do not provide optimal sensitivity and specificity when used as the only diagnostic test prior to carotid endarterectomy [3-5], and can lead to misclassification rates as high as 28% [6]. These limitations necessitate the development of new techniques for the optimization of ultrasonographic criteria for treatment stratification. Clinical validation of new ultrasound diagnostic techniques can be difficult (due to lack of a standard of reference), costly, lengthy, and subject to clinical error; for these reasons, the development of clinical techniques often includes an *in vitro* component, particularly in the preliminary stages. Investigations using *in vitro* models can provide the control and reproducibility of parameters necessary for the objective evaluation of new methodology. Accordingly, Doppler ultrasound flow phantoms are an important component of basic research related to carotid artery disease [2].

[†] A version of this chapter has been published in *Ultrasound in Medicine and Biology* (2008) 34:1846-1856 in an original article entitled “Doppler ultrasound compatible plastic material for use in rigid flow models” by E. Y. Wong, M. L. Thorne, H. N. Nikolov, T. L. Poepping and D. W. Holdsworth.

Vascular flow phantoms have been previously developed that incorporate varying degrees of complexity, ranging from simple straight tubes [7-10] to straight tubes involving stenoses [11-13] and sophisticated anthropomorphic phantoms [14]. In some phantom studies, it may be desirable to mimic the mechanical distensibility of human vessels [10, 15, 16] or even to include human or animal vessel segments [17-19]. Complex carotid bifurcation phantoms can be fabricated from a single component, such as wall-less agar phantoms [20-22], or from multiple components, such as the thin-walled silicone vessel-mimicking phantom developed by Poepping *et al.* [23]. Although they provide many advantages, the common drawback of these complex models is that they require a multi-step casting process, which is time consuming, costly, and labour intensive. For these reasons, while cast or moulded flow phantoms are ideally suited to many DUS flow studies, they may be precluded from use in investigations involving large numbers of models.

Recent studies have highlighted numerous applications that would benefit from accessibility to large numbers of models, in particular if the models could easily and accurately incorporate variations in vascular geometries. Literature has identified many geometric parameters of interest in relation to the progression of carotid atherosclerosis, including outflow-to-inflow area ratios [24], bifurcation angle [25], and carotid plaque ulceration [26-28]. In addition, patient-specific modelling of vessel geometry has become more feasible, due to the development of systematic procedures for the reconstruction of patient vascular replicas from diagnostic images [29]. A robust and cost-effective phantom is needed to facilitate rigorous investigations of blood flow and clinically relevant spectral parameters, such as mean velocity, peak velocity and derived parameters (e.g. spectral broadening, turbulence intensity). Such a phantom would be particularly

useful in investigations where many variations in vascular geometry will be studied.

Rapid fabrication of multiple flow phantoms would be greatly simplified if the desired anthropomorphic vessel geometries could be machined directly into a suitable material. Direct machining using numerically controlled (NC) milling is feasible, and may provide a cost-effective, accurate and reproducible technique to produce models of patient vessel geometries (obtained from diagnostic images) or custom-designed geometries (via computer-aided design (CAD) and modelling). To demonstrate the utility of this approach, we have investigated a number of candidate plastics to determine a suitable material for the direct NC machining of rigid planar flow phantoms for use with DUS. Our results indicate that Teflon® provides the best combination of rigidity, machinability and DUS compatibility, making it a suitable choice for the fabrication of rigid flow phantoms using a direct-machining method.

2.2 Materials and Methods

2.2.1 Candidate materials

The properties considered in the selection of a suitable material for direct machining included: machinability, ease of construction, cost and availability, and matching of the acoustic properties (i.e., speed of sound and acoustic attenuation) to that of soft tissue. A highly machinable material with appropriate rigidity is required to reproduce high-fidelity vessel geometries under NC milling techniques. Furthermore, the selected material must have a speed of sound (SoS) suitably matched to that of soft tissue (1540 m s^{-1}) in order to minimize errors introduced by refraction [30-32]. The secondary acoustic criterion is an attenuation coefficient sufficiently close to that of human soft tissue ($0.5 \text{ to } 0.7 \text{ dB cm}^{-1} \text{ MHz}^{-1}$) such that adequate return power

is achieved, ensuring that errors arising from the preferential attenuation of high frequency components are secondary to those from refraction [33].

Previous materials employed for ultrasound phantoms, such as agar [20, 34], silicone rubber [35-37] and urethane rubber [38, 39], are well-suited for casting, but do not have the appropriate machinability to be used for a direct fabrication approach. Plastics used for transducer caps, acoustic lenses, mammographic compression plates [40] and other ultrasound applications – such as polymethylpentene (TPX®) and polycarbonate (Lexan®) – have appropriate rigidity but conversely have prohibitively high speeds of sound with respect to tissue (2220 m s^{-1} and 2300 m s^{-1} , respectively), making them unsuitable for use as a flow phantom material. To narrow our search for a more appropriate plastic, we selected a group of readily available and machinable plastics with reported speeds of sound similar to soft tissue [41-46]. These candidate materials included: polytetrafluoroethylene (Teflon®), urethane with Shore hardness of 90 on the A scale (Urethane-90A), urethane with Shore hardness of 75 on the D scale (Urethane-75D), high-density polyethylene (HDPE), and ultra-high molecular weight polyethylene (UHMW).

2.2.2 Characterization of acoustic properties

A pulse-transmission technique, similar to that described by Poepping *et al.* [23], was used to determine the longitudinal sound velocity and acoustic attenuation for each of the candidate materials at a clinically relevant frequency of 5 MHz. This was done by recording the signal amplitudes and time delays between the transmission and reception of a sound pulse traveling a fixed distance in a distilled water bath of known temperature for material samples of various known thicknesses. A single-element unfocused transmit transducer was driven by a function generator (FG504, Tektronix, Beaverton, OR) gated with a pulse generator (PG501, Tektronix, Beaverton,

OR) to produce 5-MHz pulses of 10- μ s duration, while a second identical transducer mounted at a fixed distance in the Fraunhofer zone of the ultrasound field received the ultrasound pulses. Measurements of the received signal were performed using a 100 MHz digital oscilloscope (PM3365A, Philips, Eindhoven, The Netherlands). A minimum of five samples of varying thickness, from 1 mm to 13 mm (± 0.02 mm), was used for each candidate material. Maximal thicknesses for each material were chosen such that adequate return signal was maintained.

Comparison of transit times and amplitudes for different sample thicknesses yielded sound speed and attenuation for the materials of interest, as calculated by Poepping *et al.* [23]. Characteristic sound velocities were determined from the slope of the linear fit of transit time versus sample thickness, taking into account the speed of sound in distilled water at the experimental temperature [47]. Attenuation coefficients and their associated errors were determined from the slope of the regression line of the logarithm of the peak-to-peak amplitudes versus sample thickness. The material with the most appropriate SoS characteristics was then evaluated to determine the frequency dependence of attenuation over a range of clinically relevant frequencies (3, 4, 5, 6, 7 MHz). For this measurement, the attenuation coefficients were fitted to the following power function of frequency:

$$\alpha(f)=a \times f^b \quad (2.1)$$

where α (dB cm⁻¹) is the attenuation coefficient, a (dB cm⁻¹ MHz^{-b}) and b are the fitting parameters and f (MHz) is frequency [23].

2.2.3 Phantom fabrication

To validate the performance of the most appropriate plastic material, direct machining was used to fabricate a flow phantom for comparison with a previously described tissue-mimicking flow phantom of identical geometry

[23]. The vessel geometry chosen was that of a previously characterized carotid bifurcation, with 50% eccentric stenosis under the North American Symptomatic Carotid Endarterectomy (NASCET) criteria [48] and a common carotid artery (CCA) diameter of 8 mm [49, 50]. To accomplish this, the NC milling instructions were first generated from three-dimensional (3-D) parametric surfaces in a CAD software package (MasterCam, CNC Software Inc., Tolland, CT), as shown in Fig. 2.1a. To ensure consistency, the phantom was constructed from the same sample of material as was used in the evaluation of acoustic properties. A sheet of stock material $152 \text{ mm} \times 305 \text{ mm} \times 6.4 \text{ mm}$ was machined to a uniform thickness of 5 mm using a numerically controlled fly cutter mounted on a numerically controlled router (Millenium Series, AXYZ Automation Inc., Burlington, ON). The final thickness of the plastic sheet was chosen based on the largest vessel diameter, such that only 0.5 mm of excess material would remain between the outer surface and the uppermost lumen boundary after fabrication, thereby minimizing the ultrasound path length and resultant attenuation through the plastic. The phantom was constructed in two parts from blocks of material each 70 mm wide \times 215 mm long \times 5 mm thick, where one-half of the vessel was machined into each of the two material blocks. Both halves of the carotid vessel geometry were machined into the 5-mm plastic sheet, appropriately spaced to allow for both vessel blocks to be machined and subsequently removed from the surrounding material. Machining of the vessel geometry was performed using a ball-nosed endmill with a diameter of 2.38 mm mounted on the NC router. Surface roughness was minimized by specifying a maximum height of 0.025 mm for the residual ridges produced by successive cuts (scallop height). In addition, four centering pinholes and 32 through holes for the insertion of fastening screws were drilled in both of the vessel blocks at mirrored locations. Once machined, the two halves of the phantom were cleaned, sealed with silicone rubber and fastened together using Nylon® screws. Exact alignment of the two halves was facilitated by

four 6.4-mm diameter dowels placed in the centering pinholes. To enable coupling with other components of the flow system, complimentary threads were made at the inlet and outlets of the vessel using an appropriate 9-mm tap. Threaded adaptors housing plastic flow connectors (APC series, Colder Products Co., St. Paul, MN) were inserted into the resultant threads and sealed with silicone rubber. The final phantom is illustrated in Fig. 2.1b and 2.1c. To compare phantom performance with a previously validated tissue-mimicking flow phantom, a distensible silicone-walled carotid phantom with the same geometry was also fabricated using the technique described by Poepping *et al.* [23].

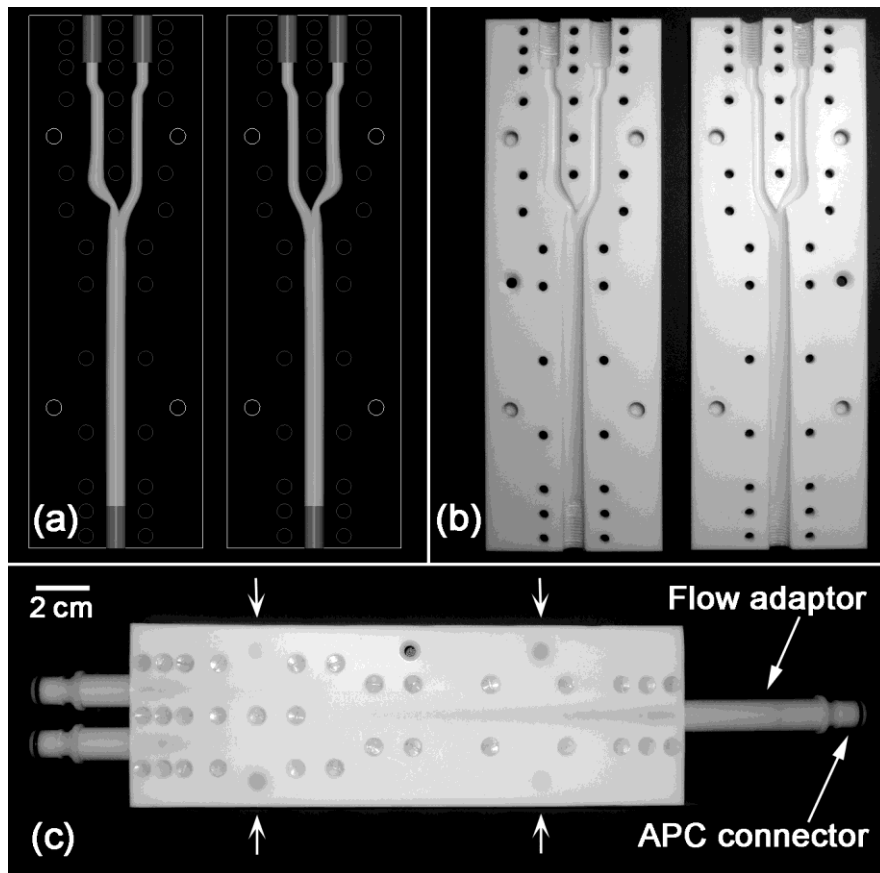


Figure 2.1: Carotid bifurcation flow phantom showing (a) 3-D CAD design of the two-part phantom, (b) photograph of the machined halves, and (c) fully assembled phantom. The *concave arrows* indicate the locations of the centering pins.

2.2.4 Non-destructive evaluation

To verify the dimensional accuracy and geometric fidelity of the directly machined flow phantom, the fully assembled model was evaluated non-destructively using high-resolution micro-computed tomography (micro-CT). A flat-panel equipped conebeam laboratory CT scanner (Locus Ultra, General Electric Healthcare Biosciences, London, ON) was used to scan the phantom, using acquisition parameters of 120 kVp and 20 mA for a 16 s total scan. The phantom was reconstructed using filtered backprojection in a conebeam geometry to provide a 3-D image with isotropic voxel spacing of 0.15 mm. To visualize the lumen surface geometry, the air-filled lumen was segmented from the surrounding plastic, based on a grey-scale threshold followed by region growing and mesh generation using the marching-cubes algorithm. The resulting triangulated surface provided information about the model shape and surface smoothness. Repeat measurements of lumen dimensions and percent stenosis from micro-CT geometries were compared to the original CAD instructions as a quantitative assessment of geometric accuracy.

2.2.5 Phantom measurements

2.2.5.1 Comparison of velocity profiles

To test for Doppler signal fidelity in the plastic phantom, flow experiments were conducted on both the plastic phantom and the tissue-mimicking phantom under identical Doppler settings and flow conditions, as described below. Experiments employed the flow simulator and semi-automated DUS acquisition systems described by Poepping *et al.* [14]. A well-characterized blood-mimicking fluid (BMF) suited to DUS was used to perfuse the vessel [51]. To ensure fully established laminar flow profiles, the Reynolds number $Re = Du/\nu$ is required to be less than 200 and an adequate entrance length, L , given empirically by $L = 0.03 \times D \times Re$ [52]

must be achieved, where D is the diameter of the tube, u is the mean fluid velocity, and ν is the kinematic viscosity. The kinematic viscosity of the BMF was verified prior to each data collection (4.02 ± 0.1 cS). A computer-controlled flow pump was used to provide a constant flow rate of 5 mL s^{-1} [53, 54], corresponding to a Re of 198 and a minimum entrance length of 5 cm for the CCA ($D=0.8$ cm). The experimental setup used provided an entrance length of greater than 50 cm at the interrogated region of both phantoms. The plastic flow phantom was mounted in a water bath during ultrasound acquisition to ensure adequate acoustic coupling. Measurements were performed at a temperature of 23 ± 1 °C.

Doppler spectra were acquired with a conventional clinical duplex DUS system (Ultramark 9, Philips-ATL, Bothell, WA) using a 4-MHz linear array transducer (L7-4 Philips-ATL, Bothell, WA) producing a focused beam with a 2.0-cm focal depth and a 1.0-mm sample volume length. To achieve a clinical Doppler angle of 60° , the ultrasound probe was tilted at a 10° angle from the vessel axis in combination with a beam steering angle of 20° (Fig. 2.2). A Doppler pulse-repetition frequency of 2,500 Hz with a 25-Hz applied wall filter was used. A semi-automated acquisition system equipped with a translating stage was used to interrogate 2,025 (45×45) data acquisition points with 0.2-mm isotropic spatial increments in an $(8.8\text{-mm})^2$ square data grid spanning a transaxial plane of the CCA. One second of audio data was acquired at each collection point and sampled at 44.1 kHz for post-processing.

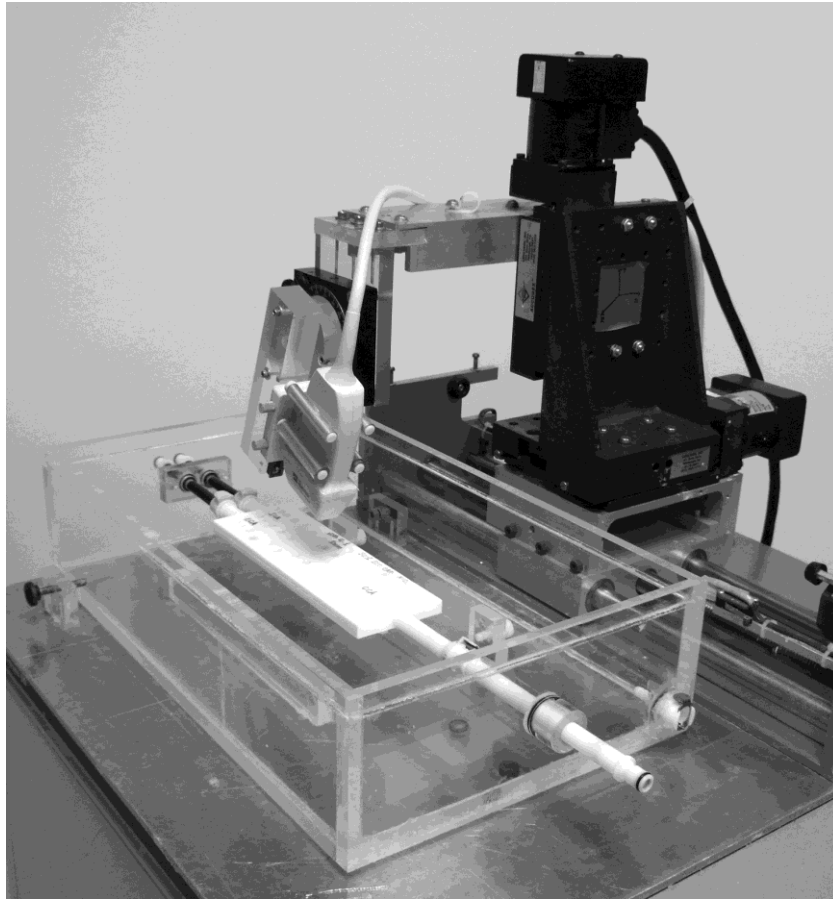


Figure 2.2: Carotid bifurcation phantom mounted in a water bath with the ultrasound probe attached to the translational stage and mechanically tilted at a 10° angle from the vessel axis.

Data analysis of each spectrum consisted of a 1,024-point fast Fourier transform (FFT) with a 1,024-point Hanning window and 50% overlap between consecutive windows, providing a velocity resolution of 1.66 cm s^{-1} . The resulting 85 power spectra calculated from each second of data were used to determine several parameters, including: mean velocity (v_{mean}), standard deviation of mean velocity, peak velocity, and total integrated power [14]. Results along the vertical and horizontal centerlines, as well as over the entire transverse plane, were compared between the phantoms. Observed

profiles were also compared to the calculated parabolic velocity profile expected for fully established steady laminar flow.

2.2.5.2 Mean velocity mapping under pulsatile flow conditions

In addition to evaluating the velocities under the well-characterized flow conditions of fully developed steady laminar flow in the CCA, flow velocity data were also collected across the central plane defined by the longitudinal axes of the bifurcation flow phantom in order to demonstrate that quantitative cardiac-gated data could be collected in the plastic phantom under pulsatile flow conditions. An average carotid flow-rate waveform [14, 55], with a mean flow rate of 6.00 mL s^{-1} , a peak flow rate of 23.46 mL s^{-1} , and a cycle length of 0.92 s , was provided to the flow phantom. The pump output waveform was that described by Poepping *et al.* [14], which compensates for damping effects and achieves the desired waveform at the inlet of the CCA. Distal flow resistors, comprised of 2-mm diameter tubing, were attached to the vessel outlets to ensure appropriate flow division of 65:35 between the ICA and the external carotid artery (ECA) [14]. In this study, resistor tubing lengths of 1 m and 2 m were required for the ICA and ECA, respectively. The same 4-MHz Doppler probe and 60° Doppler angle as described above were used with Doppler acquisition parameters of a pulse-repetition frequency of 18,519 Hz, a 50-Hz wall filter, and a 1.0-mm sample volume with a 2.0-cm focal depth. Data were collected across a longitudinal central plane of the phantom with 1-mm isotropic spacing over a defined acquisition grid consisting of 1,025 sample locations within a $78\text{-mm} \times 24\text{-mm}$ region; 10 s of cardiac-gated data was collected at each acquisition site. The FFT post-processing analysis technique described above was performed on the recorded data. In addition, mean velocities were calculated from the ensemble average of ten complete cardiac cycles (\bar{v}_{mean}), providing two-dimensional (2-D) mean velocity maps for each of 79 time points in the cardiac cycle.

2.3 Results

2.3.1 Speed of sound and attenuation characterization

The results of the speed of sound and acoustic attenuation measurements at 5 MHz are summarized in Table 2.1. Of the candidate materials, Teflon® displayed the smallest SoS mismatch with respect to tissue (10.6%), representing the only material found to have a SoS mismatch not exceeding 15%. Our measured value for the SoS in Teflon® is in agreement with the value of $1376 \pm 16 \text{ m s}^{-1}$ previously reported by Raum and Brandt [56]. HDPE provided the lowest attenuation coefficient of the materials tested and a value closest to that of soft tissue (0.5 to 0.7 dB cm^{-1}), but had the highest SoS mismatch with respect to soft tissue.

Table 2.1: Speed of sound and acoustic attenuation values measured for the five candidate materials. The percent difference in SoS is calculated with respect to the SoS value of 1540 m s^{-1} for the soft tissue average.

Material	Speed of sound (m s^{-1})	Difference from tissue (percent)	Acoustic attenuation ($\text{dB cm}^{-1} \text{ MHz}^{-1}$ at 5 MHz)
HDPE	2461 ± 18	59.8	2.7 ± 0.2
PTFE (Teflon®)	1376 ± 40	-10.6	13.0 ± 0.3
UHMW	2136 ± 33	38.7	3.4 ± 0.1
Urethane-75D	2010 ± 9	30.5	8.3 ± 0.2
Urethane-90A	2065 ± 29	34.1	8.5 ± 0.4

Teflon®, which had the most suitable SoS values, was tested for its frequency dependence of attenuation. The attenuation coefficient for Teflon® is plotted as a function of frequency from 3 – 7 MHz in Fig. 2.3. Teflon® demonstrates a nearly linear frequency dependence in attenuation rate over the diagnostic frequency range, with fitted parameter values to the power law expression in Eqn. (2.1) of $9.7 \pm 0.5 \text{ dB cm}^{-1} \text{ MHz}^{-b}$, for a (attenuation coefficient at 1 MHz), and frequency dependence of $b = 1.20 \pm 0.02$. This value falls within the range for soft tissue, which typically has a value of b between 1 and 2 [57]. Although the attenuation coefficient at 5 MHz was the highest of the materials tested, the linearity of the frequency dependence combined with the SoS characteristics led to the selection of Teflon® for the construction of the carotid bifurcation flow phantom. Figures 2.1b and 2.1c show the bifurcation geometry machined into Teflon®.

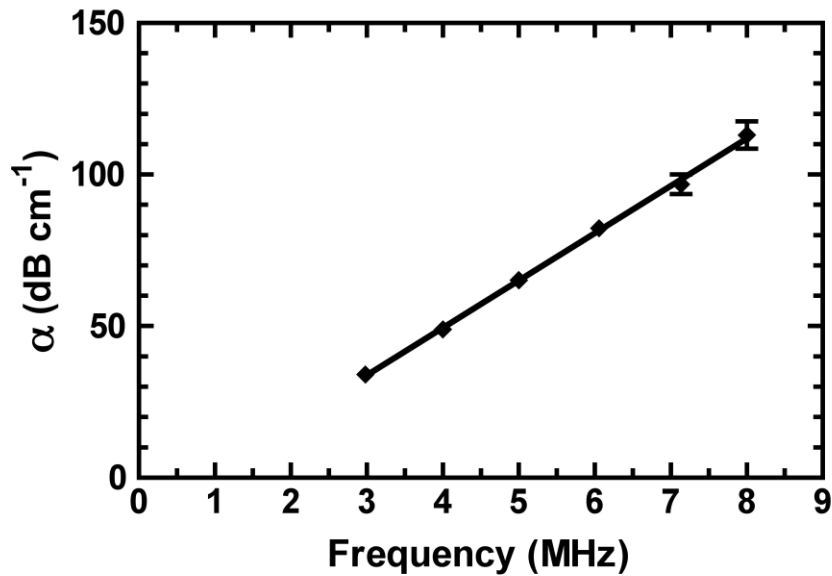


Figure 2.3: Attenuation coefficient as a function of frequency for Teflon®. Each error bar is determined from the linear regression for the corresponding attenuation coefficient. The R-squared value of the regression is 0.999.

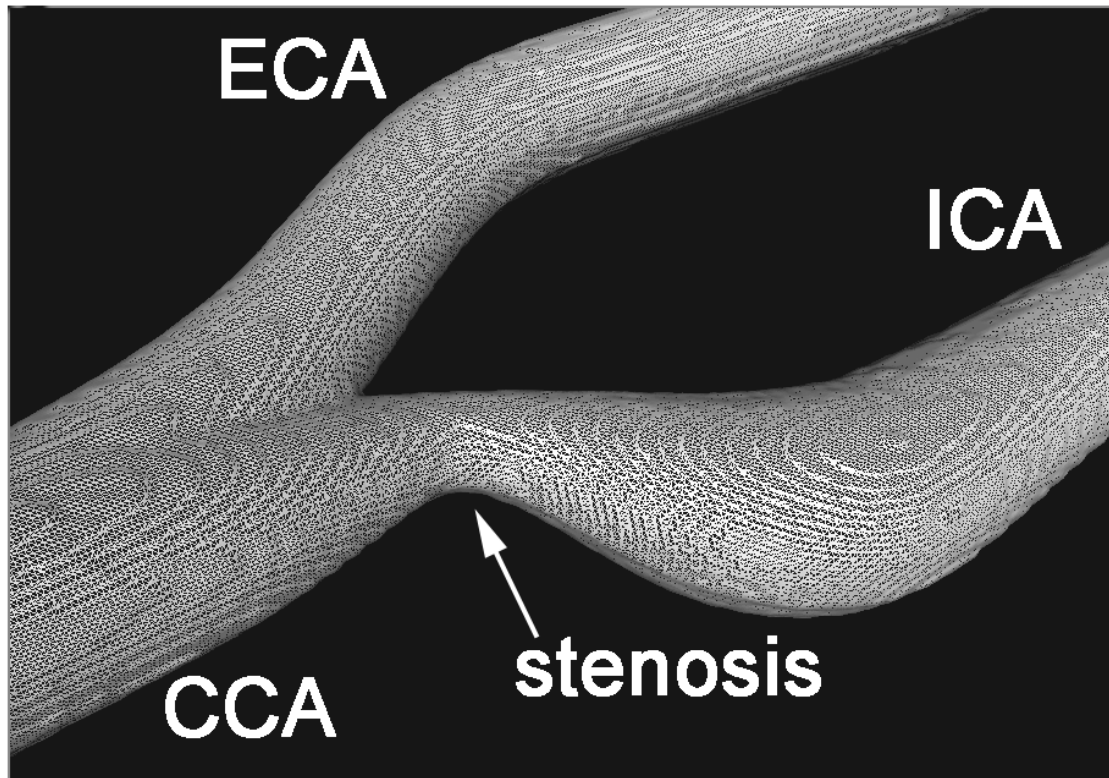


Figure 2.4: Micro-computed tomography surface mesh of the lumen geometry in the Teflon® carotid bifurcation phantom.

2.3.2 Fidelity of fabrication technique

Figure 2.4 shows the lumen boundary surface mesh of the Teflon® bifurcation phantom generated from micro-CT data reconstructions. These mesh renderings of the phantom surface geometry demonstrate that a smoothly machined surface was achieved throughout the lumen. The use of a grey-scale thresholding technique to segment the phantom lumen was possible due to the difference in CT number for air (defined to be -1000 Hounsfield units (HU)) and for Teflon® (918 HU [58]). A semi-automated threshold-based boundary determination technique was used to measure lumen dimensions at several locations in the fully constructed Teflon® phantom. Measurements of the vertical and horizontal diameters of the CCA

averaged from five repeat trials gave 7.99 ± 0.07 mm and 7.92 ± 0.10 mm, respectively, demonstrating that a closely circular cross-section for the CCA lumen was achieved. Using the NASCET definition, the measured percent stenosis averaged from five measurements was $52.5 \pm 1.4\%$, compared to 50.4% in the original CAD instructions. The results of these quantitative measurements indicate that the described NC direct-fabrication technique was able to accurately reproduce our desired vessel geometry.

2.3.3 Comparison of velocity profiles

The plots in Fig. 2.5a and 2.5b show the relative mean velocity profiles along the horizontal and vertical centerlines of the 8-mm diameter CCA for both the Teflon® phantom and the thin-walled phantom. Due to the difference in CCA diameter that results from the comparison of a rigid plastic phantom with a distensible tissue-mimicking phantom, the relative velocity profile shapes observed in the two phantoms were compared by normalizing the mean velocities (v_{mean}) to the maximum value of mean velocity for the corresponding profile. For additional comparison, the expected parabolic profile associated with fully developed laminar flow in an 8-mm cylindrical vessel is overlaid on the experimental values. The plots show that the mean velocity profiles across both the horizontal and vertical centerlines of the two phantoms are in good agreement, particularly near the centre of the lumen. These results also align well with that of the calculated parabolic profile for fully developed laminar flow in a cylindrical vessel. The corresponding plots of the standard deviations in mean velocity for the two phantoms shown in Fig. 2.5c and 2.5d also indicate that precise velocity measurements are obtained near the vessel center. However, overestimations of velocities and higher standard deviations in velocity measurements are observed near the lumen-wall boundary in both phantoms, as shown by the absolute point-by-point mean velocity differences relative to the parabolic profile in Fig. 2.6. This leads to overestimations of the parabolic profile by up to

8.35 cm s⁻¹ and 8.76 cm s⁻¹ along the vertical centerline and by up to 4.48 cm s⁻¹ and 5.49 cm s⁻¹ along the horizontal centerline in the Teflon® phantom and the thin-walled phantom, respectively. Departures of velocity values from parabolic profiles and increases in standard deviations begin at similar distances from the wall boundary in the two phantoms, providing similar bounds within which reliable measurements can be taken.

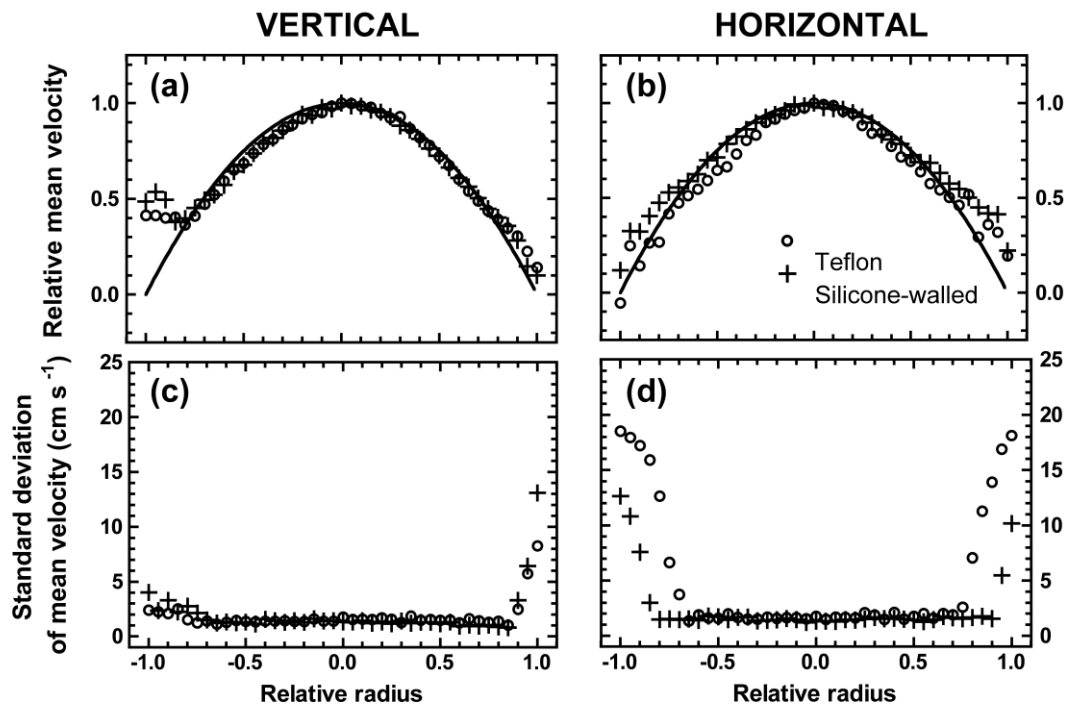


Figure 2.5: Relative (a) vertical and (b) horizontal v_{mean} profiles and relative (c) vertical and (d) horizontal standard deviations of v_{mean} profiles from the Teflon® phantom and the silicone-walled phantom. The expected parabolic velocity profile for mean velocity is shown for comparison (*solid line*).

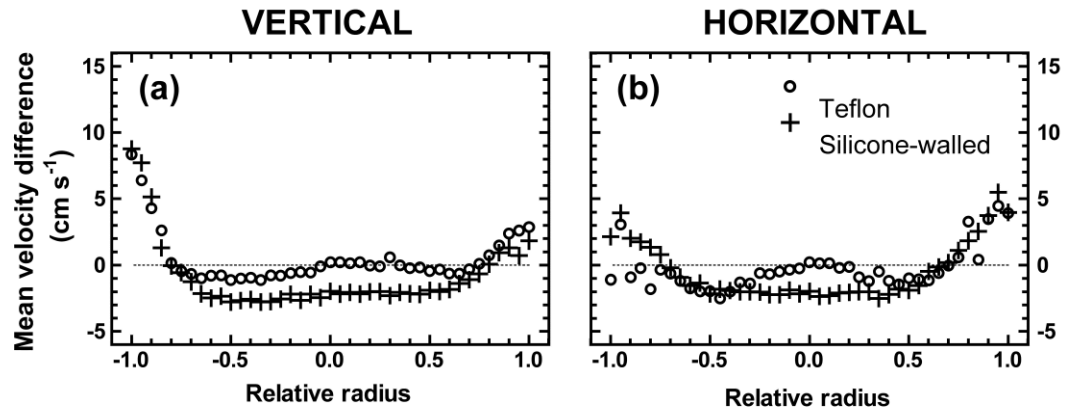


Figure 2.6: Point-by-point differences in mean velocity between the measured v_{mean} profiles and the expected parabolic profile through the centerline of the Teflon® phantom and the silicone-walled phantom. The vertical profile is shown in (a) and the horizontal profile is shown in (b).

The interrogation of a transverse cross-section of the CCA of the Teflon® phantom produced mean velocity distributions consistent with those in the CCA of the thin-walled phantom. Figures 2.7a and 2.7b show side-by-side colour-flow plots for the two phantoms. The velocity contours are reasonably circular, as is expected in a flow cylinder with fully developed laminar flow. Distributions of standard deviation of mean velocity (Fig. 2.7c and 2.7d), peak velocity (Fig. 2.7e and 2.7f) and integrated power (Fig. 2.7g and 2.7h) are also comparable between the Teflon® and thin-walled phantoms. A 2-D map of standard deviation in mean velocity also shows low and uniform deviations near the centre of the vessel; significant departures do not occur beyond approximately 0.8 mm from the vessel wall boundary, as plotted for centerlines in Fig. 2.5c and 2.5d. Greater attenuation at the edge of the vessel, due to increased path length of the beam through overlying

material, leads to a reduction in received signal near the lumen boundary and a subsequent reduction in velocity precision near the wall, as shown in Fig. 2.5d. Although the higher attenuation coefficient in Teflon® exacerbates this effect, this additional reduction in signal power does not significantly decrease the accuracy of the velocity measurements, as shown in Fig. 2.6b.

2.3.4 Mean velocity mapping under pulsatile flow conditions

We successfully collected quantitative cardiac-gated DUS data under pulsatile flow conditions in our Teflon® 50% eccentrically stenosed carotid bifurcation phantom. The 2-D colour-encoded flow map of calculated mean velocities over the longitudinal central plane of the model at peak systole is shown in Fig. 2.8. This technique was able to capture the key velocity patterns that characterize an idealized carotid geometry of moderate eccentric stenosis [59], such as the high-velocity jet in the stenosis and the recirculation zone along the outer wall of the ICA bulb, distal to the stenosis. The expected parabolic flow patterns are also observed in the CCA proximal to the stenosis and in the distal ECA and ICA. Since spectral analysis of the Doppler data is performed offline, mean velocity is one of any number of spectral parameters which can be computed.

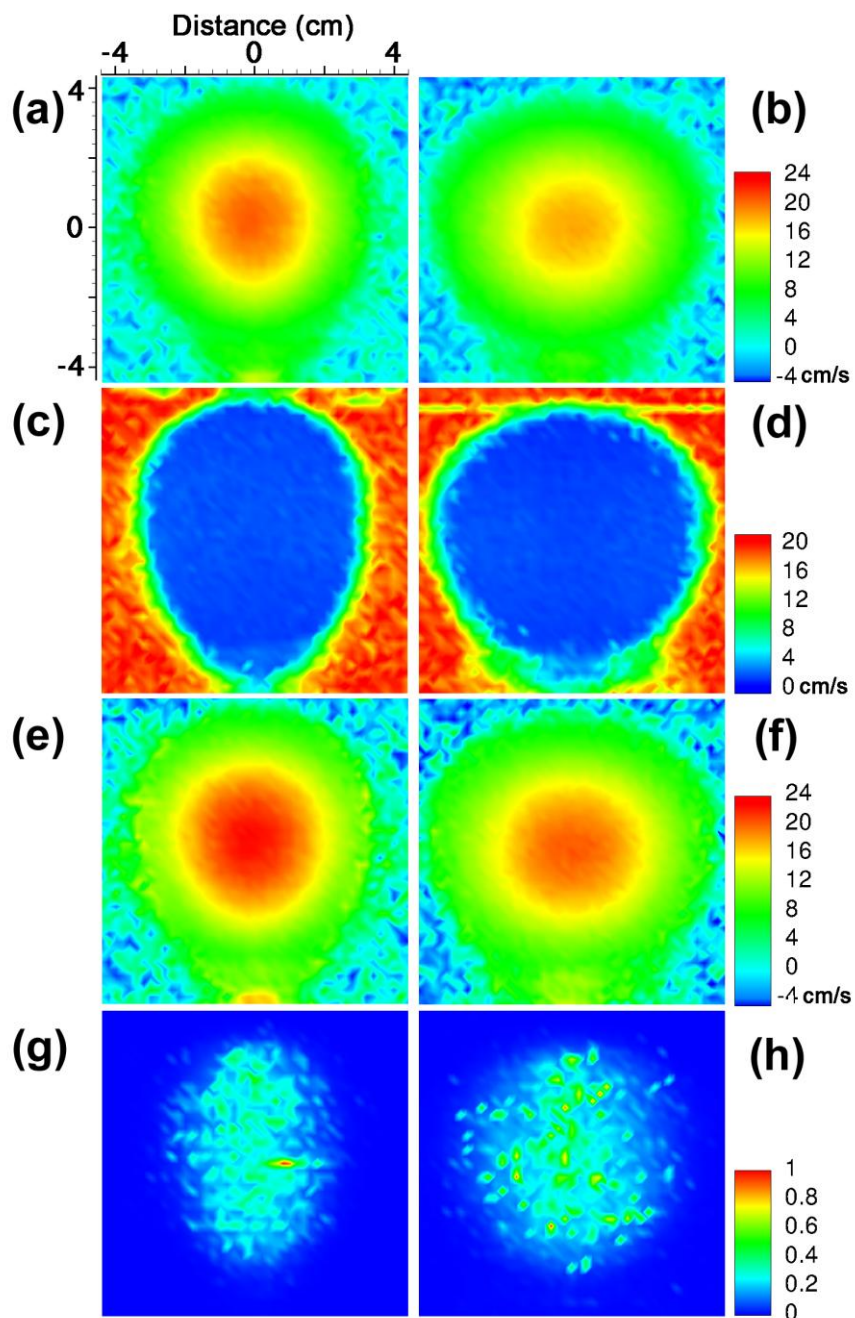


Figure 2.7: Colour-encoded maps for a transverse slice of the 8-mm CCA for the Teflon® phantom (*left panels*) and the silicone-walled phantom (*right panels*) representing (a, b) mean velocity, (c, d) standard deviation in mean velocity, (e, f) peak velocity and (g, h) integrated power.

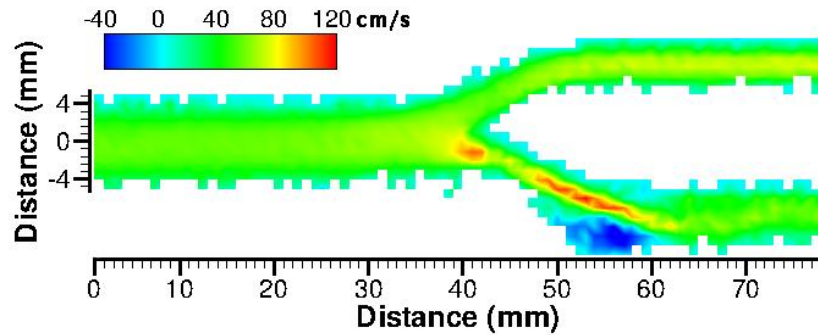


Figure 2.8: Colour-encoded flow map of ensemble-averaged mean velocity, \bar{v}_{mean} , in the longitudinal central plane of the Teflon® bifurcation phantom, measured in a 12-ms acquisition window near peak systole.

2.4 Discussion

The Teflon® flow phantom provides DUS velocity measurements consistent with the tissue-mimicking silicone-walled phantom reported by Poepping *et al.* [23], and has the added advantage of an accurate and rapid fabrication process. Although Teflon® suffers from a lower speed of sound and higher attenuation compared to soft tissue, mean velocity values in the Teflon® flow cylinder are in excellent agreement with expected parabolic profiles, especially near the centre of the vessel, as shown in Fig. 2.5 and 2.6. The overestimation of v_{mean} of the Doppler spectra near the lumen-wall boundary arises from known intrinsic causes, such as finite sample volume and beam side-lobe effects and effects of a wall filter, which is exacerbated in regions of the vessel by low integrated power. These near-wall deviations are not exclusive to the Teflon® phantom, but are observed in both wall-less and walled flow phantoms, as shown by Poepping *et al.* [23]. In the Teflon® phantom under our experimental conditions, these errors become significant within 0.8 mm of the vessel wall boundary, similar to that in the silicone-walled phantom. The acoustic properties of Teflon® are not identical

to tissue or blood, and will therefore result in an acoustic velocity mismatch and refraction effects at the interface between the vessel wall and blood-mimicking fluid [31]. However, previous research has indicated that if a SoS mismatch is unavoidable, it is better to choose a material such that the beam passes from a material of lower SoS into a lumen of higher SoS. In this case, the ultrasound beam is refracted towards the lateral walls resulting in a divergent intensity pattern, avoiding the hot and cold spots associated with a convergent intensity pattern [31, 32]. This effect makes Teflon® a better choice than other plastics, such as UHMW, acrylic [60], polyvinyl chloride [61], or polyester resin [62], and results in a more uniform power distribution across the lumen [63], as shown in Fig. 2.7. Due to some of these mitigating effects, we were able to achieve adequate return signal throughout the depth of the vessel – particularly down the vertical centerline of the lumen where the ultrasound beam traverses the shortest pathline through the material – despite Teflon® suffering from a higher attenuation relative to the thin-walled model. As a consequence of the divergent refraction of the ultrasound beam at the vessel wall boundary, there is a slight lateral shift in the velocity information obtained from the vessel lumen. Since the ultrasound beam is refracted towards the lateral walls, the source of velocity information is located closer to the lateral edges than the assumed site of interrogation. In the Teflon® phantom this leads to a small underestimation of velocity near the lateral boundaries, as shown in Fig. 2.6b, as well as to a narrowed region of low uniform standard deviations in velocity measurements as compared to the thin-walled phantom (Fig. 2.7c and 2.7d). However, data taken near the wall should be used with discretion. It should be noted that interrogations in narrow channels, such as at the point of severe stenosis in the carotid artery bifurcation, may not be as reliable as measurements in broader vessels, such as upstream from the stenosis in the CCA or downstream in the clinically relevant distal ICA.

The capability of the Teflon® phantom to provide quantitative flow velocity spectral measurements and calculated waveform indices, such as mean and peak velocity values, makes it suitable for the evaluation of Doppler ultrasound velocity techniques and experimental flow studies. While the Teflon® phantom is not appropriate for B-mode applications, such as for observations of vessel wall attributes or shadowing artifacts, it is suited to spectral Doppler techniques including colour-flow imaging. We have shown that an analysis of mean flow velocities is possible, but since spectral data can be recorded for offline analysis, post-processing can include a calculation of any number of velocity-based waveform indices. In addition, absolute knowledge of true lumen geometry and dimensions lends itself to greater statistical power for investigations in which geometric parameters are varied.

Direct machining into a rigid plastic, such as Teflon®, can produce flow phantoms with vessel lumens of arbitrary geometry – similar to alternative techniques using thin-walled silicone models and a multi-step lost-material casting process – but with a greatly simplified fabrication process. While the rigidity of Teflon® enables accurate and faithful reproduction of desired vessel geometries, the associated compromise is that Teflon® phantoms do not mimic the arterial distensibility of young human arteries [64, 65]. However, it has been shown that there is a tendency for arterial wall motion to decrease with age and disease [66, 67], and that the extent of wall motion is low in many peripheral vascular disease models [68]. Hansen *et al.* [66] reported that an elderly population typically exhibits only a 5% distension in vessel diameter, as opposed to a 12 to 14 % diameter change in the young population. Numerical simulations have indicated that this low degree of vessel compliance has little effect on the global characteristics of flow patterns [69, 70]. In addition, for cases where the effects of an isolated and deliberate change on a single geometric parameter is desired, flow studies can limit the need to mimic distensibility by using matched or paired models.

Another potential limitation of the Teflon® phantom is that it does not simulate the different ultrasound properties of heterogeneous components in an atherosclerosis model, as is possible with the silicone-walled model [23]. This is not a drawback for most Doppler flow studies, as the focus is generally the observation of flow patterns distal to the atheroma, rather than imaging the structures immediately located at the stenosis.

The direct fabrication of lumen geometry in Teflon® is a versatile method that facilitates a large number of potential applications. This method allows for the fabrication of some geometries not possible with cast- or mould-reliant techniques, such as mushroom-shaped ulcerations as described by Lovett *et al.* [28]. It is also possible to use the proposed fabrication technique to create vessel phantoms with tortuous lumen geometry, i.e. those that incorporate a curve or bend. This curvature can either be in-plane – in which case they can be machined using the technique that we have described without any modifications – or out-of-plane. A non-planar geometry with out-of-plane curvature can still be fabricated using the split model system, but would require a modification to the technique. In this case, the design would include a non-planar parting line between the two Teflon® blocks, such that the parting line defines a surface that bisects the lumen at its widest point, avoiding the need for undercutting. This approach would allow for future phantoms to incorporate tortuosity or irregular features observed in real patients, making it more feasible to conduct rapid prototyping of patient vascular geometries using 3-D diagnostic images from ultrasound [71], magnetic resonance imaging [72, 73], or CT [74, 75]. Due to the versatility of this technique, the phantom is not limited only to carotid lumen geometries, but can be applied to other vessel anatomies, such as to aortic or cerebral aneurysm models. Finally, the ability to introduce small well-defined changes into the Teflon® models makes them amenable to the stepwise variation of vascular geometry. Teflon® flow phantom studies may help to

elucidate the effect of these variations on the diagnostic accuracy of Doppler and in particular the blood-flow parameters relevant to the detection of various anatomic and disease states.

2.5 Conclusion

This study demonstrates the feasibility and efficacy of implementing a computer-aided direct-machining technique for the fabrication of vascular flow phantoms from Teflon®. Ease of fabrication, cost, and flexibility of design make Teflon® flow phantoms suitable candidates for large-scale Doppler ultrasound investigations.

2.6 References

1. Netuka D, Benes V, Mandys V, Hlasenska J, Burkert J, *et al.* (2006) Accuracy of angiography and Doppler ultrasonography in the detection of carotid stenosis: a histopathological study of 123 cases. *Acta Neurochir (Wien)* 148:511-520; discussion 520.
2. Grant EG, Benson CB, Moneta GL, Alexandrov AV, Baker JD, *et al.* (2003) Carotid artery stenosis: grayscale and Doppler ultrasound diagnosis--Society of Radiologists in Ultrasound consensus conference. *Ultrasound Q* 19:190-198.
3. Cuffe RL and Rothwell PM (2006) Effect of nonoptimal imaging on the relationship between the measured degree of symptomatic carotid stenosis and risk of ischemic stroke. *Stroke* 37:1785-1791.
4. Wardlaw JM, Chappell FM, Best JJ, Wartolowska K and Berry E (2006) Non-invasive imaging compared with intra-arterial angiography in the diagnosis of symptomatic carotid stenosis: a meta-analysis. *Lancet* 367:1503-1512.

5. Rothwell PM, Howard SC and Spence JD (2003) Relationship between blood pressure and stroke risk in patients with symptomatic carotid occlusive disease. *Stroke* 34:2583-2590.
6. Johnston DC and Goldstein LB (2001) Clinical carotid endarterectomy decision making: noninvasive vascular imaging versus angiography. *Neurology* 56:1009-1015.
7. Boote EJ and Zagzebski JA (1988) Performance tests of Doppler ultrasound equipment with a tissue and blood-mimicking phantom. *J Ultrasound Med* 7:137-147.
8. Hoskins PR, Anderson T and McDicken WN (1989) A computer controlled flow phantom for generation of physiological Doppler waveforms. *Phys Med Biol* 34:1709-1717.
9. Steel R, Ramnarine KV, Davidson F, Fish PJ and Hoskins PR (2003) Angle-independent estimation of maximum velocity through stenoses using vector Doppler ultrasound. *Ultrasound Med Biol* 29:575-584.
10. Petrick J, Zomack M and Schlieff R (1997) An investigation of the relationship between ultrasound echo enhancement and Doppler frequency shift using a pulsatile arterial flow phantom. *Invest Radiol* 32:225-235.
11. Claudon M, Waininger D, Briancon S and Pesque P (2001) Power Doppler US: evaluation of the morphology of stenoses with a flow phantom. *Radiology* 218:109-117.
12. Allard L, Cloutier G and Durand LG (1995) Doppler velocity ratio measurements evaluated in a phantom model of multiple arterial disease. *Ultrasound Med Biol* 21:471-480.

13. Whyman MR, Hoskins PR, Leng GC, Allan PL, Donnan PT, *et al.* (1993) Accuracy and reproducibility of duplex ultrasound imaging in a phantom model of femoral artery stenosis. *J Vasc Surg* 17:524-530.
14. Poepping TL, Nikolov HN, Rankin RN, Lee M and Holdsworth DW (2002) An in vitro system for Doppler ultrasound flow studies in the stenosed carotid artery bifurcation. *Ultrasound Med Biol* 28:495-506.
15. Dineley J, Meagher S, Poepping TL, McDicken WN and Hoskins PR (2006) Design and characterisation of a wall motion phantom. *Ultrasound Med Biol* 32:1349-1357.
16. Meagher S, Poepping TL, Ramnarine KV, Black RA and Hoskins PR (2007) Anatomical flow phantoms of the nonplanar carotid bifurcation, part II: experimental validation with Doppler ultrasound. *Ultrasound Med Biol* 33:303-310.
17. Levy DJ, Westra SJ, Sayre J and Kimme-Smith C (1996) Validation of volume flow measurements in blood vessels with quantitative color velocity imaging using a physiologic model of the circulation. *Acad Radiol* 3:383-388.
18. Dabrowski W, Dunmore-Buyze J, Cardinal HN and Fenster A (2001) A real vessel phantom for flow imaging: 3-D Doppler ultrasound of steady flow. *Ultrasound Med Biol* 27:135-141.
19. Dabrowski W, Dunmore-Buyze J, Rankin RN, Holdsworth DW and Fenster A (1997) A real vessel phantom for imaging experimentation. *Med Phys* 24:687-693.
20. Rickey DW, Picot PA, Christopher DA and Fenster A (1995) A wall-less vessel phantom for Doppler ultrasound studies. *Ultrasound Med Biol* 21:1163-1176.

21. Deverson S and Evans DH (2000) Using doppler signal power to detect changes in vessel size: a feasibility study using a wall-less flow phantom. *Ultrasound Med Biol* 26:593-602.
22. Ramnarine KV, Anderson T and Hoskins PR (2001) Construction and geometric stability of physiological flow rate wall-less stenosis phantoms. *Ultrasound Med Biol* 27:245-250.
23. Poepping TL, Nikolov HN, Thorne ML and Holdsworth DW (2004) A thin-walled carotid vessel phantom for Doppler ultrasound flow studies. *Ultrasound Med Biol* 30:1067-1078.
24. Schulz UG and Rothwell PM (2001) Major variation in carotid bifurcation anatomy: a possible risk factor for plaque development? *Stroke* 32:2522-2529.
25. Thomas JB, Antiga L, Che SL, Milner JS, Steinman DA, *et al.* (2005) Variation in the carotid bifurcation geometry of young versus older adults: implications for geometric risk of atherosclerosis. *Stroke* 36:2450-2456.
26. Eliasziw M, Streifler JY, Fox AJ, Hachinski VC, Ferguson GG, *et al.* (1994) Significance of plaque ulceration in symptomatic patients with high-grade carotid stenosis. North American Symptomatic Carotid Endarterectomy Trial. *Stroke* 25:304-308.
27. Rothwell PM, Gibson R and Warlow CP (2000) Interrelation between plaque surface morphology and degree of stenosis on carotid angiograms and the risk of ischemic stroke in patients with symptomatic carotid stenosis. On behalf of the European Carotid Surgery Trialists' Collaborative Group. *Stroke* 31:615-621.

28. Lovett JK, Gallagher PJ, Hands LJ, Walton J and Rothwell PM (2004) Histological correlates of carotid plaque surface morphology on lumen contrast imaging. *Circulation* 110:2190-2197.
29. Redaelli A, Rizzo G, Arrigoni S, Di Martino E, Origgi D, *et al.* (2002) An assisted automated procedure for vessel geometry reconstruction and hemodynamic simulations from clinical imaging. *Comput Med Imaging Graph* 26:143-152.
30. Christopher DA, Burns PN, Hunt JW and Foster FS (1995) The effect of refraction and assumed speeds of sound in tissue and blood on Doppler ultrasound blood velocity measurements. *Ultrasound Med Biol* 21:187-201.
31. Thompson RS and Aldis GK (1996) Effect of a cylindrical refracting interface on ultrasound intensity and the CW Doppler spectrum. *IEEE Trans Biomed Eng* 43:451-459.
32. Thompson RS, Aldis GK and Linnett IW (1990) Doppler ultrasound spectral power density distribution: measurement artefacts in steady flow. *Med Biol Eng Comput* 28:60-66.
33. Holland SK, Orphanoudakis SC and Jaffe CC (1984) Frequency-dependent attenuation effects in pulsed Doppler ultrasound: experimental results. *IEEE T Biomed-Eng* BME-31:626-631.
34. Burlew MM, Madsen EL, Zagzebski JA, Banjavic RA and Sum SW (1980) A new ultrasound tissue-equivalent material. *Radiology* 134:517-520.
35. Weskott HP (1997) Amplitude Doppler US: slow blood flow detection tested with a flow phantom. *Radiology* 202:125-130.
36. Weizsacker HW and Pinto JG (1988) Isotropy and anisotropy of the arterial wall. *J Biomech* 21:477-487.

37. Melbin J, Gopalakrishnan R, Riffle R and Noordergraaf A (1982) Construction and characterization of branched, elastic, transparent vessel models. *Am J Physiol* 242:H122-126.
38. Browne JE, Ramnarine KV, Watson AJ and Hoskins PR (2003) Assessment of the acoustic properties of common tissue-mimicking test phantoms. *Ultrasound Med Biol* 29:1053-1060.
39. Kondo T, Kitatuji M, Shikinami Y, Tuta K and Kanda H (2005) New tissue mimicking materials for ultrasound phantoms. In: Proc IEEE Ultrason Symp, Rotterdam, pp 1664-1667.
40. Booi RC, Krucker JF, Goodsitt MM, O'Donnell M, Kapur A, *et al.* (2007) Evaluating thin compression paddles for mammographically compatible ultrasound. *Ultrasound Med Biol* 33:472-482.
41. Hung B-N and Goldstein A (1983) Acoustic parameters of commercial plastics. *IEEE Trans Sonics Ultrason* SU-30:249-254.
42. Ping H and Jun Z (2001) Acoustic dispersion and attenuation measurement using both transmitted and reflected pulses. *Ultrasonics* 39:27-32.
43. Lochab J and Singh VR (2004) Acoustic behaviour of plastics for medical applications. *Indian J Pure Appl Math* 42:595-599.
44. Kondo T, Kishimoto S and Sato Y (1992) Acoustic properties of plastics for applications to probes of an ultrasonic diagnostic instrument. *Jpn J Appl Phys* 31:163-165.
45. Fujii H, Nakaya C, Takeuchi H, Kondo T and Ishikawa Y (1995) Acoustic properties of lens materials for ultrasonic probes. *Jpn J Appl Phys, Part 1* 34:312-315.

46. Selfridge AR (1985) Approximate material properties in isotropic materials. *IEEE Trans Sonics Ultrason* SU-32:381-394.
47. Bilaniuk N and Wong GSK (1993) Speed of sound in pure water as a function of temperature. *J Acoust Soc Am* 93:1609-1612.
48. Fox AJ (1993) How to measure carotid stenosis. *Radiology* 186:316-318.
49. Smith RF, Rutt BK, Fox AJ, Rankin RN and Holdsworth DW (1996) Geometric characterization of stenosed human carotid arteries. *Acad Radiol* 3:898-911.
50. Smith RF, Rutt BK and Holdsworth DW (1999) Anthropomorphic carotid bifurcation phantom for MRI applications. *J Magn Reson Imaging* 10:533-544.
51. Ramnarine KV, Nassiri DK, Hoskins PR and Lubbers J (1998) Validation of a new blood-mimicking fluid for use in Doppler flow test objects. *Ultrasound Med Biol* 24:451-459.
52. Evans DH and McDicken WN (2000) *Doppler Ultrasound: Physics, Instrumentation and Signal Processing*. Wiley, Chichester.
53. Holdsworth DW, Rickey DW, Drangova M, Miller DJ and Fenster A (1991) Computer-controlled positive displacement pump for physiological flow simulation. *Med Biol Eng Comput* 29:565-570.
54. Frayne R, Holdsworth DW, Gowman LM, Rickey DW, Drangova M, *et al.* (1992) Computer-controlled flow simulator for MR flow studies. *J Magn Reson Imaging* 2:605-612.
55. Holdsworth DW, Norley CJ, Frayne R, Steinman DA and Rutt BK (1999) Characterization of common carotid artery blood-flow waveforms in normal human subjects. *Physiol Meas* 20:219-240.

56. Raum K and Brandt J (2003) Simultaneous determination of acoustic impedance, longitudinal and lateral wave velocities for the characterization of the elastic microstructure of cortical bone. In: Proc World Congress on Ultrasonics, Paris, pp 321-324.
57. Hill CR (1986) *Physical Principles of Medical Ultrasonics*. Ellis Horwood Ltd., Chichester.
58. Eubanks BA, Cann CE and Brant-Zawadzki M (1985) CT measurement of the diameter of spinal and other bony canals: effects of section angle and thickness. *Radiology* 157:243-246.
59. Steinman DA, Poepping TL, Tambasco M, Rankin RN and Holdsworth DW (2000) Flow patterns at the stenosed carotid bifurcation: effect of concentric versus eccentric stenosis. *Ann Biomed Eng* 28:415-423.
60. Douville Y, Johnston KW, Kassam M, Zuech P, Cobbold RS, *et al.* (1983) An in vitro model and its application for the study of carotid Doppler spectral broadening. *Ultrasound Med Biol* 9:347-356.
61. Landwehr P, Schindler R, Heinrich U, Dolken W, Krahe T, *et al.* (1991) Quantification of vascular stenosis with color Doppler flow imaging: in vitro investigations. *Radiology* 178:701-704.
62. Frayne R, Gowman LM, Rickey DW, Holdsworth DW, Picot PA, *et al.* (1993) A geometrically accurate vascular phantom for comparative studies of x-ray, ultrasound, and magnetic resonance vascular imaging: construction and geometrical verification. *Med Phys* 20:415-425.
63. Aldis GK and Thompson RS (1992) Calculation of Doppler spectral power density functions. *IEEE Trans Biomed Eng* 39:1022-1031.

64. Benetos A, Waeber B, Izzo J, Mitchell G, Resnick L, *et al.* (2002) Influence of age, risk factors, and cardiovascular and renal disease on arterial stiffness: clinical applications. *Am J Hypertens* 15:1101-1108.
65. Giannattasio C and Mancia G (2002) Arterial distensibility in humans. Modulating mechanisms, alterations in diseases and effects of treatment. *J Hypertens* 20:1889-1899.
66. Hansen F, Mangell P, Sonesson B and Lanne T (1995) Diameter and compliance in the human common carotid artery--variations with age and sex. *Ultrasound Med Biol* 21:1-9.
67. Van Bortel LM and Spek JJ (1998) Influence of aging on arterial compliance. *J Hum Hypertens* 12:583-586.
68. Mancia G, Giannattasio C and Grassi G (1998) Arterial distensibility in cardiovascular diseases. *J Nephrol* 11:284-288.
69. Perktold K and Rappitsch G (1995) Computer simulation of local blood flow and vessel mechanics in a compliant carotid artery bifurcation model. *J Biomech* 28:845-856.
70. Zhao SZ, Xu XY, Hughes AD, Thom SA, Stanton AV, *et al.* (2000) Blood flow and vessel mechanics in a physiologically realistic model of a human carotid arterial bifurcation. *J Biomech* 33:975-984.
71. Augst AD, Barratt DC, Hughes AD, Thom SA and Xu XY (2003) Various issues relating to computational fluid dynamics simulations of carotid bifurcation flow based on models reconstructed from three-dimensional ultrasound images. *Proc Inst Mech Eng [H]* 217:393-403.

72. Thomas JB, Jong L, Spence JD, Wasserman BA, Rutt BK, *et al.* (2005) Anthropometric data for magnetic resonance imaging of the carotid bifurcation. *J Magn Reson Imaging* 21:845-849.
73. Thomas JB, Milner JS, Rutt BK and Steinman DA (2003) Reproducibility of image-based computational fluid dynamics models of the human carotid bifurcation. *Ann Biomed Eng* 31:132-141.
74. Knox K, Kerber CW, Singel SA, Bailey MJ and Imbesi SG (2005) Stereolithographic vascular replicas from CT scans: choosing treatment strategies, teaching, and research from live patient scan data. *AJNR Am J Neuroradiol* 26:1428-1431.
75. Knox K, Kerber CW, Singel SA, Bailey MJ and Imbesi SG (2005) Rapid prototyping to create vascular replicas from CT scan data: making tools to teach, rehearse, and choose treatment strategies. *Catheter Cardiovasc Interv* 65:47-53.

Chapter 3

Clinical Doppler Ultrasound for the Assessment of Plaque Ulceration in the Stenosed Carotid Bifurcation By Detection of Distal Turbulence Intensity: A Matched Model Study[†]

3.1 Introduction

The degree of internal carotid artery (ICA) stenosis is an independent predictor of ischemic stroke and a parameter by which plaques can be graded and patients selected for appropriate therapy [1-4]. This has led to the current use of diagnostic indicators based on the linear reduction in the ICA arterial lumen diameter, to identify patients with significant stenoses who would benefit from the surgical removal of the high-risk lesion [5-12]. Doppler ultrasound (DUS) examinations – utilizing peak-systolic velocity measurements within the high-velocity jet of the ICA as a surrogate measure of stenosis severity – are commonly the first-line diagnostic technique used in the assessment of stroke patients [13, 14]. However, atherosclerotic carotid vessels of similar stenosis or hemodynamic severity do not necessarily pose the same risk of thromboembolic events, and current examinations based solely on the evaluation of stenosis severity do not provide optimal sensitivity and specificity for the selection of patients appropriate for surgery [3, 15-17]. Plaque surface morphology and composition are now recognized to be additional risk factors in determining the clinical significance of carotid atherosclerotic disease [18-21].

[†] A version of this chapter has been published in *European Radiology* (2009) 19: 2739-2749 in an original article entitled “Clinical Doppler ultrasound for the assessment of plaque ulceration in the stenosed carotid bifurcation by detection of distal turbulence intensity: a matched model study” by E. Y. Wong, H. N. Nikolov, M. L. Thorne, R. N. Rankin, T. L. Poepping, and D. W. Holdsworth.

In addition to the degree of ICA stenosis, the North American Symptomatic Carotid Endarterectomy Trial (NASCET) identified one other angiographic parameter – the presence of carotid plaque ulceration – as an independent risk factor for stroke [22]; this finding has also been corroborated by subsequent studies [23, 24]. Although there are some contradictory reports [25-28], numerous investigations have established significant associations between the disruption of the carotid plaque surface by ulceration and pathological evidence of plaque vulnerability as evidenced by: intraplaque hemorrhage [29-31]; adherent surface thrombus [32]; and overall plaque instability [21]. There is also evidence that carotid plaque ulceration is a source of cerebral emboli even when the percent stenosis is less than severe (i.e. < 70% by NASCET standard) [33, 34], perhaps accounting in part for the disparities in risk presented by vessels of similar stenosis severity [35-37].

Carotid plaque surface ulceration is imputed as a cause of thrombosis and a source of cerebral embolisms, but the mechanisms that link ulceration to enhanced thrombogenicity and risk of stroke are still not understood. There is strong evidence to suggest that a combination of biochemical factors (such as systemic factors and exposed substrate-related effects at the site of arterial wall injury) and mechanical factors (arising from the local fluid dynamics) can lead to thrombogenesis at ruptured atherosclerotic plaques, by triggering platelet activation and the coagulation cascade [38, 39]. In terms of fluid-dynamic effects, several types of local alterations in blood flow have been demonstrated to contribute to thrombus formation. Vortices [40, 41], disturbed flow [42], high or oscillating shear stress [43, 44], and turbulence [41, 45-47], have been implicated in platelet activation and thrombus fragmentation [43, 48]. Stagnation zones and regions of recirculation proximal and distal to stenotic lesions – where flow encounters the wall perpendicularly – are thought to promote the deposition or aggregation of

thrombogenic particles [49, 50]. It has been well-established that in fluid-dynamics systems, stenoses, bifurcations, and surface roughness are associated with flow disturbances [51, 52]. This is exemplified in the arterial vasculature, where the geometry of a stenosed carotid bifurcation is uniquely susceptible to complex and aberrant flow behaviour, particularly under physiological pulsatile flow conditions [53-59]. Moreover, it is likely that plaque surface morphology can further contribute to the abnormality of local hemodynamics. *In vitro* investigations performed by Lesniak and colleagues demonstrated that protruding surface irregularities were a source of flow disturbances in a stenotic carotid bifurcation geometry [60, 61], which affected the associated DUS spectra measured in the abnormal flow regions [62, 63]. More specific to ulcerations, Birchall *et al.* [64] reported that a numerical model of a stenosed carotid bifurcation with a deep ellipsoidal ulcer exhibited low-velocity turbulent flow within the ulcer cavity and swirling jets downstream. An *in vitro* flow dynamics study by Imbesi and Kerber [65] found that flow slipstreams assumed a disturbed, helical flow pattern downstream from ulcers located in a stenotic carotid bulb. These reports suggest the potential diagnostic utility of observing the post-stenotic velocity field in ulcerated atherosclerotic vessels, using a method able to detect departures from laminar flow.

In addition to the measurements of peak velocities used in current diagnostic examinations, Doppler ultrasound has the capability to observe quantitative and absolute measures of disturbed and turbulent physiological flow [66]. Several Doppler ultrasound spectral parameters are indicative of disturbances in blood flow, including indices based on the increased width of the Doppler spectrum (e.g. spectral width and spectral broadening index) [55, 67-69], enhanced Doppler backscatter [70-73] and velocity fluctuations (e.g. turbulence intensity (TI)) [74-77]. TI is of particular interest, as it is subject to fewer confounding factors than indices based on spectral width and

Doppler backscatter [78, 79]. Clinical Doppler ultrasound can be utilized in both *in vivo* [74, 80, 81] and *in vitro* [82-84] environments to non-invasively extract measurements of disturbed blood flow. Its application to *in vitro* models, where parameter control is optimal, allows for the study of geometry-related flow effects in both ulcerated and non-ulcerated stenosed vessels with clinical implications.

We describe an *in vitro* study of physiologically relevant ulceration in a stenosed anthropomorphic carotid flow phantom, using clinical Doppler ultrasound to characterize TI distal to the bifurcation. This method allows for the direct comparison of downstream flow with and without the presence of ulceration, in the same stenosis geometry and under identical physiological flow conditions. An offline analysis of data from the clinical system was used to calculate ensemble averaged velocity parameters and compare post-stenotic velocity data in the models. The effects of ulcer size and geometry on the resultant spectral parameters are presented.

3.2 Materials and Methods

A set of anthropomorphic Doppler ultrasound compatible flow phantoms were constructed using the direct-fabrication technique described in Chapter 2 [85]. This method of directly machining vessel geometries into a DUS-compatible plastic facilitated the accurate and easy fabrication of a set of phantoms with ulcers of various sizes and geometries.

3.2.1 Phantom design

3.2.1.1 Vessel and ulcer geometry

The underlying baseline vessel geometry of each phantom, before the incorporation of ulceration, was an averaged geometric representation of a human carotid bifurcation [85], with 50% eccentric stenosis under NASCET criteria [86] and a common carotid artery (CCA) diameter of 8 mm. Four

ulcer shapes – representing each of the four clinically determined categories defined by Lovett *et al.* [87] (as indicated in brackets) – were investigated: a hemispherical ulceration (Type 1), a mushroom-shaped ulcer incorporating a cavity with a small neck connecting it to the parent vessel lumen (Type 2), and ellipsoidal ulcers pointing distally (Type 3) and proximally (Type 4).

Three-dimensional (3-D) computer-aided design (CAD) models representing the reported ulcer geometries were generated in a CAD software package (MasterCam, CNC Software Inc., Tolland, CT, USA) by constructively assembling geometric primitives. The vessel lumen was defined by the intersection of the geometric primitives with the parametrically defined baseline carotid bifurcation geometry. The dimensions of each ulcer type were designed to be clinically realistic in size, proportions, angle of incidence [23, 65, 87-92], and to maintain a similar cavity volume between ulcers. Each ulcer was incorporated into a carotid vessel geometry at the level of the apex of the bifurcation on the non-flow divider wall, to be consistent with previous characterizations of frequent sites of carotid plaque ulceration [88, 91, 93-95]. A Type 1, 4-mm diameter hemispherical ulcer was achieved by incorporating a 4-mm diameter sphere centered at the vessel lumen surface. A Type 2, mushroom-shaped ulcer was constructed as a prolate ellipsoid with an aspect ratio of 2.5 (major axis 5.36 mm, minor axis 2.14 mm) coupled with a cylindrical neck of diameter 2.14 mm and length of 1.07 mm from the main lumen-wall boundary to the ellipsoidal centre. Type 3 and 4, ellipsoidal ulcers were modeled as prolate ellipsoids with an aspect ratio of 2.5 (major axis 7.37 mm, minor axis 2.95 mm) and with the centre intersecting the main lumen-wall boundary, tilted at 45° relative to the tangent of the lumen centerline at the level of the bifurcation apex. To investigate the effect of ulcer size, two additional vessel geometries incorporating hemispherical ulcers (diameters of 2 and 3 mm) were manufactured. No ulcer was allowed to extend beyond the boundary

defined by the corresponding averaged representation of a normal carotid bifurcation lumen geometry [85]. A non-ulcerated phantom with the baseline stenosis geometry was fabricated for comparison with the ulcerated models. The CAD geometries for each of the bifurcation phantoms are shown in Fig. 3.1.

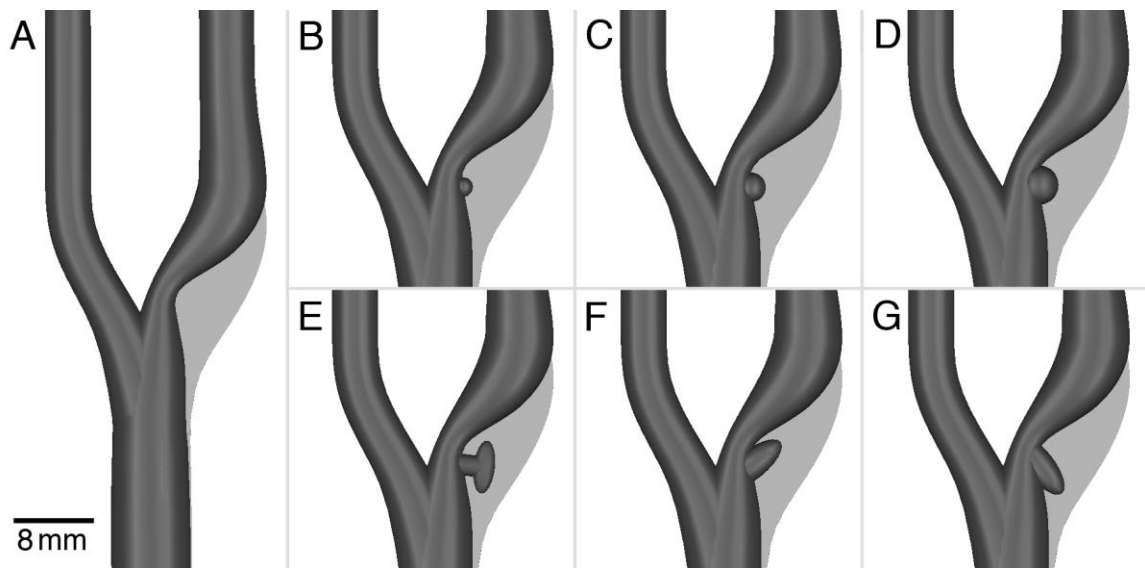


Figure 3.1: The carotid bifurcation lumen geometries used in our study. The CAD models are of an idealized 50% eccentric carotid bifurcation with (a) a smooth non-ulcerated wall; a hemispherical ulcer of (b) 2-mm, (c) 3-mm and (d) 4-mm diameter; (e) a mushroom-shaped ulcer; an ellipsoidal ulcer pointing (f) distally and (g) proximally. The boundary defined by the normal carotid bifurcation geometry is shown in *light grey* to illustrate the location of plaque deposition.

3.2.1.2 Fabrication technique

The numerically controlled (NC) milling instructions for each of these vessel geometries were generated from 3-D parametric surfaces in a CAD software package (MasterCam, CNC Software Inc., Tolland, CT, USA). Each flow phantom was designed to be symmetric about a midplane defined by the

vessel axes, facilitating fabrication as a two-part model, where each half of the phantom was machined into a block of Teflon® with dimensions 70 mm × 215 mm × 5 mm. The procedures for the milling and assembly of the phantoms are described in detail in Chapter 2 [85]. Note that, due to the relatively high acoustic attenuation of Teflon®, it is important to minimize the thickness of plastic overlying the vessel lumen; in our models, the maximum thickness of Teflon® that must be penetrated in the distal ICA was limited to 2.5 mm. Coupling of the phantom to other components of the flow system was facilitated by the incorporation of plastic flow connectors (APC series, Colder Products Co., St. Paul, MN, USA) at the inlet and outlets of the vessel.

3.2.1.3 *Evaluation of vessel geometry*

Dimensional accuracy and geometric fidelity of the flow phantoms were evaluated non-destructively using high-resolution micro-computed tomography (micro-CT), as previously described in Chapter 2. Measurements of lumen dimensions from the micro-CT geometries determined using Microview visualization software (version 2.2.a5, GE Healthcare, London, ON, Canada) were compared to the prescribed CAD instructions as a quantitative assessment of geometric accuracy. Root-mean-square (RMS) departures from prescribed dimensions are reported.

3.2.2 **Doppler data acquisition**

Cardiac-gated Doppler flow velocity data were collected in each of the carotid bifurcation phantoms under identical Doppler acquisition parameters and physiological pulsatile flow conditions using an *in vitro* flow simulator and semiautomated DUS acquisition system (Appendix B, Fig. B.1), as described by Poepping *et al.* [82]. A well-characterized blood-mimicking fluid (BMF) suited to DUS blood-velocity measurements under both laminar and turbulent flow conditions was used [83, 97]. A simulated average carotid

flow-rate waveform [98], with a mean flow rate of 6.00 mL s^{-1} , a peak flow rate of 23.46 mL s^{-1} , and a cycle length of 0.92 s , was provided to the CCA inlet of the flow phantom using a computer-controlled flow pump [99, 100], resulting in a mean Reynolds number of 238 and a Womersley number of 5.2. In the stenosis (2.8-mm diameter), the mean and peak Reynolds numbers were 450 and 1,770, respectively. The pump output flow waveform was that described by Poepping *et al.* [82], which compensates for damping effects to achieve the desired waveform at the inlet of the CCA. Distal flow resistors, comprised of 2-mm diameter tubing of lengths 1 m and 2 m, were attached to the ICA and the ECA outlets, respectively, to establish an appropriate ICA:ECA flow division of 65:35 [82]. The flow phantoms were mounted in a water bath during ultrasound acquisition to ensure adequate acoustic coupling. Experiments were conducted at a temperature of $23 \pm 1 \text{ }^\circ\text{C}$.

Doppler spectral data were acquired at a clinical Doppler collection angle of 60° with a conventional clinical duplex DUS system (Ultramark 9, Philips-ATL, Bothell, WA, USA) using a 4-MHz linear array transducer (L7-4 Philips-ATL, Bothell, WA, USA) producing a focused beam with a 2.0-cm focal depth and a 1.0-mm sample volume length. A pulse-repetition frequency of 18,519 Hz was used to prevent aliasing of the Doppler signal in the high velocity regions. The lowest available wall filter setting of 50 Hz was applied. A semi-automated acquisition system equipped with a computer-controlled 3-D translating stage was used to collect DUS data over the central plane of the phantom defined by the longitudinal axes of the bifurcation flow phantom, as described by Poepping *et al.* [82]. The acquisition grid consisted of 1,025 sample locations with an isotropic spacing of 1 mm within a $78\text{-mm} \times 24\text{-mm}$ region, extending 43 mm proximal to the bifurcation apex in the CCA and 35 mm distal to the bifurcation apex in the ECA and ICA. Note that a 1 mm sample spacing is appropriate, as the effective spatial resolution of clinical DUS is approximately 1 mm [82]. In

order to ensure consistent positioning of the acquisition grid in relation to each flow phantom, registration to the apex of the bifurcation was performed prior to data collection for each experiment. Ten seconds of Doppler audio data were acquired at each collection site and digitized with a sampling rate of 44.1 kHz for offline post-processing and analysis.

To allow for statistical analysis in the post-stenotic region, additional measurements were performed in a region of interest (ROI) within the distal ICA. The location of the ROI was optimized based on colour-encoded maps of central plane data in all of the phantoms. The ROI was defined as a 6-mm diameter circular grid consisting of 24 points with 1-mm isotropic spacing, located 2 CCA diameters (16 mm) distal to the bifurcation in the centre of the ICA (Appendix C, Fig. C.2). Ten independent measurements were performed for each point in the grid, each containing ten seconds of audio data collected using the acquisition parameters described above.

3.2.3 Data analysis

Data analysis of each spectrum consisted of a 1,024-point fast Fourier transform (FFT) with a 1,024-point Hanning window and 50% overlap between consecutive windows, producing an instantaneous Doppler spectrum every 12 ms with a velocity resolution of 1.66 cm s⁻¹. Each of the resulting 85 velocity power spectra calculated from each second of data were used to determine mean velocity (v_{mean}), peak velocity (v_{peak}), and spectral width [82]. To characterize the spread associated with the velocity spectrum, spectral width was determined from the full width at half maximum of the velocity spectrum, and the spectral broadening index was calculated as $1 - v_{mean} / v_{peak}$ [101]. Several derived parameters were calculated from the periodic ensemble average of ten complete cardiac cycles, including: TI; standard deviation in peak velocities (SDPV); and ensemble-averaged mean velocity (\bar{v}_{mean}), peak velocity (\bar{v}_{peak}), spectral width (SW), and spectral

broadening index (SBI) [82]. The absolute TI was calculated as the RMS deviation in v_{mean} about \bar{v}_{mean} (Appendix C, Fig. C.1) [102], while SDPV was defined as the standard deviation in v_{peak} about \bar{v}_{peak} .

Two-dimensional (2-D) velocity parameter maps were rendered for each of the 79 time points in the cardiac cycle. To visualize differences in DUS-measured spectral velocity parameters between the non-ulcerated phantom and an ulcerated phantom, the corresponding 2-D velocity parameter maps were compared using site-by-site subtraction maps. An intensity-based threshold filter was applied to remove data points collected from outside the lumen.

3.2.4 Statistical analysis

For each of the 79 time points in the cardiac cycle, statistical tests were performed on each DUS parameter, using the mean of ten repetitions (each calculated from the gated ensemble of ten cardiac cycles) at each of the acquisition points in the ROI ($N=24$). Paired t-tests were performed to test for differences between two models. For quantitative comparisons between models at a specific time point, mean values and corresponding standard errors calculated from ten repetitions at each of the 24 points in the ROI ($N=240$) are reported. The maximum mean value (and corresponding time point) was determined from the mean TI ($N=240$) at each of the 79 time points, and defined as the maximum TI for the model. Repeated measures one-way analysis of variance (ANOVA) was used to test for the effects of shape and size of ulceration. Each ANOVA was performed on mean values of TI ($N=240$) for 79 time points in the cardiac cycle ($N=79$).

3.3 Results

3.3.1 Verification of phantom geometry

Visual inspection of the lumen boundary of each phantom determined from micro-CT images demonstrated that a smoothly machined surface was achieved throughout the lumen. The average RMS error in dimensions was 0.15 mm, based on ten measurements of lumen dimension from locations both within the vessel and the ulcer of each phantom. This indicated that the NC direct-fabrication technique was able to reproduce the prescribed vessel geometries with high fidelity.

3.3.2 Turbulence intensity (TI)

Increased TI was observed in the distal ICA downstream from the site of ulceration. This is indicated in Fig. 3.2 for the hemispherical ulcer models, where the differences in TI between the ulcerated and non-ulcerated models are visually evident in the corresponding subtraction maps (Fig. 3.2 c, e, g). The region of elevated TI was located approximately 2 CCA diameters (16 mm) distal to the apex of the bifurcation, with an extent of approximately 1 CCA diameter (8 mm). The elevation of TI was most pronounced between 12 ms preceding peak systole and 60 ms following peak systole, as shown in Fig. 3.3 and 3.4. During this window around peak systole, the TI measured in the distal ROI (located at an axial distance of 55 to 60 mm in Fig. 3.2) was persistently higher in all of the ulcer phantoms than during any phase of the cardiac cycle in the non-ulcerated phantom. The maximum TI ($N=240$) measured in the distal ROI with corresponding standard error and the time point of occurrence are listed in Table 3.1. The time of maximum TI occurred between 12 and 36 ms post-peak systole in each phantom. The 2-mm hemispherical ulcer phantom exhibited the smallest maximum differences in TI of $6.2 \pm 0.7 \text{ cm s}^{-1}$ relative to the non-ulcerated model, whereas the largest maximum difference of $10.3 \pm 0.7 \text{ cm s}^{-1}$ was observed in the ulcer phantom

with the distally pointing ellipsoid. Statistically significant differences in TI (95% confidence) were found between the non-ulcerated phantom and each of the ulcerated phantoms. At the time point in the cardiac cycle where the maximum value of TI was measured in the ROI, there was a significant difference in TI in each of the ulcerated phantoms compared to the non-ulcerated phantom with p -values of < 0.001 , as shown in Table 3.1. Two time intervals in the cardiac cycle during which TI did not exhibit significant differences between all ulcer models and the non-ulcerated model were observed. These occurred at 140 – 190 ms (i.e. 20 – 70 ms preceding peak systole) and 430 – 700 ms (i.e. 220 – 490 ms following peak systole), corresponding to the two major acceleration phases of the cardiac cycle where downswings in TI were observed. Significant elevations in TI were found in the ulcerated models as compared to the non-ulcerated model for all other phases of the cardiac cycle, including during the deceleration phase following peak systole and during diastole when the ulcerated models exhibited a heightened level of steady-state TI. The level of TI measured in the laminar flow region near the CCA midline of the models was $2.2 \pm 0.5 \text{ cm s}^{-1}$ (mean \pm standard deviation) and was not significantly different between models ($P = 0.87$).

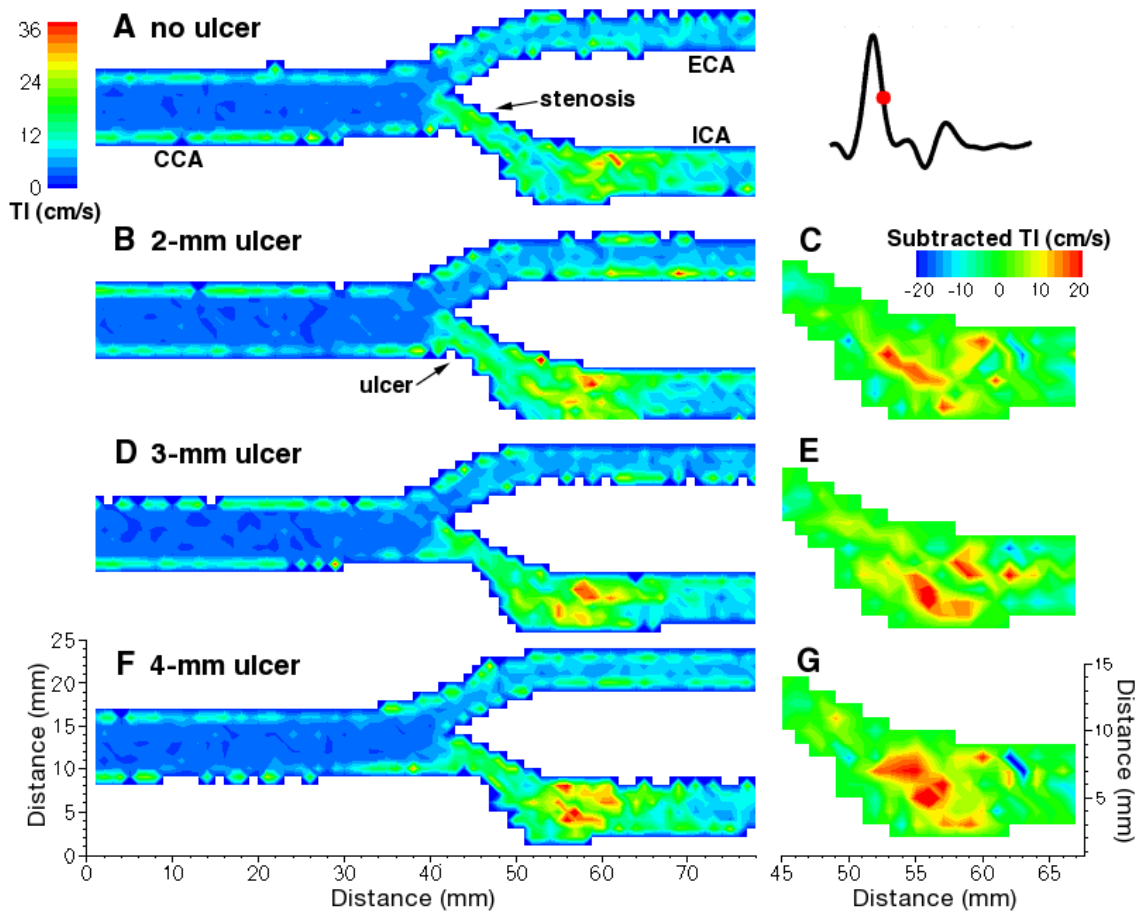


Figure 3.2: Colour-encoded maps of turbulence intensity in the central plane of the (a) non-ulcerated phantom and the (b, c) 2-mm, (d, e) 3-mm, and (f, g) 4-mm hemispherical ulcer phantoms, at 48 ms post-peak systole, where (c, e, g) are subtraction maps of turbulence intensity in the ICA of the ulcer phantom relative to the non-ulcerated phantom.

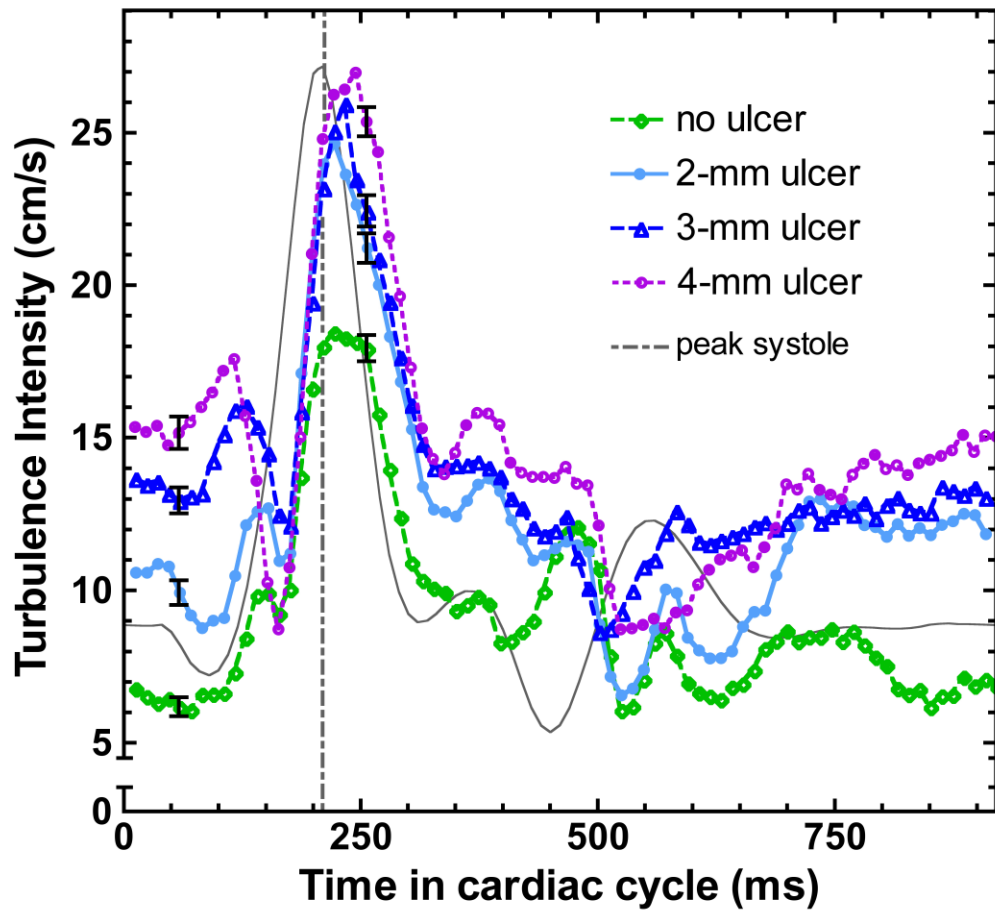


Figure 3.3: Turbulence intensity versus cardiac cycle time in the ROI for the non-ulcerated phantom, and the 2-mm, 3-mm and 4-mm hemispherical ulcer phantoms. The value of turbulence intensity at each time point is an average of ten repetitions (each of ten cardiac cycles) at each of the 24 acquisition sites in the ROI ($N=240$). Standard errors are shown for two time points: in end diastole (seen at a time of 60 ms) and at 48 ms post-peak systole (seen at a time of 264 ms). A schematic of the carotid flow-rate waveform is overlaid (*solid grey line*) to indicate the relative positions of systole and diastole. Peak systole occurs at approximately 210 ms, as indicated by the *vertical dashed line*.

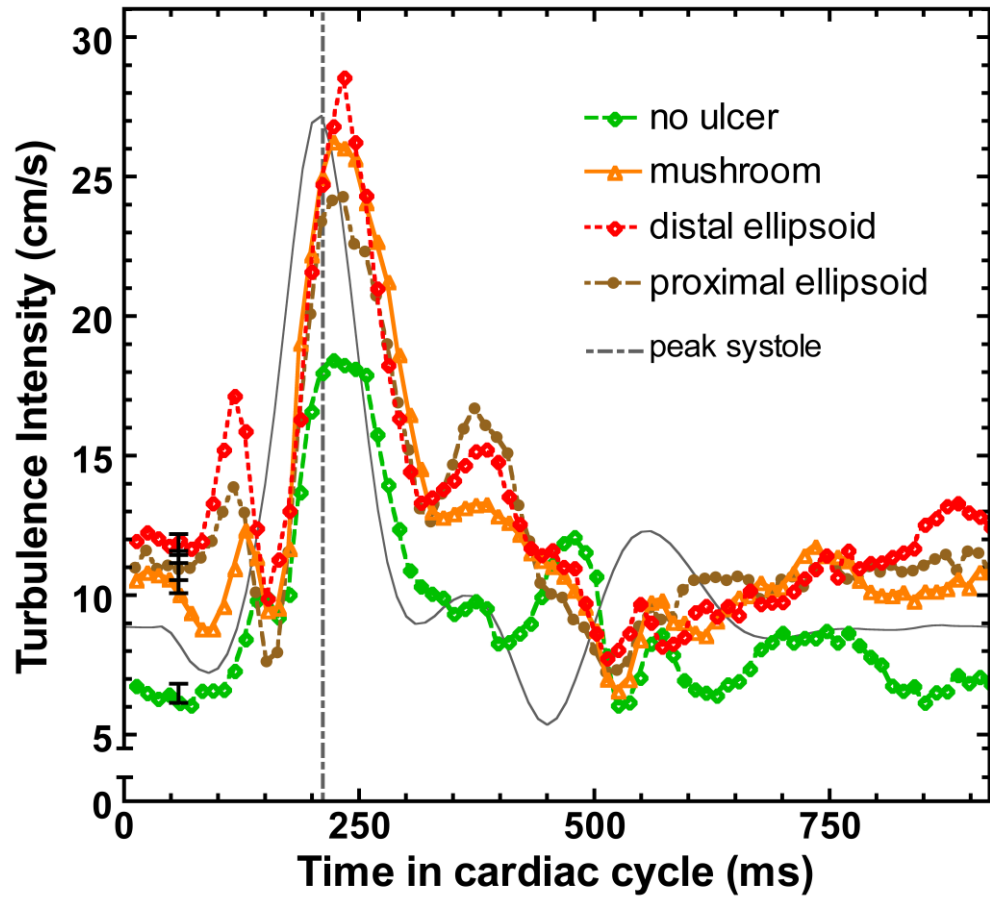


Figure 3.4: Turbulence intensity versus cardiac cycle time in the ROI for ulcer phantoms of various shapes (mushroom, ellipsoidal pointing distally and ellipsoidal pointing proximally) and for the non-ulcerated phantom. Standard errors are shown in end diastole (seen at a time of 60 ms). A schematic of the carotid flow-rate waveform is overlaid (*solid grey line*) to indicate the relative positions of systole and diastole. Peak systole occurs at approximately 210 ms.

3.3.2.1 *Ulcer size and shape*

TI in the post-stenotic region increased as the diameter of the hemispherical ulcer was increased from 2 mm to 4 mm, as indicated in Fig. 3.2 and 3.3 and in Table 3.1. One measure of the effect of ulcer size is maximum TI measured in the ROI in the distal ICA, which increased 1.3 cm s^{-1} between the 2- and 3-mm diameter ulcers and 1.1 cm s^{-1} between the 3- and 4-mm diameter ulcers. Maximum TI presented at a later time point in the cardiac cycle with increasing diameter of hemispherical ulceration, shifting from 12 ms to 36 ms post-peak systole between the 2-mm and 4-mm diameter hemispherical ulcer phantoms. Diastolic values of TI also increased with ulcer size, as shown in Fig. 3.3. In addition, the spatial extent of elevated TI increased with the diameter of ulceration, although the region of elevation was consistently located at approximately 2 CCA diameters distal to the bifurcation apex (Fig. 3.2). A statistically significant effect of ulcer size was observed ($P < 0.001$), as determined by a repeated measures one-way ANOVA of TI in the ROI at 79 time points in the cardiac cycle. A Tukey post-hoc test showed that TI increased as the diameter of ulceration increased (3 mm > 2 mm, and 4 mm > 3 mm, with $P < 0.001$).

A statistically significant effect of ulcer shape ($P < 0.001$) was also indicated by a repeated measures one-way ANOVA of TI in the ROI at 79 points in the cardiac cycle. The ellipsoidal ulcer models with opposite orientations with respect to the direction of blood flow (distal vs. proximal), displayed significantly different levels of TI at 24 ms post-peak systole ($P < 0.001$), where TI was $4.3 \pm 0.8 \text{ cm s}^{-1}$ higher downstream from the Type 3 (distally pointing) ellipsoidal ulcer (Table 3.1).

Table 3.1: Maximum TI in the ROI located within the distal ICA.

Ulcer geometry	TI (cm s ⁻¹) *	<i>P</i> **	Time post-peak systole (ms)
No ulcer	18.5 ± 0.4		12
2-mm hemisphere	24.6 ± 0.6	< 0.001	12
3-mm hemisphere	25.9 ± 0.7	< 0.001	24
4-mm hemisphere	27.0 ± 0.5	< 0.001	36
Mushroom	26.6 ± 0.6	< 0.001	12
Ellipsoid pointing distally	28.6 ± 0.6	< 0.001	24
Ellipsoid pointing proximally	24.3 ± 0.5	< 0.001	24

* Values are maximum mean TI ± standard error ($N=240$).

** *P*-values indicate the significance of the differences in means of TI in the ROI ($N=24$) between the non-ulcerated and ulcerated models at the indicated phase in the cardiac cycle.

TI indicates turbulence intensity; ROI, region of interest.

3.3.3 Other velocity parameters

As indicated by the mean and peak velocity maps of the longitudinal central plane shown in Fig. 3.5, the major flow features characteristic of a carotid bifurcation of 50% eccentric stenosis were observed in each of the flow phantoms, including the high-velocity jet through the stenosis and the recirculation zone along the non-flow divider wall of the distal ICA. Peak-systolic velocities of approximately 110 cm s⁻¹ (mean) and 180 cm s⁻¹ (peak) corresponding to a 50% (NASCET) stenosis [13], were found in the jet of the stenosis in both non-ulcerated and ulcerated models. The recirculation

zone appears near peak systole and persists for 200 ms through the deceleration phase following peak systole. The zone of recirculating flow then reappears to a lesser extent during the smaller deceleration phases of end systole and following the diastolic notch during diastole.

A comparison of other spectral indices (spectral width, spectral broadening index and standard deviation in peak velocity) in the central plane of the non-ulcerated and 4-mm ulcer phantoms at 60 ms post-peak systole are shown in Fig. 3.6. No distinct differences in SW, SBI or SDPV were observed during the systolic phase of the cardiac cycle as a result of ulceration. This is further demonstrated in Fig. 3.7, which shows the time course of these additional spectral parameters over the cardiac cycle in the distal ROI. Moderate differences in the values of SW, SBI and SDPV were observed in the ROI for a period of approximately 300 ms during the end of the diastole phase, which roughly coincides with the interval in diastole for which differences in TI were observed. Statistical analyses from the repeated measures one-way ANOVA post-hoc tests are summarized in Appendix C, Table C.1.

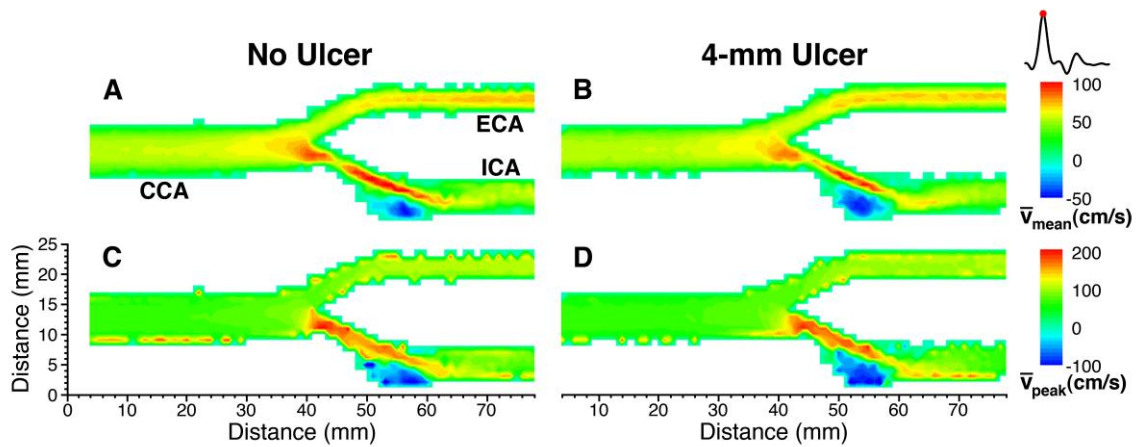


Figure 3.5: Colour-encoded maps of ensemble-averaged (a, b) mean velocity and (c, d) peak velocity in the central plane of the non-ulcerated phantom (*left column*) and the 4-mm hemispherical ulcer phantom (*right column*) at peak systole.

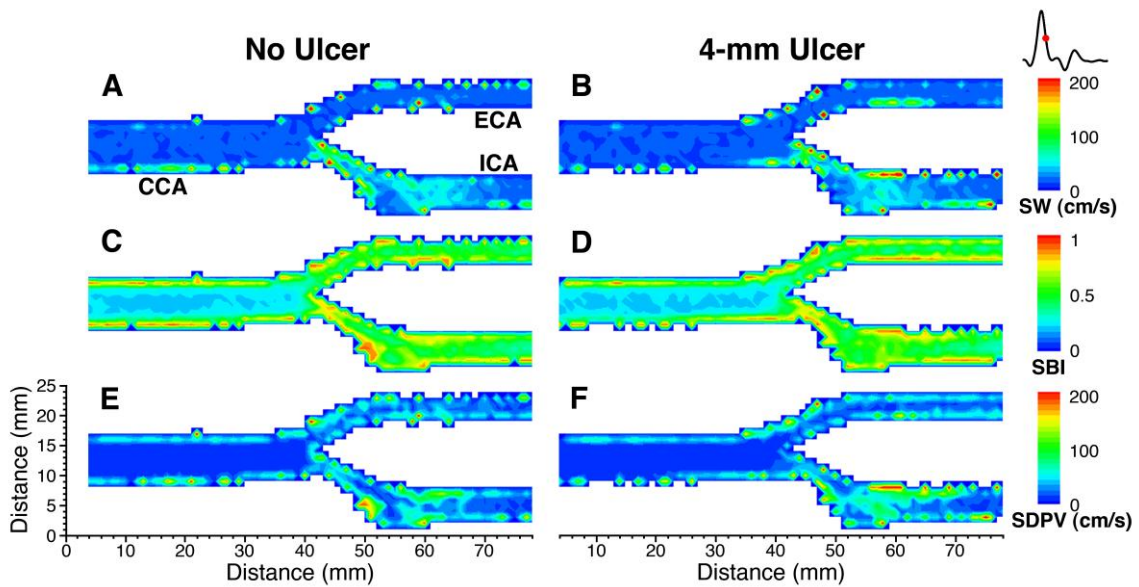


Figure 3.6: Colour-encoded maps of ensemble-averaged (a, b) spectral width, (c, d) spectral broadening index, and (e, f) standard deviation in peak velocity in the central plane of the non-ulcerated phantom (*left column*) and the 4-mm hemispherical ulcer phantom (*right column*) at 48 ms post-peak systole.

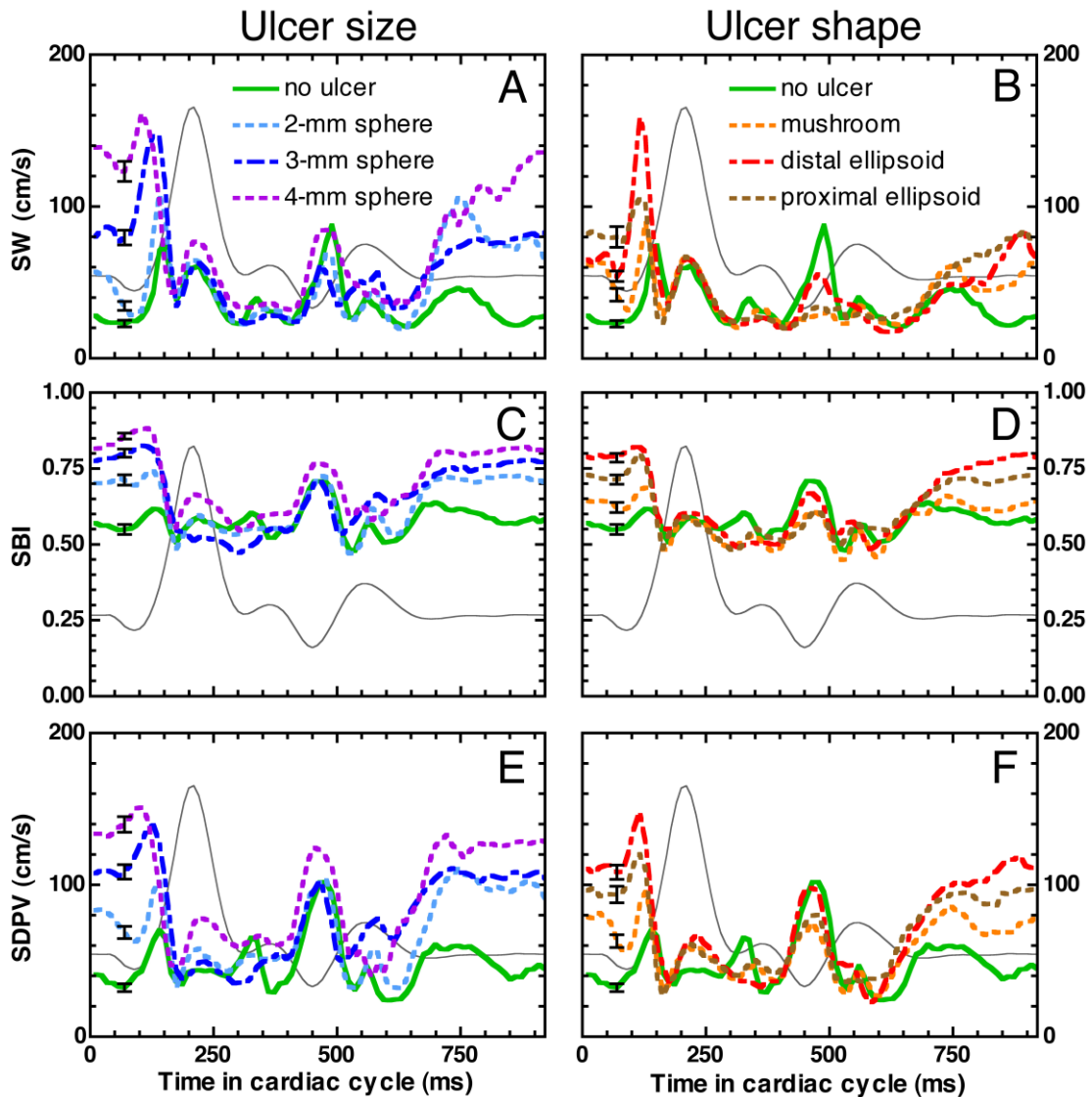


Figure 3.7: The Doppler ultrasound parameters (a, b) spectral width, (c, d) spectral broadening index, and (e, f) standard deviation in peak velocity versus cardiac cycle time in the ROI, where a comparison with ulcer size is shown in the *left column* (2-mm, 3-mm and 4-mm hemispherical ulcers) and a comparison with ulcer shape is shown in the *right column* (mushroom, ellipsoidal pointing distally and ellipsoidal pointing proximally). Schematics of the carotid flow-rate waveform are overlaid on each graph (*solid grey line*) to indicate the relative positions of systole and diastole. Peak systole occurs at approximately 210 ms. Standard errors are shown for a representative time point of 60 ms.

3.4 Discussion

We have shown that the presence of ulceration within a carotid stenosis leads to a significant increase in TI in the distal ICA, as measured by clinical Doppler ultrasound. Offline analysis of velocity spectra, acquired over ten cardiac cycles, indicated regions of elevated TI approximately 2 CCA diameters (16 mm) distal to the stenosis that peaked between 12 – 36 ms post-peak systole, as shown in Fig. 3.3 and 3.4, but remained higher than maximum TI values in the non-ulcerated model for more than 60 ms. In the case of the 4-mm hemispherical ulcer, the severe elevation in TI near peak systole endures for almost 100 ms, which may indicate a window for the detection of ulcers in a clinical setting. While TI is elevated throughout a majority of the cardiac cycle in each of the ulcer models, we believe that the sharp increase just following peak systole is of diagnostic value.

From our study of three hemispherical ulcer models, we observed an effect of ulcer dimension on TI, as might be expected. With increasing ulcer diameter, both the area of elevated TI and the absolute TI increased (Fig. 3.2 and 3.3). While overall ulcer size may be important, the mushroom-shaped ulcer in this study, which had a neck diameter of 2.14 mm, produced distal TI values intermediate to that of the 3- and 4-mm diameter hemispherical ulcers, even though it had a total cavity volume equivalent to the 4-mm diameter hemispherical ulcer. Inlet size therefore may be a determinant factor, although the volume of the ulcer cavity may affect the aggregation of platelets and other thrombogenic particles by influencing the degree of circulating flow within the ulcer. In contrast, two ellipsoidal ulcers with identical cavity volumes and neck diameters but opposite orientation with respect to the adjacent bulk flow in the stenosis, produced TI values that differed by as much as $4.3 \pm 0.1 \text{ cm s}^{-1}$. Ulcers with either a larger inlet area or a more accessible configuration may permit greater flow entry into the

ulcer cavity during diastole, when acceleration at the stenosis is low, and a greater degree of exiting flow into the high-velocity jet during peak systole [65]. All of these factors of ulcer morphology are likely to influence the flow entering, circulating, and exiting the ulcer.

We also investigated additional parameters that can provide an indication of flow disturbances. In contrast to turbulence intensity, the Doppler parameters spectral width, spectral broadening index and standard deviation in peak velocity were not sensitive indicators of carotid ulcerated lesion surface, exhibiting little or no significant difference during the dynamic phases of the cardiac cycle with varying condition of ulceration. While not providing a clear diagnostic window, these parameters did display a stratification of values based on ulcer size and shape for approximately 300 ms during the diastolic phase of the cardiac cycle, when the pulsatile response is diminished and steady-state levels are more apparent (Fig. 3.7). This stratification effect is also observed with TI during the same time period (Fig. 3.4 and 3.5), and suggests that spectral data extracted from diastolic measurements may provide some information to aid in the classification of ulcer size and shape. It should be noted however, that conventional clinical DUS is susceptible to large errors in estimations of peak velocities and spectral width [79, 103]. Confounding factors such as intrinsic spectral broadening, along with algorithmic challenges in automatic determinations of spectral maximum values, make estimations of spectral peak velocities difficult to define robustly [79, 103, 104]. Spectral width is a non-specific parameter of velocity fluctuations due to flow disturbances, as it also has contributions from spatial velocity gradients within the sampling volume, intrinsic spectral broadening and system-specific factors [78, 79, 105]. In practice, estimates of spectral width based on full width at half maximum criteria, can be limited by complex distributions of velocities (e.g. bimodal) and the removal of velocities near the zero crossing by action of the

wall-thump filter. TI, on the other hand, is a truer representation of velocity variance within the flow field, since it is based on mean velocities calculated from the first moment of the average velocity spectrum [78]. Consequently, it is also relatively immune to intrinsic spectral broadening, which has a symmetric effect on the shape of the Doppler spectrum [79]. For these reasons, TI is a more robust and appropriate diagnostic indicator for the assessment of flow disturbances associated with the ulcerated carotid lesion.

Our results agree with previous studies, which have shown that the introduction of ulceration in a stenosed carotid bifurcation produces observable flow disturbances, using numerical simulation [65] and experimental slipstream visualization techniques [64]. While Lesniak *et al.* [62] have previously utilized Doppler techniques (using a laser Doppler anemometer and a pulsed Doppler flowmeter) to observe alterations in blood-velocity patterns due to surface irregularities in the carotid artery vessel, our approach differed in that surface irregularity in the current study was modeled as physiologically realistic ulcerations, as opposed to simple protrusions on the vessel wall surface. In addition, our precise control of ulcer shape and size allowed us to investigate the effect of ulcer geometry rather than simply introducing a higher frequency of protrusion. Our use of a conventional clinical DUS system combined with offline analysis is also more amenable to future applications in a clinical setting.

While the rigidity of the phantoms used in this study enabled desired vessel geometries with small well-defined features to be reproduced accurately and faithfully, the associated compromise is that they did not model the effects of vessel compliance observed in human vasculature [106, 107]. However, it has been shown that there is a tendency for vessel wall motion to decrease considerably with age and disease [108, 109], where vessels in an elderly population exhibit a distension of only 5%, as opposed to 12–14% change in vessel diameter in a young population [110].

Computational flow simulations [111, 112] and fluid dynamics derivations [113, 114] have demonstrated that this small degree of vessel compliance has little effect on the global characteristics of flow behaviour in the carotid stenosis. Furthermore, by employing matched model geometries for this study, where all parameters are maintained except for the plaque morphology at the level of the apex on the non-flow divider wall, the effects of ulceration can be isolated.

Due to the sample volume limitations of medical DUS, our described technique does not enable the characterization of flow within the ulcer or distinction between turbulence and coherent disturbances in the downstream flow field. However, the use of a clinical diagnostic system makes our measurements in the distal ICA more representative of clinically available data. Further studies in basic research, using experimental techniques (e.g. particle imaging velocimetry (PIV)) or numerical methods (e.g. computational fluid dynamics (CFD)), could be used to improve the understanding of flow within the ulcer and the initiation of flow disturbances downstream. They may also elucidate the involvement of these hemodynamic factors in the underlying thrombogenic process [50, 115]. Note that because vessel lumen geometries can be non-invasively extracted from the phantoms with high fidelity using high-resolution micro-CT, the same geometries can be used to create transparent optical phantoms for study using PIV, and for CFD models [116]. Fundamental research – combined with advancements in clinical techniques – will lead to a greater understanding of ulcer plaque conditions and thereby more accurate patient assessment and management.

We have reported an effect of ulceration in the development of post-stenotic flow disturbances in the carotid bifurcation, indicating that it may be beneficial to evaluate the DUS measurement of TI as a potential diagnostic indicator of plaque surface roughness. A measure of plaque

irregularity using DUS may complement the evaluation of percent stenosis in assessing the risk of carotid artery related stroke, particularly for moderate grade stenoses. The detection of ulcers in moderate stenoses, such as demonstrated in this study, is of importance for the identification of patients who are not currently indicated for carotid endarterectomy based solely on stenosis severity, but may in fact benefit from surgical therapy due to their higher risk of stroke. The clinical assessment of TI could be easily integrated as an adjunct to the current conventional DUS examination using peak systolic velocity, with little interruption to the clinical workflow. Since calculations of TI are performed using offline analysis, the examination procedure would simply require a modification to collect data from multiple cardiac cycles. In addition, this method of using measures of TI for ulcerated plaque detection has the potential to be implemented using alternate techniques that have the capability to temporally resolve and quantify velocity fluctuations, such as with phase-contrast magnetic resonance imaging (MRI) [117]. Nevertheless, we would like to caution that although we found statistically significant increases in TI due to the effect of ulceration, the absolute increase in TI was moderate (i.e. $6 - 10 \text{ cm s}^{-1}$). By controlling for parameters of flow and stenosis geometry, our *in vitro* setup was designed to detect such differences in downstream TI. However, it will certainly be more difficult to discriminate between diseased carotid vessels with and without ulceration *in vivo*, due to the natural inter-patient variation in vascular geometry [118, 119] and hemodynamic conditions [98, 120-122], as well as greater measurement uncertainties in the clinical environment. If ulcer detection beyond a moderate stenosis grade is desired, it may be important to determine the co-relation of stenosis severity and ulceration to distal TI, as TI is also expected to increase with stenosis grade [82]. It is also possible that elevated levels of turbulence intensity will be a useful indication of overall risk, regardless of the source. Apart from identifying a parameter of potential diagnostic utility, our observation of exacerbated levels of

disturbed flow downstream from ulceration has the parallel implication that distal hemodynamics may play a role in the process of thrombogenesis. Our findings support other studies that implicate both hemodynamic and biochemical factors in ischemic stroke.

3.5 Conclusion

In vitro flow experiments facilitated a direct comparison of Doppler velocity data and derived blood-flow parameters between ulcerated and non-ulcerated plaque geometries in the stenosed carotid bifurcation. We have demonstrated that clinical Doppler ultrasound is able to detect modifications of the distal flow field produced by ulceration in the carotid lesion, using the velocity-based parameter turbulence intensity.

3.6 References

1. North American Symptomatic Carotid Endarterectomy Trial (NASCET) Collaborators (1991) Beneficial effect of carotid endarterectomy in symptomatic patients with high-grade carotid stenosis. *New Engl J Med* 325:445-453.
2. European Carotid Surgery Trialists' (ECST) Collaborative Group (1998) Randomised trial of endarterectomy for recently symptomatic carotid stenosis: final results of the MRC European Carotid Surgery Trial (ECST). *Lancet* 351:1379-1387.
3. European Carotid Surgery Trialists' (ECST) Collaborative Group (1991) MCT European Carotid Surgery Trial: Interim results for symptomatic patients with severe (70%-99%) or with mild (0%-29%) carotid stenosis. *Lancet* 337:1235-1243.
4. Rothwell PM, Gutnikov SA and Warlow CP (2003) Reanalysis of the final results of the European Carotid Surgery Trial. *Stroke* 34:514-523.

5. Neschis DG, Lexa FJ, Davis JT and Carpenter JP (2001) Duplex criteria for determination of 50% or greater carotid stenosis. *J Ultrasound Med* 20:207-215.
6. Hathout GM, Fink JR, El-Saden SM and Grant EG (2005) Sonographic NASCET index: a new doppler parameter for assessment of internal carotid artery stenosis. *AJNR Am J Neuroradiol* 26:68-75.
7. Staikov IN, Nedeltchev K, Arnold M, Remonda L, Schroth G, *et al.* (2002) Duplex sonographic criteria for measuring carotid stenoses. *J Clin Ultrasound* 30:275-281.
8. Jung EM, Kubale R, Ritter G, Gallegos MT, Jungius KP, *et al.* (2007) Diagnostics and characterisation of preocclusive stenoses and occlusions of the internal carotid artery with B-flow. *Eur Radiol* 17:439-447.
9. Silvennoinen HM, Ikonen S, Soinnie L, Railo M and Valanne L (2007) CT angiographic analysis of carotid artery stenosis: comparison of manual assessment, semiautomatic vessel analysis, and digital subtraction angiography. *Am J Neuroradiol* 28:97-103.
10. De Marco JK, Nesbit GM, Wesbey GE and Richardson D (1994) Prospective evaluation of extracranial carotid stenosis: MR angiography with maximum-intensity projections and multiplanar reformation compared with conventional angiography. *Am J Roentgenol* 163:1205-1212.
11. Pelz DM, Fox AJ, Eliasziw M and Barnett HJ (1993) Stenosis of the carotid bifurcation: subjective assessment compared with strict measurement guidelines. *Can Assoc Radiol* 44:247-252.
12. Wardlaw JM, Chappell FM, Best JJ, Wartolowska K and Berry E (2006) Non-invasive imaging compared with intra-arterial angiography in the

diagnosis of symptomatic carotid stenosis: a meta-analysis. *Lancet* 367:1503-1512.

13. Grant EG, Benson CB, Moneta GL, Alexandrov AV, Baker JD, *et al.* (2003) Carotid artery stenosis: grayscale and Doppler ultrasound diagnosis--Society of Radiologists in Ultrasound consensus conference. *Ultrasound Q* 19:190-198.

14. Netuka D, Benes V, Mandys V, Hlasenska J, Burkert J, *et al.* (2006) Accuracy of angiography and Doppler ultrasonography in the detection of carotid stenosis: a histopathological study of 123 cases. *Acta Neurochir (Wien)* 148:511-520; discussion 520.

15. Chassin MR (1998) Appropriate use of carotid endarterectomy. *N Engl J Med* 339:1468-1471.

16. Coccheri S (2003) Asymptomatic carotid stenosis: natural history and therapeutic implications. *Pathophysiol Haemost Thromb* 33:298-301.

17. Hankey GJ (1999) Stroke prediction and prevention by carotid endarterectomy: keep an eye on the doughnut and not just the hole. *Cerebrovasc Dis* 9:345-350.

18. Ding S, Zhang M, Chen W, Yao G, Zhang P, *et al.* (2008) The role of carotid plaque vulnerability and inflammation in the pathogenesis of acute ischemic stroke. *Am J Med Sci* 336:27-31.

19. Willeit J and Kiechl S (2000) Biology of arterial atheroma. *Cerebrovasc Dis* 10 Suppl 5:1-8.

20. Falk E (2006) Pathogenesis of atherosclerosis. *J Am Coll Cardiol* 47:C7-12.

21. Hennerici MG (2004) The unstable plaque. *Cerebrovasc Dis* 17 Suppl 3:17-22.
22. Eliasziw M, Streifler JY, Fox AJ, Hachinski VC, Ferguson GG, *et al.* (1994) Significance of plaque ulceration in symptomatic patients with high-grade carotid stenosis. North American Symptomatic Carotid Endarterectomy Trial. *Stroke* 25:304-308.
23. Rothwell PM, Gibson R and Warlow CP (2000) Interrelation between plaque surface morphology and degree of stenosis on carotid angiograms and the risk of ischemic stroke in patients with symptomatic carotid stenosis. On behalf of the European Carotid Surgery Trialists' Collaborative Group. *Stroke* 31:615-621.
24. Prabhakaran S, Rundek T, Ramas R, Elkind MS, Paik MC, *et al.* (2006) Carotid plaque surface irregularity predicts ischemic stroke: the northern Manhattan study. *Stroke* 37:2696-2701.
25. Edwards JH, Kricheff, II, Riles T and Imparato A (1979) Angiographically undetected ulceration of the carotid bifurcation as a cause of embolic stroke. *Radiology* 132:369-373.
26. Eikelboom BC, Riles TR, Mintzer R, Baumann FG, DeFillip G, *et al.* (1983) Inaccuracy of angiography in the diagnosis of carotid ulceration. *Stroke* 14:882-885.
27. Lane RJ, Appleberg M, Stirling I, Roche J and Sorby W (1982) Radiological diagnosis of carotid ulceration. *Aust NZ J Surg* 52:168-170.
28. Ricotta JJ, Schenk EA, Ekholm SE and DeWeese JA (1986) Angiographic and pathologic correlates in carotid artery disease. *Surgery* 99:284-292.

29. AbuRahma AF, Kyer PD, 3rd, Robinson PA and Hannay RS (1998) The correlation of ultrasonic carotid plaque morphology and carotid plaque hemorrhage: clinical implications. *Surgery* 124:721-726; discussion 726-728.
30. Arapoglou B, Kondi-Pafiti A, Katsenis K and Dimakakos P (1994) The clinical significance of carotid plaque haemorrhage. *Int Angiol* 13:323-326.
31. Imparato AM, Riles TS, Mintzer R and Baumann FG (1983) The importance of hemorrhage in the relationship between gross morphologic characteristics and cerebral symptoms in 376 carotid artery plaques. *Ann Surg* 197:195-203.
32. Fisher M, Paganini-Hill A, Martin A, Cosgrove M, Toole JF, *et al.* (2005) Carotid plaque pathology: thrombosis, ulceration, and stroke pathogenesis. *Stroke* 36:253-257.
33. Sitzer M, Muller W, Siebler M, Hort W, Kniemeyer HW, *et al.* (1995) Plaque ulceration and lumen thrombus are the main sources of cerebral microemboli in high-grade internal carotid artery stenosis. *Stroke* 26:1231-1233.
34. Orlandi G, Parenti G, Landucci Pellegrini L, Sartucci F, Paoli C, *et al.* (1999) Plaque surface and microembolic signals in moderate carotid stenosis. *Ital J Neurol Sci* 20:179-182.
35. Sterpetti AV, Hunter WJ and Schultz RD (1991) Importance of ulceration of carotid plaque in determining symptoms of cerebral ischemia. *J Cardiovasc Surg (Torino)* 32:154-158.
36. Dixon S, Pais SO, Raviola C, Gomes A, Machleder HI, *et al.* (1982) Natural history of nonstenotic, asymptomatic ulcerative lesions of the carotid artery. A further analysis. *Arch Surg* 117:1493-1498.

37. Valton L, Larrue V, Arrue P, Geraud G and Bes A (1995) Asymptomatic cerebral embolic signals in patients with carotid stenosis. Correlation with appearance of plaque ulceration on angiography. *Stroke* 26:813-815.
38. Sakariassen KS and Barstad RM (1993) Mechanisms of thromboembolism at arterial plaques. *Blood Coagul Fibrinolysis* 4:615-625.
39. Badimon L, Chesebro JH and Badimon JJ (1992) Thrombus formation on ruptured atherosclerotic plaques and rethrombosis on evolving thrombi. *Circulation* 86:III74-85.
40. Goldsmith HL (1970) Motion of particles in a flowing stream. *Thromb Diath Haemorrhag Suppl* 40:91-110.
41. Mustard JF, Murphy EA, Rowsell HC and Downie HG (1962) Factors influencing thrombus formation in vivo. *Am J Med* 33:621-647.
42. Mustard JF and Packham MA (1970) Thromboembolism: manifestation of the response of blood to injury. *Circulation* 42:1-21.
43. Holme PA, Orvim U, Hamers MJ, Solum NO, Brosstad FR, *et al.* (1997) Shear-induced platelet activation and platelet microparticle formation at blood flow conditions as in arteries with a severe stenosis. *Arterioscler Thromb Vasc Biol* 17:646-653.
44. Sakariassen KS, Holme PA, Orvim U, Barstad RM, Solum NO, *et al.* (1998) Shear-induced platelet activation and platelet microparticle formation in native human blood. *Thromb Res* 92:S33-41.
45. Constantinides P (1989) The role of arterial wall injury in atherogenesis and arterial thrombogenesis. *Zentralbl Allg Pathol* 135:517-530.

46. Stein PD and Sabbah HN (1974) Measured turbulence and its effect on thrombus formation. *Circ Res* 35:608-614.
47. Smith RL, Blick FB, Coalson J and Stein PD (1972) Thrombus production by turbulence. *J Applied Physiology* 32:261-264.
48. Merten M, Chow T, Hellums JD and Thiagarajan P (2000) A new role for P-selectin in shear-induced platelet aggregation. *Circulation* 102:2045-2050.
49. Reininger AJ, Reininger CB, Heinzmann U and Wurzinger LJ (1995) Residence time in niches of stagnant flow determines fibrin clot formation in an arterial branching model--detailed flow analysis and experimental results. *Thromb Haemost* 74:916-922.
50. Tambasco M and Steinman DA (2003) Path-dependent hemodynamics of the stenosed carotid bifurcation. *Ann Biomed Eng* 31:1054-1065.
51. Granger RA (1995) *Fluid Mechanics*. Dover, New York.
52. Bakker PG (1991) *Bifurcations in Flow Patterns: Some Applications of the Qualitative Theory of Differential Equations in Fluid Dynamics*. Springer, New York.
53. Motomiya M and Karino T (1984) Flow patterns in the human carotid artery bifurcation. *Stroke* 15:50-56.
54. Ku DN, Giddens DP, Zarins CK and Glagov S (1985) Pulsatile flow and atherosclerosis in the human carotid bifurcation. Positive correlation between plaque location and low oscillating shear stress. *Arteriosclerosis* 5:293-302.
55. Hutchison KJ and Karpinski E (1985) In vivo demonstration of flow recirculation and turbulence downstream of graded stenoses in canine arteries. *J Biomech* 18:285-296.

56. Ku DN, Giddens DP, Phillips DJ and Strandness DE, Jr. (1985) Hemodynamics of the normal human carotid bifurcation: in vitro and in vivo studies. *Ultrasound Med Biol* 11:13-26.
57. Fei DY, Billian C and Rittgers SE (1988) Flow dynamics in a stenosed carotid bifurcation model--Part I: Basic velocity measurements. *Ultrasound Med Biol* 14:21-31.
58. Glagov S, Zarins C, Giddens DP and Ku DN (1988) Hemodynamics and atherosclerosis. Insights and perspectives gained from studies of human arteries. *Arch Pathol Lab Med* 112:1018-1031.
59. Giddens DP, Tang TD and Loth F (1995) Fluid mechanics of arterial bifurcations. In: Jaffrin MY and Caro CG (ed) *Biological Flows*, 1st edn. Plenum, New York, pp 51-68.
60. Kaluzynski K, Lesniak B, Mikolajczyk K and Liepsch D (1997) Analysis of ultrasonic Doppler velocity data obtained in models of stenosed carotid bifurcations with irregular lesion surface. *Technol Health Care* 5:199-206.
61. Kaluzynski K and Liepsch D (1995) The effect of wall roughness on velocity distribution in a model of the carotid sinus bifurcation--analysis of laser and ultrasound Doppler velocity data. *Technol Health Care* 3:153-159.
62. Lesniak B, Kaluzynski K, Liepsch D and Palko T (2002) The discrimination of stenosed carotid bifurcation models with smooth and irregular plaque surface. Part I. Laser and ultrasonic Doppler flow studies. *Med Eng Phys* 24:309-318.
63. Lesniak B, Kaluzynski K, Liepsch D and Palko T (2002) The discrimination of stenosed carotid bifurcation models with smooth and

irregular plaque surface. Part II. The multivariate statistical analysis of ultrasonic Doppler velocity data. *Med Eng Phys* 24:319-323.

64. Birchall D, Zaman A, Hacker J, Davies G and Mendelow D (2006) Analysis of haemodynamic disturbance in the atherosclerotic carotid artery using computational fluid dynamics. *Eur Radiol* 16:1074-1083.

65. Imbesi SG and Kerber CW (1998) Why do ulcerated atherosclerotic carotid artery plaques embolize? A flow dynamics study. *AJNR Am J Neuroradiol* 19:761-766.

66. Hoeks AP, Hennerici M and Reneman RS (1991) Spectral composition of Doppler signals. *Ultrasound Med Biol* 17:751-760.

67. Hutchison KJ (1993) Doppler ultrasound spectral shape in the poststenotic velocity field. *Ultrasound Med Biol* 19:649-659.

68. Morin JF, Johnston KW and Law YF (1987) In vitro study of continuous wave Doppler spectral changes resulting from stenoses and bulbs. *Ultrasound Med Biol* 13:5-13.

69. Sigel B, Gibson RJ, Amatneek KV, Felix WR, Jr., Edelstein AL, *et al.* (1970) A doppler ultrasound method for distinguishing laminar from turbulent flow. A preliminary report. *J Surg Res* 10:221-224.

70. Shung KK, Cloutier G and Lim CC (1992) The effects of hematocrit, shear rate, and turbulence on ultrasonic Doppler spectrum from blood. *IEEE Trans Biomed Eng* 39:462-469.

71. Wu SJ, Shung KK and Brasseur JG (1998) In situ measurements of Doppler power vs. flow turbulence intensity in red cell suspensions. *Ultrasound Med Biol* 24:1009-1021.

72. Bascom PA, Cobbold RS, Routh HF and Johnston KW (1993) On the Doppler signal from a steady flow asymmetrical stenosis model: effects of turbulence. *Ultrasound Med Biol* 19:197-210.
73. Bascom PA, Johnston KW, Cobbold RS and Ojha M (1997) Relation of the flow field distal to a moderate stenosis to the Doppler power. *Ultrasound Med Biol* 23:25-39.
74. Walburn FJ, Sabbah HN and Stein PD (1983) An experimental evaluation of the use of an ensemble average for the calculation of turbulence in pulsatile flow. *Ann Biomed Eng* 11:385-399.
75. Forster FK, Garbini JL and Jorgensen JE (1976) Hemodynamics turbulence measurements using ultrasonic techniques. In: Proc 4th Ann New England Bioeng Conf, New Haven, pp 1223-1226.
76. Garbini JL, Forster FK and Jorgensen JE (1982) Measurement of fluid turbulence based on pulsed ultrasound techniques - 1. Analysis. *J Fluid Mech* 118:445-470.
77. Garbini JL, Forster FK and Jorgensen JE (1982) Measurement of fluid turbulence based on pulsed ultrasound techniques - 2. Experimental investigation. *J Fluid Mech* 118:471-505.
78. Dunmire B, Pagel G, Beach KW and Labs KH (2001) Post stenotic flow disturbances in a steady flow model. In: Proceedings of the SPIE, San Diego, pp 502-513.
79. Evans DH and McDicken WN (2000) *Doppler Ultrasound: Physics, Instrumentation and Signal Processing*. Wiley, Chichester.

80. Casty M and Giddens DP (1984) 25 + 1 channel pulsed ultrasound Doppler velocity meter for quantitative flow measurements and turbulence analysis. *Ultrasound Med Biol* 10:161-172.
81. Hutchison KJ, Campbell JD and Karpinski E (1992) Pulsed Doppler ultrasound velocimetry: a comparison of clinical diagnostic criteria for arterial disease with the results of model studies. In: Labs KH, Jager KA, Fitzgerald DE, Woodcock JP and Neuerburg-Heusler D (ed) *Diagnostic Vascular Ultrasound*, 1st edn. Hodder Arnold, London, pp 97-105.
82. Poepping TL, Nikolov HN, Rankin RN, Lee M and Holdsworth DW (2002) An in vitro system for Doppler ultrasound flow studies in the stenosed carotid artery bifurcation. *Ultrasound Med Biol* 28:495-506.
83. Thorne ML, Poepping TL, Rankin RN, Steinman DA and Holdsworth DW (2008) Use of an ultrasound blood-mimicking fluid for Doppler investigations of turbulence in vitro. *Ultrasound Med Biol* 34:1163-1173.
84. Thorne ML, Poepping TL, Nikolov HN, Rankin RN, Steinman DA, *et al.* (2009) In vitro Doppler ultrasound investigation of turbulence intensity in pulsatile flow with simulated cardiac variability. *Ultrasound Med Biol* 35:120-128.
85. Smith RF, Rutt BK, Fox AJ, Rankin RN and Holdsworth DW (1996) Geometric characterization of stenosed human carotid arteries. *Acad Radiol* 3:898-911.
86. Fox AJ (1993) How to measure carotid stenosis. *Radiology* 186:316-318.
87. Lovett JK, Gallagher PJ, Hands LJ, Walton J and Rothwell PM (2004) Histological correlates of carotid plaque surface morphology on lumen contrast imaging. *Circulation* 110:2190-2197.

88. Lovett JK and Rothwell PM (2003) Site of carotid plaque ulceration in relation to direction of blood flow: an angiographic and pathological study. *Cerebrovasc Dis* 16:369-375.
89. Troyer A, Saloner D, Pan XM, Velez P and Rapp JH (2002) Major carotid plaque surface irregularities correlate with neurologic symptoms. *J Vasc Surg* 35:741-747.
90. Miskolczi L, Guterman LR, Flaherty JD and Hopkins LN (1996) Depiction of carotid plaque ulceration and other plaque-related disorders by intravascular sonography: a flow chamber study. *AJNR Am J Neuroradiol* 17:1881-1890.
91. Saba L, Caddeo G, Sanfilippo R, Montisci R and Mallarini G (2007) CT and ultrasound in the study of ulcerated carotid plaque compared with surgical results: potentialities and advantages of multidetector row CT angiography. *AJNR Am J Neuroradiol* 28:1061-1066.
92. Schminke U, Motsch L, Hilker L and Kessler C (2000) Three-dimensional ultrasound observation of carotid artery plaque ulceration. *Stroke* 31:1651-1655.
93. Dirksen MT, van der Wal AC, van den Berg FM, van der Loos CM and Becker AE (1998) Distribution of inflammatory cells in atherosclerotic plaques relates to the direction of flow. *Circulation* 98:2000-2003.
94. Masawa N, Yoshida Y, Yamada T, Joshita T, Sato S, *et al.* (1994) Three-dimensional analysis of human carotid atherosclerotic ulcer associated with recent thrombotic occlusion. *Pathol Int* 44:745-752.
95. Svindland A and Torvik A (1988) Atherosclerotic carotid disease in asymptomatic individuals: an histological study of 53 cases. *Acta Neurol Scand* 78:506-517.

96. Du LY, Umoh J, Nikolov HN, Pollmann SI, Lee TY, *et al.* (2007) A quality assurance phantom for the performance evaluation of volumetric micro-CT systems. *Phys Med Biol* 52:7087-7108.
97. Ramnarine KV, Nassiri DK, Hoskins PR and Lubbers J (1998) Validation of a new blood-mimicking fluid for use in Doppler flow test objects. *Ultrasound Med Biol* 24:451-459.
98. Holdsworth DW, Norley CJ, Frayne R, Steinman DA and Rutt BK (1999) Characterization of common carotid artery blood-flow waveforms in normal human subjects. *Physiol Meas* 20:219-240.
99. Frayne R, Holdsworth DW, Gowman LM, Rickey DW, Drangova M, *et al.* (1992) Computer-controlled flow simulator for MR flow studies. *J Magn Reson Imaging* 2:605-612.
100. Holdsworth DW, Rickey DW, Drangova M, Miller DJ and Fenster A (1991) Computer-controlled positive displacement pump for physiological flow simulation. *Med Biol Eng Comput* 29:565-570.
101. Brown PM, Johnston KW, Kassam M and Cobbold RS (1982) A critical study of ultrasound Doppler spectral analysis for detecting carotid disease. *Ultrasound Med Biol* 8:515-523.
102. Hinze JO (1959) *Turbulence. An Introduction to its Mechanism and Theory*. McGraw-Hill, New York.
103. Hoskins PR (1999) A review of the measurement of blood velocity and related quantities using Doppler ultrasound. *Proc Inst Mech Eng [H], J Eng Med* 213:391-400.
104. Steinman AH, Tavakkoli J, Myers JG, Jr., Cobbold RS and Johnston KW (2001) Sources of error in maximum velocity estimation using linear

phased-array Doppler systems with steady flow. *Ultrasound Med Biol* 27:655-664.

105. Cloutier G, Allard L and Durand LG (1996) Characterization of blood flow turbulence with pulsed-wave and power Doppler ultrasound imaging. *J Biomech Eng* 118:318-325.

106. Giannattasio C and Mancia G (2002) Arterial distensibility in humans. Modulating mechanisms, alterations in diseases and effects of treatment. *J Hypertens* 20:1889-1899.

107. Benetos A, Waeber B, Izzo J, Mitchell G, Resnick L, *et al.* (2002) Influence of age, risk factors, and cardiovascular and renal disease on arterial stiffness: clinical applications. *Am J Hypertens* 15:1101-1108.

108. Van Bortel LM and Spek JJ (1998) Influence of aging on arterial compliance. *J Hum Hypertens* 12:583-586.

109. Mancia G, Giannattasio C and Grassi G (1998) Arterial distensibility in cardiovascular diseases. *J Nephrol* 11:284-288.

110. Hansen F, Mangell P, Sonesson B and Lanne T (1995) Diameter and compliance in the human common carotid artery--variations with age and sex. *Ultrasound Med Biol* 21:1-9.

111. Perktold K and Rappitsch G (1995) Computer simulation of local blood flow and vessel mechanics in a compliant carotid artery bifurcation model. *J Biomech* 28:845-856.

112. Zhao SZ, Xu XY, Hughes AD, Thom SA, Stanton AV, *et al.* (2000) Blood flow and vessel mechanics in a physiologically realistic model of a human carotid arterial bifurcation. *J Biomech* 33:975-984.

113. Benson TJ, Nerem RM and Pedley TJ (1980) Assessment of wall shear stress in arteries, applied to the coronary circulation. *Cardiovasc Res* 14:568-576.
114. Dewey CF (1979) Fluid mechanics of arterial flow. In: Wolf W and Werthessen NT (ed) *Dynamics of Arterial Flow*, 1st edn. Plenum Press, New York, pp 55-103.
115. Raz S, Einav S, Alemu Y and Bluestein D (2007) DPIV prediction of flow induced platelet activation-comparison to numerical predictions. *Ann Biomed Eng* 35:493-504.
116. Ford MD, Nikolov HN, Milner JS, Lownie SP, Demont EM, *et al.* (2008) PIV-measured versus CFD-predicted flow dynamics in anatomically realistic cerebral aneurysm models. *J Biomech Eng* 130:021015.
117. Dyverfeldt P, Sigfridsson A, Kvitting JP and Ebbers T (2006) Quantification of intravoxel velocity standard deviation and turbulence intensity by generalizing phase-contrast MRI. *Magn Reson Med* 56:850-858.
118. Thomas JB, Antiga L, Che SL, Milner JS, Steinman DA, *et al.* (2005) Variation in the carotid bifurcation geometry of young versus older adults: implications for geometric risk of atherosclerosis. *Stroke* 36:2450-2456.
119. Schulz UG and Rothwell PM (2001) Major variation in carotid bifurcation anatomy: a possible risk factor for plaque development? *Stroke* 32:2522-2529.
120. Lauzon ML, Holdsworth DW, Frayne R and Rutt BK (1994) Effects of physiologic waveform variability in triggered MR imaging: theoretical analysis. *J Magn Reson Imaging* 4:853-867.

121. Younis HF, Kaazempur-Mofrad MR, Chan RC, Isasi AG, Hinton DP, *et al.* (2004) Hemodynamics and wall mechanics in human carotid bifurcation and its consequences for atherogenesis: investigation of inter-individual variation. *Biomech Model Mechanobiol* 3:17-32.

122. Ford MD, Alperin N, Lee SH, Holdsworth DW and Steinman DA (2005) Characterization of volumetric flow rate waveforms in the normal internal carotid and vertebral arteries. *Physiol Meas* 26:477-488.

Chapter 4

The Effect of Both Plaque Ulceration and Stenosis Grade on Distal Turbulence Intensity in the Carotid Bifurcation Using Clinical Doppler Ultrasound[†]

4.1 Introduction

The risk of ischemic stroke and adverse neurological symptoms due to extracranial carotid artery atherosclerosis may be mitigated by surgical management given the appropriate categorization of patients with high-risk lesions. Risk stratification of carotid artery disease and selection for surgical therapy is currently determined from Doppler ultrasound (DUS) assessment of the degree of internal carotid artery (ICA) stenosis – using peak-systolic velocities in the stenotic jet as a surrogate measure of stenosis severity [1]. However, due to the influence of other risk factors, such as plaque surface morphology and composition, carotid atherosclerotic plaques that impose the same degree of stenosis severity (luminal and hemodynamic) frequently exhibit disparate susceptibility to major ischemic events [2]. Consequently, current examinations using diagnostic criteria based solely on the degree of stenosis have suboptimal predictive value for selecting appropriate surgical candidates [3-5].

Along with the degree of stenosis, the multi-centre North American Symptomatic Endarterectomy Trial (NASCET) determined that the presence of plaque ulceration on carotid angiography is an independent predictor of

[†] A version of this chapter has been prepared for submission to *European Radiology* as an original article entitled “The effect of both plaque ulceration and stenosis grade on distal turbulence intensity in the carotid bifurcation using clinical Doppler ultrasound” by E. Y. Wong, H. N. Nikolov, R. N. Rankin, D. W. Holdsworth, and T. L. Poepping.

ischemic stroke risk [6]. Several prospective clinical trials have established that ulcerated or irregular carotid artery plaques represent a greater than two-fold increase in the risk of stroke over plaques with a smooth surface morphology [7-10]. The higher risk of stroke associated with irregular plaque surface morphology holds regardless of the degree of stenosis, and remains predictive of stroke for longer. The risk of stroke in patients with moderate stenosis with irregular morphology is comparable to those with severe category stenosis with smooth surface morphology [8, 11]. Furthermore, disruption of the carotid plaque surface by ulceration has pathological correlations with plaque vulnerability as evidenced by: thrombotic complications; plaque rupture; intraplaque hemorrhage [12-14]; adherent surface thrombus [9]; cerebral emboli [15]; and overall plaque instability [16, 17] – even when stenosis grade is not severe [8, 18].

In addition to the measurement of stenotic flow velocities, conventional diagnostic DUS has the potential to provide diagnostic information on plaque surface morphology by detecting alterations to the measured blood-velocity spectrum associated with distal disturbances in physiological blood flow. Recent *in vitro* work (Chapter 3) has demonstrated that plaque ulcerations in the carotid bifurcation can induce distal flow disturbances that are detectable using clinical DUS [19]. Using the parameter turbulence intensity (TI) as a direct measure of velocity fluctuations, plaque surface ulcerations as small as 2 mm can produce statistically significant elevations of post-stenotic flow disturbances in a moderately stenosed carotid bifurcation, relative to the same stenosis geometry with smooth morphology. Aberrant and disturbed blood flow in the human vasculature is known to contribute to thromboembolic risk [20-26]. As such, a diagnostic indicator based on hemodynamic disturbances also has the potential to provide information on the enhanced risk of ischemic stroke due to flow-induced pathological thrombogenesis [27, 28]. To this point, the impact of ulceration on

post-stenotic TI has only been assessed in a moderate carotid artery stenosis, and a knowledge of the TI produced by ulceration over a range of vessel stenoses would be valuable in determining the feasibility of distal TI as a diagnostic indicator of carotid artery disease – potentially for detecting ulceration at a specified stenosis grade or as an indicator of the combined severity of stenosis and ulceration.

We demonstrate the interrelationship of stenosis severity and ulceration with distal TI in the carotid bifurcation measured using conventional, clinical DUS. Distal TI was evaluated in a series of anthropomorphic carotid bifurcation flow phantoms with various degrees of eccentric ICA stenosis, with and without plaque ulceration, derived from diagnostic DUS audio data and offline analysis.

4.2 Methods

4.2.1 Carotid bifurcation flow phantoms

A family of matched-pairs of anthropomorphic carotid bifurcation DUS-compatible flow phantoms, with and without the inclusion of ulceration, were constructed with various severities of eccentric ICA stenosis: mild (30%), moderate (50% and 60%) and severe (70%) under NASCET criteria [29]. Each of the underlying baseline non-ulcerated carotid bifurcation geometries was an averaged representation of the human stenotic carotid artery [30], with eccentric ICA stenosis and 8-mm common carotid artery (CCA) diameter. For each stenosis geometry, a matched ulcerated and non-ulcerated pair were manufactured, using the direct-fabrication method described in Chapter 2 [31], facilitating their direct comparison and allowing for the isolation of flow effects due to ulceration. The ulcerated vessel geometries incorporated a prolate ellipsoid with an aspect ratio of 2.5 (major axis 7.37 mm, minor axis 2.95 mm), with the centre intersecting the main lumen-wall boundary, and tilted 45° with respect to the tangent of the lumen

centerline, at the level of the apex of the bifurcation on the non-flow divider wall proximal to the point of maximal stenosis. This ellipsoidal ulcer is representative of a Type 3 ulcer (Chapter 3) [17], which is frequently observed clinically [32] and has been previously reported to yield high levels of distal TI [19]. The vessel geometries for each of the bifurcation phantoms are shown in Fig. 4.1.

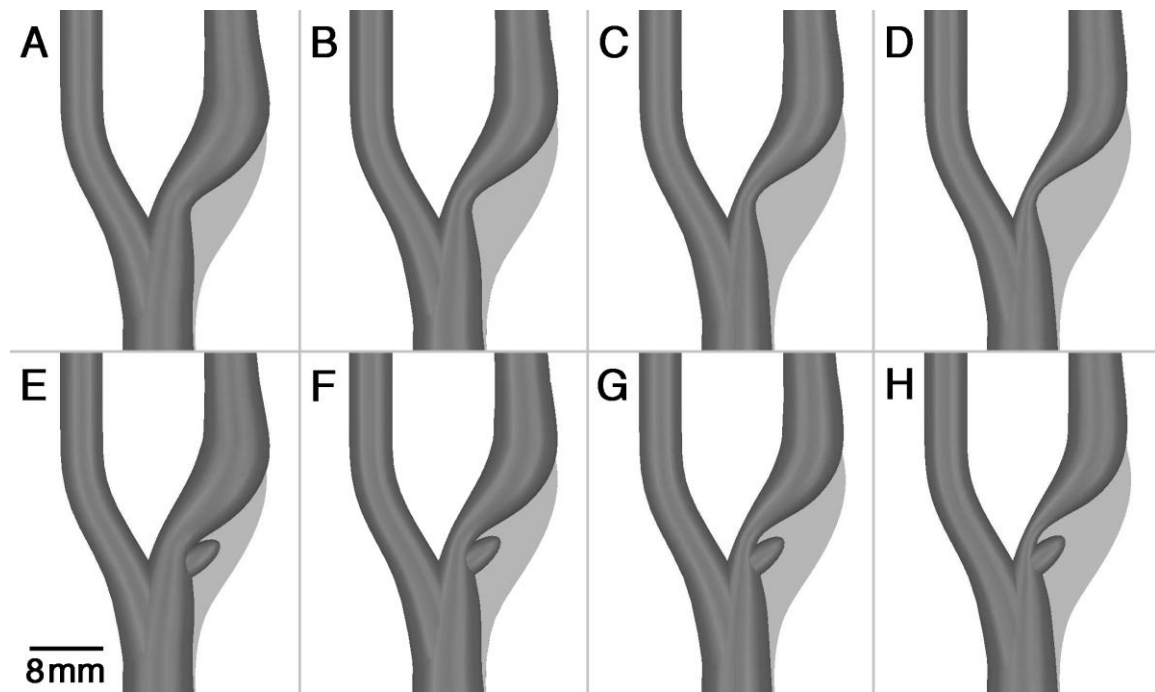


Figure 4.1: Carotid bifurcation geometries used in this study. The *top row* (a–d) consists of the non-ulcerated geometries corresponding to 30%, 50%, 60% and 70% stenosis, by NASCET criteria (left to right). The *bottom row* (e–h) consists of the respective ulcerated geometries. Phantoms extended from over 100 mm proximal to 50 mm distal to the apex of the bifurcation. The normal carotid bifurcation geometry is shown in *light grey* to illustrate the location of plaque deposition.

4.2.2 Doppler data acquisition

In vitro evaluation of Doppler ultrasound TI was implemented in each of the carotid bifurcation flow phantoms using a conventional clinical DUS system under identical physiological pulsatile flow conditions. A well-characterized blood-mimicking fluid with a viscosity of 4.01 ± 0.10 cS, suited to DUS blood-velocity measurements under both laminar and turbulent flow conditions, was used [33, 34]. A computer-controlled pump was calibrated to provide a physiologically realistic pulsatile carotid flow-rate waveform to the CCA inlet of the phantom [35, 36], with peak and mean flow rates of 23.46 mL s^{-1} and 6.00 mL s^{-1} , respectively, and a 0.92 s cardiac cycle length. Distal flow resistors, comprised of 2-mm diameter tubing of lengths 1 m and 2 m, were attached to the ICA and external carotid artery (ECA) outlets, respectively, to establish a physiological ICA:ECA flow division of 65:35 [37]. The phantom was mounted in a water bath during ultrasound acquisition to ensure adequate acoustic coupling. A schematic of the *in vitro* set-up is shown in Appendix B (Fig. B.1) for reference.

Pulsed-wave Doppler flow-velocity measurements were acquired with a conventional clinical duplex ultrasound machine using a 4-MHz linear transducer (L7-4, Philips-ATL, Bothell, WA, USA with either an Ultramark 9, Philips-ATL or a HDI 5000, Philips-ATL) with a sample volume length of 1 mm, a clinical Doppler acquisition angle of 60° and with the lowest available wall filter setting. A minimum pulse-repetition frequency of 18,519 Hz was used to prevent aliasing of the Doppler signal in the regions of high velocity. A computer-controlled three-directional translating stage with probe mount permitted the semi-automated interrogation of the flow field and the acquisition of cardiac-gated DUS audio data at specified coordinate positions [37]. The acquisition grid consisted of 1,025 sites with 1-mm isotropic spacing within the central plane of the phantom defined by the

longitudinal axes of the phantom, encompassing a region 43 mm proximal (in the CCA) to 35 mm distal (in the ECA and ICA) to the apex of the bifurcation. In order to ensure consistent positioning of the acquisition grid in relation to each flow phantom, registration to the apex of the bifurcation was performed prior to data collection for each experiment. Ten seconds of prospectively cardiac-gated Doppler audio data was collected at each measurement site, and digitized at a sampling rate of 44.1 kHz for offline analysis.

For further statistical analysis of TI in the post-stenotic region, additional measurements were taken in a region of interest (ROI) in the distal ICA. The ROI consisted of 24 interrogation points with 1-mm isotropic spacing located within a 6-mm diameter circular grid, centered at just over two CCA diameters (17.5 mm) distal to the apex of the bifurcation in the ICA lumen. Ten seconds of Doppler audio data were collected at each of the 24 sites within the ROI, using the acquisition parameters described above. The ROI acquisition was repeated a total of ten times, yielding ten independent sets of measurements of TI at the 24 ROI sites.

4.2.3 Data analysis

Offline post-processing of the DUS data consisted of a 1,024-point fast Fourier transform utilizing a 1,024-point Hanning window with 50% overlap between consecutive windows, producing an instantaneous Doppler power spectrum every 12 ms (equivalent to 79 time points per cardiac cycle), with a velocity resolution of 1.66 cm s⁻¹. Spectral mean velocity, v_{mean} , was determined for each of the resultant 79 Doppler power spectra within each cardiac cycle [37]. Ensemble-averaged mean velocity (\bar{v}_{mean}) was calculated from the periodic ensemble average of ten complete successive cardiac cycles. The absolute turbulence intensity was determined from an ensemble average of ten cardiac cycles, and defined as the root-mean-square deviation in v_{mean} about the ensemble-averaged mean velocity, \bar{v}_{mean} , at a given time point in

the cardiac cycle [37]. Calculated in this way, TI is a direct measure of velocity fluctuations and an indicator of blood-flow disturbances [38].

4.2.4 Statistical analysis

Statistical analyses were performed using TI measurements acquired in the ROI. To attain a representative value of TI within the ROI, the average TI value was calculated for each set of ROI acquisitions (average of single TI measurements at each of the 24 ROI sites), and defined as $\overline{\text{TI}}_{24}$. The mean and standard deviation (SD) of the ten $\overline{\text{TI}}_{24}$ from the ten repeated ROI acquisitions are reported, and are displayed as a function of the cardiac cycle in Fig. 4.2.

Post-peak systolic TI was calculated as the average TI from three consecutive time points (24-ms window) centered on the time point of maximum TI in the cardiac cycle. To determine the effect of percent stenosis and presence of ulceration on post-peak systolic TI, a two-way analysis of variance (ANOVA) with Bonferroni multiple comparisons post-hoc analysis (with $P < 0.05$ denoting statistical significance) was performed on TI from the same three consecutive time points (24-ms window) centered on the time point of maximum TI in the cardiac cycle ($30 \overline{\text{TI}}_{24}$ from 3 time points $\times 10 \overline{\text{TI}}_{24}$).

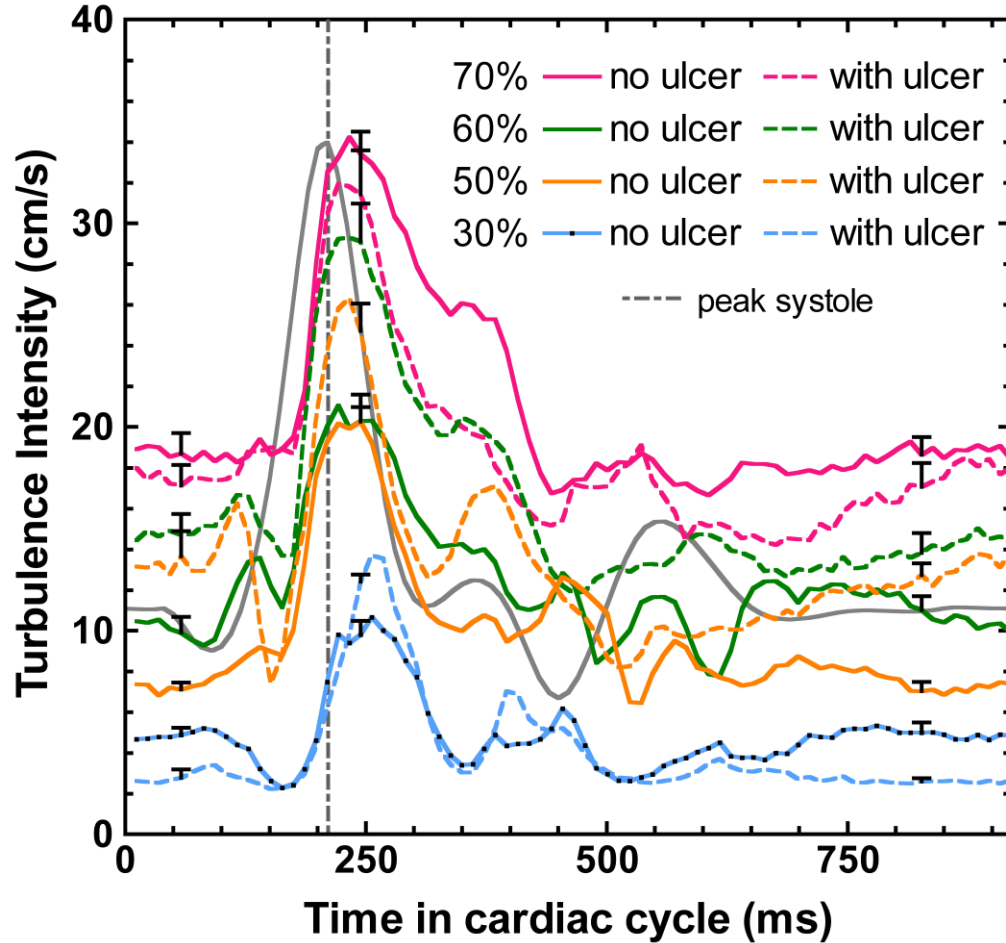


Figure 4.2: Distal TI from ten $\overline{\text{TI}}_{24}$ versus cardiac cycle time for the non-ulcerated (*solid-line*) and ulcerated (*dashed-line*) phantoms. The value of TI at each time point is an average of ten repetitions of $\overline{\text{TI}}_{24}$ from the distal ICA. Standard deviations of ten $\overline{\text{TI}}_{24}$ are shown at three representative time points: 156 ms prior to peak systole, and 36 ms and 636 ms following peak systole. A schematic of the carotid flow-rate waveform is overlaid (*solid grey line*) to indicate the relative positions of systole and diastole. Peak systole occurs at approximately 210 ms, as indicated by the *vertical dashed line*.

4.3 Results

Distal TI in the ICA, calculated as the average of TI measurements from the 24 sites in the ROI ($\overline{\text{TI}}_{24}$), varied in the cardiac cycle, as seen in Fig. 4.2. TI rose sharply just prior to peak systole in the cardiac cycle and peaked during the downstroke of systole in each of the models. The height of the systolic TI curve was clearly higher in each of the ulcerated versions of the mild and moderate stenoses (30%, 50%, 60%) and also increased with stenosis severity in both the ulcerated and non-ulcerated series. Maximum TI in the cardiac cycle (Table 4.1) increased by $3.0 \pm 1.0 \text{ cm s}^{-1}$, $6.0 \pm 2.2 \text{ cm s}^{-1}$ and $8.2 \pm 1.5 \text{ cm s}^{-1}$, due to the inclusion of ulceration in the 30%, 50% and 60% stenosed models, respectively, and decreased by $2.3 \pm 3.1 \text{ cm s}^{-1}$ in the 70%.

A two-curve plot of the effect of stenosis grade and condition of ulceration on TI averaged from a 24-ms window centered on the time of maximum TI is shown in Fig. 4.3. TI increased considerably with the degree of ICA stenosis in both of the vessel series, increasing by $18.2 \pm 1.4 \text{ cm s}^{-1}$ and $23.6 \pm 2.7 \text{ cm s}^{-1}$ from 30% to 70% stenosis, in the series with and without ulceration, respectively. As seen in Fig. 4.3, the two curves progressed in a similar parallel manner for the 30% to 60% stenoses, with the ulcerated curve elevated over the non-ulcerated curve for the mild and moderate stenosis grades, and both reached similarly high values in the 70% stenosis. TI in the ulcerated models was significantly elevated over their non-ulcerated counterparts ($P < 0.001$), increasing the TI in the time window from 10.2 cm s^{-1} to 13.2 cm s^{-1} (30%), 19.8 cm s^{-1} to 25.6 cm s^{-1} (29%), and 20.4 cm s^{-1} to 29.2 cm s^{-1} (44%), in the 30%, 50% and 60% stenoses, respectively (Table 4.1). The difference in distal TI was statistically significant between any pair of models ($P < 0.05$), with the exception of the 50% and 60% non-ulcerated models. Statistical results are summarized in Table 4.2.

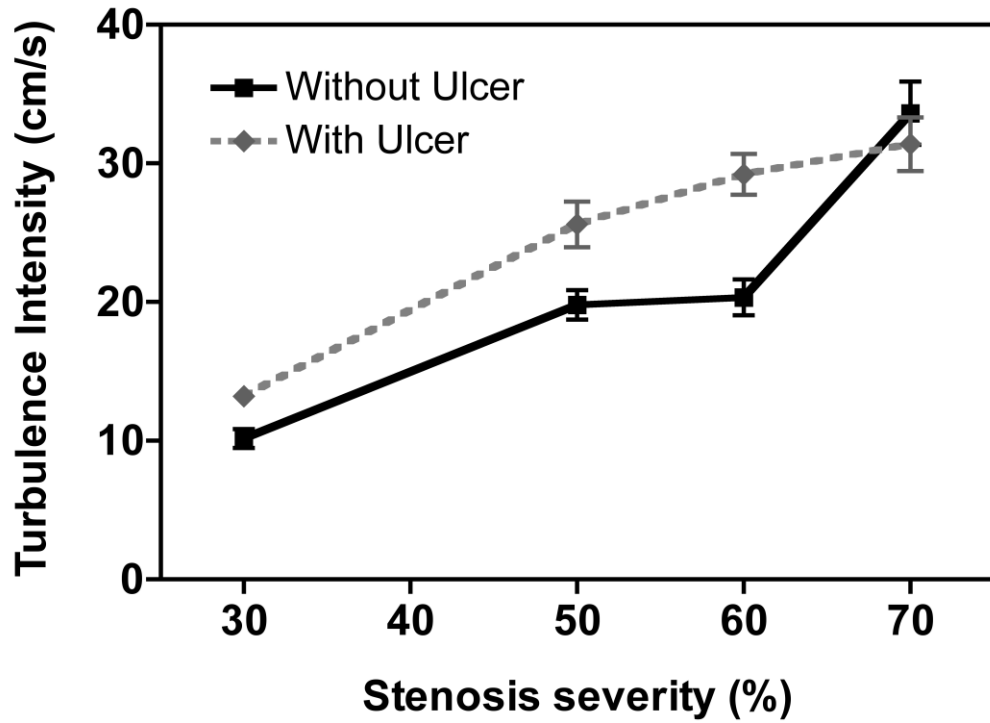


Figure 4.3: Distal TI according to stenosis severity and plaque morphology. The value of TI is the average of $30 \overline{TI}_{24}$ from three consecutive time points for a 24-ms window centered on the time of maximum TI. Error bars depict standard deviation in $30 \overline{TI}_{24}$.

Table 4.1: TI values from the ROI located within the distal ICA. Maximum TI in the cardiac cycle, TI averaged over a 24-ms window (3 time points) centred on the time of maximum TI, and highest TI value from a single site in the ROI are reported. Values are mean TI \pm SD based on ^a10 $\overline{\text{TI}}_{24}$, ^b30 $\overline{\text{TI}}_{24}$ ($3 \times 10 \overline{\text{TI}}_{24}$), and ^c10 repeated measurements of TI at a single location in the ROI.

Model geometry	Maximum TI ^a (cm s ⁻¹)	TI averaged over time window ^b (cm s ⁻¹)	Time of maximum TI post-peak systole (ms)	Maximum single-site measurement of TI within ROI ^c (cm s ⁻¹)
30%	10.7 \pm 0.7	10.2 \pm 0.5	48	21.7 \pm 3.1
30% with ulcer	13.7 \pm 0.7	13.2 \pm 1.0	48	28.2 \pm 5.0
50%	20.3 \pm 1.3	19.8 \pm 1.2	36	30.7 \pm 11.2
50% with ulcer	26.3 \pm 1.8	25.6 \pm 1.3	24	37.4 \pm 7.5
60%	21.1 \pm 1.0	20.4 \pm 1.3	12	30.8 \pm 9.4
60% with ulcer	29.3 \pm 1.2	29.2 \pm 1.4	24	42.6 \pm 7.4
70%	34.2 \pm 2.8	33.6 \pm 3.2	24	51.4 \pm 21.5
70% with ulcer	31.9 \pm 1.3	31.4 \pm 1.5	12	41.3 \pm 12.5

Table 4.2: Differences in post-peak systolic TI and p -values from two-way ANOVA post-hoc analysis. TI values are averaged from three consecutive time points for a 24-ms window following peak systole centred on the time of maximum TI. ns = not statistically significant ($P > 0.05$). Δ TI is calculated as the TI value in the row-indicated model subtracted from the TI value in the column-indicated model.

	30% ulcer		50%		50% ulcer		60%		60% ulcer		70%		70% ulcer	
	Δ TI (cm/s)	P -value	Δ TI (cm/s)	P -value	Δ TI (cm/s)	P -value	Δ TI (cm/s)	P -value	Δ TI (cm/s)	P -value	Δ TI (cm/s)	P -value	Δ TI (cm/s)	P -value
30%	3.1	<0.001	9.7	<0.001	15.5	<0.001	10.2	<0.001	19.1	<0.001	23.5	<0.001	21.2	<0.001
30% ulcer			6.6	<0.001	12.4	<0.001	7.1	<0.001	16.0	<0.001	20.4	<0.001	18.2	<0.001
50%					5.8	<0.001	0.5	ns	9.4	<0.001	13.8	<0.001	11.6	<0.001
50% ulcer							-5.3	<0.001	3.6	<0.001	8.0	<0.001	5.8	<0.001
60%									8.9	<0.001	13.3	<0.001	11.0	<0.001
60% ulcer											4.4	<0.001	2.2	< 0.05
70%													-2.2	< 0.05

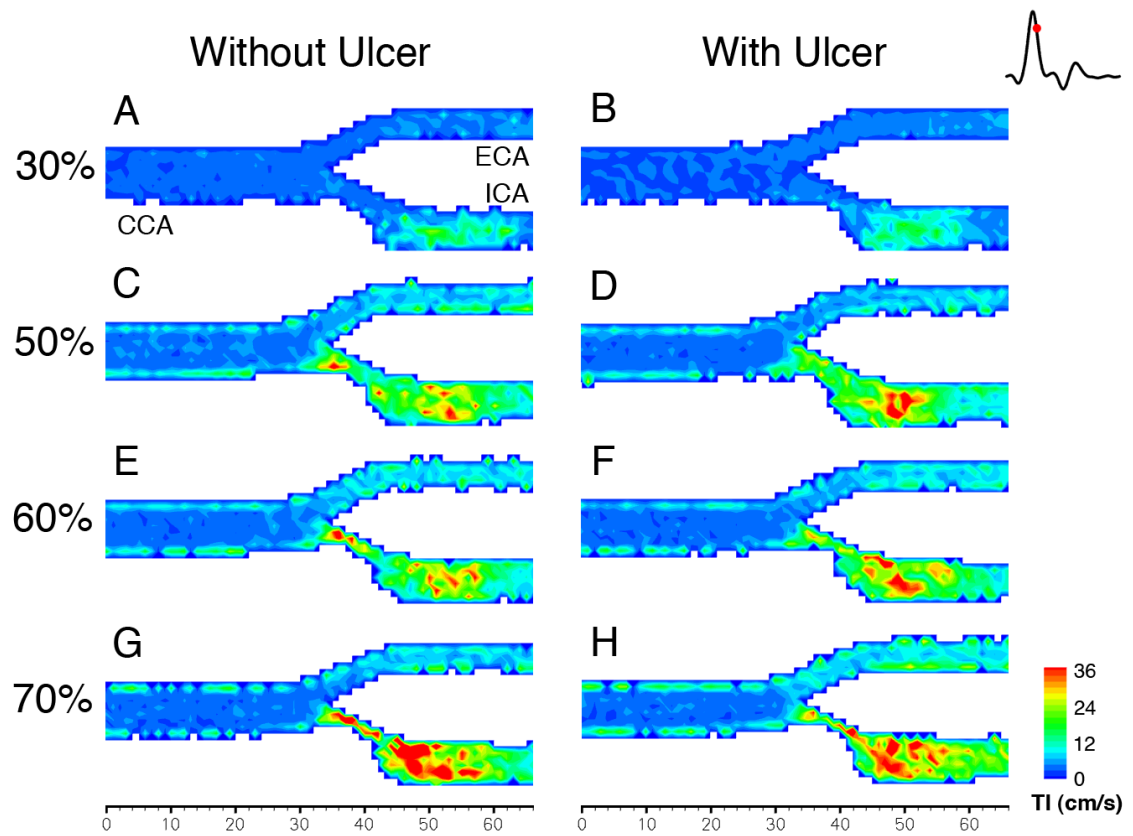


Figure 4.4: Colour-encoded maps of TI in the central plane of the non-ulcerated (*left*) and ulcerated (*right*) (a, b) 30%, (c, d) 50%, (e, f) 60%, and (g, h) 70% phantoms at 24 ms following peak systole.

Colour-encoded maps of TI during the downstroke of systole (24 ms post-peak systole) in the central plane of each of the models exhibited a region of elevated TI in the post-stenotic ICA, and are shown in Fig. 4.4. Levels of post-stenotic TI remained above maximum CCA levels within a region extending approximately 3.5 CCA diameters distal to the apex of the bifurcation in the mildly stenosed models, and over 4 CCA diameters distal in all other models. The region of elevated TI in the 30 – 60% ulcerated models began at a more proximal location than their non-ulcerated counterparts, while high levels of TI were observed immediately distal to the stenosis in both of the 70% models. The extent and magnitude of TI elevation due to increased stenosis severity and ulceration in the 50% and 60% stenosed models are apparent in the colour-encoded maps.

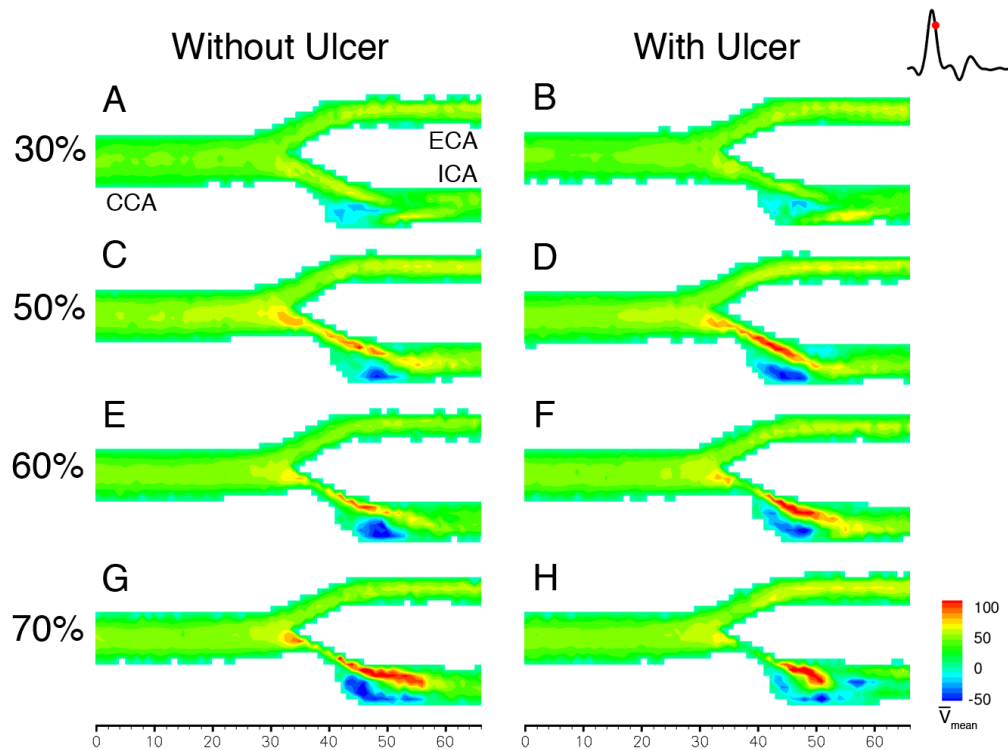


Figure 4.5: Colour-encoded maps of ensemble-averaged mean velocity, \bar{v}_{mean} , in the central plane of the non-ulcerated (*left*) and ulcerated (*right*) (a, b) 30%, (c, d) 50%, (e, f) 60%, and (g, h) 70% phantoms at 24 ms following peak systole.

As seen in the maps of spectral mean velocity for the corresponding phase of the cardiac cycle (24 ms following peak systole) (Fig. 4.5), the region of substantially elevated TI ($> 30 \text{ cm s}^{-1}$, Fig. 4.4) in the distal ICA downstream of the mild and moderate stenoses coincided with the distal portion of the recirculation zone on the non-flow divider side of the carotid sinus; in particular, this region encompassed both reverse flow and the tail of the stenotic jet. During the systolic peak, the region of recirculating flow in the mildly stenosed models did not appear before peak systole and remained subdued until disappearing approximately 120 ms later. In the models with moderate stenosis, the recirculation zones were well-defined and firmly established prior to peak systole, encompassing negative mean velocities below negative 60 cm s^{-1} , and persisted throughout the systolic peak. The greater extent of elevated TI distal to the ulcerated moderate stenoses and the 70% stenoses (with or without ulceration) corresponded to the more proximal location of the upstream edge of the recirculation zone.

Variability statistics at the time of maximum TI are summarized in Table 4.3. Precision in the determination of average TI in the distal ROI ($\overline{\text{TI}}_{24}$) was estimated by the SD in ten measurements of $\overline{\text{TI}}_{24}$ in each of the models (Table 4.3, data column 1). The SD in $\overline{\text{TI}}_{24}$ was less than 10% of the value of $\overline{\text{TI}}_{24}$. Spatial variation within the ROI, calculated from the SD in one set of TI (a single $\overline{\text{TI}}_{24}$) was high, and was elevated due to ulceration in the 30%, 50% and 60% models (Table 4.3, data column 2). Repeatability of TI measurements at each site in the ROI was estimated by the SD in ten single-site repeated measures of TI (Table 4.3, data column 3). Comparisons between the HDI 5000 and Ultramark 9 systems showed that TI measured throughout the systolic peak differed by less than 10%. In contrast, diastolic values of TI were less consistent between systems, varying by as much as 55%, likely due to differences in beam shape and noise characteristics.

Table 4.3: Variability statistics in TI measured in the distal ROI at the time of maximum TI in the cardiac cycle in each model. Reported SD are in cm s^{-1} .

	Repeated measures variability in $\overline{\text{TI}}_{24}$	Spatial variability in TI	Repeated measures variability in single-site TI
Model geometry	SD in 10 repeated measurements of $\overline{\text{TI}}_{24}$	SD in single measurements of TI across 24 sites in ROI	SD in 10 repeated measurements of TI at each site in the ROI given as <i>range (and mean) of 24 SD values</i>
30%	0.7	3.7	1.0 – 6.1 (2.8)
30% with ulcer	0.7	7.2	1.1 – 8.0 (3.6)
50%	1.3	5.0	2.0 – 7.7 (5.4)
50% with ulcer	1.8	9.2	4.5 – 10.1 (7.5)
60%	1.0	7.5	3.3 – 14.1 (6.4)
60% with ulcer	1.2	10.3	3.4 – 11.7 (7.6)
70%	2.8	12.3	5.8 – 13.5 (9.4)
70% with ulcer	1.3	10.4	4.0 – 15.8 (8.7)

4.4 Discussion

Using a conventional clinical DUS system, physiologically realistic plaque ulceration in the mild and moderately stenosed carotid bifurcation can be distinguished *in vitro* by the level of TI in the post-stenotic ICA. Our investigations have established a two-curve relationship of distal TI according to the degree of carotid artery stenosis and condition of ulceration, elucidating the differential effect of ulceration with progressive luminal reduction due to carotid artery disease. The level of TI distal to the ulcerated moderate stenosis measured following peak systole in the cardiac cycle was higher than that of the moderate stenosis without ulceration by more than 5 cm s^{-1} , and by more than 10 cm s^{-1} relative to a mild stenosis with or without ulceration. Distal TI in the ulcerated 60% stenosed model was more similar to that of the severe stenosis than to the non-ulcerated moderate stenoses. The ECST analysis of risk of ischemic stroke associated with angiographic plaque surface morphology and degree of stenosis reported that the two-year risk for moderate stenoses with irregular plaque morphology or severe stenoses was higher than 14%, while the risk was lower for moderate stenoses with smooth plaque surfaces or mild grade stenoses ($< 50\%$ in ECST, $< 30\%$ under NASCET categorization) [8, 11]. In our study, a value of distal TI above 22 cm s^{-1} indicated an ulcerated moderate stenosis or a severe stenosis, demonstrating that there is a potential diagnostic threshold for designating carotid plaques in a high-risk category. Ulceration elevated the distal TI post-peak systole by 3.1 cm s^{-1} , 5.8 cm s^{-1} and 8.9 cm s^{-1} (30%, 29%, and 44%) in the 30%, 50% and 60% ulcerated models, respectively. While ulceration induced a statistically significant elevation of distal TI in each of the 30% to 60% stenosed vessels ($P < 0.001$), the degree of stenosis was the dominant factor in determining TI, with distal TI increasing by over 18 cm s^{-1} with increased stenosis severity from 30% to 70% in both the ulcerated and non-ulcerated series.

In agreement with previous *in vitro* [39-42] and animal model [43-47] investigations, increased stenosis severity was accompanied by enhanced flow disturbances in the post-stenotic region. Not only do peak velocities in the stenotic jet, and accordingly the maximum Reynolds number (Re) in the cardiac cycle, increase with the severity of stenosis, but the critical Re has also been shown to decrease, indicating that flows separate and transition from laminar to turbulent at lower velocities [48]. The observed variation in the effect of ulceration at different degrees of stenosis is also not unexpected, given the velocity dependence of flow disturbances. The major determinant of flow disturbances in a stenotic vessel is the balance of stabilizing and destabilizing factors that affect the shear layer at the interface between the edge of the high velocity jet and the recirculating fluid in the adjacent separation zone within the post-stenotic vessel expansion. Destabilizing factors include: (1) pulsatile flow deceleration (i.e. time-dependent component), such as during the downstroke of the systolic peak; (2) divergent vessel walls producing convective flow deceleration (i.e. time-independent geometric component), such as in the carotid sinus distal to the plaque stenosis; and (3) further perturbations of the shear layer, such as by disorderly flow within the stenosis. Flows in a mildly stenosed vessel are likely more stable and less susceptible to the propagation of flow perturbations, as the maximum jet velocities during peak systole and accordingly the deceleration during the systolic downstroke are lower. Stenotic jet velocities during peak systole, and consequently post-stenotic deceleration and Re -indicated instability, increase with stenosis severity. With greater instability of the shear layer, it follows that intrastenotic flow disturbances induced by ulceration would be more likely to promote further destabilization.

As the degree of stenosis was increased further to 70%, the vessel stenosis was the dominant source of distal TI and the effect of ulceration was

observed to level off. Furthermore, the inclusion of ulceration produced a slight decline in the absolute value of distal TI. This effect at higher stages of vessel narrowing may indicate that a change in the interplay between direct induction of flow fluctuations by the ulcer and the development of turbulent fluctuations due to the decelerative dissipation of the jet occurs in the 70% stenosis. Previous research has indicated that while coherent flow disturbances occur in moderately stenosed vessels, the onset of full turbulence in vascular flows is not likely to occur until the degree of vessel stenosis is severe [40, 49, 50]; several studies have found that the critical degree of stenosis for considerable turbulence is 65 – 75% diameter reduction [40, 50-53].

As hemodynamic and geometric factors were matched in our study, we were able to show that ulceration had a direct effect on the local flow disorder. Since the ulceration is a considerable flow cavity (same length order as the stenosis) rather than a simple roughened surface, its effect on flow instabilities is particularly complex. With the inclusion of ulceration, the vessel stenotic geometry is altered from a streamline stenosis, instead producing a small expansion of the vessel on the proximal side of the ulcer cavity, and a severe convergence at the distal edge of the ulcer, followed immediately by an expansion into the post-stenotic carotid sinus. Although the degree of vessel stenosis is typically the dominant geometric parameter determining the critical Re for transitional flow [54], the specific contour (e.g. shape and length) of the stenosis is also known to be influential [39, 45, 55, 56]. Both a more severe stenotic angle and shorter stenotic length are known to decrease the critical Re [48]. In addition, Imbesi and Kerber [57] showed using a dye slipstream visualization technique, that an ulceration in the carotid bifurcation allows flow slipstreams to enter and slowly circulate within the ulcer cavity during diastole, re-enter the stenotic flow during peak systole, and thereby perturb nearby stenotic slipstreams. In our study, due

to proximity of the ulceration and the shear layer, local flow perturbances caused by the ulcer are likely to directly impact shear layer stability.

Our findings agree with numerous studies that show a strong positive correlation between stenosis severity and downstream flow disturbances. In contrast, there are a limited number of studies on the flow effects of ulceration. Several reported that the presence of ulceration in a stenosed carotid bifurcation induced substantial distal flow disturbances, using numerical simulation [58] and experimental slipstream visualization techniques [57], but only examined the effect of plaque ulceration in a single patient-specific carotid stenosis geometry. Lesniak *et al.* [59-61] investigated the effect of simple vessel roughness in controlled model series (using a laser Doppler anemometer and a pulsed Doppler flowmeter), but looked at simple protrusions on the vessel wall surface, rather than the physiologically realistic ulcer cavity geometry used in our study. In addition, our use of a conventional clinical DUS system combined with offline analysis is more amenable to further applications in a clinical setting. By separating the effects of stenosis grade and ulceration, we were able to observe a clear and significant relationship of ulceration and distal TI in the mild and moderate grade stenosis, indicating that DUS-measured TI in the distal flow region may provide valuable diagnostic information in conjunction with peak systolic velocities.

Spectral TI is a quantitative and direct measure of disturbed and turbulent physiological flow [38, 62]. Whereas DUS spectral indices of disturbed blood flow based on the increased width of the Doppler spectrum (e.g. spectral width and spectral broadening index) [44, 63-65] or enhanced Doppler backscatter [66-69] are subject to confounding system-specific factors [62, 70, 71], TI is based simply on mean velocities calculated from the first moment of the Doppler spectrum, and relatively immune to intrinsic spectral broadening, which has a symmetric effect on the Doppler spectrum [70]. We

observed that TI values throughout the systolic peak were relatively similar between the two systems used in our study, but varied in diastolic measurements, likely due to differences in beam and noise characteristics. Accordingly, TI is a robust and appropriate diagnostic indicator for clinical assessment of abnormal hemodynamic conditions associated with disease states.

Since TI values are collected using a conventional DUS system with analysis performed offline, a basic clinical implementation of TI could be directly incorporated into current carotid sonographic examinations – as an adjunct to measurements of peak systolic velocities within the stenotic jet – with little interruption to the clinical workflow. Previous studies have shown that it is feasible to assess TI in patients using DUS [72-74]. TI has also been shown to be detectable even under normal physiological and exaggerated variability in cardiac output [75]. Importantly, it was recently demonstrated that TI measurements could be obtained with high precision during a clinical DUS examination. Skilled ultrasound technologists were able to precisely locate specified sites within the carotid artery, including in the CCA and within the region of extreme flow disturbances in the distal ICA, identified using local mean velocity fluctuations indicated on colour Doppler imaging. Despite the potential effects of patient and transducer motion during an acquisition time over multiple cardiac cycles, repeated measurements with repositioning of the sample volume location was shown to be highly reproducible; averaged TI from three measurements had an SD of less than 2 cm s^{-1} in the distal ICA for all stenosis grades [74].

One challenge to the accurate *in vivo* characterization of ulceration and stenosis severity of the vessel is that it will likely require multiple measurements to produce an averaged TI over a region of interest, rather than a single measurement at an arbitrary site of extreme TI elevation. Single measurements can obscure the distinction between moderate stenoses

with and without ulceration. Hotspots of high TI of $58 - 65 \text{ cm s}^{-1}$ are observed from single measurements of TI even in the non-ulcerated moderately stenosed models, similar to the $58 - 70 \text{ cm s}^{-1}$ found in the moderately stenosed models with ulceration. Mean TI averaged from repeated measurements at a TI hotspot ($N=10$) fared better at stratifying the critical disease categories, with greater than 6 cm s^{-1} elevation due to ulceration in each of the mild and moderately stenosed vessels (Table 4.1). It has yet to be determined whether the location of highest TI can be consistently established, for example, by qualitative interpretations of colour Doppler displays of velocity fluctuations. This may be further complicated as single measurements of extreme TI exhibit at varying times in the cardiac cycle.

In contrast, a value of averaged TI from a set of 24 measurements within the post-stenotic vessel region ($\overline{\text{TI}}_{24}$) was more reproducible, with SD of less than 1.3 cm s^{-1} and 1.8 cm s^{-1} in the non-ulcerated and the ulcerated 30 – 60% stenoses, respectively, during the systolic peak when SD in TI is maximal ($N=10 \overline{\text{TI}}_{24}$). Consistent, repeatable values may be obtained with the sampling and averaging of multiple measurements from within a ROI to attain representative values of distal TI. Averaging is recommended not because TI in the distal ICA is not reproducible, but because there is a spatially non-uniform distribution in TI that is due to the underlying coherent flow structure [40]. While disturbed and turbulent flows are complex and time-dependent, they are, in fact, associated with well-defined and predictable statistical features, including root-mean-square velocity [39]. Variation between TI measurements within the ten $\overline{\text{TI}}_{24}$ primarily arose from varying location than from repeated measurements (Table 4.3). Note that post-stenotic TI values in the ulcerated geometries were accompanied by higher SD than their non-ulcerated counterparts, except for the 70% stenosis,

which may be an indication of the disease state and the nature of the source of velocity fluctuations.

In our experience, serial measurements of TI at multiple target sites may be possible with precise and reproducible free-hand positioning by skilled ultrasound technologists [74]. Furthermore, to obtain measurements over a ROI with shorter acquisition times and lower operator-dependence, it is possible to develop custom automated acquisition sequences that collect and analyze spectral DUS blood flow data at multiple sites. Simultaneous or sequential data collection at multiple sample sites has been adapted to other DUS applications using a commercial scanner with multiple receiver gates (multi-gating) or programmable beamforming techniques [76, 77]. The recent availability of commercial ultrasound systems with add-on research interfaces enables the user control and programming of custom transmission strategies, making it feasible to develop a more effective dedicated clinical protocol.

While significant elevations in TI were observed with the inclusion of ulceration or increased stenosis severity *in vitro*, the absolute differences in TI were modest. It will naturally be more challenging to distinguish the moderate differences due to ulcerated plaques in patients, given physiological variability in carotid vessel geometry and hemodynamic conditions, as well as greater measurement uncertainties in the clinical setting. Inter-patient variation in absolute TI values may be accounted for potentially, by normalizing distal ICA values using patient baseline TI values acquired from the laminar flow region in the pre-stenotic CCA, a measurement site already commonly interrogated in current clinical practice [1]. Another confounding factor may be secondary flows generated by vessel bends that can contribute to transverse velocity components or further destabilize the jet, increasing TI, but this may be a small effect compared to the stenosis geometry [48].

Lovett *et al.* [17] classified carotid plaque ulcerations in terms of four categories of clinically observed shapes, which can also occur in a range of sizes. Our study addresses only the effect of one size of one shape (Type 3) of these ulcer categories. However, the effect of ulcer size and shape has been previously investigated in a moderate 50% carotid artery stenosis geometry; whereas ulcer shape had limited effect, increasing ulcer size had the expected result of progressively augmenting distal TI [19].

While the rigidity of the phantoms used in this study enabled desired vessel geometries with small well-defined features to be reproduced accurately and faithfully, the associated compromise is that they did not model the effects of vessel compliance observed in human vasculature [78, 79]. However, it has been shown that there is a tendency for vessel wall motion to decrease considerably with age and disease [80, 81], where vessels in an elderly population exhibit a distension of only 5%, as opposed to 12 – 14% change in vessel diameter in a young population [82]. Computational flow simulations [83, 84] and fluid dynamics derivations [85, 86] have demonstrated that this small degree of vessel compliance has little effect on the global characteristics of flow behaviour in the carotid stenosis, particularly when compared to effects of flow and anatomical variation [87]. Moreover, by employing matched-model geometries for this study, where all parameters are maintained except for the plaque morphology at the level of the apex on the non-flow divider wall, the effects of ulceration can be isolated.

Due to the sample volume limitations of medical DUS, our described technique does not enable the characterization of flow within the ulcer or distinction between turbulence and coherent disturbances in the downstream flow field. However, the use of a clinical diagnostic system makes our measurements in the distal ICA more representative of clinically available data. Further studies in basic research, using experimental techniques (e.g. particle imaging velocimetry (PIV)) or numerical methods

(e.g. computational fluid dynamics (CFD)), could be used to improve the understanding of flow within the ulcer and the initiation of flow disturbances downstream; CFD analysis will be the topic of Chapter 5.

A growing number of studies have emphasized that patients with a moderate grade of internal carotid artery stenosis should be evaluated on the basis of plaque features that indicate vulnerability to ischemic events and low intraoperative risk [88, 89]. Evidence from multi-centre prospective clinical trials has shown a modest overall benefit from CEA even in an indiscriminate group of patients with 50 – 69% stenosis. Yet, this does not consider that patient subgroups with irregular plaque surface morphology are associated with a two- to three-fold increase in stroke risk [6, 10], elevating the two-year risk of an ulcerated moderate grade stenosis to a level comparable or higher than that of a 70% stenosis with a smooth plaque surface [8]. It is clear that DUS examinations of the carotid artery have the potential to be improved by incorporating an assessment of the risk represented by plaque ulceration, as an adjunct to current protocols used solely to identify carotid artery vessels with severe ICA narrowing. Measurements of post-stenotic TI obtained with minor modifications to the current DUS examination protocol could provide a non-invasive method for the evaluation of carotid plaque surface morphology, and may be of particular benefit for patients with moderate grade stenosis. Distal TI, indicating elevated distal flow disturbances, increased with both ulceration and stenosis severity, in a manner reflecting their interrelationship as two major independent risk factors for ischemic stroke. As hemodynamic conditions of disturbed aberrant flow are known to promote shear-induced thromboembolic activity [26], it is possible that the level of post-stenotic TI may also provide functional information regarding an overall indication of ischemic risk.

4.5 Conclusion

By employing matched models *in vitro*, we have determined a two-curve relationship of distal TI with ulceration and varying grade of stenosis in the carotid artery bifurcation as measured using a clinical DUS system. We report statistically significant elevations in distal TI due to ulceration in the mild and moderate stenosis, and with increasing stenosis grade in both the ulcerated and non-ulcerated series ($P < 0.001$). The parameter TI may provide a diagnostic index to assess the condition of ulceration in the mild and moderate carotid artery stenosis using clinical DUS, provided that reliable measurements can be obtained within a vessel region within the post-stenotic ICA.

4.6 References

1. Grant EG, Benson CB, Moneta GL, Alexandrov AV, Baker JD, *et al.* (2003) Carotid artery stenosis: grayscale and Doppler ultrasound diagnosis--Society of Radiologists in Ultrasound consensus conference. *Ultrasound Q* 19:190-198.
2. Hankey GJ (1999) Stroke prediction and prevention by carotid endarterectomy: keep an eye on the doughnut and not just the hole. *Cerebrovasc Dis* 9:345-350.
3. Wardlaw JM, Chappell FM, Best JJ, Wartolowska K and Berry E (2006) Non-invasive imaging compared with intra-arterial angiography in the diagnosis of symptomatic carotid stenosis: a meta-analysis. *Lancet* 367:1503-1512.
4. Chassin MR (1998) Appropriate use of carotid endarterectomy. *N Engl J Med* 339:1468-1471.

5. Coccheri S (2003) Asymptomatic carotid stenosis: natural history and therapeutic implications. *Pathophysiol Haemost Thromb* 33:298-301.
6. Eliasziw M, Streifler JY, Fox AJ, Hachinski VC, Ferguson GG, *et al.* (1994) Significance of plaque ulceration in symptomatic patients with high-grade carotid stenosis. North American Symptomatic Carotid Endarterectomy Trial. *Stroke* 25:304-308.
7. Handa N, Matsumoto M, Maeda H, Hougaku H and Kamada T (1995) Ischemic stroke events and carotid atherosclerosis. Results of the Osaka Follow-up Study for Ultrasonographic Assessment of Carotid Atherosclerosis (the OSACA Study). *Stroke* 26:1781-1786.
8. Rothwell PM, Gibson R and Warlow CP (2000) Interrelation between plaque surface morphology and degree of stenosis on carotid angiograms and the risk of ischemic stroke in patients with symptomatic carotid stenosis. On behalf of the European Carotid Surgery Trialists' Collaborative Group. *Stroke* 31:615-621.
9. Fisher M, Paganini-Hill A, Martin A, Cosgrove M, Toole JF, *et al.* (2005) Carotid plaque pathology: thrombosis, ulceration, and stroke pathogenesis. *Stroke* 36:253-257.
10. Prabhakaran S, Rundek T, Ramas R, Elkind MS, Paik MC, *et al.* (2006) Carotid plaque surface irregularity predicts ischemic stroke: the northern Manhattan study. *Stroke* 37:2696-2701.
11. Rothwell PM, Gutnikov SA and Warlow CP (2003) Reanalysis of the final results of the European Carotid Surgery Trial. *Stroke* 34:514-523.
12. AbuRahma AF, Kyer PD, 3rd, Robinson PA and Hannay RS (1998) The correlation of ultrasonic carotid plaque morphology and carotid plaque hemorrhage: clinical implications. *Surgery* 124:721-726; discussion 726-728.

13. Arapoglou B, Kondi-Pafiti A, Katsenis K and Dimakakos P (1994) The clinical significance of carotid plaque haemorrhage. *Int Angiol* 13:323-326.
14. Imparato AM, Riles TS, Mintzer R and Baumann FG (1983) The importance of hemorrhage in the relationship between gross morphologic characteristics and cerebral symptoms in 376 carotid artery plaques. *Ann Surg* 197:195-203.
15. Sitzer M, Muller W, Siebler M, Hort W, Kniemeyer HW, *et al.* (1995) Plaque ulceration and lumen thrombus are the main sources of cerebral microemboli in high-grade internal carotid artery stenosis. *Stroke* 26:1231-1233.
16. Hennerici MG (2004) The unstable plaque. *Cerebrovasc Dis* 17 Suppl 3:17-22.
17. Lovett JK, Gallagher PJ, Hands LJ, Walton J and Rothwell PM (2004) Histological correlates of carotid plaque surface morphology on lumen contrast imaging. *Circulation* 110:2190-2197.
18. Orlandi G, Parenti G, Landucci Pellegrini L, Sartucci F, Paoli C, *et al.* (1999) Plaque surface and microembolic signals in moderate carotid stenosis. *Ital J Neurol Sci* 20:179-182.
19. Wong EY, Nikolov HN, Thorne ML, Poepping TL, Rankin RN, *et al.* (2009) Clinical Doppler ultrasound for the assessment of plaque ulceration in the stenosed carotid bifurcation by detection of distal turbulence intensity: a matched model study. *Eur Radiol* 19:2739-2749.
20. Mustard JF, Murphy EA, Rowsell HC and Downie HG (1962) Factors influencing thrombus formation in vivo. *Am J Med* 33:621-647.

21. Mustard JF and Packham MA (1970) Thromboembolism: manifestation of the response of blood to injury. *Circulation* 42:1-21.
22. Goldsmith HL (1970) Motion of particles in a flowing stream. *Thromb Diath Haemorrhag Suppl* 40:91-110.
23. Smith RL, Blick FB, Coalson J and Stein PD (1972) Thrombus production by turbulence. *J Applied Physiology* 32:261-264.
24. Holme PA, Orvim U, Hamers MJ, Solum NO, Brosstad FR, *et al.* (1997) Shear-induced platelet activation and platelet microparticle formation at blood flow conditions as in arteries with a severe stenosis. *Arterioscler Thromb Vasc Biol* 17:646-653.
25. Sakariassen KS, Holme PA, Orvim U, Barstad RM, Solum NO, *et al.* (1998) Shear-induced platelet activation and platelet microparticle formation in native human blood. *Thromb Res* 92:S33-41.
26. Nesbitt WS, Westein E, Tovar-Lopez FJ, Tolouei E, Mitchell A, *et al.* (2009) A shear gradient-dependent platelet aggregation mechanism drives thrombus formation. *Nat Med* 15:665-673.
27. Stein PD and Sabbah HN (1974) Measured turbulence and its effect on thrombus formation. *Circ Res* 35:608-614.
28. Cloutier G and Shung KK (1993) Study of red cell aggregation in pulsatile flow from ultrasonic Doppler power measurements. *Biorheology* 30:443-461.
29. Fox AJ (1993) How to measure carotid stenosis. *Radiology* 186:316-318.
30. Smith RF, Rutt BK, Fox AJ, Rankin RN and Holdsworth DW (1996) Geometric characterization of stenosed human carotid arteries. *Acad Radiol* 3:898-911.

31. Wong EY, Thorne ML, Nikolov HN, Poepping TL and Holdsworth DW (2008) Doppler ultrasound compatible plastic material for use in rigid flow models. *Ultrasound Med Biol* 34:1846-1856.
32. de Weert TT, Cretier S, Groen HC, Homburg P, Cakir H, *et al.* (2009) Atherosclerotic plaque surface morphology in the carotid bifurcation assessed with multidetector computed tomography angiography. *Stroke* 40:1334-1340.
33. Ramnarine KV, Nassiri DK, Hoskins PR and Lubbers J (1998) Validation of a new blood-mimicking fluid for use in Doppler flow test objects. *Ultrasound Med Biol* 24:451-459.
34. Thorne ML, Poepping TL, Rankin RN, Steinman DA and Holdsworth DW (2008) Use of an ultrasound blood-mimicking fluid for Doppler investigations of turbulence in vitro. *Ultrasound Med Biol* 34:1163-1173.
35. Holdsworth DW, Rickey DW, Drangova M, Miller DJ and Fenster A (1991) Computer-controlled positive displacement pump for physiological flow simulation. *Med Biol Eng Comput* 29:565-570.
36. Frayne R, Holdsworth DW, Gowman LM, Rickey DW, Drangova M, *et al.* (1992) Computer-controlled flow simulator for MR flow studies. *J Magn Reson Imaging* 2:605-612.
37. Poepping TL, Nikolov HN, Rankin RN, Lee M and Holdsworth DW (2002) An in vitro system for Doppler ultrasound flow studies in the stenosed carotid artery bifurcation. *Ultrasound Med Biol* 28:495-506.
38. Hinze JO (1959) *Turbulence. An Introduction to its Mechanism and Theory*. McGraw-Hill, New York.
39. Yongchareon W and Young DF (1979) Initiation of turbulence in models of arterial stenoses. *Journal of Biomechanics* 12:185-196.

40. Ojha M, Johnston KW, Cobbold RS and Hummel RL (1989) Potential limitations of center-line pulsed Doppler recordings: an in vitro flow visualization study. *J Vasc Surg* 9:515-520.
41. Tamura T and Fronek A (1990) Detection of moving flow separation in pulsatile flow and the degree of stenosis by power of Doppler shift signals. *Circ Res* 67:166-174.
42. Loree HM, Kamm RD, Atkinson CM and Lee RT (1991) Turbulent pressure fluctuations on surface of model vascular stenoses. *Am J Physiol* 261:H644-H650.
43. Sacks AH, Tickner EG and Macdonald IB (1971) Criteria for the onset of vascular murmurs. *Circ Res* 29:249-256.
44. Hutchison KJ and Karpinski E (1985) In vivo demonstration of flow recirculation and turbulence downstream of graded stenoses in canine arteries. *J Biomech* 18:285-296.
45. Hjortdal JO, Pedersen EM, Hjortdal VE, Hasenkam JM, Nygaard H, *et al.* (1991) Velocity field studies at surgically imposed arterial stenoses on the abdominal aorta in pigs. *J Biomech* 24:1081-1093.
46. Nygaard H, Hasenkam JM, Pedersen EM, Kim WY and Paulsen PK (1994) A new perivascular multi-element pulsed Doppler ultrasound system for in vivo studies of velocity fields and turbulent stresses in large vessels. *Med Biol Eng Comput* 32:55-62.
47. Bendick PJ and Glover JL (1982) Detection of subcritical stenoses by Doppler spectrum analysis. *Surgery* 91:707-711.

48. Solzbach U, Wollschlager H, Zeiher A and Just H (1987) Effect of stenotic geometry on flow behaviour across stenotic models. *Med Biol Eng Comput* 25:543-550.
49. Young DF (1979) Fluid mechanics of arterial stenoses. *J Biomech Eng* 101:157-175.
50. Ojha M, Cobbold RSC, Johnston KW and Hummel RL (1989) Pulsatile flow through constricted tubes: an experimental investigation using photochromic tracer methods. *J Fluid Mech* 203:173-197.
51. Ahmed SA and Giddens DP (1984) Pulsatile poststenotic flow studies with laser Doppler anemometry. *J Biomech* 17:695-705.
52. Talukder N, Fulenwider JT, Mabon RF and Giddens DP (1986) Poststenotic flow disturbance in the dog aorta as measured with pulsed Doppler ultrasound. *J Biomech Eng* 108:259-265.
53. Ku DN (1997) Blood flow in arteries. *Annu Rev Fluid Mech* 29:399-434.
54. Ku DN, Klafta JM, Gewertz BL and Zarins CK (1987) The contribution of valves to saphenous vein graft resistance. *J Vasc Surg* 6:274-279.
55. Young DF and Tsai FY (1973) Flow characteristics in models of arterial stenoses. II. Unsteady flow. *J Biomech* 6:547-559.
56. Deshpande MD, Giddens DP and Mabon RF (1976) Steady laminar flow through modelled vascular stenoses. *J Biomech* 9:165-174.
57. Imbesi SG and Kerber CW (1998) Why do ulcerated atherosclerotic carotid artery plaques embolize? A flow dynamics study. *AJNR Am J Neuroradiol* 19:761-766.

58. Birchall D, Zaman A, Hacker J, Davies G and Mendelow D (2006) Analysis of haemodynamic disturbance in the atherosclerotic carotid artery using computational fluid dynamics. *Eur Radiol* 16:1074-1083.
59. Kaluzynski K, Lesniak B, Mikolajczyk K and Liepsch D (1997) Analysis of ultrasonic Doppler velocity data obtained in models of stenosed carotid bifurcations with irregular lesion surface. *Technol Health Care* 5:199-206.
60. Lesniak B, Kaluzynski K, Liepsch D and Palko T (2002) The discrimination of stenosed carotid bifurcation models with smooth and irregular plaque surface. Part I. Laser and ultrasonic Doppler flow studies. *Med Eng Phys* 24:309-318.
61. Lesniak B, Kaluzynski K, Liepsch D and Palko T (2002) The discrimination of stenosed carotid bifurcation models with smooth and irregular plaque surface. Part II. The multivariate statistical analysis of ultrasonic Doppler velocity data. *Med Eng Phys* 24:319-323.
62. Dunmire B, Pagel G, Beach KW and Labs KH (2001) Post stenotic flow disturbances in a steady flow model. In: Proceedings of the SPIE, San Diego, pp 502-513.
63. Hutchison KJ (1993) Doppler ultrasound spectral shape in the poststenotic velocity field. *Ultrasound Med Biol* 19:649-659.
64. Morin JF, Johnston KW and Law YF (1987) In vitro study of continuous wave Doppler spectral changes resulting from stenoses and bulbs. *Ultrasound Med Biol* 13:5-13.
65. Sigel B, Gibson RJ, Amatneek KV, Felix WR, Jr., Edelstein AL, *et al.* (1970) A doppler ultrasound method for distinguishing laminar from turbulent flow. A preliminary report. *J Surg Res* 10:221-224.

66. Shung KK, Cloutier G and Lim CC (1992) The effects of hematocrit, shear rate, and turbulence on ultrasonic Doppler spectrum from blood. *IEEE Trans Biomed Eng* 39:462-469.
67. Wu SJ, Shung KK and Brasseur JG (1998) In situ measurements of Doppler power vs. flow turbulence intensity in red cell suspensions. *Ultrasound Med Biol* 24:1009-1021.
68. Bascom PA, Cobbold RS, Routh HF and Johnston KW (1993) On the Doppler signal from a steady flow asymmetrical stenosis model: effects of turbulence. *Ultrasound Med Biol* 19:197-210.
69. Bascom PA, Johnston KW, Cobbold RS and Ojha M (1997) Relation of the flow field distal to a moderate stenosis to the Doppler power. *Ultrasound Med Biol* 23:25-39.
70. Evans DH and McDicken WN (2000) *Doppler Ultrasound: Physics, Instrumentation and Signal Processing*. Wiley, Chichester.
71. Cloutier G, Allard L and Durand LG (1996) Characterization of blood flow turbulence with pulsed-wave and power Doppler ultrasound imaging. *J Biomech Eng* 118:318-325.
72. Casty M and Giddens DP (1984) 25 + 1 channel pulsed ultrasound Doppler velocity meter for quantitative flow measurements and turbulence analysis. *Ultrasound Med Biol* 10:161-172.
73. Isaaq K, Bruntz JF, Da Costa A, Winninger D, Cerisier A, *et al.* (2003) Noninvasive quantitation of blood flow turbulence in patients with aortic valve disease using online digital computer analysis of Doppler velocity data. *J Am Soc Echocardiogr* 16:965-974.

74. Thorne ML, Rankin RN, Steinman DA and Holdsworth DW (2010) In vivo Doppler ultrasound quantification of turbulence intensity using a high-pass frequency filter method. *Ultrasound Med Biol* 36:761-771.
75. Thorne ML, Poepping TL, Nikolov HN, Rankin RN, Steinman DA, *et al.* (2009) In vitro Doppler ultrasound investigation of turbulence intensity in pulsatile flow with simulated cardiac variability. *Ultrasound Med Biol* 35:120-128.
76. Haberman S and Friedman Z (1998) Multigated simultaneous spectral Doppler imaging: a new ultrasound modality. *Obstet Gynecol* 92:299-302.
77. Tortoli P, Bassi L, Boni E, Dallai A, Guidi F, *et al.* (2009) ULA-OP: an advanced open platform for ultrasound research. *IEEE Trans Ultrason Ferroelectr Freq Control* 56:2207-2216.
78. Giannattasio C and Mancia G (2002) Arterial distensibility in humans. Modulating mechanisms, alterations in diseases and effects of treatment. *J Hypertens* 20:1889-1899.
79. Benetos A, Waeber B, Izzo J, Mitchell G, Resnick L, *et al.* (2002) Influence of age, risk factors, and cardiovascular and renal disease on arterial stiffness: clinical applications. *Am J Hypertens* 15:1101-1108.
80. Van Bortel LM and Spek JJ (1998) Influence of aging on arterial compliance. *J Hum Hypertens* 12:583-586.
81. Mancia G, Giannattasio C and Grassi G (1998) Arterial distensibility in cardiovascular diseases. *J Nephrol* 11:284-288.
82. Hansen F, Mangell P, Sonesson B and Lanne T (1995) Diameter and compliance in the human common carotid artery--variations with age and sex. *Ultrasound Med Biol* 21:1-9.

83. Perktold K and Rappitsch G (1995) Computer simulation of local blood flow and vessel mechanics in a compliant carotid artery bifurcation model. *J Biomech* 28:845-856.
84. Zhao SZ, Xu XY, Hughes AD, Thom SA, Stanton AV, *et al.* (2000) Blood flow and vessel mechanics in a physiologically realistic model of a human carotid arterial bifurcation. *J Biomech* 33:975-984.
85. Benson TJ, Nerem RM and Pedley TJ (1980) Assessment of wall shear stress in arteries, applied to the coronary circulation. *Cardiovasc Res* 14:568-576.
86. Dewey CF (1979) Fluid mechanics of arterial flow. In: Wolf W and Werthessen NT (ed) *Dynamics of Arterial Flow*, 1st edn. Plenum Press, New York, pp 55-103.
87. Lee KW and Xu XY (2002) Modelling of flow and wall behaviour in a mildly stenosed tube. *Med Eng Phys* 24:575-586.
88. Rundek T (2007) Beyond percent stenosis: carotid plaque surface irregularity and risk of stroke. *Int J Stroke* 2:169-171.
89. Ahmed RM, Harris JP, Anderson CS, Makeham V and Halmagyi GM (2010) Carotid endarterectomy for symptomatic, but "haemodynamically insignificant" carotid stenosis. *Eur J Vasc Endovasc Surg* 40:475-482.

Chapter 5

Numerical Evaluation of Ulceration on Simulated Blood-Particle Shear Exposure and Turbulence Intensity Index in the Stenosed Bifurcation[†]

5.1 Introduction

Carotid artery atherosclerosis is frequently the source of pathological thrombosis leading to cerebral ischemic stroke. The severity of carotid artery stenosis has been shown to correlate with the long-term benefit of patient carotid endarterectomy, but has limited specificity and sensitivity as the sole indicator for predicting the true risk of carotid embolic stroke [1]. This indicates that other factors of carotid artery disease are conducive to enhanced thrombogenic potential. In addition to the degree of internal carotid artery (ICA) stenosis, the multi-centre North American Symptomatic Carotid Endarterectomy Trial (NASCET) identified one other angiographic parameter – the presence of carotid plaque ulceration – as an independent risk factor for stroke [2]. Moreover, carotid plaque surface ulceration has been imputed as a cause of thrombosis and a source of cerebral embolisms [3, 4]. The mechanisms that link ulceration to increased thrombogenicity and risk of stroke, however, are still not understood.

[†] Portions of this chapter have been published in the *Proceedings of SPIE Medical Imaging: Visualization, Image-guided Procedures and Modeling*, Orlando, Florida, February 2009 (paper no. 7261-66) in an article entitled “Numerical analysis of the hemodynamic effect of plaque ulceration in the stenotic carotid artery bifurcation” by E. Y. Wong, J. S. Milner, T. L. Poepping and D. W. Holdsworth and in the *Proceedings of the IEEE International Ultrasonics Symposium: Medical Ultrasonics: Blood Flow Measurement*, Beijing, China, November 2008 (paper no. 451) in an article entitled “Doppler ultrasound and numerical analysis for the assessment of hemodynamic disturbances in ulcerated carotid arteries” by E. Y. Wong, J. S. Milner, M. L. Thorne, H. N. Nikolov, T. L. Poepping, R. N. Rankin, and D. W. Holdsworth.

Recently, experimental *in vitro* flow studies using Doppler ultrasound (DUS) have demonstrated that carotid plaque ulcerations induce post-stenotic flow disturbances in the moderately stenosed carotid bifurcation (Chapter 3) [5]. Helical and disturbed flow have also been observed in the ulcerated carotid artery geometry using numerical and dye slipstream visualization techniques [6, 7]. It has long been known that mechanical factors arising from local changes in intravascular fluid dynamics can influence thrombus formation. Specifically, fluid shear stress is known to have profound effects on blood particles [8-12]; in particular, abnormally high shear stresses can induce activation of blood platelets, even in the absence of injury to the vascular wall [13, 14].

There is recent compelling evidence that mechanosensory platelet activation, resulting from fluid shear stress, is the principal mechanism for triggering and sustaining platelet activation and aggregation, thereby in determining thrombus growth and stability [8]. Shear stress histories of blood platelets are now known to play a crucial role in the risk of thromboembolic stroke, and can even influence the biochemical constitution of the resultant thrombi [15, 16]. Several models have been proposed for calculating platelet activation potential based on shear exposure, and can be used to evaluate the physiological impact of hemodynamics changes due to arterial lumen geometry [17-20]. Thus, there is an impetus to evaluate the shear stress histories of blood platelets in the carotid artery bifurcation with ulceration.

While conventional clinical DUS is the primary technique for evaluating blood flow *in vivo* – and may provide relevant diagnostic information related to blood-flow velocities distal to ulceration – it has inadequate spatial resolution to obtain accurate shear stress information [21, 22]. Computational fluid dynamics (CFD) can provide high resolution, time-resolved three-dimensional (3-D) flow information in vascular

geometries, allowing for the determination of local shear stress. Simulated particle tracking with CFD allows for the calculation of dynamic path-dependent shear exposure histories, as well as local residence times [23, 24]. CFD has been shown to be valuable in characterizing flow dynamics in the stenosed carotid bifurcation, but has not previously been used to evaluate pathline-dependent platelet activation parameters in the ulcerated atherosclerotic carotid artery.

Furthermore, by coupling CFD pre-computed flow solutions with numerical simulations of DUS, CFD has been shown to be a valuable and practical tool to develop and test DUS applications. In particular, numerical simulations of DUS have been developed for use as teaching and training tools for sonographers [25] and to compare the performance of different ultrasound flow imaging methods [26]. Such an approach is of improving palatability to researchers due to the growing accessibility of commercially and publicly available CFD packages. Here, we investigate the use of CFD for simulating the DUS spectral parameter turbulence intensity (TI), which has been shown to be a potential DUS diagnostic indicator for plaque surface ulceration in the stenosed carotid artery bifurcation. Using our *in vitro* flow facility, we have been able to demonstrate that a proximally located ulceration of various shapes and sizes can produce elevated levels of TI in the downstream vessel region (Chapter 3); however, the numerical evaluation of TI would provide a means of assessing the effect of various vessel and ulcer geometries, without the requirement of a specialized experimental flow setup. A direct CFD comparison of the detailed time-resolved flow patterns in the ulcerated and non-ulcerated geometries may also further the understanding of the role of plaque ulceration in the underlying mechanism of flow disruption and cycle-to-cycle velocity fluctuations previously observed.

We studied the effect of a physiologically relevant ulceration on the time-varying 3-D hemodynamics in a moderately stenosed carotid artery

bifurcation using CFD, with comparison to experimental DUS blood-flow velocities and spectral TI. We present a direct, quantitative comparison of shear exposure parameters along simulated particle tracks, to evaluate the effect of ulceration on thromboembolic potential in the post-stenotic carotid artery.

5.2 Methods

5.2.1 Model geometries

The carotid artery vascular geometries used in this study were ulcerated and non-ulcerated models based on the same anthropomorphic idealized geometric representation of a 50% eccentrically stenosed carotid bifurcation, as defined under NASCET criteria, with a common carotid artery (CCA) diameter of 8 mm [27, 28], for which post-stenotic flow disturbances have previously been characterized *in vitro* using DUS velocity-based parameters (Chapters 3 and 4) [5].

In the ulcerated model, a distally pointing ellipsoidal ulceration geometry (major axis 7.37 mm, minor axes 2.95 mm) was incorporated into the baseline geometry, with the centre intersecting the main lumen-wall boundary and tilted 45° relative to the lumen centerline at the level of the bifurcation apex. The selected ulcer geometry was determined by our previous *in vitro* characterizations of the effect of ulcer shape to produce the highest distal TI [5], and represents a clinically realistic Type 3 ulceration [29].

A pair of ulcerated and non-ulcerated DUS-compatible *in vitro* flow phantoms were fabricated using our direct-machining technique, as detailed in Chapter 2 [30]. The geometric surface model representing the lumen boundaries of the non-ulcerated model used for CFD was generated from the computer-aided design model, while the lumen boundaries of the ulcerated

model were determined directly from the *in vitro* flow phantom using image-based modelling techniques, to ensure that the geometry of ulceration matched that of the fabricated DUS flow phantom. The micro-computed tomography (micro-CT) imaging protocol and the segmentation technique used to generate a geometric surface model directly from the 3-D image data are described previously in Chapter 2 [5].

Discretization of the spatial volumes enclosed by the resultant ulcerated and non-ulcerated surface models, forming their respective fluid domains, was carried out via commercial mesh generation software (ICEM CFD, ANSYS Inc., Canonsburg, PA, USA) using quadratic (second-order) tetrahedral elements. Meshing criteria specified a maximum spacing of 0.40 mm in the well-defined laminar flow regions of the CCA inlet extension and ECA outlet extension, and a maximum spacing of 0.20 mm in the critical region encompassing the bifurcation, ulceration, carotid bulb and downstream region of complex flow in the ICA branch. A further tetrahedral subdivision step was prescribed in the stenosis neck and distal attachment of the ulcer, in order to better resolve high velocity gradients, as well as the narrow geometry and high curvature in those areas. The resultant unstructured grid for the ulcerated case contained 763,276 nodes and 538,065 second-order tetrahedral elements (equivalent to 4,304,520 linear tetrahedral elements).

Post-hoc analysis of the mesh demonstrated minimum and median internodal spacings of 0.06 mm and 0.20 mm, respectively (or normalized values of $0.015R$ and $0.050R$, where R is the CCA inlet radius in mm), which is consistent with values found in other studies [7, 31, 32]. Discretization of the non-ulcerated model followed the same conventions described above and is overlaid on the ulcerated CT image volume in Fig. 5.1 to exhibit the matched-model geometries. A grid refinement study was performed for the ulcerated model to determine convergence of the velocity fields. Figure D.1 in Appendix D shows the differences in computed L_2 norms for each of the meshes in the grid independence analysis. Mesh independence was considered achieved when the difference in L_2 relative error norms for successive mesh refinements was less than 2% at twice-mean flow rate.

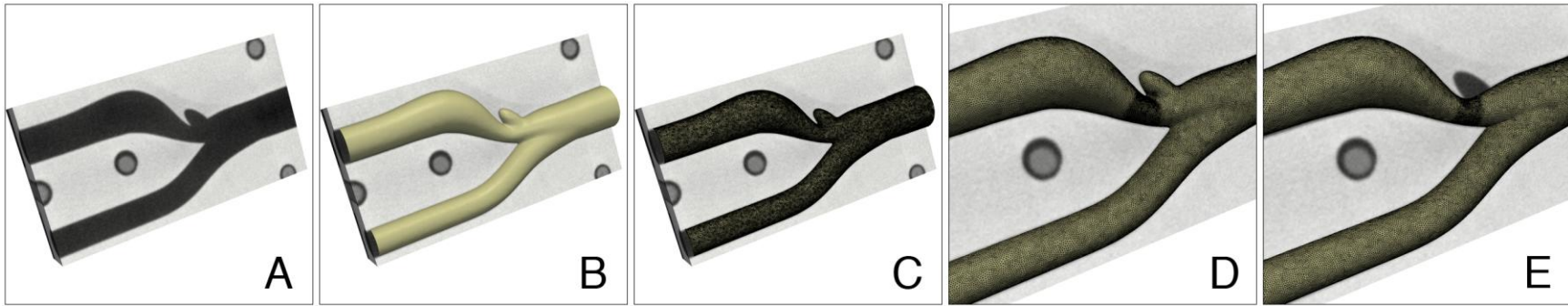


Figure 5.1: 3-D geometry of the 50% eccentrically stenosed carotid bifurcation with ellipsoidal ulcer used in this study, showing (a) the 3-D micro-CT image volume of the original DUS phantom, and the corresponding (b) extracted geometric surface model and (c) surface mesh. The *two right panels* show the finite element mesh of (d) the ulcerated and (e) the non-ulcerated models (overlaid on the image data of the ulcerated model for comparison) used in this study, with mid-side nodes tessellated in order to illustrate the nodal distribution.

5.2.2 Doppler ultrasound *in vitro* flow measurements

DUS flow measurements were performed in the flow phantoms, under realistic physiological flow conditions, using a previously described *in vitro* setup [33]. Acquisition protocols and post-processing spectral analysis were as detailed in Chapters 3 and 4 [5]. In brief, a computer-controlled pump provided the inlet of the flow phantom with a realistic pulsatile carotid flow-rate waveform, with a cycle length of 0.92 s, and peak and mean flow rates of 23.46 mL s^{-1} and 6.00 mL s^{-1} , respectively. Downstream flow resistors provided a physiologically realistic ICA:ECA flow split of 65:35 to the phantom. Cardiac-gated measurements were acquired using a conventional clinical Doppler ultrasound system (Ultramark 9, Philips-ATL, Bothell, WA, USA), with a 4.0 MHz transducer (L7-4 Philips-ATL) and a Doppler angle of 60° , using a pulse-repetition frequency of 18,519 Hz, sample volume of 1-mm axial length, and a wall filter of 50 Hz. Ensemble-averaged mean velocity and TI were defined as in Chapters 3 and 4, with ensemble-averaged mean velocity (\bar{v}_{mean}) calculated from the periodic ensemble average of ten complete successive cardiac cycles, and TI determined as the root-mean-square (RMS) deviation in spectral mean velocity about the ensemble-averaged mean velocity, \bar{v}_{mean} , at a given time point in the cardiac cycle [33].

5.2.3 CFD simulations

To obtain matching flow boundary conditions for the CFD simulations, the resultant DUS experimental mean flow-rate waveforms at the CCA inlet and ECA outlet were measured using an electromagnetic flow meter [33]. Corresponding fully developed pulsatile carotid velocity waveforms were imposed at the CCA inlet and ECA outlet, while traction-free boundary conditions were applied at the ICA outlet, producing the desired ICA:ECA flow division of 65:35, consistent with DUS experimental conditions. No-slip

boundary conditions were imposed at the walls of the vessel models. Rigid walls and a constant kinematic viscosity of 4.01 cS were assumed to match DUS experimental conditions, which resulted in mean and peak Reynolds numbers of 236 and 923 respectively, and a Womersley number of 5.25, at the CCA inlet.

In order to adequately resolve the input pulsatile flow waveform, a temporal discretization of 9,600 equally spaced time steps per cardiac cycle was used, ensuring that sufficient velocity field solutions were generated. The solution was carried out for 13 cardiac cycles using a well-validated, in-house finite element CFD solver [34-36], where three cardiac cycles were required to damp initial transients due to zero-velocity initial conditions. The CFD solver utilized a generalized time-splitting approach to solve the incompressible Navier-Stokes equations. The algorithm used a point-wise characteristic integration of the convective terms, and a pressure correction solver for the remaining generalized Stokes problem [36].

5.2.4 CFD simulated turbulence intensity (TI)

In order to determine whether CFD has the ability to capture realistic cycle-to-cycle velocity fluctuations such as are observed empirically in DUS flow experiments, TI results from experimental DUS and CFD were compared. To perform a valid comparison of the CFD-computed instantaneous point velocities to the velocities measured by DUS, the computed CFD velocity field in each of the models was interrogated at locations across the central plane using a 1 mm \times 1 mm grid, to match the acquisition grid used in the DUS experiments. A spherical sample volume with Gaussian power distribution and 1,000 sampling points matching DUS sampling characteristics was used [25]. Each sampled velocity was converted to an angle-corrected velocity corresponding to measurements at a Doppler angle of 60°. Details of this simulation are described by Khoshniat *et al.* [25].

Intrinsic spectral broadening was simulated by convolving each of the point velocities with a semi-empirical broadening function. A velocity-based threshold filter with a cutoff velocity of 2 cm s^{-1} was applied to account for the DUS wall-thump filter. Simulated sample-volume based TI at each location in the sampling grid was calculated as the RMS deviation of the sample-volume based mean velocity about the ensemble-averaged mean velocity from ten cardiac cycles. Simulated TI values from 24 sites in a region of interest (ROI) in the distal ICA were calculated. The ROI consisted of a set of 24 interrogation points with 1-mm isotropic spacing located within a 6-mm diameter circular grid, centered at just over 2 CCA diameters (17.5 mm) distal to the apex of the bifurcation, corresponding to the previously characterized ROI described in Chapter 4. In addition, RMS deviations in velocity based on instantaneous nodal velocities were extracted from the same time point within an ensemble of ten cardiac cycles, on a per node basis. The velocity-field solutions from the last ten consecutive cardiac cycles (cycles 4 to 13) were used for calculations of both simulated sample-volume based TI and RMS instantaneous velocities.

5.2.5 Virtual particle tracking

To simulate the Lagrangian motion of blood particles, such as platelets, through the 3-D pulsatile fluid domain, simulated particle trajectories were calculated from the CFD-computed velocity field, as detailed by Steinman [37]. Velocity data from the seventh computed cardiac cycle were used for particle tracking. Tracks were initialized by seeding particles near the inlet plane of the CCA. The particles were assumed to be massless, neutrally buoyant, non-diffusive tracers that move with the local velocity field. Particle trajectories were then computed by integrating the pre-computed time-varying velocity field, using a fourth-order Runge-Kutta method with adaptive time-stepping [37]. To ensure accuracy and minimize cumulative errors in calculated trajectories, the maximum distance travelled between

track steps was restricted to be less than 0.016 mm. Pathline simulations were continued until either the particle exited the flow domain, or encountered a local velocity of less than 1×10^{-6} cm s⁻¹ due to proximity to the zero-velocity wall conditions.

For calculations of the frequency distributions of path-based parameters, over 250,000 particles were seeded with a uniform random distribution spanning a transaxial plane of the 8-mm diameter CCA inlet and a uniform random temporal seeding within the cardiac cycle. For still-frame visualizations, a sparser 10×10 seeding scheme with uniform spacing at specified time points in the cardiac cycle was used, which allowed for the qualitative comparison of 3-D flow patterns between the two models. In addition, based on the results of a transaxial seeding scheme, pathlines of particles directly influenced by the ulceration were compared by visualizing particles introduced within a distance of one tenth of the CCA diameter (approximately 0.8 mm) from the outer, non-flow divider wall of the CCA on the same side as the ICA branch, specifically in the region outside the boundary of a square grid perpendicular to the central plane and a length of eight-tenths of the CCA diameter. The resultant 3-D particle tracks were colour-encoded according to the local value of various calculated parameters.

5.2.6 Assessment of particle shear stress history

Experimental studies have shown that two factors of particle shear stress exposure influence the activation and aggregation of platelets in physiological conditions: shear stress magnitude and duration of shear stress exposure. Therefore, to assess the potential effect of hemodynamic conditions on platelet activation, several parameters of shear exposure were calculated along particle pathlines.

Bluestein *et al.* [17] defined a non-thresholded parameter of cumulative shear exposure, to provide an overall parameter of shear history

or “level of activation” of platelets. Similarly, we define the non-thresholded *cumulative shear exposure*, CSE , as the summation of the product of shear stress magnitude, $\bar{\tau}_{max}$, and exposure time, Δt , for each time interval along the particle trajectory:

$$CSE = \sum_{t=0}^T (\bar{\tau}_{max} \times \Delta t) \quad (5.1)$$

Note that $\bar{\tau}_{max}$ is defined as the tensor maximum shear stress for a track step in the particle trajectory, calculated as the product of dynamic viscosity and one-half the difference between the largest and smallest eigenvalues of the rate-of-strain tensor [23]. Although this is typically called the “maximum shear stress” in fluid mechanics, we will denote this tensor maximum shear stress as $\bar{\tau}_{max}$. From this point forward, the term maximum shear stress will be reserved to refer to the peak or maximum value of $\bar{\tau}_{max}$ observed along a particle track, or the peak or maximum value of the tensor maximum shear stress in the velocity field.

Two additional parameters were derived to take into account that a minimum shear activation threshold is likely required to induce platelet activation. The *step-thresholded cumulative shear exposure*, CSE_{step} , was calculated as the cumulative product of shear exposure for track steps only when $\bar{\tau}_{max}$ exceeded a shear stress threshold of 105 dynes cm^{-2} :

$$CSE_{step} = \sum_{t=0}^T (\bar{\tau}_{max}^* \times \Delta t^*) \quad (5.2)$$

where $\bar{\tau}_{max}^*$ and Δt^* are the $\bar{\tau}_{max}$ and corresponding time step for which the critical shear stress threshold is exceeded.

In addition, the *cumulative shear exposure post-threshold*, CSE_{post} , was determined as the cumulative product of shear exposure for all time steps following the time, t^* , when $\bar{\tau}_{max}$ first exceeds 105 dynes cm^{-2} :

$$CSE_{post} = \sum_{t \geq t^*}^T (\bar{\tau}_{max} \times \Delta t) \quad (5.3)$$

In each case, $t = 0$ corresponds to the time that the particle is seeded 4.6 cm proximal to the apex of the bifurcation; T is the time the particle reaches 6.0 cm distal to the apex of the bifurcation in the axial direction; and t^* is the time when a particle first exceeds the shear stress activation threshold. An activation threshold of 105 dynes cm^{-2} was used for both CSE_{step} and CSE_{post} . This threshold value was chosen as a shear stress level of 105 dynes cm^{-2} has been shown to produce a considerable platelet activation and aggregation response in whole blood [38], and has also been used in a previous study that analyzed the effect of plaque symmetry using CFD path-dependent parameters [23].

In addition, to compare particle residence time, the total transit time was calculated as the total elapsed time that a particle remained within the fluid domain from 4.6 cm proximal to 6.0 cm distal to the apex of the bifurcation in the vessel axial direction. The transit time post-threshold was calculated as the residence time of the particle in the fluid domain following the time, t^* , when $\bar{\tau}_{max}$ first exceeds 105 dynes cm^{-2} . The maximum $\bar{\tau}_{max}$ experienced along each particle track were also calculated.

5.3 Results

5.3.1 Flow features

Figure 5.2 shows colour-encoded velocity maps comparing the axial component of velocities in the central plane of the CFD models during the downslope of systole (35 ms following peak systole) in two non-consecutive

cardiac cycles (5 and 7), along with experimental DUS spectral mean velocity measurements. As shown in Fig. 5.2, CFD velocity solutions compare well to spectral mean velocity maps obtained experimentally with DUS. Both CFD and DUS show a steeper jet angle in the ulcerated model, and more severe negative velocities in the distal portion of the main recirculation zone in the ICA bulb. Note that the shortened well-defined jet core – displaying particularly high velocities in the distal half and distal segmentation as seen in cycle 7 of the CFD solution (Fig. 5.2d) – agrees remarkably well with experimental observations from DUS (Fig. 5.2f). As expected, CFD instantaneous nodal velocities are higher than DUS ensemble-averaged spectral mean velocities, which are averaged over the sample volume and multiple cardiac cycles.

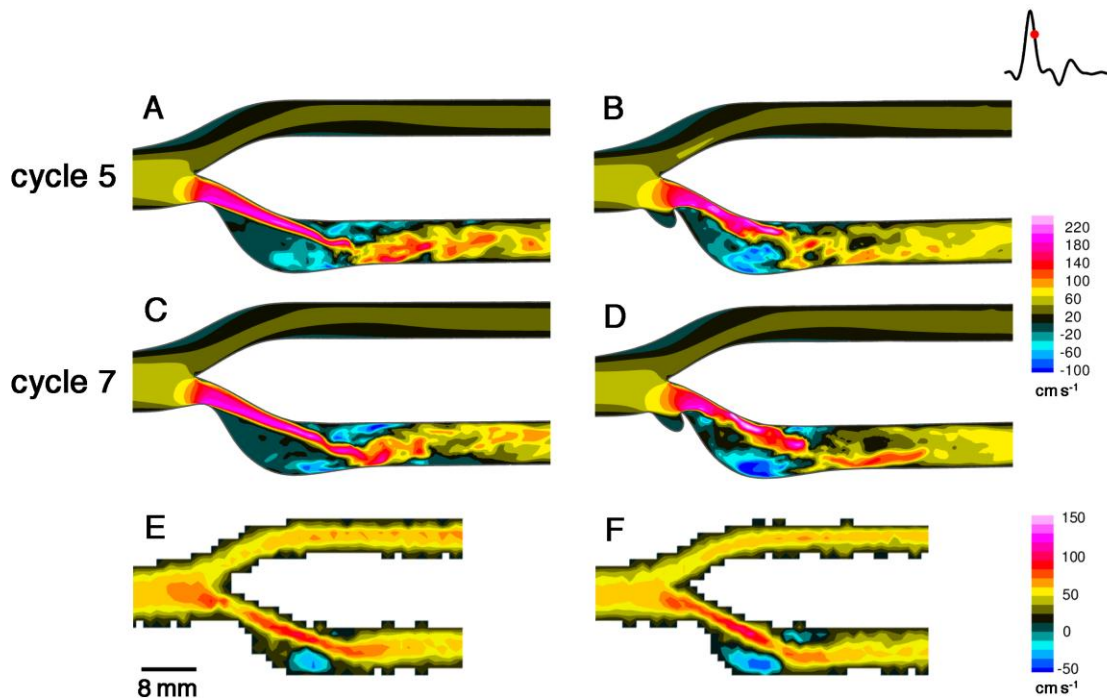


Figure 5.2: Colour-encoded maps of the CFD-computed flow field in (a, c) the non-ulcerated model and (b, d) the ulcerated model at 35 ms following peak systole for cycle 5 (*first row*) and cycle 7 (*second row*); and of (e, f) spectral mean velocities from experimental DUS measurements. The axial component of velocities in the central plane of the models is shown in the CFD velocity fields.

As seen in Fig. 5.2, the high velocity jet exhibits oscillatory motion, and in particular, the flickering of the tail end of the jet produces cycle-to-cycle variations in both models. However, while the core of the jet in the non-ulcerated model is similar between different cardiac cycles, manifesting a streamlined and coherent shape, the body of the jet in the ulcerated model displays differences along the length of the jet and a perturbative interaction with the adjacent recirculation zones. In the ulcerated model, slow, reverse flow is observed in the ulcer cavity throughout the cardiac cycle, particularly during the systolic peak beginning shortly prior to peak systole. Flow exiting the region of the ulcer cavity effects notable differences in the shape and orientation of the jet, introducing transverse velocity components and a steeper jet angle relative to the longitudinal vessel axis (approximately 25° in the ulcerated model compared to 21° in the non-ulcerated model). The altered jet characteristics lead to a greater impingement of the tail of the jet on the non-flow divider wall of the distal ICA; this can be compared to the jet in the non-ulcerated model, which glances off the lateral wall and results in a more ordered flow recirculation.

5.3.2 CFD simulated turbulence intensity (TI)

In agreement with DUS *in vitro* measurements, simulated TI and RMS velocity fluctuations from CFD are elevated in the ulcerated model relative to the non-ulcerated model in the distal ICA bulb, with highest values observed following peak systole. CFD is able to capture both the pattern and extent of TI observed with DUS (Fig. 5.3). In particular, we see that the main region of TI elevation is approximately 2 CCA diameters downstream in the non-ulcerated model, and is found more upstream, only 1.5 CCA diameters downstream from the apex of the bifurcation, in the ulcerated model (Fig. 5.3). Both CFD and DUS show two hotspots of maximally elevated TI in

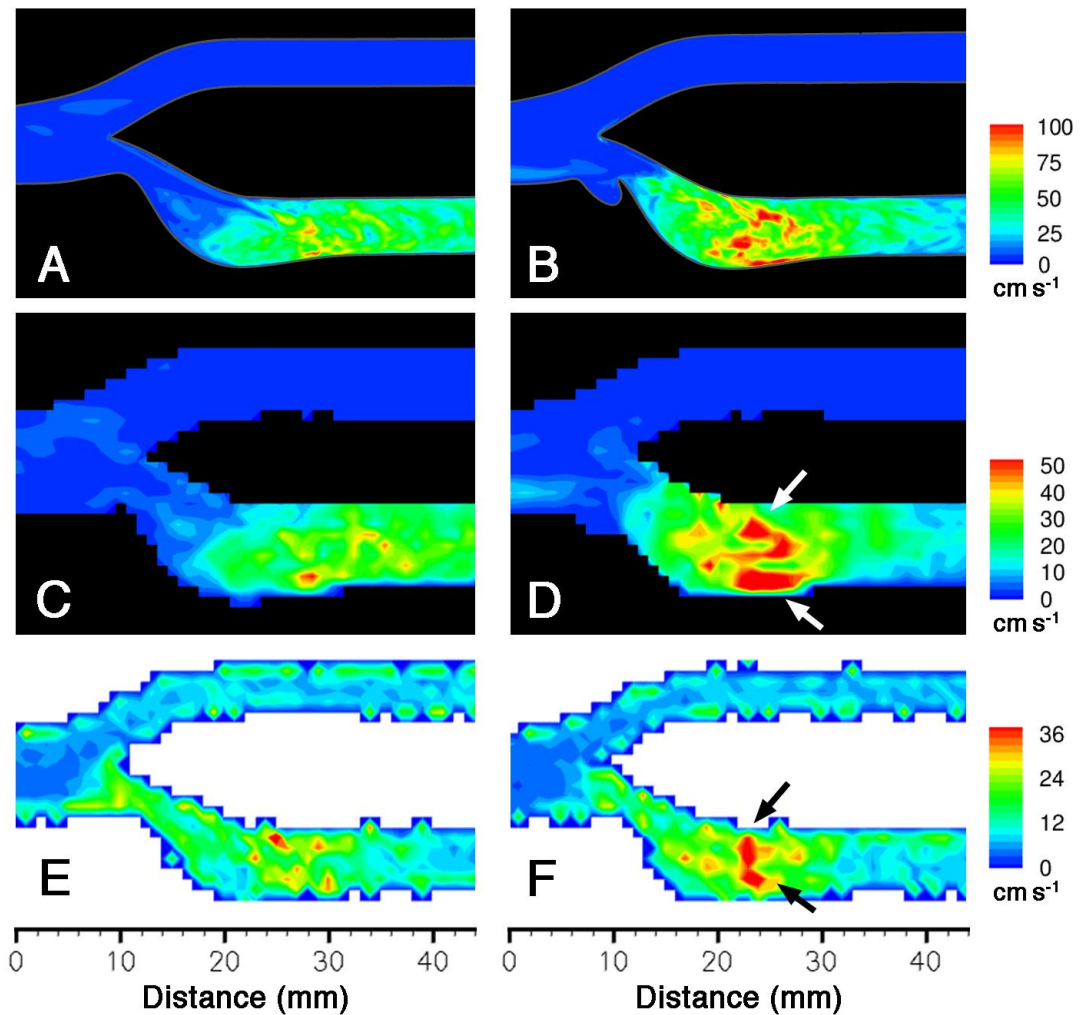


Figure 5.3: Colour-encoded TI maps in the central plane of the non-ulcerated geometry (*left column*) and ulcerated geometry (*right column*) in the CFD models using (a, b) RMS deviations in instantaneous nodal velocities and (c, d) finite volume sampling, shown at approximately 35 ms following peak systole; and from (e, f) experimental DUS measurements.

the ulcerated model, indicated by the arrows in Fig. 5.3d and 5.3f. From the CFD results, we observe that this corresponds to the two edges of the distal end of the shortened jet; one region arises where the tail of the jet impinges on the distal non-flow divider wall and the second region occurs where the opposite side of the jet interacts with the smaller recirculation zone on the flow-divider wall. As well, CFD and DUS both show moderate elevations in TI along the body of the jet at the complex interface between the jet edge and the disorderly recirculating flow (Fig. 5.3). TI in the non-ulcerated model is also comparable between CFD and DUS, showing two fainter regions of elevated TI further downstream, corresponding to the two edges of the tail end of the jet. The CFD flow fields reveal that the more proximal of the two regions occurs where the jet impacts the vessel wall, whereas the distal region of velocity fluctuations results from the flickering of the tail of the jet.

Values of nodal RMS velocity fluctuations in the CFD flow fields are higher than experimentally determined DUS TI, corresponding with the higher magnitudes of instantaneous point velocities from CFD. When computed CFD point velocities are modelled for the effects of DUS sample volume geometry, intrinsic spectral broadening and wall filtering, the CFD simulated TI values are in better agreement with DUS values, but remain higher. Averaged TI calculated from 24 sites in the distal ROI in the non-ulcerated and ulcerated models are respectively, 33.6 cm s^{-1} and 39.4 cm s^{-1} from CFD finite sampling, compared to 20.3 cm s^{-1} and 24.7 cm s^{-1} from DUS measurements, at approximately 36 ms following peak systole; the relative increase in TI due to ulceration is 17.3% from CFD and 21.7% from DUS.

5.3.3 Virtual particle tracking

5.3.3.1 Particle pathlines

The non-ulcerated and ulcerated models display markedly different particle path histories, as seen in Fig. 5.4 and Fig. 5.5. The non-ulcerated model exhibits a highly segregated stenotic jet stream within which pathlines generally do not cross. The particle tracks in Fig. 5.4a and 5.4b also reveal the presence of counter-rotating recirculation zones on either side of the jet. Particularly within the large region of recirculation in the ICA bulb, the circulation of the particles is well-ordered and predominantly in-plane. Particles which engage in the recirculation zone in the outer ICA bulb tend to arise from the outer edge of the jet stream. In contrast, the jet core in the ulcerated model is not clearly delineated, encompassing a wider and more perturbed set of paths (Fig. 5.4c and 5.4d). Substantial mixing of the edge of the jet with the out-of-plane recirculation is evident, and appears to be exacerbated by the flow from the jet tail impingement at a steeper impact angle on the outer ICA wall.

In the presence of a proximal ulceration, pathlines through the throat of the stenosis are altered. Most of the particles that enter the ulcer have only a shallow diversion into the ulcer cavity, but some are observed to enter the ulcer on the distal side and circulate within the inner cavity. Particles that enter the ulcer do not tend to reside in the ulcer for longer than a cardiac cycle (typically only one loop around), exiting via the proximal side of the ulcer during the high velocity, low radial pressure impulse phase of the cardiac cycle at peak systole.

5.3.3.2 Particle shear stress histories

The highest shear stress in the flow field occurs during peak systole, particularly at the edge of the jet through the throat of the stenosis, at the apex of the bifurcation, and at the location on the wall of the distal ICA bulb

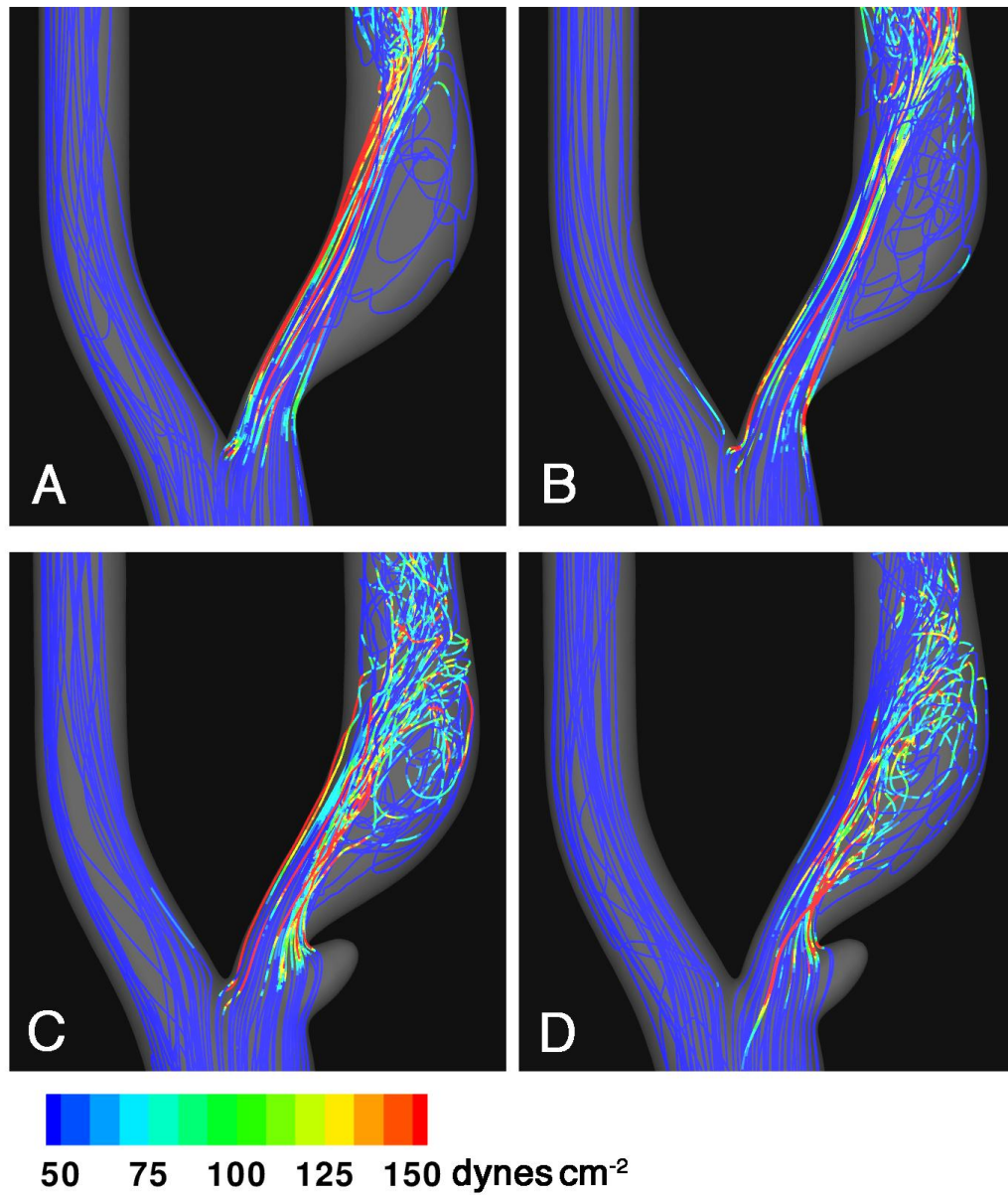


Figure 5.4: Shear stress-encoded particle tracks for 10×10 uniform seeding in the non-ulcerated (*top row*) and ulcerated (*bottom row*) CFD models for two representative seeding time points during diastole. Colour-encoding indicates the shear stress, $\bar{\tau}_{max}$, experienced at each point along the particle track.

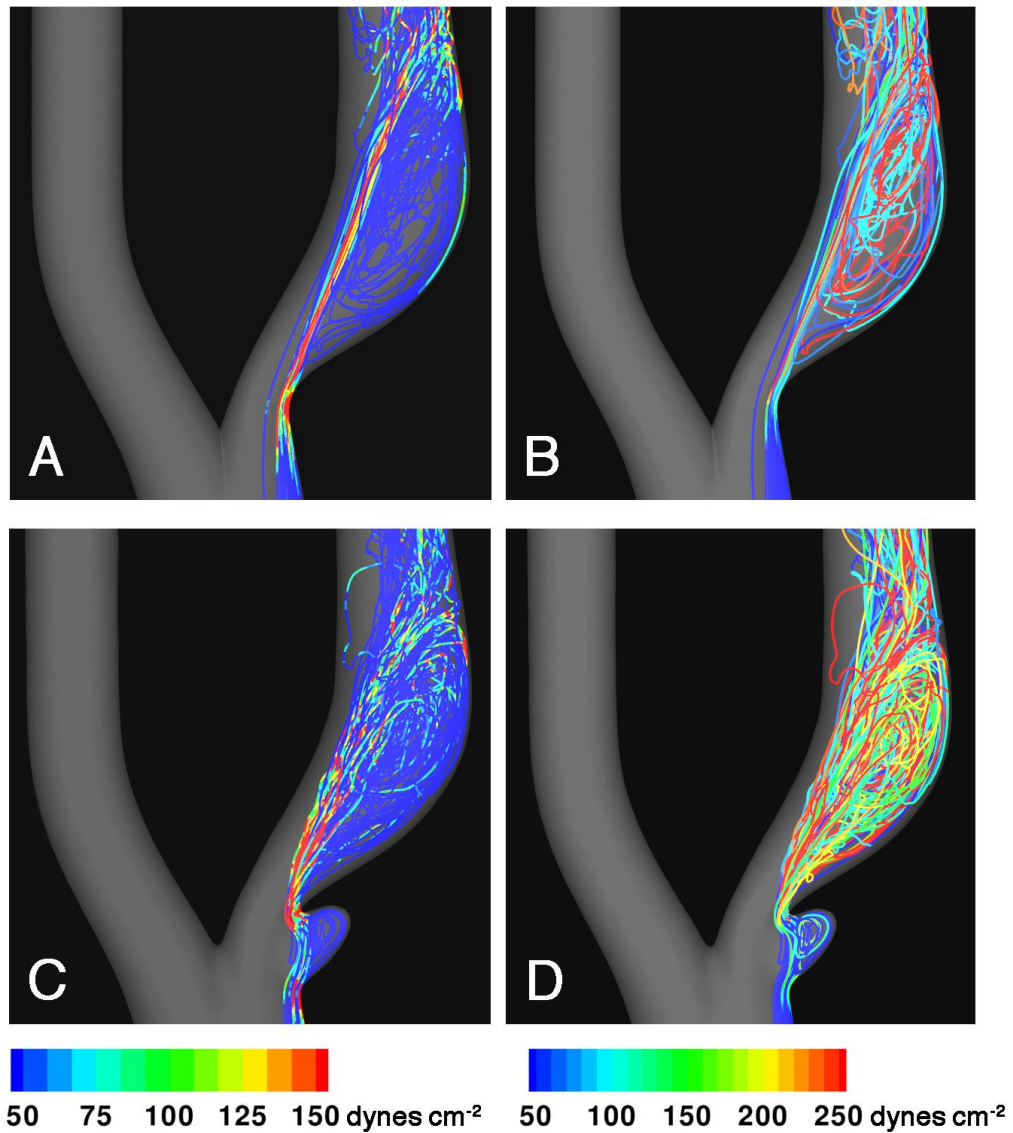


Figure 5.5: Shear stress-encoded particle tracks for near-wall seeding in the non-ulcerated (*top row*) and ulcerated (*bottom row*) CFD models for a representative seeding time point during late diastole. Colour-encoding indicates (a, c) the shear stress, $\bar{\tau}_{max}$, experienced at each point along the track and (b, d) the maximum $\bar{\tau}_{max}$ experienced up to the indicated point in the particle track.

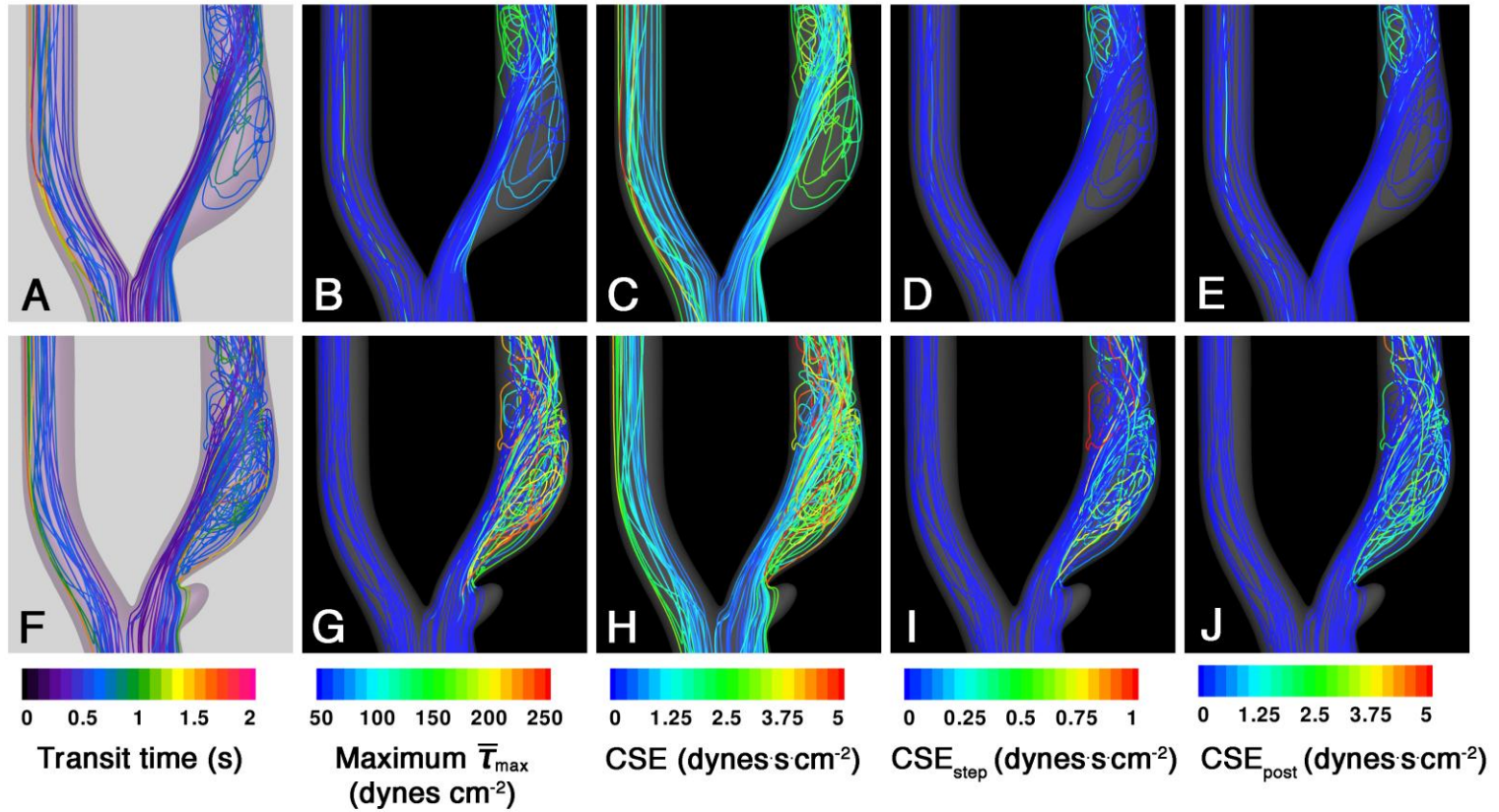


Figure 5.6: (a, f) Transit time; (b, g) maximum shear stress up to the point in the track; and cumulative shear exposure parameters: (c, h) CSE , (d, i) CSE_{step} and (e, j) CSE_{post} along particle tracks for 10×10 uniform seeding in the non-ulcerated model (*top row*) and ulcerated model (*bottom row*), corresponding to a seeding time point in early diastole.

where the jet impinges. In the ulcerated model, high shear stress also occurs at the distal edge of the mouth of the ulcer. Particles experience high shear through the throat, but while these particles tend to travel with the stenotic jet flow in the non-ulcerated model, in the ulcerated model, such particles have a higher tendency to divert into the recirculation zone. This is evident in Fig. 5.5d and Fig. 5.6g which illustrate the maximum \bar{v}_{max} that a particle has experienced up to that point along the particle track, wherein we see that particles in the recirculation zone tend to have a history of greater shear exposure in the ulcerated model.

The relative number of particles (of over 250,000 seeded in each model) that experience levels of shear stress exceeding the critical level of 105 dynes cm^{-2} is 18% in the non-ulcerated and 23% in the ulcerated models, a difference which can be seen in the histogram, for maximum shear stresses of 150 dynes cm^{-2} and higher (Fig. 5.7a, bins 175 – 475 dynes cm^{-2}). Transit time distributions were similar in the two models, with 89% of particles seeded traversing the model within two cardiac cycles (Fig. 5.7b, bins 0.3 – 1.5 s). In contrast, there are a greater number of particles in the ulcerated model that experience longer transit times post-threshold (Fig 5.7c, +4% of the total number of seeded particles for bins 0.5 to 2.9 s), reflecting the greater number of particles that experience a critical level of shear stress and enter the recirculation zone with a history of greater shear exposure. Frequency distributions of non-thresholded CSE show little or no difference between the two models (Fig. 5.8a). In contrast, CSE_{step} is higher in the ulcerated model for moderate levels (Fig. 5.8b, bins 0.3 – 0.9 dynes s cm^{-2}) and higher in the non-ulcerated model for higher levels (Fig. 5.8b, bins 1.1 – 1.9 dynes s cm^{-2}). Frequency distributions of CSE_{post} exhibit the clearest differences, as a higher relative number of particles in the ulcerated model experience levels from 2 – 6 dynes s cm^{-2} (Fig. 5.8c).

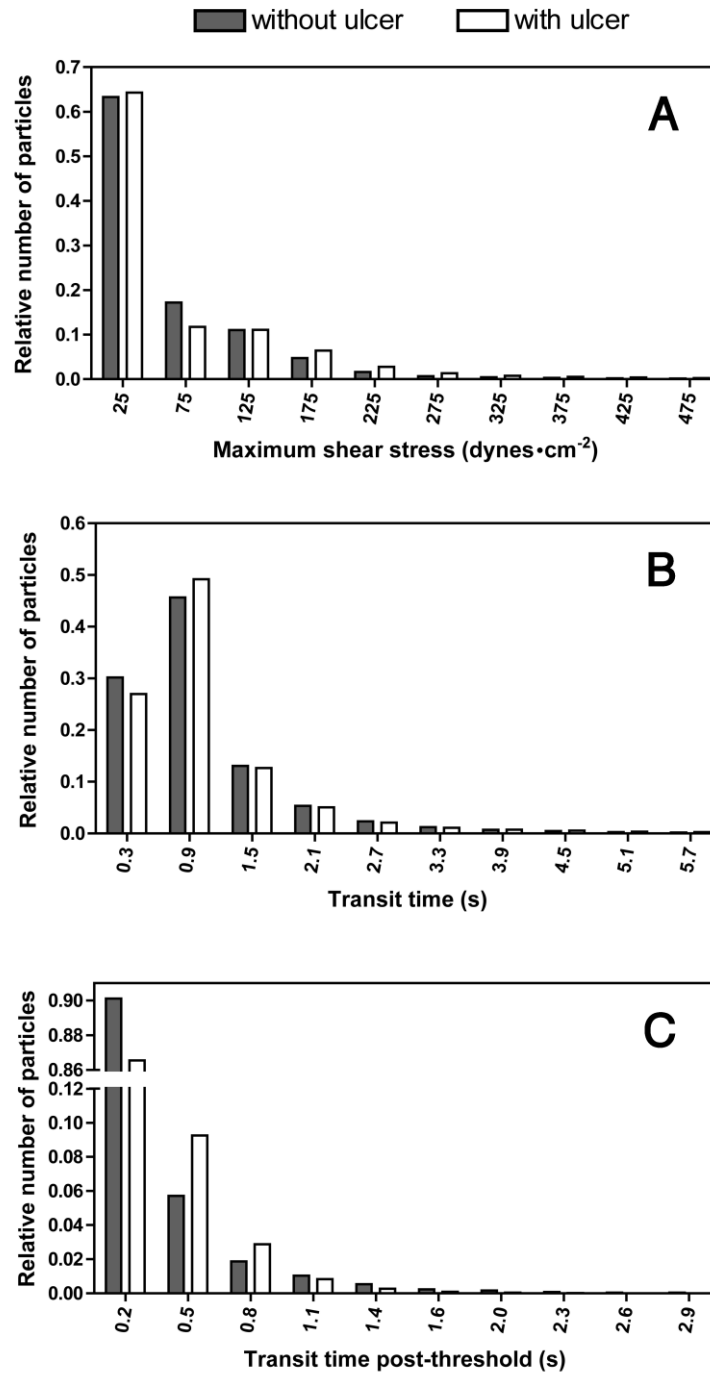


Figure 5.7: Frequency distributions of (a) maximum shear stress (maximum \bar{v}_{max}), (b) total transit time, and (c) transit time post-threshold for over 250,000 seeded particles. *Grey bars* represent particle frequency distributions for the non-ulcerated model and *white bars* for the ulcerated model. Less than 1% of the seeded particles are excluded from the histograms by the upper cutoff.

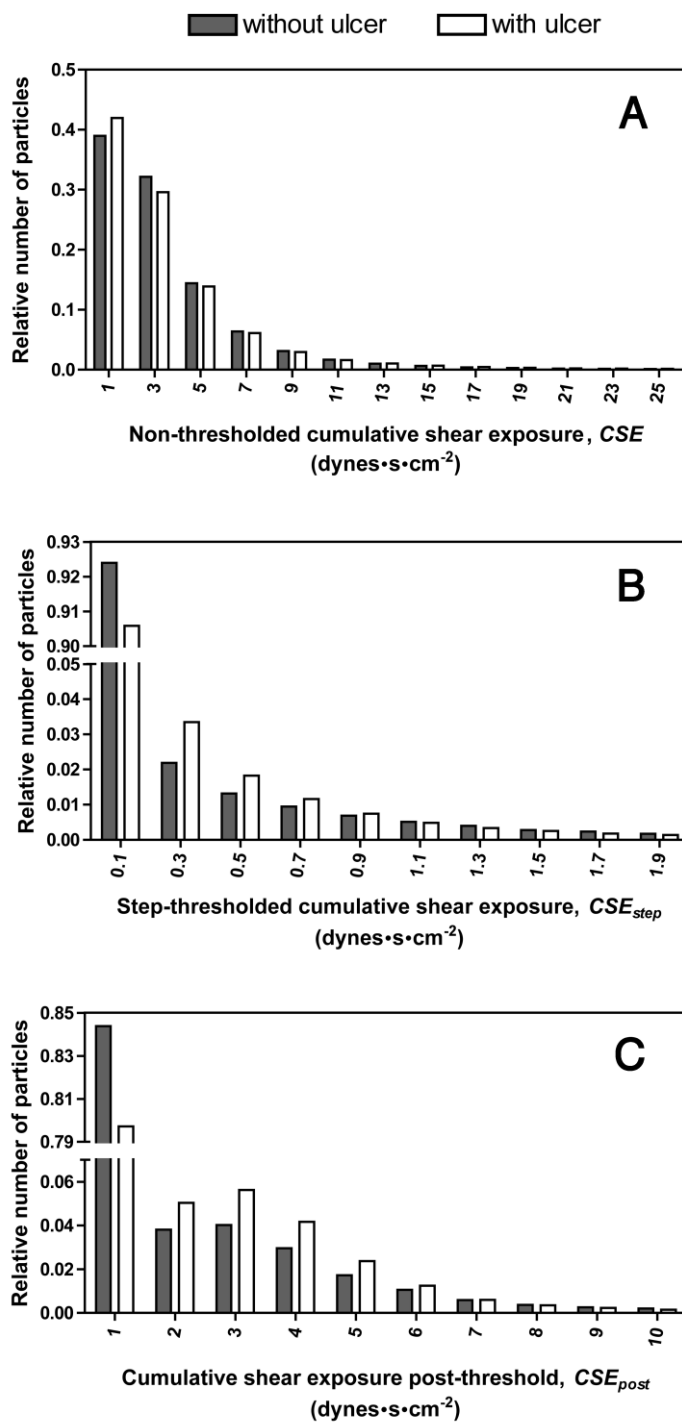


Figure 5.8: Frequency distributions of cumulative shear stress particle track parameters for over 250,000 seeded particles. *Grey bars* represent particle frequency distributions for the non-ulcerated model and *white bars* for the ulcerated model. Less than 1% of the seeded particles are excluded from the histograms by the upper cutoff.

5.4 Discussion

Our observation of local flow dynamics in the vicinity of the ulcer – with flow entry at the distal edge of the ulcer cavity, low-velocity circulating flow, and clearing of particles from the proximal side of the ulcer cavity during peak systole – is congruent with results from a previous dye slipstream analysis in an ulcerated model of the carotid bifurcation [6]. We found that most particles that enter the ulcer have only a shallow diversion into the ulcer (Fig. 5.5d). However, this slight perturbation has a notable effect on the resulting particle trajectories and consequently on downstream flow disturbances. The deflection of particles as they re-enter the fast-flowing jet stream contributes to the out-of-plane recirculation. This may have implications for the importance of the geometry and location of ulceration on distal flow disruption in the carotid stenosis. The shallow entry into the ulcer for most near-wall particles suggests that beyond a critical depth, a deeper ulcer may have a limited effect on the downstream flow patterns. Observations from our previous experimental DUS study, which examined different sizes and shapes of ulceration (Chapter 3), suggest that inlet aperture may have a greater influence on distal flow disturbances than overall ulcer volume in certain cases [5]. However, the depth and overall ulcer volume may still affect the aggregation of thrombogenic blood particles due to slowly circulating flow within the ulcer cavity, although our CFD results indicate little flow stagnation within the cavity of a distally pointing ulcer. In addition, the pre-stenotic location of the ulceration may be a configuration that is particularly conducive to effecting perturbances of the jet. If this is true, it may have clinical implications, as ulcerations have been shown to more frequently occur on the proximal side of the carotid lesion [39, 40].

5.4.1 Simulated turbulence intensity (TI)

Numerical simulations of DUS TI – using pre-computed pulsatile velocity fields from CFD combined with point velocity interrogation of the pre-computed data over a prescribed sample volume – are able to predict the patterns and approximate relative differences in distal TI (17.3% versus 21.7% from DUS) due to the inclusion of ulceration in a 50% stenosed carotid bifurcation geometry. Future studies employing numerical predictions of distal TI could be performed in a series of models with variations in vascular and plaque morphology. Such studies may be able to determine the relationship between geometric parameters of the carotid bifurcation with distal TI, or assess the utility of TI as a diagnostic parameter under various physiological conditions.

Although CFD is able to predict the patterns and relative difference in TI, even in the complex and dynamic ICA flow during the deceleration phase of the cardiac cycle, the absolute values of mean velocities and TI from finite sampling simulations are higher than experimental values from DUS. The differences may result from underestimations of spectral broadening effects in the complex flow region [25]. One limitation to the generated spectral broadening is that the empirically derived spectral broadening function employed is based on experimental data that was obtained with a maximum flow rate of 20 mL s^{-1} and with a different ultrasound system [25]. It is possible that the functional form of this derived broadening scheme underestimates the spectral broadening at higher velocities. Furthermore, our current simulations do not take into account non-stationarity broadening due to the interaction between a finite sampling window and temporal velocity gradients in the velocity field for each interrogation point in the sample volume [41]. This could be accounted for by randomizing the sampling time within a finite window centered on the time point of interest, with a width and shape matching that of the experimental analysis, although

it would require additional computational time due to the requirement for temporal interpolation for each sample point.

5.4.2 Virtual particle tracking

From our frequency distributions of path-dependent parameters, we observe a slightly greater number of particles that experience a higher maximum shear stress and *cumulative shear exposure post-threshold* (CSE_{post}) during their time in the carotid artery bifurcation. In particular, the relative number of particles that are exposed to shear stresses exceeding 105 dynes s⁻² are 18% and 23% in the non-ulcerated and ulcerated models, respectively.

Previously, Tambasco and Steinman [23] performed particle tracking in a CFD model of a 30% eccentrically stenosed carotid bifurcation based on idealized geometries described by Smith *et al.* [27, 28], which were from the same geometric characterization study used for our 50% models. In their CFD model, less than 12% of particles remained within the 30% eccentrically stenosed carotid bifurcation for more than one cardiac cycle after seeding, compared to over 22% in our 50% stenosed models. This is not unexpected however, as our experimental DUS results established that the recirculation zone in a 50% stenosed carotid bifurcation is greater in extent and duration than that in a 30% stenosis geometry (Chapter 4), likely increasing residence time. Tambasco and Steinman [23] also showed that less than 0.4% of seeded particles in a 30% eccentric stenosis experienced maximum $\bar{\tau}_{max}$ exceeding 105 dynes cm⁻². In contrast, we found that 8% and 13% of particles encounter $\bar{\tau}_{max}$ exceeding 105 dynes cm⁻² in the non-ulcerated and ulcerated 50% eccentric stenosis respectively, which is consistent with the higher stenotic velocities and shear gradients observed in a more severely stenosed vessel.

While our CFD models indicate that ulceration in the stenosed carotid artery may result in only a small increase in particles experiencing higher shear stress exposure, such levels may still represent a physiologically

relevant elevation in thrombogenic potential over time, due to the dense, continuous flow of platelets through the carotid artery [23]. Although platelet activation is thought to be influenced by both shear stress level and duration of shear stress exposure [20, 38, 42, 43], the specific model describing the relevant combination of these two factors is still unresolved [44]. Here, we calculate three parameters: (1) *cumulative shear exposure, CSE*, (2) *step-thresholded cumulative shear exposure, CSE_{step}*, and (3) *cumulative shear exposure post-threshold, CSE_{post}*, to describe, respectively: (1) a model where the cumulative product of shear stress level and the duration of shear stress exposure determine the level of platelet activation, regardless of the magnitude of shear stress [17, 18], (2) a model where cumulative shear exposure is relevant, but a critical level of shear stress is necessary to contribute to platelet activation response [19, 23, 45], and (3) a model where a platelet becomes susceptible to subsequent exposure to shear stress only once it has been exposed to a critical level of shear stress [46]. While more experimental evidence is needed to determine which model is more accurate, our results based on model (3) suggest that plaque ulceration may have a physiologically relevant effect on shear-dependent platelet activation in the eccentrically stenosed carotid bifurcation.

To model blood particle dynamic histories, we employed an approach evaluating the Lagrangian motion of particles determined from pre-computed velocity fields. As discussed in a previous report [23], this method makes the assumption that particle-to-particle interactions and their coupled effects on the flow field are negligible. The relevance of such interactions is unclear [23]. It has been shown that particle interactions can cause platelets, and other blood particles, to assume a non-uniform concentration, with platelets assuming a preferential spatial distribution towards the outer vessel wall; however, this has only been characterized under steady flow conditions [47] or in smaller vessels [48, 49]. Therefore, due to the paucity of empirical data

on the physiological distribution of platelets in the carotid artery under pulsatile flow, we used a uniform distribution of blood particles at the CCA inlet to determine particle parameter distributions. Although the use of a uniform seeding distribution limits the direct quantitative interpretation of histogram values, our comparisons do enable the study of the relative effects of flow differences due to variations in vessel morphology. Future experimental determinations of spatial and temporal distributions of blood particles in the CCA under pulsatile flow could be taken into account simply by retrospectively weighting the cumulative shear exposure value associated with a particle by the relative concentration at its initial seeding time and location at the inlet. If it is found that the effects of particle-to-particle interactions are important, then a more sophisticated simulation could incorporate a physical model of the fluid (blood plasma) and the deformable blood cell components of blood.

5.5 Conclusion

Computational fluid dynamics – with numerical DUS modelling and particle track analysis – facilitated the study of time-varying 3-D flow patterns and cycle-to-cycle velocity fluctuations downstream from the site of ulceration in a moderate 50% stenosed carotid artery bifurcation. In particular, the CFD pulsatile flow solution carried out over thirteen cardiac cycles, captured the elevation in sample-volume based TI due to ulceration in the moderate stenosis, relative to a smooth-walled model of the same vessel geometry. Using numerical simulations of DUS, CFD models may provide a practical tool to study TI in the carotid artery bifurcation with various vessel and surface plaque ulceration geometries, facilitating the evaluation of the robustness of TI as a diagnostic parameter of ulceration in the stenosed carotid artery. Our observation of enhanced flow disruption, cycle-to-cycle velocity fluctuations, and shear exposure in the ulcerated model support the hypothesis that differences in local fluid dynamic behaviour may influence

the potential thrombogenic risk associated with plaque ulcerations in the stenotic carotid artery bifurcation [3, 6, 7, 50].

5.6 References

1. Hankey GJ (1999) Stroke prediction and prevention by carotid endarterectomy: keep an eye on the doughnut and not just the hole. *Cerebrovasc Dis* 9:345-350.
2. Eliasziw M, Streifler JY, Fox AJ, Hachinski VC, Ferguson GG, *et al.* (1994) Significance of plaque ulceration in symptomatic patients with high-grade carotid stenosis. North American Symptomatic Carotid Endarterectomy Trial. *Stroke* 25:304-308.
3. Sitzer M, Muller W, Siebler M, Hort W, Kniemeyer HW, *et al.* (1995) Plaque ulceration and lumen thrombus are the main sources of cerebral microemboli in high-grade internal carotid artery stenosis. *Stroke* 26:1231-1233.
4. Orlandi G, Parenti G, Landucci Pellegrini L, Sartucci F, Paoli C, *et al.* (1999) Plaque surface and microembolic signals in moderate carotid stenosis. *Ital J Neurol Sci* 20:179-182.
5. Wong EY, Nikolov HN, Thorne ML, Poepping TL, Rankin RN, *et al.* (2009) Clinical Doppler ultrasound for the assessment of plaque ulceration in the stenosed carotid bifurcation by detection of distal turbulence intensity: a matched model study. *Eur Radiol* 19:2739-2749.
6. Imbesi SG and Kerber CW (1998) Why do ulcerated atherosclerotic carotid artery plaques embolize? A flow dynamics study. *AJNR Am J Neuroradiol* 19:761-766.

7. Birchall D, Zaman A, Hacker J, Davies G and Mendelow D (2006) Analysis of haemodynamic disturbance in the atherosclerotic carotid artery using computational fluid dynamics. *Eur Radiol* 16:1074-1083.
8. Nesbitt WS, Westein E, Tovar-Lopez FJ, Tolouei E, Mitchell A, *et al.* (2009) A shear gradient-dependent platelet aggregation mechanism drives thrombus formation. *Nat Med* 15:665-673.
9. Slager CJ, Wentzel JJ, Gijzen FJ, Thury A, van der Wal AC, *et al.* (2005) The role of shear stress in the destabilization of vulnerable plaques and related therapeutic implications. *Nat Clin Pract Cardiovasc Med* 2:456-464.
10. Ruggeri ZM, Orje JN, Habermann R, Federici AB and Reininger AJ (2006) Activation-independent platelet adhesion and aggregation under elevated shear stress. *Blood* 108:1903-1910.
11. Zhang JN, Bergeron AL, Yu Q, Sun C, McBride L, *et al.* (2003) Duration of exposure to high fluid shear stress is critical in shear-induced platelet activation-aggregation. *Thromb Haemost* 90:672-678.
12. Purvis NB, Jr. and Giorgio TD (1991) The effects of elongational stress exposure on the activation and aggregation of blood platelets. *Biorheology* 28:355-367.
13. Mody NA and King MR (2008) Platelet adhesive dynamics. Part II: high shear-induced transient aggregation via GPIIb/IIIa-vWF-GPIIb/IIIa bridging. *Biophys J* 95:2556-2574.
14. Nobili M, Sheriff J, Morbiducci U, Redaelli A and Bluestein D (2008) Platelet activation due to hemodynamic shear stresses: damage accumulation model and comparison to in vitro measurements. *Asaio J* 54:64-72.

15. Strony J, Beaudoin A, Brands D and Adelman B (1993) Analysis of shear stress and hemodynamic factors in a model of coronary artery stenosis and thrombosis. *Am J Physiol* 265:H1787-1796.
16. Cadroy Y, Horbett TA and Hanson SR (1989) Discrimination between platelet-mediated and coagulation-mediated mechanisms in a model of complex thrombus formation in vivo. *J Lab Clin Med* 113:436-448.
17. Bluestein D, Niu L, Schoephoerster RT and Dewanjee MK (1997) Fluid mechanics of arterial stenosis: relationship to the development of mural thrombus. *Ann Biomed Eng* 25:344-356.
18. Rubenstein DA and Yin W (2010) Quantifying the effects of shear stress and shear exposure duration regulation on flow induced platelet activation and aggregation. *J Thromb Thrombolysis* 30:36-45.
19. Holme PA, Orvim U, Hamers MJ, Solum NO, Brosstad FR, *et al.* (1997) Shear-induced platelet activation and platelet microparticle formation at blood flow conditions as in arteries with a severe stenosis. *Arterioscler Thromb Vasc Biol* 17:646-653.
20. Boreda R, Fatemi RS and Rittgers SE (1995) Potential for platelet stimulation in critically stenosed carotid and coronary arteries. *J Vasc Invest* 1:26-37.
21. Cheng CP, Herfkens RJ and Taylor CA (2003) Inferior vena caval hemodynamics quantified in vivo at rest and during cycling exercise using magnetic resonance imaging. *Am J Physiol Heart Circ Physiol* 284:H1161-1167.
22. Forsberg F, Morvay Z, Rawool NM, Deane CR and Needleman L (2000) Shear rate estimation using a clinical ultrasound scanner. *J Ultrasound Med* 19:323-327.

23. Tambasco M and Steinman DA (2003) Path-dependent hemodynamics of the stenosed carotid bifurcation. *Ann Biomed Eng* 31:1054-1065.
24. Raz S, Einav S, Alemu Y and Bluestein D (2007) DPIV prediction of flow induced platelet activation-comparison to numerical predictions. *Ann Biomed Eng* 35:493-504.
25. Khoshniat M, Thorne ML, Poepping TL, Hirji S, Holdsworth DW, *et al.* (2005) Real-time numerical simulation of Doppler ultrasound in the presence of nonaxial flow. *Ultrasound Med Biol* 31:519-528.
26. Swillens A, Segers P, Torp H and Lovstakken L (2010) Two-dimensional blood velocity estimation with ultrasound: speckle tracking versus crossed-beam vector Doppler based on flow simulations in a carotid bifurcation model. *IEEE Trans Ultrason Ferroelectr Freq Control* 57:327-339.
27. Smith RF, Rutt BK, Fox AJ, Rankin RN and Holdsworth DW (1996) Geometric characterization of stenosed human carotid arteries. *Acad Radiol* 3:898-911.
28. Smith RF, Rutt BK and Holdsworth DW (1999) Anthropomorphic carotid bifurcation phantom for MRI applications. *J Magn Reson Imaging* 10:533-544.
29. Lovett JK, Gallagher PJ, Hands LJ, Walton J and Rothwell PM (2004) Histological correlates of carotid plaque surface morphology on lumen contrast imaging. *Circulation* 110:2190-2197.
30. Wong EY, Thorne ML, Nikolov HN, Poepping TL and Holdsworth DW (2008) Doppler ultrasound compatible plastic material for use in rigid flow models. *Ultrasound Med Biol* 34:1846-1856.

31. Kock SA, Nygaard JV, Eldrup N, Frund ET, Klaerke A, *et al.* (2008) Mechanical stresses in carotid plaques using MRI-based fluid-structure interaction models. *Journal of Biomechanics* 41:1651-1658.
32. Groen HC, Simons L, van den Bouwhuijsen QJA, Bosboom EMH, Gijsen FJH, *et al.* (2010) MRI-based quantification of outflow boundary conditions for computational fluid dynamics of stenosed human carotid arteries. *J Biomech* 43:2332-2338.
33. Poepping TL, Nikolov HN, Rankin RN, Lee M and Holdsworth DW (2002) An in vitro system for Doppler ultrasound flow studies in the stenosed carotid artery bifurcation. *Ultrasound Med Biol* 28:495-506.
34. Minev PD and Ethier CR (1999) A characteristic/finite element algorithm for the 3D Navier-Stokes equations using unstructured grids. *Comput Methods Appl Mech Engrg* 178:39-50.
35. Ethier CR, Prakash S, Steinman DA, Leask RL, Couch GG, *et al.* (2000) Steady flow separation patterns in a 45 degree junction. *J Fluid Mech* 411:1-38.
36. Prakash S and Ethier CR (2001) Requirements for mesh resolution in 3D computational hemodynamics. *J Biomech Eng* 123:134-144.
37. Steinman DA (2000) Simulated pathline visualization of computed periodic blood flow patterns. *J Biomech* 33:623-628.
38. Hellums JD (1994) 1993 Whitaker Lecture: biorheology in thrombosis research. *Ann Biomed Eng* 22:445-455.
39. Lovett JK and Rothwell PM (2003) Site of carotid plaque ulceration in relation to direction of blood flow: an angiographic and pathological study. *Cerebrovasc Dis* 16:369-375.

40. de Weert TT, Cretier S, Groen HC, Homburg P, Cakir H, *et al.* (2009) Atherosclerotic plaque surface morphology in the carotid bifurcation assessed with multidetector computed tomography angiography. *Stroke* 40:1334-1340.
41. Fish PJ (1991) Nonstationarity broadening in pulsed Doppler spectrum measurements. *Ultrasound Med Biol* 17:147-155.
42. Jesty J, Yin W, Perrotta P and Bluestein D (2003) Platelet activation in a circulating flow loop: combined effects of shear stress and exposure time. *Platelets* 14:143-149.
43. Ramstack JM, Zuckerman L and Mockros LF (1979) Shear-induced activation of platelets. *J Biomech* 12:113-125.
44. Wootton DM and Ku DN (1999) Fluid mechanics of vascular systems, diseases, and thrombosis. *Annu Rev Biomed Eng* 1:299-329.
45. Pieniazek P, Musialek P, Kablak-Ziembicka A, Tekieli L, Motyl R, *et al.* (2008) Carotid artery stenting with patient- and lesion-tailored selection of the neuroprotection system and stent type: early and 5-year results from a prospective academic registry of 535 consecutive procedures (TARGET-CAS). *J Endovasc Ther* 15:249-262.
46. Hellums JD, Peterson DM, Stathopoulos NA, Moake JL and Giorgio TD (1987) *Studies on the Mechanisms of Shear-Induced Platelet Activation*. Springer-Verlag, New York.
47. Aarts PA, van den Broek SA, Prins GW, Kuiken GD, Sixma JJ, *et al.* (1988) Blood platelets are concentrated near the wall and red blood cells, in the center in flowing blood. *Arteriosclerosis* 8:819-824.

48. Woldhuis B, Tangelder GJ, Slaaf DW and Reneman RS (1992) Concentration profile of blood platelets differs in arterioles and venules. *Am J Physiol* 262:H1217-1223.
49. Tangelder GJ, Teirlinck HC, Slaaf DW and Reneman RS (1985) Distribution of blood platelets flowing in arterioles. *Am J Physiol* 248:H318-323.
50. Liapis CD and Tzortzis EA (2004) Carotid ulcers as a source of embolism. *J Cardiovasc Surg (Torino)* 45:391-392.

Chapter 6

Summary and Future Work

6.1 Summary

6.1.1 Summary of Chapter 2

In Chapter 2, we detailed the development of a technique for the rapid but accurate fabrication of Doppler ultrasound (DUS)-compatible flow phantoms with variations in vascular geometry, using a numerically controlled direct-machining approach. To determine an appropriate material, various candidate plastics were tested for longitudinal speed of sound and acoustic attenuation at the diagnostic frequency of 5 MHz. Teflon® was found to have the most appropriate speed of sound compared to that of soft tissue. Using non-destructive imaging techniques, we were able to verify the geometric accuracy of a vessel geometry machined directly into Teflon®. Although Teflon® displayed a higher attenuation coefficient than other tested materials, DUS data acquired in the Teflon® flow model indicated that sufficient signal was delivered throughout the depth of the vessel and provided comparable velocity profiles to those obtained in a tissue-mimicking phantom. This study concluded that Teflon® provides the best combination of machinability and DUS compatibility, making it an appropriate choice for the fabrication of rigid DUS flow models using a direct-machining method. This work has been published in *Ultrasound in Medicine and Biology* [1].

6.1.2 Summary of Chapter 3

Chapter 3 described an *in vitro* evaluation of clinical DUS for the assessment of carotid plaque ulceration using various DUS velocity-derived parameters. Specifically, we evaluated the effect of ulceration in a moderately stenosed carotid bifurcation on distal turbulence intensity (TI), and other spectral

parameters, measured using clinical DUS in matched anthropomorphic models. Several physiologically relevant ulcer geometries (hemispherical; mushroom-shaped; and ellipsoidal pointing distal and proximal) and sizes (2-mm, 3-mm and 4-mm diameter hemispheres) were investigated. In this study, an offline analysis was performed to determine several velocity-based parameters from ensemble-averaged spectral data, including TI. We determined that the presence of physiologically relevant ulceration in a stenosed carotid bifurcation can generate disturbances in the distal flow field that are detectable with TI measured using clinical Doppler ultrasound ($P < 0.001$). We also found that both the size and shape of ulceration had a significant effect on TI in the distal region ($P < 0.001$). Due to the use of a clinical system combined with offline analysis, this method can provide the means to evaluate for plaque ulcerations in patients with carotid atherosclerosis using DUS. This work has been published in the journal *European Radiology* [2].

6.1.3 Summary of Chapter 4

In extension to the work in Chapter 3, Chapter 4 described an *in vitro* flow study to determine the effect of both stenosis grade and ulceration on distal TI in the carotid bifurcation measured using conventional, clinical DUS, in order to establish the feasibility of TI as a diagnostic parameter for the detection of plaque ulceration with variation in stenosis severity. In this study, DUS TI was assessed in matched ulcerated and smooth-walled (non-ulcerated) carotid bifurcation phantoms with various stenosis severities (30%, 50%, 60%, 70%), where the ulcerated models incorporated a physiologically relevant Type 3 ulceration at the level of the apex of the bifurcation. A clinical DUS system combined with offline analysis was used to analyze cardiac-gated velocity-based TI in the phantoms under a physiologically pulsatile carotid flow-rate waveform.

This study established a two-curve relationship of distal TI according to the degree of carotid artery stenosis and condition of ulceration, and demonstrated that the level of TI in the post-stenotic region was significantly elevated due to ulceration in the mild and moderate stenosis. The elevation in TI due to ulceration was 30%, 29%, and 44% in the 30%, 50%, and 60% stenosed models, respectively. This study also concluded that although ulceration produced significant elevations in distal TI, the degree of stenosis was the dominant factor in determining TI, increasing significantly with stenosis severity in both the ulcerated and non-ulcerated series. Finally, our results showed that a value of distal TI above 22 cm s^{-1} indicated an ulcerated moderate stenosis or a severe stenosis (with or without ulceration), while a value below was associated with a mild (30%) or a non-ulcerated moderate (50% and 60%) stenosis, indicating a potential diagnostic threshold value for designating carotid plaques in a high-risk category. Based on TI variability statistics, we determined that reliable clinical assessment of TI should involve DUS measurement from multiple sites within the distal internal carotid artery. This work has been prepared for submission to *European Radiology*.

6.1.4 Summary of Chapter 5

In Chapter 5, we performed a CFD study to investigate numerical simulations of sample volume-based TI and time-resolved flow patterns in the stenosed carotid bifurcation with proximal ulceration. Direct CFD comparisons of the detailed time-resolved pulsatile flow patterns in the ulcerated and non-ulcerated geometries were able to demonstrate the role of plaque ulceration in the underlying mechanism of flow disruption and cycle-to-cycle velocity fluctuations. Results from dynamic shear exposure histories calculated along simulated particle trajectories indicated jet perturbances in the ulcerated model due to the interaction of the edge of the jet stream with out-of-plane flow that arose from the altered trajectories of

near-wall particles due to the presence of ulceration. Based on a platelet activation model wherein a blood platelet becomes more susceptible to subsequent exposure to shear stress once it has been exposed to a critical level of shear stress, shear-dependent platelet activation in the eccentrically stenosed carotid bifurcation was enhanced in the presence of ulceration. However, models of cumulative shear stress exposure that reflect reversible platelet activation on short time scales indicated little difference in shear-dependent platelet response due to the inclusion of plaque ulceration. CFD pre-computed flow solutions with numerical simulations of DUS were able to predict the patterns and relative differences in distal TI due to the inclusion of ulceration in a moderately stenosed carotid bifurcation geometry. Preliminary findings from this work, based on different finite element mesh models than reported here, have been published in the *Proceedings of SPIE Medical Imaging 2009: Visualization, Image-guided Procedures and Modeling* (paper no. 7261-66) and in the *Proceedings of the 2008 IEEE International Ultrasonics Symposium* (paper no. P2A023-01).

6.2 Future Directions

6.2.1 Directly machined Doppler ultrasound compatible phantoms

The computer-aided direct-machining of vascular geometries into Teflon® facilitates the easy fabrication of multiple DUS-compatible flow phantoms, with well-defined geometric features, for comprehensive *in vitro* investigations of carotid atherosclerosis. Although the work in this thesis investigated thirteen unique carotid plaque geometries, there are countless other geometric parameters that may be clinically relevant [3, 4]. Although carotid plaque ulcerations are more frequently found on the side of the plaque proximal to the point of maximum stenosis, the physiological significance of ulcer site is not known [5, 6]. Interestingly, we found that distal TI increased with the size of hemispherical ulceration (Chapter 3). However, it is

uncertain what the effect would be on distal TI if the diameter were to be decreased further (e.g. 1 mm, 0.5 mm, etc.); in particular, whether and how distal TI would decrease to the levels in the non-ulcerated model for vanishingly small sizes of ulceration. It may be interesting to determine the functional dependence of TI on ulcer size, although there is some evidence that ulcers with a small diameter (< 2 mm) are not correlated with ipsilateral clinical events [7].

In future work, this technique for phantom fabrication could be employed for the *in vitro* study of local flow dynamics in vessels with varying ulcer location, multiple ulcerations [6], and concentric rather than eccentric stenosis geometries. Arterial geometries could be extended to include imaged-based patient-specific geometries with ulceration, rather than idealized geometries [8, 9]. In addition, vessel anatomies other than atherosclerotic plaque ulcerations, such as aortic or cerebral aneurysms models, could be studied using the direct-fabrication technique described. Although this technique is easiest to implement for planar geometries with ultrasound interrogation in the central plane, it is also possible to create out-of-plane curvature using a non-planar parting line between the two halves of the phantom.

6.2.2 Doppler ultrasound turbulence intensity (TI)

Future studies could determine the clinical utility of DUS measurements of TI for the detection of carotid plaque ulcerations *in vivo*, by establishing the clinical correlation of the DUS TI index to stenosis severity and ulceration evaluated on lumenography. DUS velocity waveform data could be collected in individuals with symptomatic carotid occlusive disease and compared with reliable imaging techniques. As discussed in Chapter 1 (Section 1.5.1), multi-detector computed tomography angiography [10, 11] or three-dimensional (3-D) gadolinium-enhanced magnetic resonance

angiography (Gd-MRA) [12] may provide the necessary sensitivity and specificity to ensure accuracy of comparison.

As discussed in Chapter 4 (Section 4.4), a robust evaluation of TI in the post-stenotic region for the detection of ulceration *in vivo* would likely require measurements of TI from multiple sample sites within a region of interest. One method that may be used to estimate TI at multiple sites is to simply collect conventional Doppler flow velocity data at each of the target locations, as we have done *in vitro* using a semi-automated acquisition system (Chapters 2 – 5). In the clinic, multiple-site collection could be implemented using either free-hand positioning or custom automated transmission strategies, which could utilize multi-gating techniques or sweeping of the ultrasound beam. For data acquisition, a handheld MP3 recording device or portable laptop computer could be connected to the audio output ports of the ultrasound system to collect DUS data directly from a conventional clinical instrument in the hospital [13, 14].

Alternatively, it may be worthwhile to explore the possibility of real-time two-dimensional (2-D) mapping of TI over an area of interest using mean velocity estimations from colour flow imaging. Colour flow imaging, or colour Doppler imaging, provides real-time display of mean blood-flow velocity and direction (i.e. towards or away from the transducer) over a 2-D region of interest, and is available on standard modern clinical ultrasound machines. Using the mean velocity estimator of a colour flow mapping system combined with cardiac gating, it may be possible to continuously display a map of TI over time for an area of interest, where each value of TI could be calculated using the latest determination of mean velocity and stored mean velocity values from previous cardiac cycles at the same time point based on cardiac gating. One challenge to this approach would be to determine whether the mean velocity estimators implemented in colour Doppler provide adequate accuracy for robust TI estimation. In colour flow

imaging, the number of samples (RF lines) available for each velocity estimation is limited due to the restrictions of 2-D flow mapping with real-time frame rates, and are typically lower than the number used in conventional Doppler ultrasound. Mean velocity estimators in colour flow Doppler are, therefore, typically less accurate than conventional DUS measurements based on longer observation times and a greater number of time samples [15].

The clinical assessment of carotid plaque ulceration using a DUS velocity-derived parameter could be integrated as an adjunct to the current conventional DUS examination, and has the potential to increase the reliability of the diagnosis of carotid artery disease without the use of costly, less widely available and invasive angiographic techniques that present higher risks to the patient [16, 17].

6.2.3 Numerical analysis of Doppler ultrasound TI

In this thesis, the numerical simulation of DUS with a finite sampling method was implemented for the prediction of altered TI due to plaque ulceration. Similar to the potential applications of a rapidly machinable flow phantom, the numerical simulation of DUS could be extended to include additional vessel geometries. In particular, it would be of interest to determine whether the two-curve relation of degree of stenosis and condition of ulceration (Chapter 4, Fig. 4.3) can be accurately predicted by numerical simulations for mild and moderate stenoses. Note that current CFD techniques restrict us to the study of mild and moderately stenosed vessels, as conventional CFD solvers are not able to accurately predict flows in fully turbulent conditions, which are known to occur in severely stenosed vessels [18-22], although future simulations could incorporate a turbulence model or direct numerical simulation of small-scale turbulence [23]. As well, future studies could model ulceration in imaged-based patient-specific geometries [8,

9], rather than idealized geometries. The numerical evaluation of TI may provide a means of assessing the effect of various vessel and ulcer geometries in other laboratories, without the requirement of a specialized experimental flow setup.

6.3 References

1. Wong EY, Thorne ML, Nikolov HN, Poepping TL and Holdsworth DW (2008) Doppler ultrasound compatible plastic material for use in rigid flow models. *Ultrasound Med Biol* 34:1846-1856.
2. Wong EY, Nikolov HN, Thorne ML, Poepping TL, Rankin RN, *et al.* (2009) Clinical Doppler ultrasound for the assessment of plaque ulceration in the stenosed carotid bifurcation by detection of distal turbulence intensity: a matched model study. *Eur Radiol* 19:2739-2749.
3. Thomas JB, Antiga L, Che SL, Milner JS, Steinman DA, *et al.* (2005) Variation in the carotid bifurcation geometry of young versus older adults: implications for geometric risk of atherosclerosis. *Stroke* 36:2450-2456.
4. Bressloff NW (2006) Parametric geometry exploration of the human carotid artery bifurcation. *J Biomech* 40:2483-2491.
5. de Weert TT, Cretier S, Groen HC, Homburg P, Cakir H, *et al.* (2009) Atherosclerotic plaque surface morphology in the carotid bifurcation assessed with multidetector computed tomography angiography. *Stroke* 40:1334-1340.
6. Lovett JK and Rothwell PM (2003) Site of carotid plaque ulceration in relation to direction of blood flow: an angiographic and pathological study. *Cerebrovasc Dis* 16:369-375.

7. Troyer A, Saloner D, Pan XM, Velez P and Rapp JH (2002) Major carotid plaque surface irregularities correlate with neurologic symptoms. *J Vasc Surg* 35:741-747.
8. Ladak HM, Thomas JB, Mitchell JR, Rutt BK and Steinman DA (2001) A semi-automatic technique for measurement of arterial wall from black blood MRI. *Med Phys* 28:1098-1107.
9. Moore JA, Steinman DA, Holdsworth DW and Ethier CR (1999) Accuracy of computational hemodynamics in complex arterial geometries reconstructed from magnetic resonance imaging. *Annals of Biomedical Engineering* 27:32-41.
10. Saba L, Caddeo G, Sanfilippo R, Montisci R and Mallarini G (2007) CT and ultrasound in the study of ulcerated carotid plaque compared with surgical results: potentialities and advantages of multidetector row CT angiography. *AJNR Am J Neuroradiol* 28:1061-1066.
11. Schuknecht B (2007) High-concentration contrast media (HCCM) in CT angiography of the carotid system: impact on therapeutic decision making. *Neuroradiology* 49 Suppl 1:S15-26.
12. Remonda L, Senn P, Barth A, Arnold M, Lovblad KO, *et al.* (2002) Contrast-enhanced 3D MR angiography of the carotid artery: comparison with conventional digital subtraction angiography. *AJNR Am J Neuroradiol* 23:213-219.
13. Poepping TL, Gill J, Fenster A and Holdsworth DW (2003) MP3 compression of Doppler ultrasound signals. *Ultrasound Med Biol* 29:65-76.
14. Thorne ML, Rankin RN, Steinman DA and Holdsworth DW (2010) In vivo Doppler ultrasound quantification of turbulence intensity using a high-pass frequency filter method. *Ultrasound Med Biol* 36:761-771.

15. Szabo TL (2004) *Diagnostic ultrasound imaging*. Elsevier Academic Press, Burlington.
16. Randoux B, Marro B, Koskas F, Duyme M, Sahel M, *et al.* (2001) Carotid artery stenosis: prospective comparison of CT, three-dimensional gadolinium-enhanced MR, and conventional angiography. *Radiology* 220:179-185.
17. Cinat ME, Casalme C, Wilson SE, Pham H and Anderson P (2003) Computed tomography angiography validates duplex sonographic evaluation of carotid artery stenosis. *Am Surg* 69:842-847.
18. Ahmed SA and Giddens DP (1984) Pulsatile poststenotic flow studies with laser Doppler anemometry. *J Biomech* 17:695-705.
19. Talukder N, Fulenwider JT, Mabon RF and Giddens DP (1986) Poststenotic flow disturbance in the dog aorta as measured with pulsed Doppler ultrasound. *J Biomech Eng* 108:259-265.
20. Ojha M, Johnston KW, Cobbold RS and Hummel RL (1989) Potential limitations of center-line pulsed Doppler recordings: an in vitro flow visualization study. *J Vasc Surg* 9:515-520.
21. Ojha M, Cobbold RSC, Johnston KW and Hummel RL (1989) Pulsatile flow through constricted tubes: an experimental investigation using photochromic tracer methods. *J Fluid Mech* 203:173-197.
22. Ku DN (1997) Blood flow in arteries. *Annu Rev Fluid Mech* 29:399-434.
23. Varghese SS and Frankel SH (2003) Numerical modeling of pulsatile turbulent flow in stenotic vessels. *J Biomech Eng* 125:445-460.

Appendix A

Copyright Permissions

WOLTERS KLUWER HEALTH LICENSE TERMS AND CONDITIONS

Dec 02, 2010

This is a License Agreement between Emily Y Wong ("You") and Wolters Kluwer Health ("Wolters Kluwer Health") provided by Copyright Clearance Center ("CCC"). The license consists of your order details, the terms and conditions provided by Wolters Kluwer Health, and the payment terms and conditions.

All payments must be made in full to CCC. For payment instructions, please see information listed at the bottom of this form.

License Number	2542120176971
License date	Nov 04, 2010
Licensed content publisher	Wolters Kluwer Health
Licensed content publication	Circulation
Licensed content title	Histological Correlates of Carotid Plaque Surface Morphology on Lumen Contrast Imaging
Licensed content author	J.K. Lovett
Licensed content date	Oct 12, 2004
Volume Number	110
Issue Number	15
Type of Use	Dissertation/Thesis
Requestor type	Individual
Title of your thesis / dissertation	Hemodynamics in the Stenosed Carotid Bifurcation with Plaque Ulceration
Expected completion date	Jan 2011
Estimated size(pages)	200

**ELSEVIER LICENSE
TERMS AND CONDITIONS**

Dec 02, 2010

This is a License Agreement between Emily Y Wong ("You") and Elsevier ("Elsevier") provided by Copyright Clearance Center ("CCC"). The license consists of your order details, the terms and conditions provided by Elsevier, and the payment terms and conditions.

All payments must be made in full to CCC. For payment instructions, please see information listed at the bottom of this form.

Supplier	Elsevier The Boulevard, Langford Kidlington, Oxford, OX5 1GB, UK	Limited Lane
Registered Company Number	1982084	
Customer name	Emily Y Wong	
License number	2551440114314	
License date	Nov 17, 2010	
Licensed content publisher	Elsevier	
Licensed content publication	Ultrasound in Medicine & Biology	
Licensed content title	Doppler Ultrasound Compatible Plastic Material for Use in Rigid Flow Models	
Licensed content author	Emily Y. Wong, Meghan L. Thorne, Hristo N. Nikolov, Tamie L. Poepping, David W. Holdsworth	
Licensed content date	November 2008	
Licensed content volume number	34	
Licensed content issue number	11	
Number of pages	11	
Type of Use	reuse in a thesis/dissertation	
Intended publisher of new work	Other	
Portion	full article	
Format	both print and electronic	
Are you the author of this Elsevier article?	Yes	
Will you be translating?	No	
Order reference number		
Title of your thesis/dissertation	Hemodynamics in the Stenosed Carotid Bifurcation with Plaque Ulceration	
Expected completion date	Jan 2011	
Estimated size (number of pages)	200	



Vienna, November 5, 2010

Dear Dr. Wong,

You are hereby granted permission from the European Society of Radiology (ESR) to reproduce the following content:

Wong, E.Y., H.N. Nikolov, M.L. Thorne, R.N. Rankin, T.L. Poepping, and D.W. Holdsworth (2009). Clinical Doppler ultrasound for the assessment of plaque ulceration in the stenosed carotid bifurcation by detection of distal turbulence intensity: a matched model study. Eur Radiol 19: 2739-2749

Permission must also be granted by the author(s) and full credit given to the original publication:
E. Y. Wong

Material must be reproduced as originally published and may be reproduced in print or electronic format for use in the following publication:

Title: Hemodynamics in the Stenosed Bifurcation with Plaque Ulceration

Authors: Emily Yee-Wah Wong

To be published in: Doctoral Thesis

Signature:

Date: 20-Mar-2011

This permission is strictly limited to a **single-use, non-exclusive** license for **English language** use within the terms stipulated above. Permission is granted under the condition that full credit is prominently and correctly placed as follows:

"Article reproduced from: Wong, E.Y., H.N. Nikolov, M.L. Thorne, R.N. Rankin, T.L. Poepping, and D.W. Holdsworth (2009) Clinical Doppler ultrasound for the assessment of plaque ulceration in the stenosed carotid bifurcation by detection of distal turbulence intensity: a matched model study. Eur Radiol 19:2739-2749."

This permission becomes effective upon receipt of this signed contract. Please return a signed copy via e-mail to office@european-radiology.org or via fax to +43-1-533 4064-441 and keep a copy for your files.

Thank you for your interest in our publication!

Kind regards,

European Radiology - Editorial Office
c/o European Society of Radiology



Appendix B

In Vitro System for Doppler Ultrasound Flow Studies

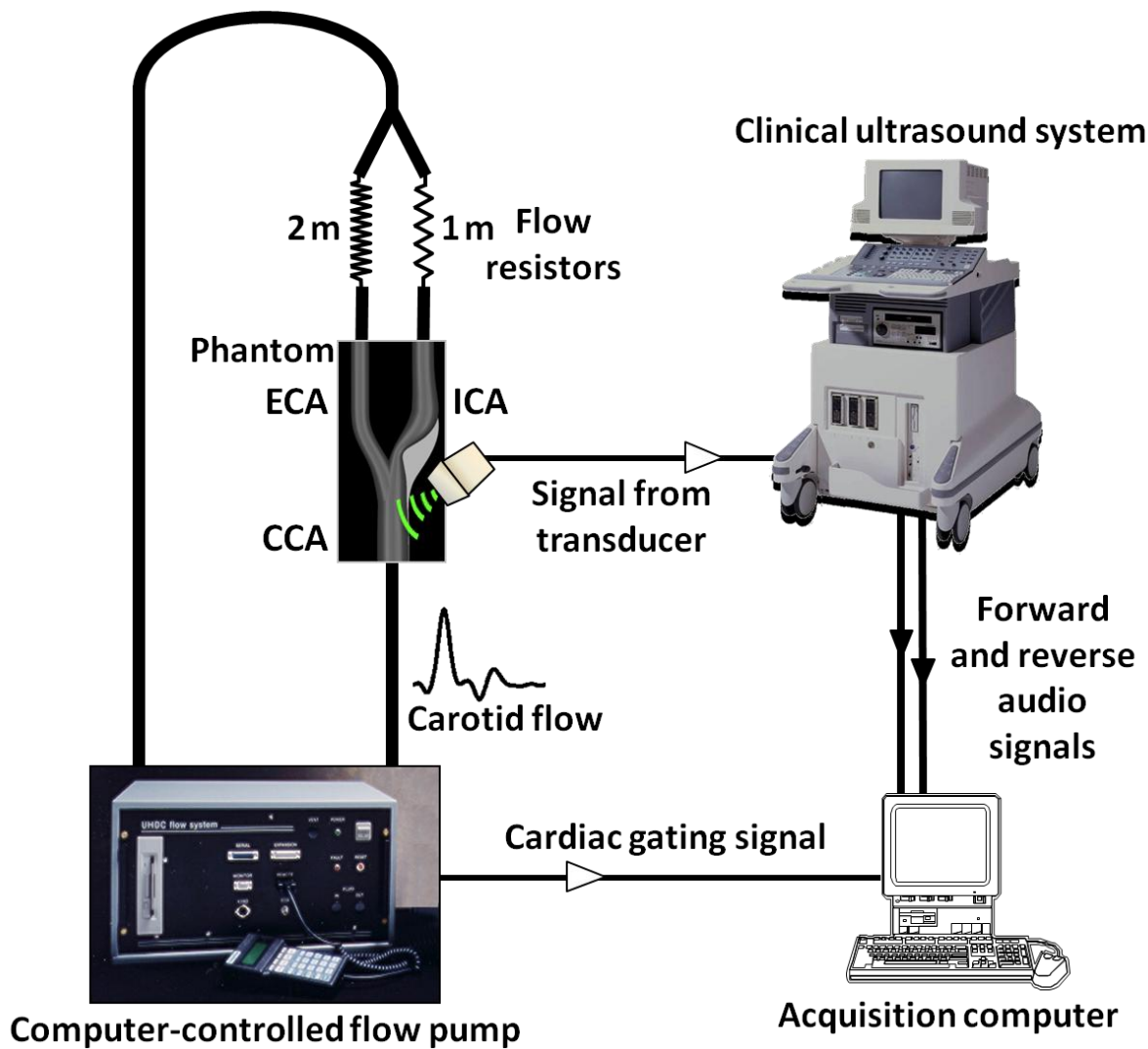


Figure B.1: Schematic of the *in vitro* Doppler ultrasound acquisition system.

The programmable computer-controlled flow pump is used to produce a physiologically realistic carotid flow-rate waveform [1]. The blood-mimicking fluid used has physical properties (i.e. viscosity, density and size of scattering particles (5- μm diameter)) and acoustic properties (i.e. backscatter power and attenuation) closely matched to blood [2], and is suitable for use in Doppler test flow objects under both laminar and turbulent flow conditions [3]. Doppler ultrasound data are acquired using a clinical ultrasound machine. The ultrasound transducer is mounted onto a three-axis mechanical translational stage, which allows for one axis of rotation and three axes of translation. A computer is used to control the 3-D translation stage, in order to position the stage-mounted probe at prescribed coordinate locations. This enables the semi-automated acquisition of Doppler data from prescribed sampling sites throughout the phantom [4]. The computer also uses the cardiac gating signal from the pump to control recording time in order to collect prospectively cardiac-gated data. Further details of the *in vitro* system are described by Poepping *et al.* [4].

References

1. Holdsworth DW, Rickey DW, Drangova M, Miller DJ and Fenster A (1991) Computer-controlled positive displacement pump for physiological flow simulation. *Med Biol Eng Comput* 29:565-570.
2. Ramnarine KV, Nassiri DK, Hoskins PR and Lubbers J (1998) Validation of a new blood-mimicking fluid for use in Doppler flow test objects. *Ultrasound Med Biol* 24:451-459.
3. Thorne ML, Poepping TL, Rankin RN, Steinman DA and Holdsworth DW (2008) Use of an ultrasound blood-mimicking fluid for Doppler investigations of turbulence in vitro. *Ultrasound Med Biol* 34:1163-1173.
4. Poepping TL, Nikolov HN, Rankin RN, Lee M and Holdsworth DW (2002) An in vitro system for Doppler ultrasound flow studies in the stenosed carotid artery bifurcation. *Ultrasound Med Biol* 28:495-506.

Appendix C

Turbulence Intensity (TI) Analysis

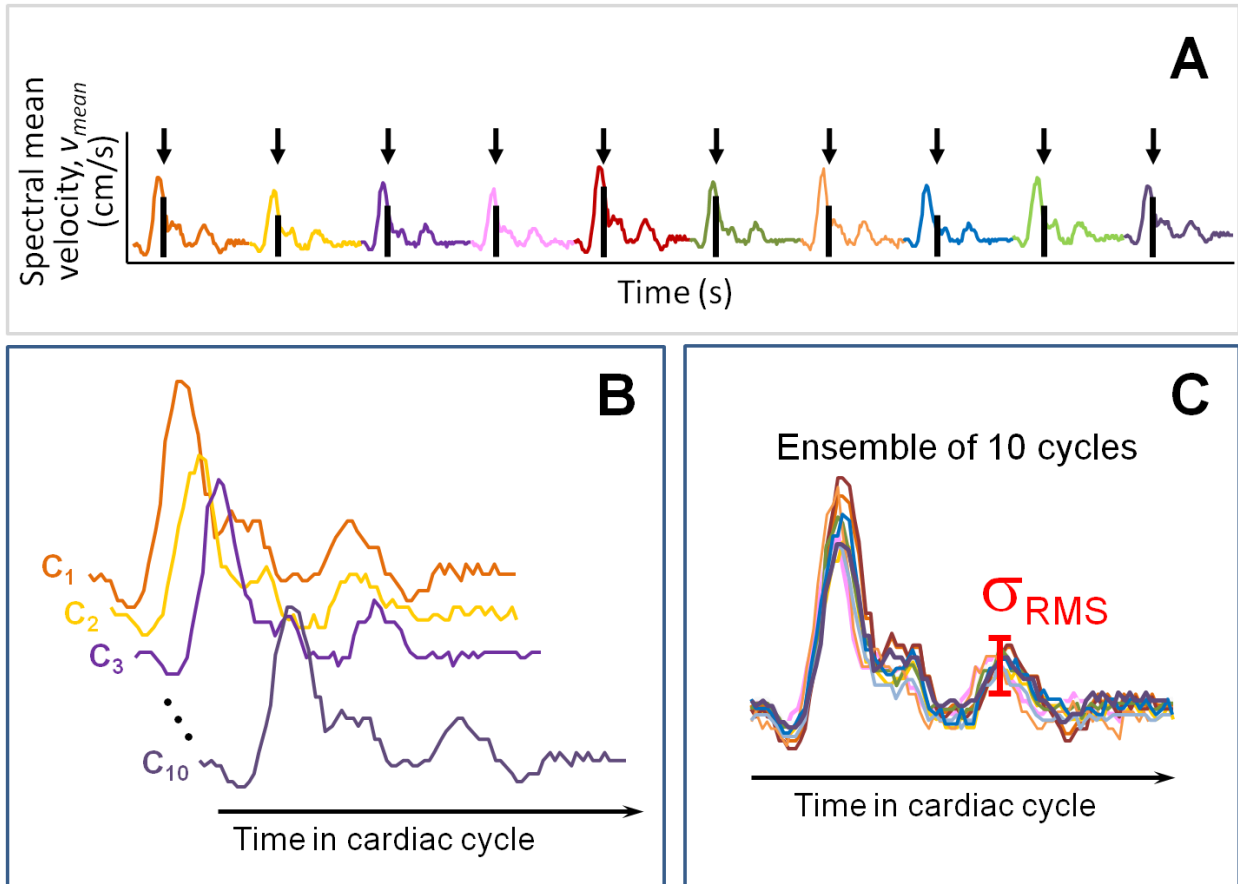


Figure C.1: (a) Cardiac-gated spectral mean velocity (v_{mean}) over ten successive cardiac cycles allowing for the determination of v_{mean} at the same time point in each cardiac cycle (*black lines and arrows*). (b) The v_{mean} from ten successive cardiac cycles (C_1, C_2, \dots, C_{10}) displayed in terms of cardiac cycle time for the generation of (c) an ensemble of ten cardiac cycles of data. Turbulence intensity (TI) is calculated as the root-mean-square (RMS) fluctuation in v_{mean} about the ensemble-averaged v_{mean} at a given time point in the cardiac cycle, and is indicated in (c) as σ_{RMS} .

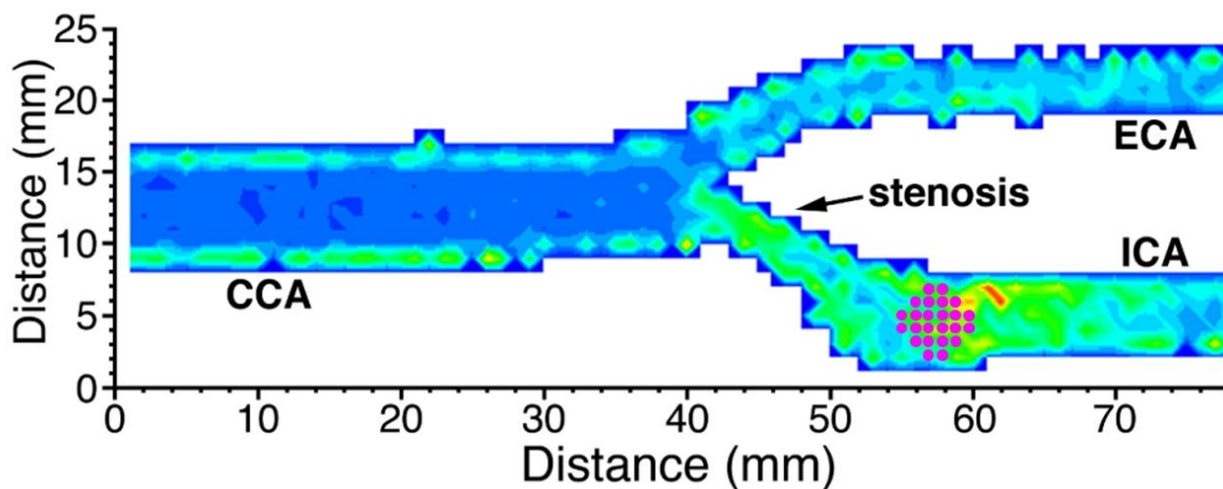


Figure C.2: Schematic indicating the location of the 24 measurement sites in the distal region of interest used for the calculation of \overline{TI}_{24} in Chapter 3 (*pink dots*). The 24 measurement sites used for the calculation of \overline{TI}_{24} in Chapter 4 are located 1 mm more distal to the apex of the bifurcation.

Table C.1: Mean differences and p -values from repeated measures one-way ANOVA post-hoc analysis for the parameters spectral width (SW), spectral broadening index (SBI), standard deviation in peak velocity (SDPV) and turbulence intensity (TI), corresponding to data in Chapter 3. Mean differences (mean Δ) are calculated as the difference in the value of the parameter ($N=240$) within the distal ROI in Model B subtracted from the value of the parameter in Model A, averaged for 79 time points ($N=79$). ns = not statistically significant ($P > 0.05$).

		SW		SBI		SDPV		TI	
Model A	Model B	Mean Δ (cm s ⁻¹)	P value	Mean Δ	P value	Mean Δ (cm s ⁻¹)	P value	Mean Δ (cm s ⁻¹)	P value
No ulcer	2-mm Type 1	15.1	< 0.001	0.055	< 0.001	22.0	< 0.001	3.06	< 0.001
No ulcer	3-mm Type 1	23.6	< 0.001	0.084	< 0.001	33.9	< 0.001	4.66	< 0.001
No ulcer	4-mm Type 1	41.6	< 0.001	0.135	< 0.001	47.6	< 0.001	5.40	< 0.001
No ulcer	Type 2	4.5	ns	-0.004	ns	10.1	< 0.001	3.00	< 0.001
No ulcer	Type 3	11.6	< 0.001	0.067	< 0.001	27.1	< 0.001	3.81	< 0.001
No ulcer	Type 4	12.8	< 0.001	0.040	< 0.001	20.4	< 0.001	3.21	< 0.001
2-mm Type 1	3-mm Type 1	8.5	< 0.05	0.028	< 0.01	11.9	< 0.001	1.60	< 0.001
2-mm Type 1	4-mm Type 1	26.5	< 0.001	0.080	< 0.001	25.6	< 0.001	2.34	< 0.001
2-mm Type 1	Type 2	-10.6	< 0.01	-0.059	< 0.001	-11.9	< 0.001	-0.06	ns
2-mm Type 1	Type 3	-3.5	ns	0.012	ns	5.1	ns	0.75	< 0.01
2-mm Type 1	Type 4	-2.3	ns	-0.015	ns	-1.6	ns	0.15	ns
3-mm Type 1	4-mm Type 1	18.0	< 0.001	0.051	< 0.001	13.7	< 0.001	0.74	< 0.01
3-mm Type 1	Type 2	-19.1	< 0.001	-0.087	< 0.001	-23.8	< 0.001	-1.66	< 0.001
3-mm Type 1	Type 3	-12.0	< 0.001	-0.016	ns	-6.8	< 0.05	-0.85	< 0.01
3-mm Type 1	Type 4	-10.8	< 0.01	-0.044	< 0.001	-13.5	< 0.001	-1.45	< 0.001
4-mm Type 1	Type 2	-37.1	< 0.001	-0.139	< 0.001	-37.5	< 0.001	-2.41	< 0.001
4-mm Type 1	Type 3	-30.0	< 0.001	-0.068	< 0.001	-20.5	< 0.001	-1.59	< 0.001
4-mm Type 1	Type 4	-28.8	< 0.001	-0.095	< 0.001	-27.2	< 0.001	-2.20	< 0.001
Type 2	Type 3	7.1	ns	0.071	< 0.001	17.0	< 0.001	0.82	< 0.01
Type 2	Type 4	8.3	< 0.05	0.043	< 0.001	10.3	< 0.001	0.21	ns
Type 3	Type 4	1.2	ns	-0.027	< 0.01	-6.7	ns	-0.61	ns

Appendix D

Computational Fluid Dynamics (CFD) Mesh Independence Study

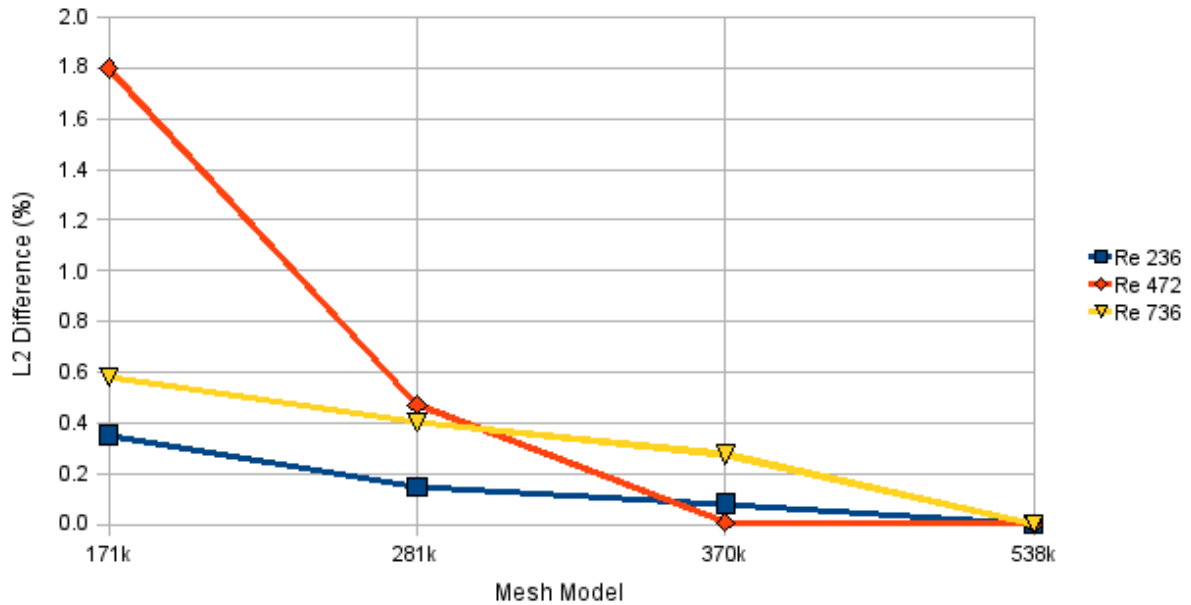


Figure D.1: The difference in three-component computed L_2 for each mesh (171k, 281k and 370k elements) at mean Re (blue squares), twice mean Re (red diamonds) and peak Re (yellow triangles) steady flow versus the highest resolution (538k elements) mesh velocity field.

Curriculum Vitae

Name: Emily Yee-Wah Wong

Place of birth: Vancouver, British Columbia, Canada

Post-secondary Education and Degrees: 2000 – 2005 (Hon.) **B.Sc.**
Biophysics
The University of British Columbia
Vancouver, British Columbia, Canada

2005 – 2011 **Ph.D.**
Graduate Program in Medical Biophysics
The University of Western Ontario
London, Ontario, Canada

Honours and Awards:

2005 – 2009 Western Graduate Research Scholarship

2007 – 2009 Schulich Scholarship for Medical Research

2007, 2008 Margaret Moffat Graduate Research Day Poster Awards

2008 – 2010 Ontario Graduate Scholarship

2008 – 2010 Schulich Ontario Graduate Scholarship

2008 Western Research Forum Award for Oral Presentation

2009 – 2010 Canadian Institutes of Health Research Frederick Banting and Charles Best Canada Graduate Scholarships Doctoral Award

2009 – 2011 Heart and Stroke Foundation of Canada Doctoral Research Award (declined)

2009 J. Allyn Taylor Symposium Cardiovascular Poster Competition Poster Award

- 2009 Institute of Circulatory and Respiratory Health's (ICRH's) Young Investigators Research Forum – Heart and Stroke Foundation of Canada Best Lay Summary Award
- 2009 ICRH's Young Investigators Research Forum Poster Award
- 2009 ICRH's Young Investigators Research Forum Travel Award

Related work experience:

- 2008 – 2010 **Teaching Assistant**
 Department of Medical Biophysics
 The University of Western Ontario
 London, Ontario, Canada

Publications:

Peer-reviewed Journal Articles

1. **Wong, E.Y.**, H.N. Nikolov, M.L. Thorne, R.N. Rankin, T.L. Poepping, and D.W. Holdsworth. Clinical Doppler ultrasound for the assessment of plaque ulceration in the stenosed carotid bifurcation by detection of distal turbulence intensity: a matched model study. *Eur Radiol* 2009, 19(11): 2739-2749.
2. **Wong, E.Y.**, M.L. Thorne, H.N. Nikolov, T.L. Poepping, and D.W. Holdsworth. Doppler ultrasound compatible plastic material for use in rigid flow models. *Ultrasound Med Biol* 2008, 34(11): 1846-1856.
3. Poepping T.L., M.L. Thorne, **E.Y. Wong**, R.N. Rankin, and D.W. Holdsworth. Recent flow analysis studies in vascular models using Doppler ultrasound. *Canadian Acoustics* 2007;35(2):25-34.

Refereed Conference Proceedings

1. Hussain, B., **E.Y. Wong**, and T.L. Poepping. “Numerical design and evaluation of vector Doppler ultrasound systems for accurate 3-D velocity measurements”, *Proceedings of IEEE International Ultrasonics Symposium: Vector Flow Imaging Methods*, San Diego, California, Sept 2010, paper no. 1023.

2. **Wong, E.Y.**, J.S. Milner, D.A. Steinman, T.L. Poepping, and D.W. Holdsworth. "Characterization of 3-D flow structures in the stenosed carotid bifurcation with plaque ulceration", *Proceedings of IEEE International Ultrasonics Symposium: Blood Flow Measurement*, Rome, Italy, Sept 2009, paper no. 1246.
3. **Wong, E.Y.**, J.S. Milner, D.A. Steinman, T.L. Poepping, and D.W. Holdsworth. "Numerical analysis of the hemodynamic effect of plaque ulceration in the stenotic carotid artery bifurcation", *Proceedings of SPIE Medical Imaging 2009: Visualization, Image-guided Procedures and Modeling*, Orlando, Florida, February 2009, paper no. 7261-66.
4. **Wong, E.Y.**, J.S. Milner, M.L. Thorne, H.N. Nikolov, T.L. Poepping, R.N. Rankin, and D.W. Holdsworth. "Doppler ultrasound and numerical analysis for the assessment of hemodynamic disturbances in ulcerated carotid arteries", *Proceedings of IEEE International Ultrasonics Symposium: Blood Flow Measurement*, Beijing, China, November 2008, paper no. 451.
5. **Wong, E.Y.**, M.L. Thorne, H.N. Nikolov, T.L. Poepping, R.N. Rankin, and D.W. Holdsworth. "Investigation of Doppler-ultrasound velocity-based indices for carotid plaque ulcerations using in vitro flow models", *Proceedings of IEEE International Ultrasonics Symposium: Blood Flow Measurement*, Vancouver, British Columbia, October 2006, paper no. 955.

Other Presentations

1. **Wong, E.Y.**, H.N. Nikolov, R.N. Rankin, T.L. Poepping, and D.W. Holdsworth. "An in vitro flow study on the interrelationship of carotid plaque surface ulceration and stenosis severity on Doppler ultrasound turbulence intensity", European Stroke Conference, Barcelona, Spain, May 2010 (oral).
2. **Wong, E.Y.**, J.S. Milner, D.A. Steinman, T.L. Poepping, and D.W. Holdsworth. "Numerical analysis of hemodynamic disturbances in the atherosclerotic carotid artery with plaque ulceration", J. Allyn Taylor Symposium, London, Ontario, Nov 2009 (poster).
3. **Wong, E.Y.**, J.S. Milner, D.A. Steinman, T.L. Poepping, and D.W. Holdsworth. "3-D Blood flow patterns in the diseased carotid artery", Institute of Circulatory and Respiratory Health's Young Investigators Forum, Ottawa, Ontario, May 2009 (poster).

4. **Wong, E.Y.**, J.S. Milner, D.A. Steinman, T.L. Poepping, and D.W. Holdsworth. “Effect of plaque ulceration on 3-D blood flow patterns in the atherosclerotic carotid artery determined by computational fluid dynamics”, Margaret Moffat Graduate Research Day, London, Ontario, March 2009 (poster).
5. **Wong, E.Y.**, J.S. Milner and D.W. Holdsworth. “Analysis of hemodynamic disturbances associated with ulcerated atherosclerotic carotid arteries”, Western Research Forum, London, Ontario, March 2008 (oral).
6. **Wong, E.Y.**, J.S. Milner and D.W. Holdsworth. “Analysis of hemodynamic disturbances and thrombogenic factors in ulcerated atherosclerotic carotid arteries”, Margaret Moffat Graduate Research Day, London, Ontario, March 2008 (poster).
7. **Wong, E.Y.**, J.S. Milner and D.W. Holdsworth. “CFD for the assessment of hemodynamic disturbances in ulcerated atherosclerotic carotid arteries”, Canadian Student Conference on Biocomputing, Toronto, Ontario, March 2008 (poster).
8. **Wong, E.Y.**, M.L. Thorne, H.N. Nikolov, T.L. Poepping, R.N. Rankin, and D.W. Holdsworth. “A statistical comparison of Doppler ultrasound turbulence intensity for various carotid plaque ulcer geometries in in vitro studies”, IEEE International Ultrasonics Symposium, New York City, New York, October 2007 (poster).
9. **Wong, E.Y.**, M.L. Thorne, H.N. Nikolov, T.L. Poepping, R.N. Rankin, and D.W. Holdsworth. “Investigation of Doppler-ultrasound turbulence intensity for carotid plaque ulceration geometry using in vitro flow models”, London Imaging Discovery conference, London, Ontario, June 2007 (poster).
10. **Wong, E.Y.** and D.W. Holdsworth. “An in vitro investigation of carotid plaque ulcerations using Doppler ultrasound”, New England Doppler conference, Maastricht, Netherlands, May 2007 (oral).
11. **Wong, E.Y.**, M.L. Thorne, H.N. Nikolov, T.L. Poepping, R.N. Rankin, and D.W. Holdsworth. “Investigation of Doppler-ultrasound turbulence intensity for carotid plaque ulceration geometry using in vitro flow models”, Margaret Moffat Graduate Research Day, London, Ontario, March 2007 (poster).
12. **Wong, E.Y.** and D.W. Holdsworth. “In vitro investigation of Doppler ultrasound velocity-based indices for the detection of hemispherical plaque ulcerations”, Canadian Student Conference on Biocomputing, London, Ontario, March 2007 (oral).

13. **Wong, E.Y.** and D.W. Holdsworth. “Investigation of carotid plaque ulcerations using Doppler ultrasound flow models”, Robarts Research Day, London, Ontario, February 2007 (poster).
14. **Wong, E.Y.**, M.L. Thorne, H.N. Nikolov, T.L. Poepping, and D.W. Holdsworth. “Doppler-ultrasound compatible plastic material for use in rigid flow models”, London Imaging Discovery conference 2006, London, Ontario, June 2006 (poster).